

~~N72-14671~~
~~X71-73584~~
NASA CR-116926
~~F71-00068~~

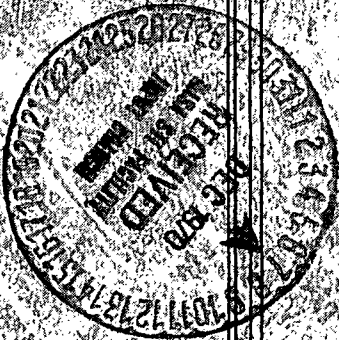
B-678

GUIDANCE AND NAVIGATION REQUIREMENTS
FOR UNMANNED FLYBY AND SWINGBY
MISSIONS TO THE OUTER PLANETS

VOLUME III Low Thrust Missions

MAY 1970

**CASE FILE
COPY**



**CHARLES STARK DRAPER
LABORATORY**

MASSACHUSETTS INSTITUTE OF TECHNOLOGY

CAMBRIDGE, MASSACHUSETTS 02139

GUIDANCE AND NAVIGATION REQUIREMENTS FOR UNMANNED

FLYBY AND SWINGBY MISSIONS TO THE OUTER PLANETS

(Final Technical Report on Phase B of Contract NAS-2-5043)

VOLUME III LOW THRUST MISSIONS

May 1970

CHARLES STARK DRAPER LABORATORY

MASSACHUSETTS INSTITUTE OF TECHNOLOGY

CAMBRIDGE, MASSACHUSETTS

Approved:

Donald C. Fraser Date: 19 October 1970

Dr. Donald C. Fraser, Program Manager

Approved:

David G. Hoag Date: 26 Oct 70

David G. Hoag, Associate Director

Charles Stark Draper Laboratory

Approved:

Ralph R. Ragan Date: 26 Oct 70

Ralph R. Ragan, Deputy Director

Charles Stark Draper Laboratory

ACKNOWLEDGEMENT

This report was prepared under DSR Project 55-32700, sponsored by the Ames Research Center, National Aeronautics and Space Administration through Contract NAS 2-5043.

The following are the contributors to this Phase B technical report:

Donald C. Fraser
Harvey L. Malchow
Patricia C. Pollock
Lester L. Sackett
Richard Tompkins
Michael Venturino
M. Edward Womble

The publication of this report does not constitute approval by the National Aeronautics and Space Administration of the findings or the conclusions contained therein. It is published only for the exchange and stimulation of ideas.

ABSTRACT

This volume reports the results of a study of guidance and navigation requirements for unmanned missions to the outer planets, assuming constant, low thrust, ion propulsion. The objective of the study is to examine the navigational capability of the ground based Deep Space Network in relation to the improvements in navigational capability brought about by the addition of guidance and navigation related onboard sensors. Relevant onboard sensors include the optical onboard navigation sensor, the attitude reference sensors, and highly sensitive accelerometers.

The totally ground based, and the combination ground based and onboard sensor systems are compared by means of the estimated errors in target planet ephemeris, and the spacecraft position with respect to the planet. Comparisons are made for two missions:

- a) Jupiter Orbiter,
- b) Saturn Orbiter,

and each mission is divided into interplanetary and near planet legs. The near planet leg does not include the orbital phase.

The results show that onboard navigation produces substantial fractional reductions in planet arrival errors based on purely DSN data, but these are already small. Consequently onboard navigation cannot be justified purely from a navigational standpoint. Onboard accelerometers are shown to reduce navigation errors by aiding in the reduction of thrust vectoring errors and spacecraft mass uncertainty. The results assume one arcminute attitude control by the attitude control system. It is also shown that first perturbation guidance is adequate to null reasonable trajectory perturbations.

Page intentionally left blank

TABLE OF CONTENTS

ABSTRACT	PAGE
CHAPTER 1. INTRODUCTION	1
CHAPTER 2. THE SIMULATION MODEL	7
2.1 General Remarks	7
2.2 Statistical Model	8
2.3 Navigational Uncertainties	9
2.4 Navigation	9
2.5 The Nominal Trajectory	10
2.6 Guidance	11
2.6.1 General Remarks	11
2.6.2 A Nonoptimal Scheme	12
2.6.3 Optimal Perturbation Schemes	13
2.7 Organization of Computation Procedure	14
CHAPTER 3. ONBOARD SENSOR STUDIES	17
3.1 Accelerometers	17
3.2 Attitude Control Sensors	20
3.3 Onboard Navigation	26
CHAPTER 4. MISSION SIMULATION RESULTS	29
4.1 Introduction	29
4.2 Tables of Results	29
4.3 Jupiter Interplanetary Results	34
4.4 Jupiter Near Planet Results	37
4.5 Saturn Interplanetary Results	38
4.6 Saturn Near Planet Results	39
CHAPTER 5. CONCLUSIONS AND RECOMMENDATIONS	43
APPENDIX A DYNAMICS	47
APPENDIX B INTERPLANETARY TRAJECTORY GEOMETRIES	51

APPENDIX C	PLANETARY PASSAGE TRAJECTORY GEOMETRIES	67
APPENDIX D	STATISTICS	87
D.1	State	87
D.2	Variational Equations	88
D.3	Statistical Propagation	94
D.4	Coordinate Change	98
D.5	Accelerometer Measurements	99
D.6	DSN Measurements	102
D.7	Onboard Measurements	105
D.8	Measurement Selection	107
APPENDIX E	GUIDANCE	113
E.1	Nominal Suboptimal Control	113
E.2	A Non optimal Perturbation Guidance Scheme	117
E.3	Terminal Controller with Quadratic Cost	123
APPENDIX F	GUIDANCE SENSITIVITY RESULTS	125
F.1	Introduction	125
F.2	Characteristics of the Plots	126
F.3	Example 1	128
F.4	Example 2	131
APPENDIX G	ONBOARD SYSTEMS CONFIGURATIONS	191
G.1	Navigation Sensor, Weight, Power, Volume	191
G.2	Low Thrust Accelerometers	192
G.3	Thrust Vector Misalignment	198
REFERENCES		203

CHAPTER 1

INTRODUCTION

The study reported in this volume represents the second phase of a sequence of studies funded by NASA under contract NAS2-5043, and directed by the Mission Analysis Division of the Office of Advanced Research and Technology. The first part (or Phase A) of the study was concerned with guidance and navigation requirements for outer planet missions in which trajectory corrections are made exclusively by means of short duration, impulsive velocity changes after transplanetary injection. Missions studied under Phase A included a Jupiter flyby, a Jupiter swingby to Saturn, and a four planet grand tour. The second (or Phase B) part of the study, reported in this volume, is also concerned with guidance and navigation requirements, but for missions involving spacecraft with constant low-thrust propulsion. The Phase B studies considered direct missions to Jupiter and Saturn. The analysis of a Neptune mission was not completed due to computational problems and contract time limitations. The total trajectory for each mission is an optimized combination of chemical propulsion and low thrust propulsion. The chemical propulsion is used for planet departure and planet arrival while the low thrust is used for the interplanetary stage. The use of high thrust chemical propulsion avoids the need for a spiral type of planetary departure and arrival maneuver. This report concentrates on the low thrust portion of the missions.

For the Phase B studies, the general objectives have been the same as for Phase A, namely:

- 1) determine the characteristics associated with (a) totally Earth-based, and (b) a combination of Earth-based and onboard navigation concepts;
- 2) determine the associated navigation and guidance subsystem weight, power, and volume for representative navigation and guidance subsystem concepts applied to mission objectives;

- 3) determine the accuracy requirements placed on the midcourse propulsion and attitude control subsystems by each of the above combinations;
- 4) perform trade off analyses which compare on a total guidance and navigation subsystem basis, the three navigation concepts for each nominal mission, considering both the heliocentric and near planet portions of the missions.

In addition to these general objectives, there was a requirement in Phase B to develop a suitable guidance control algorithm for the low thrust missions.

Some of the interesting characteristics of the low thrust missions are listed in Table 1.1. The ion thrusters to be used for these missions develop about 6×10^{-3} lbs. of thrust. Applied to a spacecraft with a 10^3 kg mass this thrust gives about 10^{-5} g of acceleration, or about one millionth of the acceleration of a typical high thrust case. The small acceleration levels are offset by the long thrust periods of one to four years as shown in the fourth row of Table 1.1. The combination of low thrust level and long thrust periods produces the substantial ΔV 's shown in the last row of the table. These in turn lead to the shorter flight times listed near the top. For a Jupiter mission, the ion thrust mission is slightly longer than the high thrust, but for Saturn there is a time-savings of over 25%. For flights to planets beyond Saturn, the time savings would increase substantially.

The low constant thrust, with changing direction in the celestial sphere, complicates the equations of motion (see Appendix A) of the spacecraft sufficiently so that they must be integrated numerically. The associated trajectories were supplied by the NASA Mission Analysis Division for these missions. However, the trajectories were reproduced for this study by the MIT Draper Laboratory in order to have nominal trajectory reference points for arbitrary time during the flight, rather than at specific preselected times. This allows changes in measurement schedules and key navigation

Table 1.1

Low Thrust Mission Characteristics

	Missions	
	Jupiter	Saturn
Launch Date	23 Sept. 1979	10 August 1980
Arrival Date	13 Oct. 1981	1 July 1983
Total		
Low Thrust Flight Time (Yr)	2.0	2.7
Direct Ballistic Flight (Yr)	1.7	3.7
Total Thrust on Time (Yr)	1.0	1.7
Periplanet Radius (planetary radii)	2	3
Time Within Sphere of Influence (Days)	65	69
Approximate Total ΔV (km/sec)	9.2	20.8

and guidance systems parameters to be analyzed. The trajectories are fully described in Appendices B and C.

Chapter 2, following this introductory chapter, presents a discussion of the navigation simulation. Included in Chapter 2 are discussions of the computational procedure, the way in which thrust vector misalignment affects the navigation results, problems of extrapolating error covariance matrices, and guidance algorithms that could be applied to these missions. Chapter 3 discusses general problems associated with the design of those onboard sensors which are closely related to guidance and navigation. These sensors include accelerometers, optical attitude control reference sensors, and onboard navigation instruments. Only onboard navigation instruments of the scanning photometer type have been considered for Phase B.

In Chapter 4 the navigation results are presented. Feedback effects on navigation errors are not represented in the results because of an inability to achieve coupling of navigation and guidance simulations within allotted time and computer availability constraints. Results listed include errors in spacecraft position, planetary ephemeris, velocity, spacecraft mass and thrust vector alignment. The listed errors represent the errors at the target planet sphere of influence and at periplanet.

Chapter 5 presents general conclusions, a results summary, and recommended further studies.

The Appendices are in seven sections, and contain the more detailed information about calculations, derivations, trajectories etc. In Appendix A mathematical symbols are defined including coordinate systems and control angles, and the equations of motion of the spacecraft are displayed.

Appendix B contains system related curves for the interplanetary leg of the missions. The curves include trajectories in solar system coordinates, time varying aspect angles between the spacecraft and various

navigation and attitude reference objects, and ranges to planetary satellites. Appendix C contains similar information for the near planet portion of the missions.

In Appendix D the equations used for propagation of statistical errors are derived, including contributions from onboard navigation instruments, the Deep Space Network (DSN), accelerometers, and the uncertainties considered.

Appendix E contains guidance derivations including a derivation of the nominal optimal control, and descriptions of the candidate perturbation guidance schemes.

Appendix F presents a series of curves from which guidance accuracies may be obtained. Since guidance and navigation were not simulated simultaneously for the reasons cited above, the navigational accuracies must be used in conjunction with these plots to approximate the obtainable guidance accuracies. Three pieces of information can be obtained from these curves: 1) the maximum deviation from the reference trajectory which can be corrected by the end of the mission as a function of time to go; 2) the position error which will result at arrival if the maximum deviation is exceeded; 3) the perturbation in the control required to cancel the effects of the deviation from the reference trajectory.

Finally, Appendix G presents system related information on specific accelerometer types and problems in thrust vectoring.

Page intentionally left blank

CHAPTER 2

THE SIMULATION MODEL

2.1 General Remarks

In this chapter is a general discussion of the simulation. The model used, uncertainties considered, the navigational and guidance aspects of the simulation and the organization of the computer program used in the simulations are described. The mathematical details are omitted here and are presented instead in Appendices D and E.

In Phase B, interplanetary propulsion is achieved using the fixed low thrust level which would be characteristic of a nuclear powered ion engine. The nominal trajectories were furnished by the NASA Mission Analysis Division and were determined as the solution to a minimum fuel, fixed terminal time, position, and velocity optimization problem, where the Earth departure and the planet arrival are partly performed by chemical stages. These trajectories are characterized by a long thrusting period, a long coast period, and another thrust period. Since the thrust magnitude is fixed, trajectory error correction is accomplished by steering or varying the thrust on/off switch times.

One aspect of this phase of the study was to develop and incorporate into the simulation a guidance system appropriate to the low thrust missions, and to see if with such a guidance system, deviations from the nominal could be kept sufficiently small. Since there is no control during the coast period and since the missions are long, small velocity errors at the beginning of a coast can grow into large positional errors at the end of the coast period.

As with the high-thrust phase of this study, the navigational aspect of the study involved the relative value of using Earth based radar

measurements (DSN), onboard measurements, or combinations of these two. In addition accelerometer measurements were considered with various combinations of DSN and onboard measurements.

2.2 Statistical Model

In the present phase of the study, a statistical error analysis was performed similar to that done in Phase A. We consider the statistics of first order deviations from a reference trajectory. Since all random processes were assumed Gauss-Markov processes, only second order statistics were necessary. The reference trajectory was the nominal minimum fuel trajectory. Measurements were linearized about the nominal values which were obtained using the mission reference trajectory.

Since for these missions we were using piecewise continuous thrusting, the "mid-course velocity corrections" also represent a piecewise continuous process. Thus, discrete velocity corrections were not incorporated as they were for Phase A. The extrapolation of statistics and the course corrections are combined as the solution of a set of differential equations describing the statistics.

As with Phase A the statistics of interest are $E(t) = \overline{e(t) e(t)^T}$ and $X(t) = \delta \underline{x}(t) \delta \underline{x}(t)^T$ where $\delta \underline{x}(t)$ is the deviation from the nominal and $e(t)$ is the error in the estimate, $\delta \hat{\underline{x}}$, i.e. $e(t) = \delta \hat{\underline{x}}(t) - \delta \underline{x}(t)$. The overbar indicates we are taking the expected value over the ensemble. E is thus the estimation error covariance and X the covariance matrix of deviations from the reference trajectory. In order to write the differential equation for X and E , one must also define other correlation matrices. These are given in Appendix D.

A statistical analysis is required to see what the effects of various initial errors are on the mission outcome. The various uncertainties considered were in thrust vector alignment, mass flow rate, thrust magnitude, planetary or solar mass, destination planet position, and the

spacecraft injection state. The two-dimensional thrust vector misalignment was made part of the 12 dimensional state and was assumed to be driven by white noise with a known covariance. The uncertainty in thrust magnitude was modeled as white noise. The uncertainty in mass flow rate was modeled as white noise plus a bias. The planet and sun mass uncertainties were considered as biases, as were the two dimensional station location errors, which are uncertainties in the longitude and off spin axis distance of the radar stations which make DSN measurements.

2.3 Navigational Uncertainties

Besides the uncertainties which affect the dynamical behavior of the spacecraft, there were uncertainties in the quantities which were used for onboard measurements. These were, for example, uncertainties in planetary radii, satellite radii, planetary horizon altitude, and planet and satellite ephemerides. The incorporation of those uncertainties and the source of values used is discussed in Vol. II, Ch. 2, Sec. C.

2.4 Navigation

The navigational technique and program used for the low-thrust mission simulations is essentially identical to that used in Phase A for the high thrust missions with the exception that accelerometer measurements were used here for navigation purposes. As in Phase A of this study, radar measurements from Earth (DSN) and onboard measurements (e.g. star and planet sightings, planet radii) were used for navigation and their relative worth was compared.

The incorporation of these measurements was done in the same general way as in Phase A, where a nine dimensional state made up of spacecraft position and velocity and target planet position was used. In this phase the state has the above nine components plus the spacecraft mass and two thrust vector misalignment angles. The onboard navigation sensor (except accelerometer) and DSN measurements do not directly measure these last

three components of the state, so that the equations used for navigation were altered only so as to use the 12 dimensional state with zeroes added to the relevant matrices to make them dimensionally consistent.

Accelerometers measure the thrust acceleration. Since a low thrust spacecraft is thrusting over long periods of time and since small deviations in the thrust direction and magnitude would significantly affect the trajectory over these long periods, it was of interest to see how accelerometer measurements affect the navigation error.

Two cases of accelerometer measurement incorporation were considered. In the first it was assumed that 3 accelerometers were used. This gives an estimate of the vector thrust acceleration. The elements of the state directly influenced by this measurement are the mass and the thrust vector misalignment angles. In the second case it was assumed that one accelerometer was mounted along the nominal thrust vector direction. One accelerometer yields information about mass flow rate but little about the misalignment angles. Accelerometer measurements were added to both the DSN only and to the DSN and onboard measurement cases. The derivations and equations are given in detail in Appendix D.

2.5 The Nominal Trajectory

This section discusses the solution of the optimal control problem which results in the nominal trajectory used in the study. Some discussion of the boundary value problem which results is also included.

The problem can be stated as follows. Assume we are given a spacecraft which starts at a given fixed initial time, position and velocity and with a given initial mass, and we wish to find the trajectory which takes the spacecraft to a fixed terminal position and velocity at a fixed terminal time and minimizes fuel consumption. The spacecraft moves in the gravitational field of the sun and one (target) planet. Thrust can be turned on and off and the thrust directions varied, but thrust magnitude is

fixed. This is a well posed problem in optimization theory and is treated mathematically in detail in Appendix E. To solve this problem a seven dimensional state is defined which includes the position and velocity and mass of the spacecraft. The planet position is obtained from an ephemeris.¹ In solving the optimization problem, one also defines a seven dimensional costate. Applying necessary conditions leads to a two point boundary value problem in the state and costate where some components of the state and costate are specified at the initial time and some are specified at the final time. This two point boundary value problem was solved numerically by the NASA Mission Analysis Division, in providing the nominal trajectories.

2.6 Guidance

2.6.1 General Remarks

In this section the nonoptimal guidance system used, and also other guidance schemes which were considered are discussed. "Deterministic" guidance schemes were considered which could be applied to a statistical analysis.

The navigation system is used to determine where the spacecraft is. This information is then acted on by the guidance system to get the spacecraft to its target while meeting various mission criteria. For the missions considered in this study, the target was a particular position and velocity in space at a particular final time. In addition we would like to use as little additional fuel as possible.

The object of the guidance scheme was to determine what the deviational control should be if deviations from the nominal path occur. The deviational or variational control could be either a change in the thrust direction or the switching of the thrust on or off at non-nominal times. It was desired to get a feedback law given by a gain matrix $\Lambda(t)$ such that

$$\delta \underline{u}(t) = \Lambda(t) \delta \underline{x}(t),$$

where $\delta \underline{x}(t)$ is the deviation from the nominal state at time t . Methods were considered for obtaining a change in the switch times, Δt_s , as a function of $\delta \underline{x}(t)$, but the guidance scheme utilized assumed that switches occurred at the nominal times and all guidance was by steering only. Once the gain matrix is developed for the deterministic problem it can be applied to the statistical problem by assuming

$$\delta \underline{u}(t) = \Lambda(t) \hat{\delta \underline{x}}(t)$$

where $\hat{\delta \underline{x}}(t)$ is the estimate of $\delta \underline{x}$. This expression is substituted into the variational differential equations for $\hat{\delta \underline{x}}$ and $\delta \underline{x}$ from which the matrix differential equations for the error covariance matrix

$$E = \overline{\underline{e} \underline{e}^T}$$

$$(\underline{e} = \hat{\delta \underline{x}} - \delta \underline{x})$$

and the deviational covariance matrix

$$X = \overline{\delta \underline{x} \delta \underline{x}^T}$$

are formed.

2.6.2 A Nonoptimal Scheme

A nonoptimal guidance scheme was developed which had as its object the nulling of the components of the deviation in position which are perpendicular to the nominal velocity direction at the final time. The component of position in the direction of velocity is uncontrollable by steering alone. This component could however be diminished by altering the switch times if the last switch has not already occurred. If during the last thrust period we find that we are further from the target than the nominal distance, due to revised spacecraft position knowledge or because the planet is not where we originally thought it to be, it is impossible to arrive at the final

position at the fixed final time using constant thrust. If we are closer than anticipated, however, the engine could be turned off early. The nonoptimal scheme results in a gain matrix (Appendix E) which, when multiplied by the state deviation, gives the constant (in time) control which would null the components of position perpendicular to final nominal velocity at the final time assuming that $\delta \underline{x}$ was not later altered by new measurements or other "random" influences.

Guidance was not included in the statistical results. However, it is possible to get some useful information from the guidance scheme directly (see Appendix F). For example it is possible to specify the maximum state deviations which can be "nulled" (i.e. the positional components perpendicular to the nominal velocity at the final time can be nulled) given a maximum value for the magnitude of the variational control. We can also obtain the values for the two positional components if those maximum state deviations are exceeded. Given a state deviation we can also get the perturbed control angles that would result.

2.6.3 Optimal Perturbation Guidance Schemes

One possibility considered was using a second variation scheme as discussed in Ch. 6 of Bryson and Ho.² Under the assumptions needed for this scheme, a perturbed trajectory is extremal in the sense of the nominal trajectory. For our case this would be a minimum fuel trajectory. However, because we have a constant thrust engine and a fixed terminal time, after the last thrust switch, when the thrust is on for the rest of the trajectory for the nominal case, it is impossible to meet the terminal conditions for certain perturbations. In fact, over this part of the trajectory there cannot be any perturbed optimization of fuel, since the fuel consumption is fixed, the thrust is on until the final time. Thus there are no "neighboring extremals", and the second variational scheme cannot be used over this part of the trajectory. In an actual mission, there would be some ability to throttle the thrust level, although that was not considered in this study.

Another possible optimization scheme is to use a terminal controller. (See Ref. 2, Sec. 5.2.) Here we would fix the switch times at their nominal values. The system would be the linearized variational state equations and the performance index would be made up of a positive definite quadratic form in the terminal deviational state plus an integral of positive definite forms in the deviational state and control. It is possible to get an exact explicit feedback law for this problem. The gain matrix is the solution to a Ricatti equation. Although this method was attempted, (see Appendix E.) it was given up in favor of the nonoptimal scheme discussed earlier due to numerical difficulties in solving the Ricatti equation and lack of time to resolve this difficulty.

2.7 Organization of Computation Procedure

Three programs were used in addition to the main program which performed the error analysis. The first created and stored the reference trajectory. Using this stored information the guidance program then created gain matrices which also were stored. These matrices were used to get the variational control as a function of the state deviations. The third program generated cost matrices used for the measurement selection. Thus the nominal trajectory, gains matrices, and cost matrices were stored for each mission prior to the running of the main program.

Figure 2.1, shows a flow chart of the major elements of the main computer program. The input is the various correlation matrices for the initial injection or the terminal correlation matrices for a previous leg of the same mission. The number of "decision points" is preselected at the time of input. At each decision point the program determines if a DSN or onboard measurement should be taken. If accelerometer measurements are taken during a leg, these are incorporated "continuously", there being no decision on whether or not to incorporate them.

The first step was to extrapolate the correlation matrices to the first decision point. This is done by numerically integrating the matrix differential equations for the various correlation matrices. The effect of the

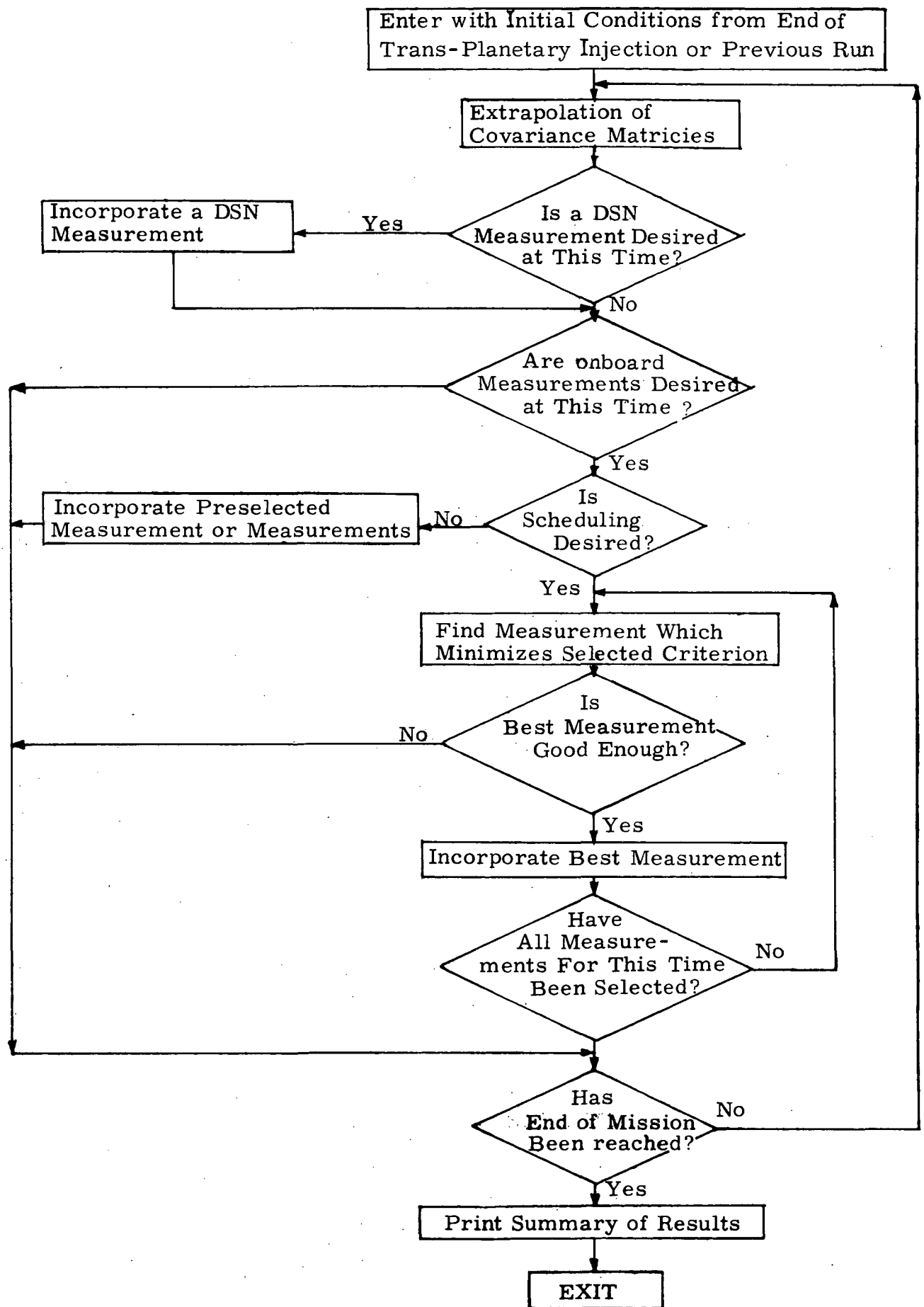


Fig. 2.1 Simulation Logic Diagram

guidance is included in these differential equations. After this, if it is time to incorporate a DSN measurement, this is done. Then the onboard measurement options are considered, i.e., whether to take an onboard measurement or not, and if so, whether to incorporate a predetermined measurement or sequence of measurements, or enter the measurement selection process.

The selection of individual measurements is determined by minimizing the mean squared position estimation error at a preselected target point (usually the destination point). This criterion utilizes the cost matrices which had been computed and stored before running the main program. The details of this process are discussed in the Measurement Selection section of Appendix D. The measurements were chosen from the same types as listed in Vol. II, Ch. II, Sec. E. Namely, 1) planet/moon diameter 2) planet/moon center to star, 3) star occultation, 4) planet/moon limb to star 5) sun-star. Lists of navigational stars and of planetary satellites are given in Vol. II, Table II-7 and 8 respectively. The error associated with making each type of measurement is modeled as an appropriate combination of the basic instrument pointing error and the uncertainty involved in defining a planet limb. Different numerical values are used for each planet and for the dark and light edge sightings. Once the best measurement is found, it is incorporated if it gives a sufficient reduction in the selection criterion. Once the required number of measurements for this decision point have been selected and incorporated, the statistics are extrapolated to the time of the next decision point and the entire process is repeated until all decision points have been processed.

CHAPTER 3

SENSOR SYSTEM STUDIES

In relation to the high thrust outer planet missions, the functional requirements of onboard sensors for the low thrust spacecraft remain essentially unchanged. The same types of sensors are required for attitude control, thrust vectoring, navigation, etc. However, changes in the sensor operational environment due to the long period continuous thrusting have a number of new implications for the system design. For example the changing thrust vector orientation throughout the flight implies that the thrusters and communications antenna have to be gimballed with respect to each other. Arbitrary beam pointing with respect to a fixed spacecraft attitude will lead to unwanted torques, and therefore communication antenna gimbaling appears likely. This raises the possibility that the location of the spacecraft inertial centroid will be changed as the antenna is rotated, and a feedback problem involving torque reduction, thrust vectoring, and antenna pointing will be produced. Changes in the sensor operational environment for ion thrust missions also imply long life requirements for certain other design changes. Requirements placed on the various navigation and guidance related sensors are the subjects of this section.

3.1 Onboard Accelerometers

The placing of highly sensitive accelerometers on the ion thrusted spacecraft results in improved navigation by means of reduction in the thrust vector misalignment. The accelerometer sensitive axes can be precision aligned with respect to attitude control optical sensors to within a few seconds of arc. Thrust direction with respect to the accelerometer axes can then be accurately determined depending on accelerometer accuracy, and can be referenced to celestial coordinates via the attitude control system. Although the low thrust acceleration places requirements on the accelerometers that depend on the mode of usage, the accelerometer

sensitivity levels necessary to achieve a given thrust vectoring accuracy are directly established by the nominal thrust acceleration level of 10^{-5} g's. From Figure G.2 of Appendix G it can be seen that 2 arcsecond thrust vectoring (assuming that the attitude control system is good enough) requires an accelerometer with 10^{-10} g sensitivity. Requirements on null bias measurement and scale factor accuracy depend on the attitude control system accuracy and the details of the measurement process. First order null bias effects can be calibrated to sufficient accuracy by allowing momentary thrust interruptions. In time there will, of course, be bias drifts, and as a consequence, the null calibration rate will have to be geared to drift rates. These in turn may have to be determined in flight under actual working conditions. Second order null variations will be caused by fluxuations in the thermal environment control, and also there will be apparent second order null fluxuations related to the limiting accuracy of null calibrations. In a pulsed type accelerometer, null calibration accuracy is limited by pulse rate variations and pulse energy variations which are due to fluxuations in the trigger level voltage, the pulse generating electronics, and the pulse counting device. One of the driving sources of these fluxuations will be temperature variations. To decide how to calibrate null with maximum expediency it will be necessary to study the trade between short thrust shutdowns and their associated small smoothing time, and long thrust interruptions which would allow larger samples to be taken, but which might require that a separate attitude control system be turned on, which would in turn degrade thrust pointing from a previously well established vectoring. However null is calibrated, there will result a residual null uncertainty which will be an estimated noise source for thrust vectoring at a level of some small percentage of the null measurement.

Accelerometer scale factor accuracy determination presents a similar, and in some ways more difficult problem to that of null bias measurement. There will be mechanical scale factor errors which at a given output is equivalent to a null bias. Unfortunately there is no simple independent standard against which scale factor errors can be calibrated. Several possibilities suggest themselves. The gravity gradient could be

used in the period just after trajectory injection, however, there would be drifts in the resulting value later in the flight when gravity gradient was too small to use as a reference. Accelerometers could be mounted on tracks allowing them to be moved outward from the spacecraft center of mass by precision amounts, thus using the self gravitation of the craft as a reference. This procedure would be seriously complicated by complex gravitational fields caused by spacecraft asymmetries for a 3-orthogonal-accelerometer system. Scale factor bias errors are unimportant with regard to thrust pointing as long as they are identical for each accelerometer of the set. This suggests that the accelerometers might be gimballed as a set and placed and calibrated in identical positions to make the scale factor biases equal. Residual scale factor fluxuations are treated as a random noise source.

Although it is easy to speculate on the process of calibrating accelerometers at the 10^{-10} g level, examination of some of the g levels intrinsic to the ion propulsion situation illustrates the smallness of 10^{-10} g in relation to some of the other force levels that might occur. For example the surface gravity of a 10^3 kg sphere with a 1 meter radius is about 10^{-8} g's. If the sphere is rotating at 1 arcsecond/second, the centrifugal acceleration is roughly 10^{-7} g's. This implies that spacecraft rotational oscillations within an attitude control deadband would result in strong accelerometer outputs that varied over the deadband cycle unless, of course, the accelerometers are located at the center of rotation. Gravity gradient force near earth, with a 1 meter separation between the spacecraft center of mass and the accelerometer, would be of the order of 10^{-7} g.

Processing of the accelerometer output represents another problem area. For pulsed rebalance accelerometers, pulses would be counted and averaged over an interval the length of which depends on the pulse frequency and variability, and also on the drift rates. The variance on null and scale factor fluxuations could be determined early in the flight, and would serve to establish the sampling interval from a statistical standpoint. Bias drifts could be determined only by independent measurements. If thrust magnitude

is relatively drift free it might be used to detect scale factor bias drift. As a basis for this study it has been assumed that accelerometer pulses would be counted and stored for several days and then be transmitted to earth along with null bias calibration data taken at the beginning and end of each sample interval. Fluxuations in null and scale factor were assumed to have an rms value of $3 \times 10^{-7} g$. Uncalibrated bias errors were assumed to be about 1% of the rms noise or $3 \times 10^{-9} g$ and were not treated separately in the mathematical model. Figure 3.1 illustrates the rate of decrease of thrust vector misalignment as governed by the accelerometers. Because of numerical problems in the DSN incorporation, the ability of DSN measurements to decrease thrust vector misalignment uncertainties was fixed around the one arcminute level. The significant feature of the figure is that the three accelerometer system drops the thrust vectoring error down very rapidly immediately after injection.

3.2 Attitude Control Sensors

The results presented in Chapter 4 show marked decreases in position and ephemeris errors when accelerometers are added to the spacecraft system. Implicit in these improved values are two assumptions regarding the attitude sensor accuracy. First, that the attitude sensor accuracy is as good as, or better than, the angular accelerometer thrust vectoring and, secondly, that the attitude sensors have one arcminute absolute accuracy early in the mission. The point of these assumptions is that the Deep Space Network can establish thrust vectoring eventually to an accuracy of about three arcminutes, but for this source of control it is only required that the attitude sensors be capable of few arcminute relative accuracy. Conversely, with accelerometers as the source of thrust vector control, it is required to have sufficient absolute accuracy to give thrust vectoring with respect to celestial coordinates. Thus, the addition of accelerometers to the system is seen to strongly affect attitude sensor design. Further improvement in the results can be obtained if the accelerometers can operate at or near the ultra low g region. At $10^{-10} g$, the accelerometers are yielding two arcsecond thrust alignment according to Figure G.2. The limiting

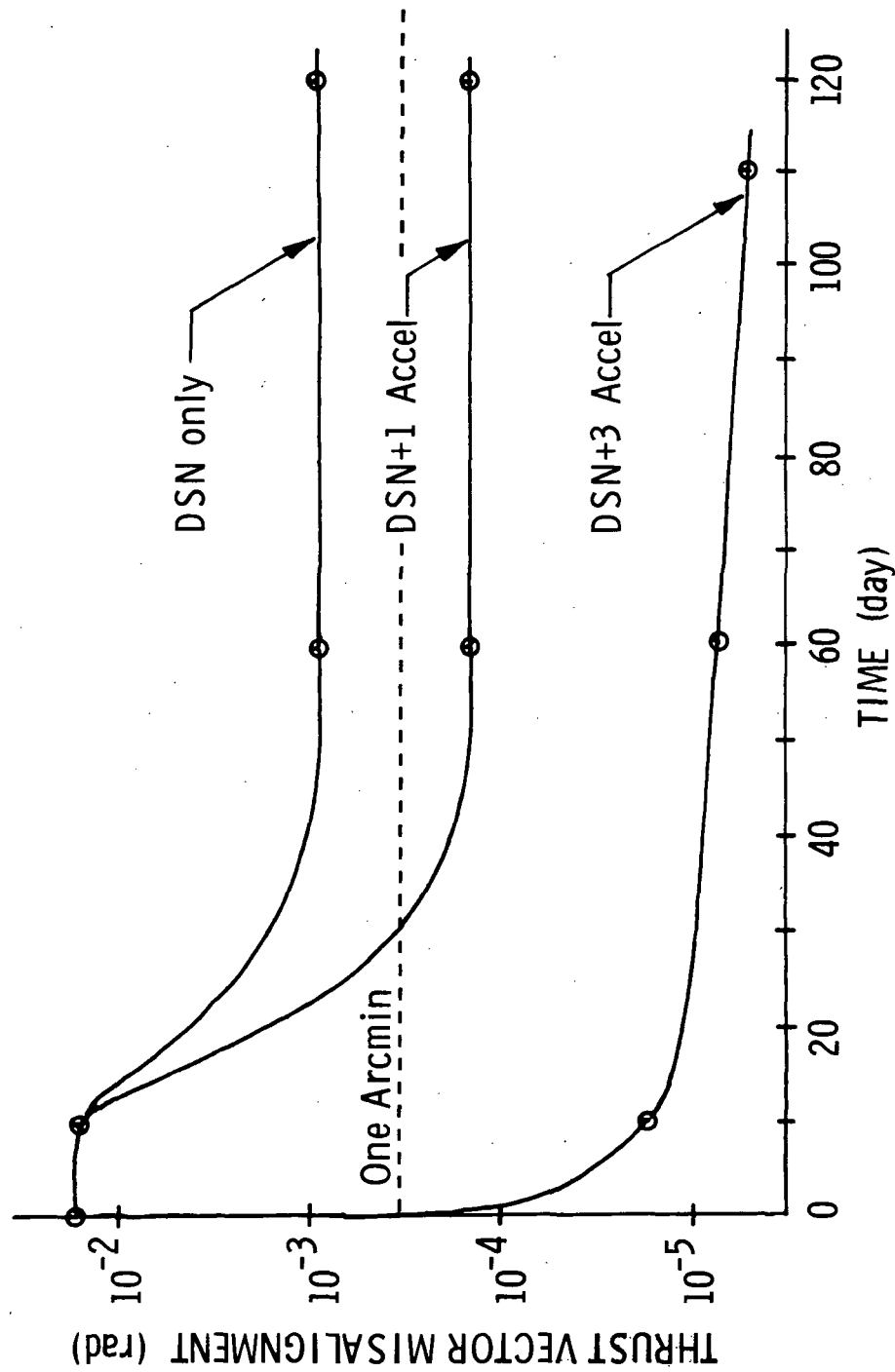


Fig. 3.1 Accelerometer Effects on Thrust Vector Misalignment

attitude, and therefore thrust pointing accuracy, would then depend on how accurately the attitude sensors and accelerometers could be aligned, and how accurate the attitude sensors were. The attitude control system would not necessarily be called upon to maintain a tight, few-arcsecond deadband but would be required to keep the deadband accurately centered and predictably oscillatory.

The attitude reference bodies will presumably be the sun and the star Canopus. Numerous sensors have been designed around these two objects, and there should be only a moderate problem obtaining sufficiently accurate sensors to match a 10^{-10} , two arcsecond, accelerometer output.

Star trackers with accuracies in the few arcsecond range are available.³ The field of view of star trackers in this range is generally on the order of 10 by 10 arcminutes which would be adequate for attitude control at the one arcminute level or lower. A simple sun sensor of the critical angle prism type has been built and tested for the Apollo Advanced Application Program by Honeywell. This device has a demonstrated accuracy of 2.5 arcseconds at one astronomical unit, but would degrade proportionally to the solar-spacecraft range. Maintaining high accuracy over a greater range would probably require a masking device using matched detectors which can be matched to within 1% thereby making the sensor accurate to within 1% of its approximately one-dimensional field of view. A number of sun sensors of this variety are described in Koso and Kollodge.⁴

Strapped-down ion thrusters, thrusting over a wide range of spacial directions for long periods, require the addition of wide total field of view coverage by the optical attitude sensors. Figs. 3.2 and 3.3 show respectively the motions of the star Canopus and the sun with respect to sun-velocity coordinates. Since the thrust vector is held at a relatively fixed angle with respect to the spacecraft velocity vector, the Canopus-velocity system (Fig. 3.2) gives a picture of how Canopus would move with respect to coordinates fixed on the spacecraft. The graphs are in polar coordinates with the polar angle indicating azimuth with respect to the indicated direction,

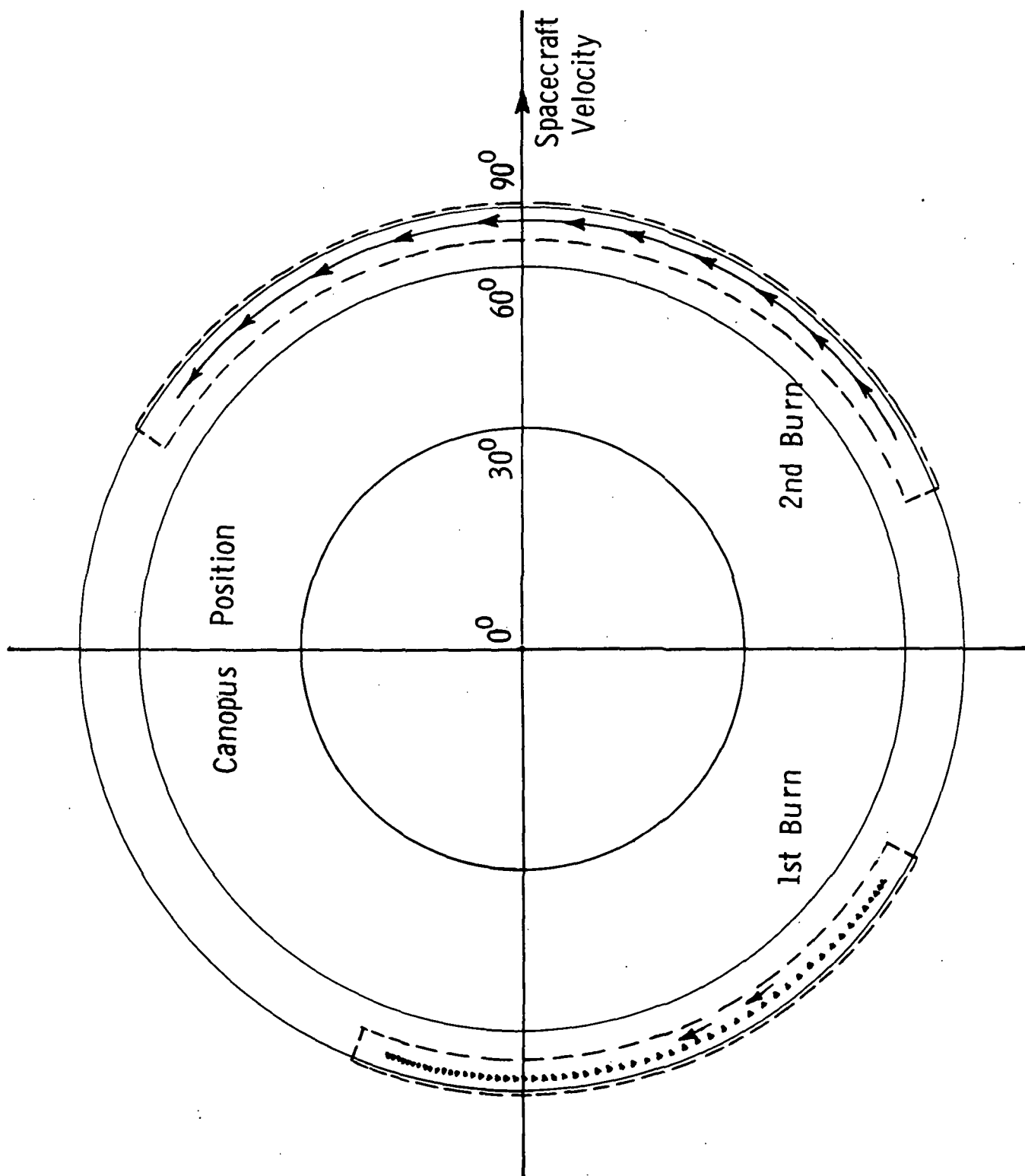


Fig. 3.2 Canopus Position During Thrust

and the radius indicating the out-of-plane component of angle with zero angle in the plane. The plane on the paper is essentially the ecliptic plane since it is defined by the vector product of the sun-spacecraft vector and the spacecraft velocity vector. Canopus (Fig. 3.2) is about 80° out of the ecliptic plane, and moves over an azimuth of about 80° during the first burn, and 120° during the second. The out-of-plane motion amounts to only a few degrees. If there were no thrust vector control for guidance purposes, the attitude reference star tracker would be required to have gimbaling about just one axis. However, guidance thrust control could add 10° to each direction thus requiring two rotational degrees of freedom for the star tracker to cover the area indicated in Fig. 3.2 by the dashed lines. Figure 3.3 shows that a sun sensor would need to have the capability of covering about half the in-plane circle, and $+15^\circ$ out of plane. The out-of-plane coverage is about at the limit attainable by a strapped down sun sensor. Since these devices are small, the possibility exists of placing a gang of sun sensors around the craft to give the required azimuthal field of view. In effect, the azimuth sensing problem would be handed off from one strapped down sensor to the next, thus stepping the thrust vector in discreet increments over the flight. The total weight of a gang of strapped down sun sensors would probably weigh about as much as a single gimbaled sensor, and would have the advantage of no moving parts.

Some other general problems with attitude optical sensors include the requirements for reliable continuous operation for periods of years, problems of shielding from the radio thermal generator power source, a changing solar signal level by a factor of one thousand on a Neptune mission, and the design of a feedback control system for attitude control using the ion thrusters. For purposes of alignment, and the avoidance of launch stress problems, it would be ideal to assemble and check out the attitude-thrust vectoring system in earth orbit. In addition to the low thrust control there will probably be a requirement for a separate set of attitude thrusters and an inertial attitude reference unit to handle the craft during wake up or reacquisition sequences, and during solar occultation at planet passage.

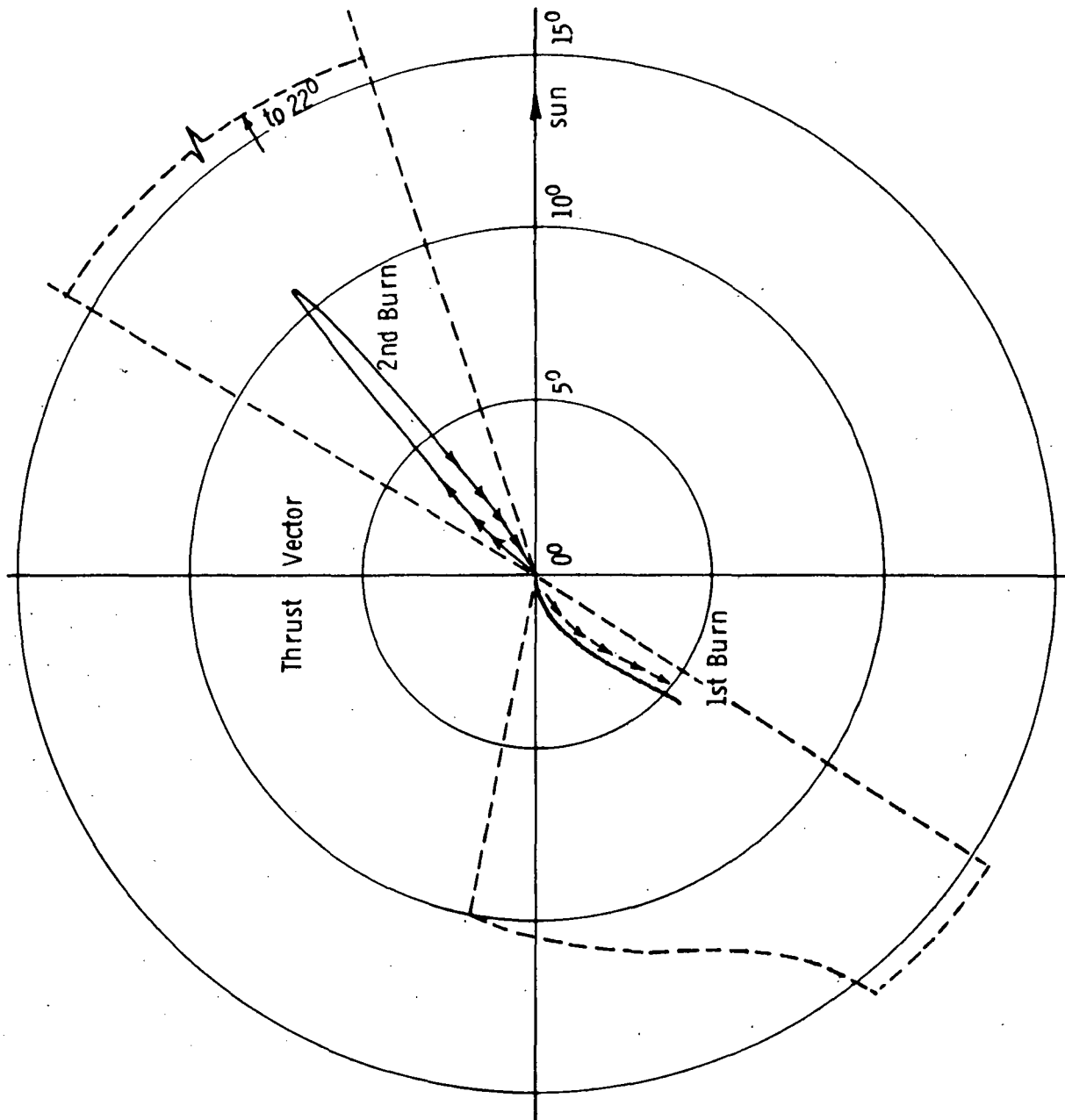


Fig. 3.3 Thrust Position During Thrust

3.3 Navigation Sensor

Examination of the navigation results given in Chapter 4 shows that onboard navigation has limited utility for error reduction. Position errors with respect to the target planet are reduced by factors of 2 to 15, but the errors that are being reduced are already in the few kilometer range, and it is therefore questionable whether further reductions are necessary. The onboard navigation system also reduces ephemeris errors early in the mission, and this reduction is directly related to the instrument accuracy. A one arcsecond instrument reduces ephemeris error by a factor of two during the Jupiter interplanetary leg, however, the ultimate reduction is limited by the uncertainty in spacecraft position as determined by the Deep Space Network.

The strongest argument for the inclusion of onboard navigation on these missions is that the navigation sensor can also be used as a scientific instrument. A scanning photometer navigation sensor can gather extremely important data about the upper atmosphere of the outer planets by means of planet limb scans. Onboard navigation may also play a useful role in the guidance scheme by reducing ephemeris errors early in the mission.

Given, as a result of overall mission considerations, that onboard navigation is used with the low thrust spacecraft, a few design implications are seen. First, because of spacecraft orientation changes throughout the flight, the navigation instrument will require full gimbaling. Even if the instrument is restricted to measurements during the second burn, there will still be a gimbaling requirement because navigation stars will move up to 120 degrees with respect to coordinates. A second implication is that extreme accuracy may not be necessary. In Fig. 3.4 it can be seen that there is little reduction in position error when the instrument accuracy is increased to 1 arcsecond from 10 arcseconds. However, if early reduction of ephemeris error is important, the more accurate instrument becomes important, especially in the Jupiter mission where Deep Space Network related position errors are not large.

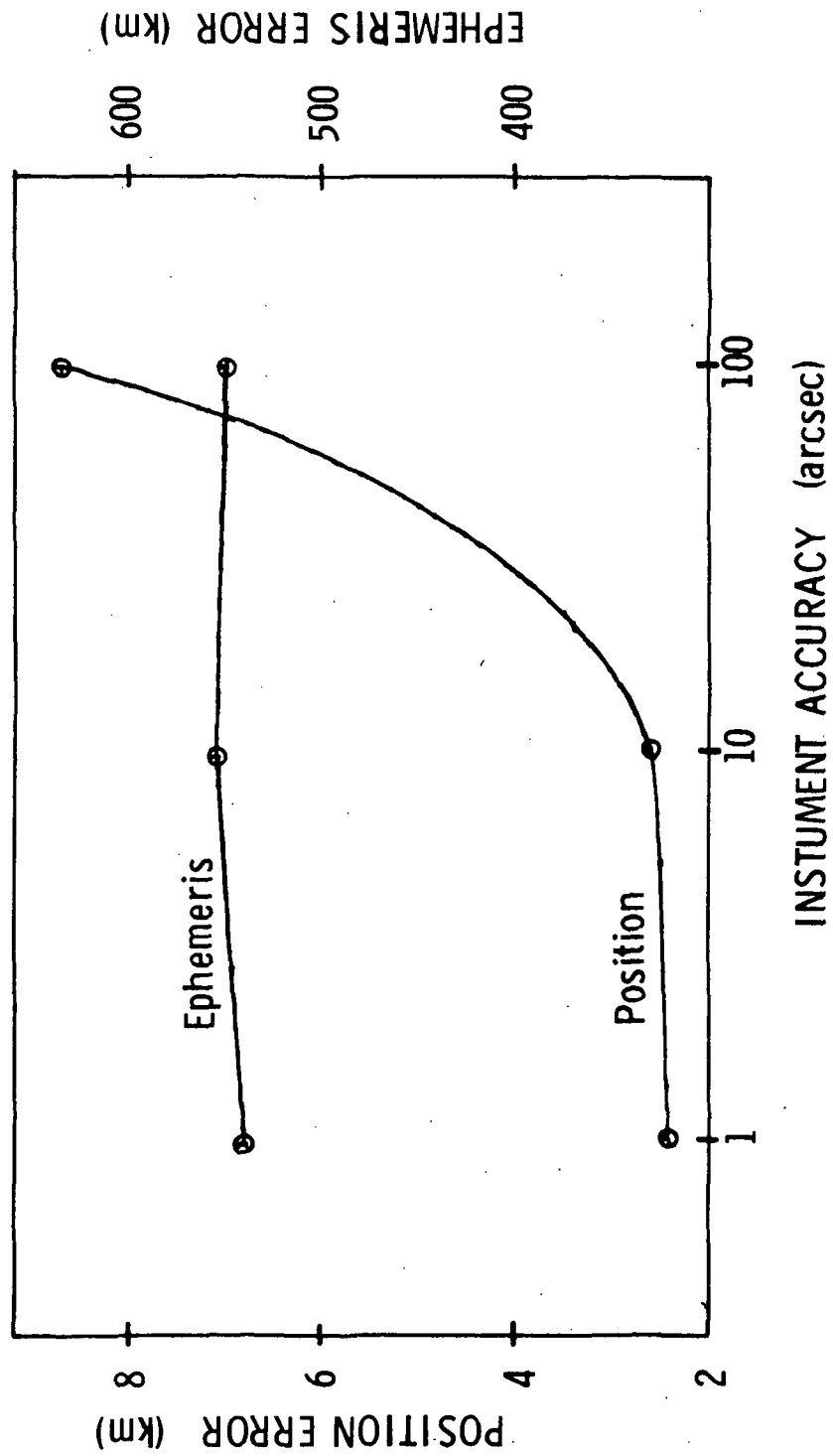


Fig. 3.4 Saturn Near Planet Onboard Accuracy Effects

Generally, the same navigation instrument problem areas exist for these missions as existed for the high thrust missions reported in Volume II of this report. Close-in measurements are still more useful for position error reduction than those obtained further out. Increased measurement frequency does result in further error reduction. Spacecraft attitude changes can affect the results as in the high thrust missions, and co-mounting of the navigation and science instruments may lead to conflicts.⁵ Figure G.1 presents what are felt to be realistic estimates of navigation sensor weights.

CHAPTER 4

MISSION SIMULATION RESULTS

4.1 Introduction

This chapter presents the navigation results which are derived from the statistical simulation in the form of an error covariance matrix. Tabulated results are the square roots of the diagonal elements of the error covariance matrix and represent 1σ uncertainties in spacecraft position, velocity, mass and thrust vector alignment, and the 1σ uncertainty in the target planet ephemeris. Results for Jupiter and Saturn missions are presented in tabular form, and the tables are followed by discussions of the meaning of the results in terms of navigation related systems.

4.2 Tables of Results

Results are listed in Tables 4.1, 4.2, 4.3, 4.4. Each of the two missions is divided into interplanetary and near planet legs, and the listed 1σ errors represent the terminal conditions for each leg. For the interplanetary leg, the terminal time is the nominal time of arrival at one Laplacian sphere of influence from the target planet, and for the near planet leg the terminal time is the nominal time of closest approach.

The lefthand column of each of the results tables, entitled "configuration", lists the characteristics of the modeled systems or the deviations of the system from the nominal case. The term nominal has the following meaning for the parameteral systems:

- a) nominal DSN doppler noise — 1 mm/sec (1σ)
- b) nominal DSN station location bias — 1 meter off of spin axis
2 meters longitude (1σ)
- c) nominal visible navigation instrument noise — 10 arcseconds (1σ)

Thus when the configuration column says "uncertainty x n" it means "n" times the nominal value.

Table 4.1

Jupiter Interplanetary

RMS Terminal Estimation Error

Configuration	DSN	OB	Position (km)	Velocity (km/sec)	Ephemeris (km)	Mass (kg)	Misalignment Angles (milliradians)
Nominal	x		149	6.45E-5	504	7.03E-2	.283
Nominal	x	x	149	6.45E-5	486	7.03E-2	.283
1 Accelerometer	x		145	4.26E-5	510	2.01E-2	.116
1 Accelerometer	x	x	144	4.26E-5	492	2.01E-2	.116
3 Accelerometers	x		64.1	4.58E-6	482	2.02E-2	.314E-2
3 Accelerometers	x	x	64.0	4.56E-6	463	2.02E-2	.314E-2
Onboard Instrument Uncertainty = 1^π	x	x	136	6.45E-5	223	7.03E-2	.283
Onboard Instrument Uncertainty = 100^π	x	x	149	6.45E-5	503	7.03E-2	.283
DSN Dopler Noise x 10	x		216	8.18E-5	523	7.17E-2	.234
DSN Dopler Noise x 10	x	x	214	8.18E-5	506	7.17E-2	.234
DSN Dopler Noise x 100	x		811	1.12E-4	551	7.17E-2	.290
DSN Dopler Noise x 100	x	x	690	1.11E-4	537	7.17E-2	.290
Station Location Error x 10	x		153	6.46E-5	507	7.04E-2	.283
Station Location Error x 10	x	x	152	6.46E-5	490	7.04E-2	.283
Station Location Error x 100	x		153	6.46E-5	507	7.04E-2	.283
Station Location Error x 100	x	x	152	6.46E-5	490	7.04E-2	.283

Table 4.2

Jupiter Near Planet

RMS Terminal Estimation Error

Configuration	DSN	OB	Position (km)	Velocity (km/sec)	Ephemeris (km)	Mass (kg)	Misalignment Angles (milliradians)
Nominal	x		12.9	8.16E-3	305	7,156.2	.188
1 Accelerometers	x	x	.681	3.05E-4	236	2.17E-2	.116
3 Accelerometers	x		2.00	1.33E-3	79.5	2.32E-2	.284E-2
3 Accelerometers	x	x	.302	1.83E-4	50.0	2.21E-2	.284E-2
Onboard Instrument Uncertainty = 100 ^u	x	x	3.07	1.27E-3	282	6.63E-2	.188
DSN Doppler Noise X 100	x		32.63	1.73E-2	388	8.30E-2	.290
DSN Doppler Noise X 100	x	x	2.27	7.14E-4	368	6.33E-2	.290
Station Location Error X10	x		14.23	8.85E-3	325	7.29E-2	.188

Table 4.3

Saturn Interplanetary

RMS Terminal Estimation Error

Configuration	DSN	OB	Position (km)	Velocity (km/sec)	Ephemeris (km)	Mass (kg)	Misalignment Angles (milliradians)
Nominal	x		1.54E3	1.90E-4	1.15E 3	9.66E-2	.171
Nominal	x	x	1.33E3	1.76E-4	1.10E3	9.66E-2	.171
1 Accelerometer	x		1.21E3	1.47E-4	1.15E3	1.82E-2	.182
1 Accelerometer	x	x	1.13E3	1.42E-4	1.08E3	1.82E-2	.182
3 Accelerometers	x		82.0	5.26E-6	1.15E3	1.82E-2	.002
3 Accelerometers	x	x	81.9	5.26E-6	1.08E3	1.82E-2	.002
Onboard Instrument Uncertainty = 1"	x	x	878	1.43E-4	840	9.65E-2	.171
Onboard Instrument Uncertainty = 100"	x	x	1.53E3	1.90E-4	1.15E3	9.65E-2	.171
DSN Doppler Noise x10	x		2.06E3	2.65E-4	1.15E3	9.74E-2	.213
DSN Doppler Noise x10	x	x	1.70E3	2.39E-4	1.11E3	9.74E-2	.213
DSN Doppler Noise x100	x		3.85E3	3.82E-4	1.15E3	7.89E-2	.342
DSN Doppler Noise x100	x	x	1.99E3	2.98E-4	1.13E3	7.89E-2	.342
Star Elevation Measurements only	x	x	1.33E3	1.76E-4	1.10E3	9.66E-2	.171

Table 4.4

Saturn Near Planet

RMS Terminal Estimation Error

Configuration	Position		Velocity (km/sec)	Ephemeris (km)	Mass (kg)	Misalignment Angles (milliradians)	
	DSN	OB					(km)
Nominal	x		7.72	9.12E-4	540	3.17E-2	.144
Nominal	x	x	7.55	9.10E-4	591	3.41E-2	.144
1 Accelerometer	x		6.80	7.75E-4	490	1.82E-2	.138
1 Accelerometer	x	x	6.26	7.14E-4	504	1.82E-2	.138
3 Accelerometers	x	x	.644	9.62E-5	974	1.68E-2	.002
Onboard Instrument Uncertainty=1 [°]	x	x	2.39	3.11E-4	543	2.98E-2	.171
Onboard Instrument Uncertainty=100 [°]	x	x	8.55	1.03E-3	550	3.28E-2	.171
DSN Doppler Noise 10x nominal	x		17.5	3.12E-3	757	4.23E-2	.213
DSN Doppler Noise 10x nominal	x	x	10.0	1.23E-3	717	3.72E-2	.213
DSN Doppler Noise 100x nominal	x		35.9	300E-3	894	4.46E-2	.251
DSN Doppler Noise 100x nominal	x	x	11.3	1.38E-3	862	3.74E-2	.251
Star Elevation Measurements only (24 Measurements)	x	x	2.59	3.13E-4	555	3.24E-2	.171
Star Elevation Measurements only (16 Measurements)	x	x	8.00	9.62E-4	595	3.34E-2	.171

The RMS values for the initial covariance matrices are given in Table 4.5.⁶ The RMS mass errors should have been the same in all cases; however, since the mass errors were quickly reduced by measurements, this numerical error had negligible effect on the navigation results.

Low thrust accelerometers were added to the system models either singly or in an orthogonal set of three. The single accelerometer is assumed to be aligned with the thrust vector and is assumed to yield only thrust magnitude information while the set of three also produces information about thrust direction.

The second two result table columns indicate whether or not Deep Space Network and onboard navigation systems were used by means of an "x". The fourth, fifth, and sixth columns list position, velocity and ephemeris errors at the terminal time for the mission leg associated with each table. Position error is relative to the earth for the interplanetary legs and relative to the target planet for the near planet legs. The last two columns list mass and thrust vector misalignment uncertainty. The latter value represents the uncertainty in the value of the difference in direction of the actual thrust vector and the desired thrust vector. To avoid numerical difficulties for DSN only and DSN with onboard navigation it was necessary to fix thrust vector misalignment at the first sample level that occurred below one arcminute. Although this makes quantitative comparison between DSN only and DSN aided by onboard accelerometers difficult after this limit is reached, the significant conclusion remains (see Fig. 3.1) that the addition of onboard accelerometers gives an early and rapid reduction of thrust vector misalignment errors.

4.3 Jupiter Interplanetary Results

This discussion is based upon the results listed in Table 4.1. Results related to systems that are augmented by onboard instruments are compared to the nominal DSN case, and comparisons are made between systems with differing values of noise parameters. Comparing, at the top of the table,

TABLE 4.5

INITIAL ESTIMATION ERROR COVARIANCES -

 1σ RMS VALUES

	Position Uncertainty (km)	Velocity Uncertainty (km/sec)	Ephemeris Uncertainty (km)	Mass Uncertainty (kg)	Thrust Vector Misalignment (milliradians)
Jupiter	51.8	.0206	551	1	11
Saturn	51.8	.0206	1149	.1	11

the nominal DSN case with the DSN plus nominal onboard case one sees no improvement when adding onboard navigation except for a small insignificant improvement in the ephemeris value. Further down the table it can be seen that if the onboard navigation instrument has a 100 arcsecond or 10 times nominal uncertainty even the ephemeris value is unimproved. However, the table shows that an onboard navigation instrument with an uncertainty of one arcsecond can drop ephemeris uncertainty by more than half. This is the only significant change of ephemeris error occurring among the various combinations of systems and system errors examined on this mission leg and indicates that to obtain a useful reduction of ephemeris error at the large planetary ranges encountered on this interplanetary leg requires an extremely accurate onboard instrument.

The lower portion of the table contains variations in the DSN noise parameters. It can be seen that increases in station location biases do not significantly alter position uncertainties. However, increases in the doppler noise levels result in considerable increases in position uncertainty particularly in the 100 times nominal case where it can be seen that the position uncertainty is raised by a factor of five. The addition of onboard navigation to the higher DSN noise systems has little effect except when DSN doppler noise gets to the extremely large value of 100 times nominal. At these doppler noise levels the onboard system tends to hold position errors down somewhat, indicating a limited need for onboard instrumentation on the interplanetary leg if use of low thrust propulsion degrades the doppler tracking accuracy by a factor of 100 or greater.

The addition of three accelerometers causes the most significant decrease in all RMS uncertainties. Position error values are cut in half compared to similar configurations without accelerometers. Velocity error values are significantly decreased. Mass errors are decreased by a factor of four when either three or one accelerometer is added. With three accelerometers, thrust vector misalignment uncertainty is about 100 times less than with other configurations. This early and significant reduction in thrust vector misalignment and in mass uncertainty eliminates a principle source of error in position and velocity.

One accelerometer gives very little information about thrust vector misalignment and therefore leads to larger errors in position and velocity than occurred with three accelerometers. However, the addition of one accelerometer to nominal DSN or DSN and onboard slightly decreases the uncertainty in position and velocity as a result of the increased knowledge of mass from the no accelerometer case.

4.4 Jupiter Near Planet Results

The discussion in this section is based on Table 4.2. Looking first at DSN by itself, it can be seen from the first and last row that station location biases do not significantly alter any of the error values. However, a doppler noise level of 100 times nominal raises position and velocity uncertainty by a factor of three and slightly increases the other uncertainties.

Addition of onboard navigation to the system, as in row five, causes a decrease in position and velocity uncertainties with a factor-of-four decrease in position and a factor of six in velocity. This case uses a 10 times nominal or 100 arcsecond instrument error, and therefore the nominal onboard instrument would be expected to yield further improvement as can be seen in row seven where onboard navigation has been added to the DSN systems having 100 times nominal doppler noise. As expected, the onboard system becomes more important as the DSN noise levels increase.

Minimal errors in all of the listed quantities occur when the spacecraft system includes three accelerometers and onboard navigation. Contributions to the reduction of position error are made by the accelerometers which reduce the spacecraft mass uncertainty, and by both the DSN and onboard navigation systems.

The primary contribution to the reduction of the ephemeris error is made by the three accelerometers which reduce thrust pointing errors and spacecraft mass uncertainties very early in the mission, and thus markedly reduce a major error source in the equations of motion. Given early and

accurate thrust pointing, the DSN system can determine the trajectory at shorter ranges where its accuracy is greatest; however, perfect thrust pointing would still leave planet mass and spacecraft mass errors. The relatively small ephemeris errors are, of course, dependent on the small associated position errors. The system configuration with the next smallest ephemeris error (79.5 km) has three accelerometers but no onboard navigation. The ephemeris error is still markedly reduced from the other listings. Since there is no onboard navigation, this case emphasizes the importance of the accelerometers for ephemeris error reduction.

When the system with onboard navigation and three accelerometers is reduced by dropping the two accelerometers perpendicular to the thrust axis, one observes a small increase of position error to 0.68 km from 0.36 km, and a large increase in ephemeris error from 50 km to 236 km. This is because one accelerometer cannot provide early, accurate thrust vectoring. The single accelerometer does aid in reducing the spacecraft mass uncertainty, and therefore produces some improvement over the system with no accelerometers.

4.5 Saturn Interplanetary Results

This section discusses the results given in Table 4.3. Most of the comments given in the discussion of the Jupiter interplanetary results also apply here. Examining first the cases involving DSN by itself it is seen that increasing doppler noise increases errors significantly with the 100-times-nominal doppler noise increasing position errors by a factor of three. For a doppler noise variance of 10 times the nominal, the addition of nominal onboard navigation reduces position uncertainty from 2060 km to 1700 km and for a doppler noise 100 times the nominal improvement is from 3850 km to 1990 km, almost halving the value. For nominal DSN the position uncertainty is 1540 km which is reduced to 1330 km for a 10 arcsecond instrument and to 878 km for a one arcsecond onboard instrument. Comparing this to the Jupiter interplanetary leg, shows the significant effect of using onboard instruments beyond the orbit of Jupiter. This is because

DSN measurements become less accurate at greater distances. Unlike the ballistic case, the advantage gained through accurate initial tracking near earth is partially lost because of the unknown low thrust perturbations.

Ephemeris error was not appreciably reduced from its initial value by any configuration except that with the most sensitive onboard instruments (one arcsecond accuracy) it is reduced to 340 km. This again points to the need for extremely accurate instruments if early ephemeris error reduction is desirable. The accelerometers greatly improve position and velocity estimates. The sensitivity of mass uncertainty to the use of one or three accelerometers and of thrust vector misalignment to the use of three, is significant and similar to that for the Jupiter Interplanetary results. Mass and thrust vector misalignment are not particularly sensitive to other configurations; the differences that do occur are not thought to be significant due to the approximating numerical methods used.

4.6 Saturn Near Planet Results

Results for the near planet leg of the Saturn Mission are shown in Table 4.4. In general, the Saturn near planet results parallel the corresponding Jupiter results, however, there are several additional cases for Saturn which allow direct comparisons that were not obtained for the Jupiter Mission, and there are cases showing the importance of the DSN noise level.

Looking first at the DSN only cases, rows one, eight, and ten show the expected increase in position and velocity uncertainties as doppler noise is increased. The one arcsecond onboard instrument is shown to yield a very slight improvement over the 10 arcsecond instrument; however, when the instrument error is increased to 10 arcseconds, a significant increase in position error, by a factor of four, results. The 100 arcsecond instrument does not cause a corresponding increase in ephemeris error because, as expected, this value is dependent primarily on DSN (assuming no accelerometers) for the near planet leg.

Some other results related to onboard navigation include the observation that onboard navigation only slightly improves the DSN with one accelerometer configuration. The larger DSN noise level related errors tend to swamp out contributions made by the onboard system. For example, a doppler noise of 10 times nominal moves position up to 10 km from the 2.6 km level with nominal doppler noise in spite of the presence of onboard navigation. However, the contribution of onboard navigation to the nominal doppler noise case is to reduce position error from 7.7 km to 2.6 km. Onboard navigation does, however, reduce the effects of increasing doppler noise. This is illustrated by a reduction, in the case with a doppler noise of 100 times nominal, of position error from 36 km to 11.3 km by the addition of onboard navigation. (Results from the near planet leg of the Saturn Mission related to the DSN only system show that the order of magnitude increase in DSN noise show a corresponding increase in position and ephemeris errors.) Onboard navigation with DSN yields a two-to-one improvement in position uncertainty over the one accelerometer case as long as the onboard instrument is capable of 10 arcsecond accuracy or greater, but that the accelerometer improves ephemeris uncertainty by 20%. It is significant that the 10 arcsecond onboard instrument case uses star-planet limb angle measurements only, and therefore that there is no requirement to design the instrument as a planet center finding device, if the radius of the planet can be determined to within a few kilometers.

The Jupiter results show that the system configuration yielding by far the smallest position and ephemeris errors has onboard navigation and three accelerometers. The significant five to one reduction in ephemeris error is repeated in the Saturn results, and there is a general scaling of ephemeris errors according to the greater distance to Saturn. These results also show that a system using one accelerometer along with onboard navigation and DSN would yield position errors that were the next lowest to the three accelerometer systems.

As in the Jupiter mission, all configurations reduce mass and thrust vector misalignment error by about the same amount except the case of

added accelerometers. For the cases of one and three accelerometers mass error is reduced to about half that for all other configurations, and with three accelerometers thrust vector misalignment is reduced by two orders of magnitude.

Page intentionally left blank

CHAPTER 5

CONCLUSIONS AND RECOMMENDATIONS

The simulation results evoke several conclusions in the areas of guidance and onboard sensor systems. As can be seen from the guidance plots in Appendix F, the constant control guidance algorithm can null out reasonable deviations in position and velocity although, since the navigation and guidance loop was not closed, additional study is necessary to prove the adequacy of this algorithm.

From the standpoint of the navigation results, the onboard navigation system proves to be of marginal value except in two particular situations. First, if the Deep Space Network doppler noise is large (100 mm/sec for a one minute smoothing time) the onboard system makes a significant reduction in position error with respect to the planet for the Jupiter near planet case. The reduction is from 33 km to 2.3 km. Secondly, during the interplanetary leg of the Jupiter mission, the onboard system can reduce ephemeris errors substantially from the 500 km level down to the vicinity of 150 km. Outside of these two special cases, on the basis of the limited data available, the onboard system can only be justified in relation to its potential use as a scientific instrument, its interaction with the guidance process, and small improvements in the general body of navigation errors.

One of the more interesting results is the marked effect that highly accurate accelerometers have on the position and ephemeris errors, and on the spacecraft mass uncertainty. At the end of the Saturn mission, interplanetary leg, for example, the spacecraft position uncertainty is reduced by a 3 accelerometer system to 82 km from the no accelerometer value of 1540 km. This occurs because two of the dominant error sources in the equations of motion are reduced by the accelerometers, namely the spacecraft mass uncertainty and the thrust vector misalignment. One accelerometer is much less useful than three mainly because it cannot distinguish thrust vector misalignment from thrust magnitude variations.

However, the single accelerometer was assumed to be strapped down. Precision gimbaling of a single accelerometer with two axis freedom and precision alignment with respect to the attitude control system would allow it to function in the same way as a set of three orthogonal strapped down accelerometers.

The navigation results given in Chapter 4 are consistent with a one arcminute attitude control system accuracy. One arcminute thrusting does give good results even in the absence of highly sensitive accelerometers. Adding accelerometers that are accurate at the $10^{-9}g$ level causes the one arcminute value to be realized immediately after trajectory injection which is one to two months earlier than the case relying on the Deep Space Network by itself. Allowing the attitude control system to be better than one arcminute would cause some further improvement in the results, although it is expected that planet and solar mass uncertainties would allow only small improvements in what are, in many cases, already very small errors.

Further studies are indicated in the areas of guidance algorithm development, simulation structuring, and parametric variations. A number of guidance schemes should be investigated including optimal guidance. These would include allowing thrust to be switched on and off at times other than the nominal trajectory times as considered for the present scheme. In addition, a study to determine the linear range of such schemes is desirable.

The statistical simulation should be restructured to produce the desired coupling between the guidance and navigation results and to eliminate the numerical problems which limited the results of this study. Part of the solution to the numerical problem involves the development of new covariance matrix propagation schemes. With this restructured simulation, the value of onboard instruments, particularly accelerometers, for decreasing guidance errors could be more accurately specified.

In the area of onboard sensor studies, it would be useful to complete

the parameter variations that were limited in the low thrust phase of the study by numerical difficulties. In addition, the range of variation of some parameters should be extended.

The problem of accelerometer output, sampling rate, and period should be investigated to determine how problems of data processing of outputs onboard or on the earth interact with error propagation from one set of measurements to the next, and how these factors affect the statistical modeling. The assumed white noise error model for accelerometers is proportional to the sampling rate, and the bias errors grow with time from last calibration.

Attitude control system importance should be determined by parameterizing the limit on thrust vector misalignment. Present results are representative of only a one arcminute system for the no accelerometer cases.

If the small improvement in navigational accuracy which results from onboard instruments is desired, then the effects of restricting the total navigational star field, and the types of navigation measurements should be investigated. Navigation errors are known to decrease with increased measurement frequency, but these effects have not been examined explicitly. Similarly, the navigation measurement range from the target planet is known to have a strong effect on the value of the measurement, but the effects of restricting the range have not been determined. Curves showing error growth versus range and time would be helpful in this area.

Page intentionally left blank

APPENDIX A

DYNAMICS

In this appendix are defined the coordinate systems and control vectors used; the equations of motion are given. These basic relationships are used throughout this volume in the mathematical description of both the guidance and navigation schemes.

We are considering a spacecraft traveling under the influence of the sun, a single target planet, and its own constant low thrust engine. The trajectory begins in interplanetary space where a sun-centered coordinate system is used. The x axis is in the direction of the vernal equinox, the y axis is perpendicular to the x axis in the ecliptic and the z axis is perpendicular to the ecliptic. At the sphere of influence of the target planet, a planet-centered coordinate system is used whose orientation is the same as that of the sun-centered system. The dynamical equations and any expressions derived from them will be dependent on the coordinate system. Planet location information is obtained from an ephemeris program which is based on a 1960 January 1.5 epoch.

The letters \underline{r} and \underline{v} will be used for the position and velocity vectors, respectively, in the coordinate system being employed. $\underline{\rho}$ is the vector from sun to spacecraft. \underline{a} is the vector from the target planet to the spacecraft. \underline{d} is the vector from the sun to the target planet. (See Fig. A.1.) $\hat{\underline{u}}$ is the three dimensional unit vector of directional cosines which defines the direction of the thrust. T is the magnitude of the thrust and is equal to the mass flow rate β ($= 0$ when the engine is off), times the exhaust velocity of the ion engine c ($= g_0 I_{sp}$ where g_0 is the standard acceleration of gravity and I_{sp} is the specific impulse of the rocket). μ_s is the gravitational constant of the sun, μ_p , that of the target planet. m is the mass of the spacecraft. The equation of motion for the spacecraft in the sun-centered coordinate system is:

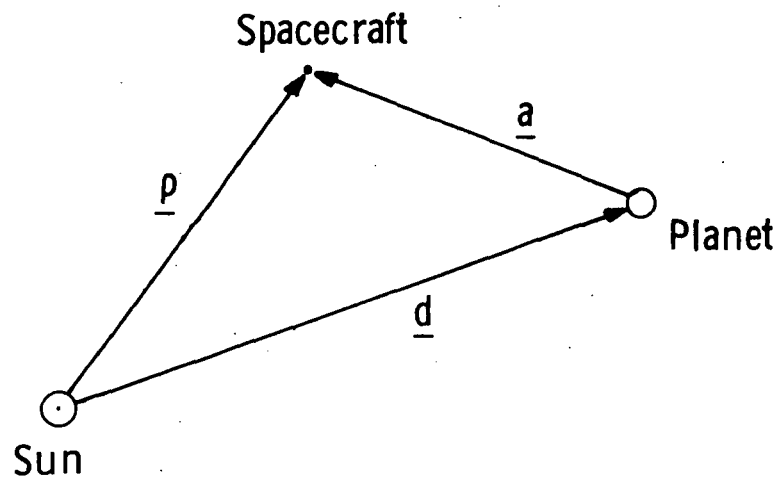


Fig. A.1 Spacecraft and Planet Position Vectors

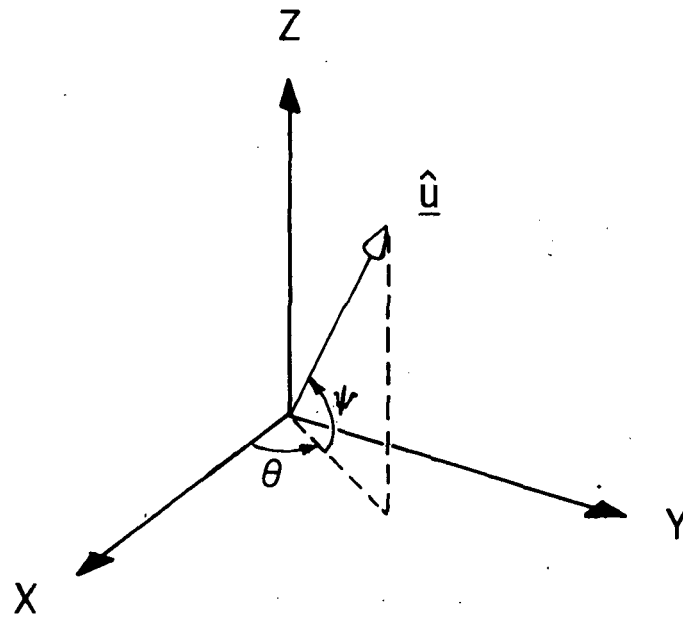


Fig. A.2 Control Angle and Direction Definition

$$\ddot{\underline{r}} = \frac{-\mu_s \underline{\rho}}{\rho^3} - \frac{\mu_p \underline{a}}{a^3} - \frac{\mu_p \underline{d}}{d^3} + \frac{\beta c \hat{\underline{u}}}{m}$$

for planet-centered coordinates:

$$\ddot{\underline{r}} = \frac{-\mu_s \underline{\rho}}{\rho^3} - \frac{\mu_p \underline{a}}{a^3} + \frac{\mu_s \underline{d}}{d^3} + \frac{\beta c \hat{\underline{u}}}{m}$$

The direction of the control can be specified by two angles θ and ψ defined by Fig. A.2 where θ is measured in the x-y plane.

Thus,

$$\hat{\underline{u}} = \begin{bmatrix} \cos \theta & \cos \psi \\ \sin \theta & \cos \psi \\ \sin \psi \end{bmatrix}$$

The control parameters are β, θ, ψ where $\beta = \beta_{\max}$ when the engine is on and $\beta = 0$ when the engine is off.

Page intentionally left blank

APPENDIX B

INTERPLANETARY TRAJECTORY GEOMETRIES

The purpose of this appendix is to present the geometrical properties of the interplanetary leg of each of the two missions used as examples in this study. The plots included herein are invaluable to the scheduling of the onboard navigation system. In addition, they display mission phenomena such as distances to navigational targets and sun angles which are basic to the design and implementation of the onboard navigation system.

There are five plots included for each interplanetary leg. The first in each series displays the overall mission geometry and is used primarily to provide geometrical support for the other plots. The markings on the spacecraft and planet trajectories are at the same equal time intervals to aid in determining the relative positions of the planets and spacecraft. Circles and arcs of circles represent planetary orbits with the innermost representing the orbit of Venus.

The second plot in each group of five gives the range to the planets of possible interest. This is valuable for deciding which planet to use for navigation sightings as the spacecraft proceeds along its trajectory. In the absence of other constraints which would prohibit the measurement, those measurements which employ the closest near body are potentially the most useful. This plot is also used to decide during what periods the various planets are too far away to detect with an IR instrument and to provide the navigation system design with information about the target ranges his sensors must deal with.

The third plot in each series gives the spacecraft-Earth-sun angle. The purpose of this plot is to identify those phases of the mission where the spacecraft line-of-sight (from Earth) comes too close to the sun line-of-sight to permit tracking of the vehicle from Earth. A check of all

these plots reveals the fact that there are very few times when the ground based antennas will not be able to track the spacecraft because it is behind the sun. Note that only on the Jupiter flyby does one of these periods even come close to an encounter time and this could be further avoided by slight changes in the thrust history.

The fourth graph in each group provides the sun-spacecraft-planet angle for each leg. This is of much use in setting up the onboard measurement schedule because it displays those periods in which the line-of-sight to the planet is too close to the line-of-sight to the sun to permit use of the planet for navigational purposes. It also informs the sensor designer what range of sun angles his instrument will encounter.

The final plot in each group gives the Earth-spacecraft-planet angle for each leg. This is of interest to the systems designer because he must be aware of the relative location of the planet and Earth so that functions related to each body can be coordinated. As an example of such coordination consider the problem of orienting the spacecraft, communications antenna, star tracker, and/or planet sensor such that a navigational sighting can be performed without losing communication with the Earth.

Tables B.1 and B.2 provide the results of using these plots to develop candidate onboard measurement schedules for all the interplanetary legs of the three missions used in this study. The actual measurements used in the results presented in Chapter IV were selected from those indicated as available in these tables.

An example of using these plots to create a candidate onboard measurement schedule is given in Appendix A of Volume II.

Table B. 1

Onboard Measurement Schedule for the Interplanetary

Leg of the Jupiter Mission

Beginning of Interval (Days)	End of Interval (Days)	Time Step for Interval (Days)	I. R. Feasible?	Venus Used?	Earth Used?	Mars Used?	Jupiter Used?	Saturn Used?	Uranus Used?	Neptune Used?
Injection	70	10	yes	no	yes	no	no	no	no	no
70	290	20	yes	no	no	yes	yes	no	no	no
290	47	20	yes	no	no	no	yes	no	no	no
470	Jupiter Sphere of Influence	10	yes	no	no	no	yes	no	no	no

Table B.2
Onboard Measurement Schedule for the Interplanetary
Leg of the Saturn Mission

Beginning of Interval (Days)	End of Interval (Days)	Time Step for Interval (Days)	I. R. Feasible?	Venus Used?	Earth Used?	Mars Used?	Jupiter Used?	Saturn Used?	Uranus Used?	Neptune Used?
Injection	70	10	yes	no	yes	no	no	no	no	no
70	630	20	yes	no	no	no	yes	no	no	no
630	830	20	yes	no	no	no	no	yes	no	no
830	Saturn Sphere of Influence	10	yes	no	no	no	no	yes	no	no

Interplanetary Trajectory Geometries

Summary of Figures

1. 1979 Jupiter Flyby

Fig. B1.1 Trajectory for Jupiter Mission.

Fig. B1.2 Ranges to Solar System Planets for Jupiter Mission.

Fig. B1.3 Spacecraft-Earth-Sun Angles for Jupiter Mission.

Fig. B1.4 Sun-Spacecraft-Planet Angles for Jupiter Mission.

Fig. B1.5 Earth-Spacecraft-Planet Angles for Jupiter Mission.

2. 1981 Saturn Flyby

Fig. B2.1 Trajectory for Saturn Mission.

Fig. B2.2 Ranges to Solar System Planets for Saturn Mission.

Fig. B2.3 Spacecraft-Earth-Sun Angles for Saturn Mission.

Fig. B2.4 Sun-Spacecraft-Planet Angles for Saturn Mission.

Fig. B2.5 Earth-Spacecraft-Planet Angles for Saturn Mission.

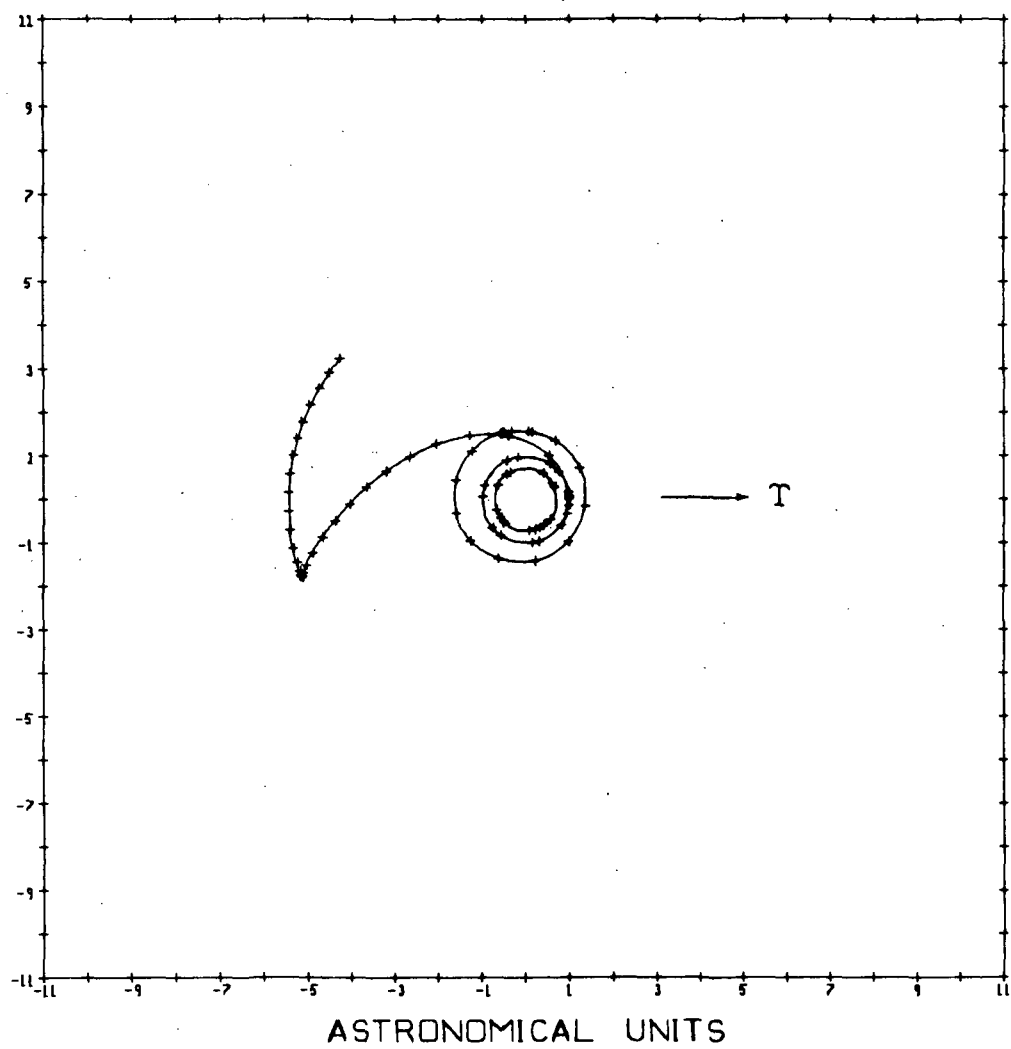


Fig. B.1.1 Trajectory for Jupiter Mission

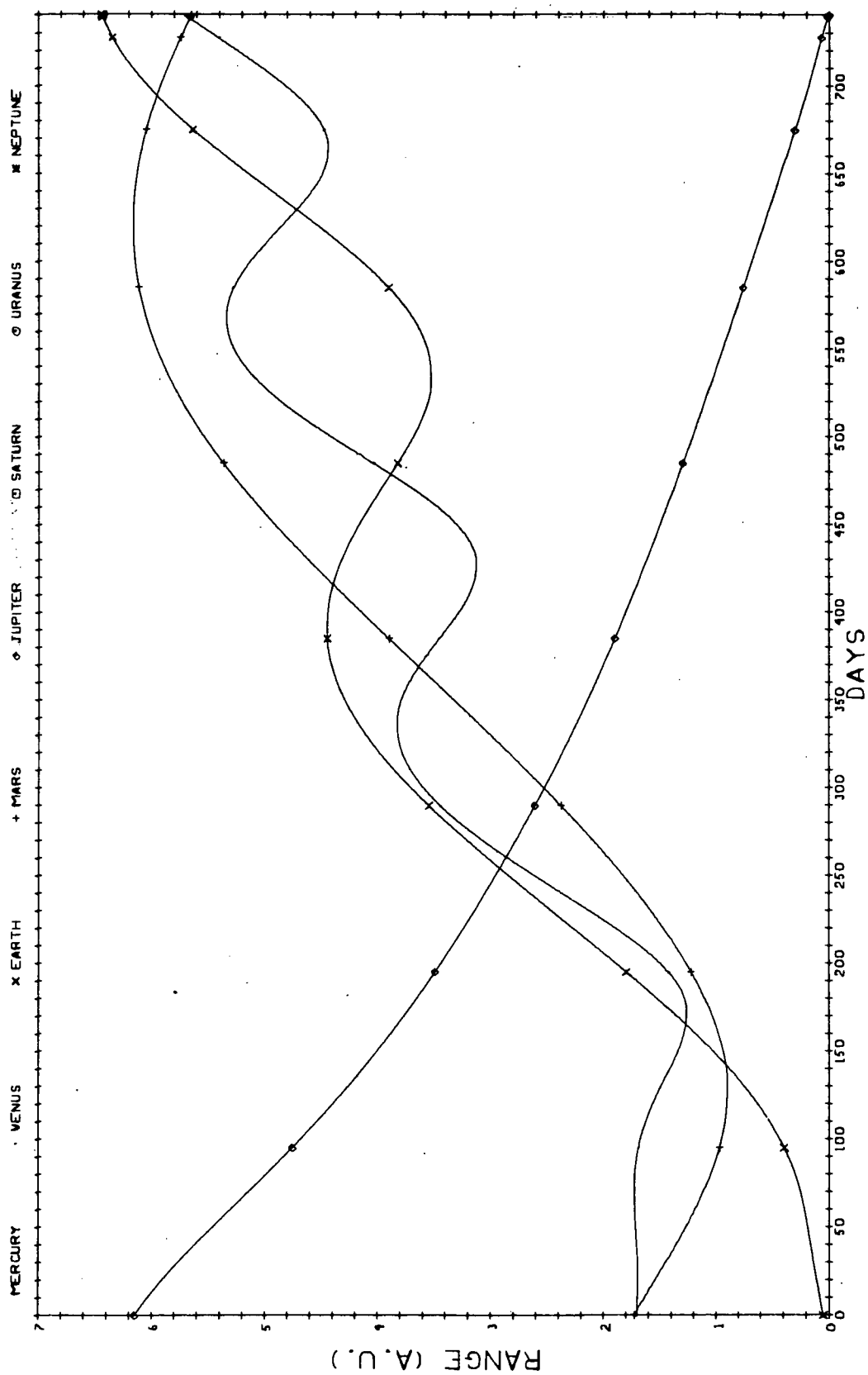


Fig. B.1.1.2 Ranges to Solar System Planets for Interplanetary
(Earth-Jupiter) Leg of the Jupiter Mission

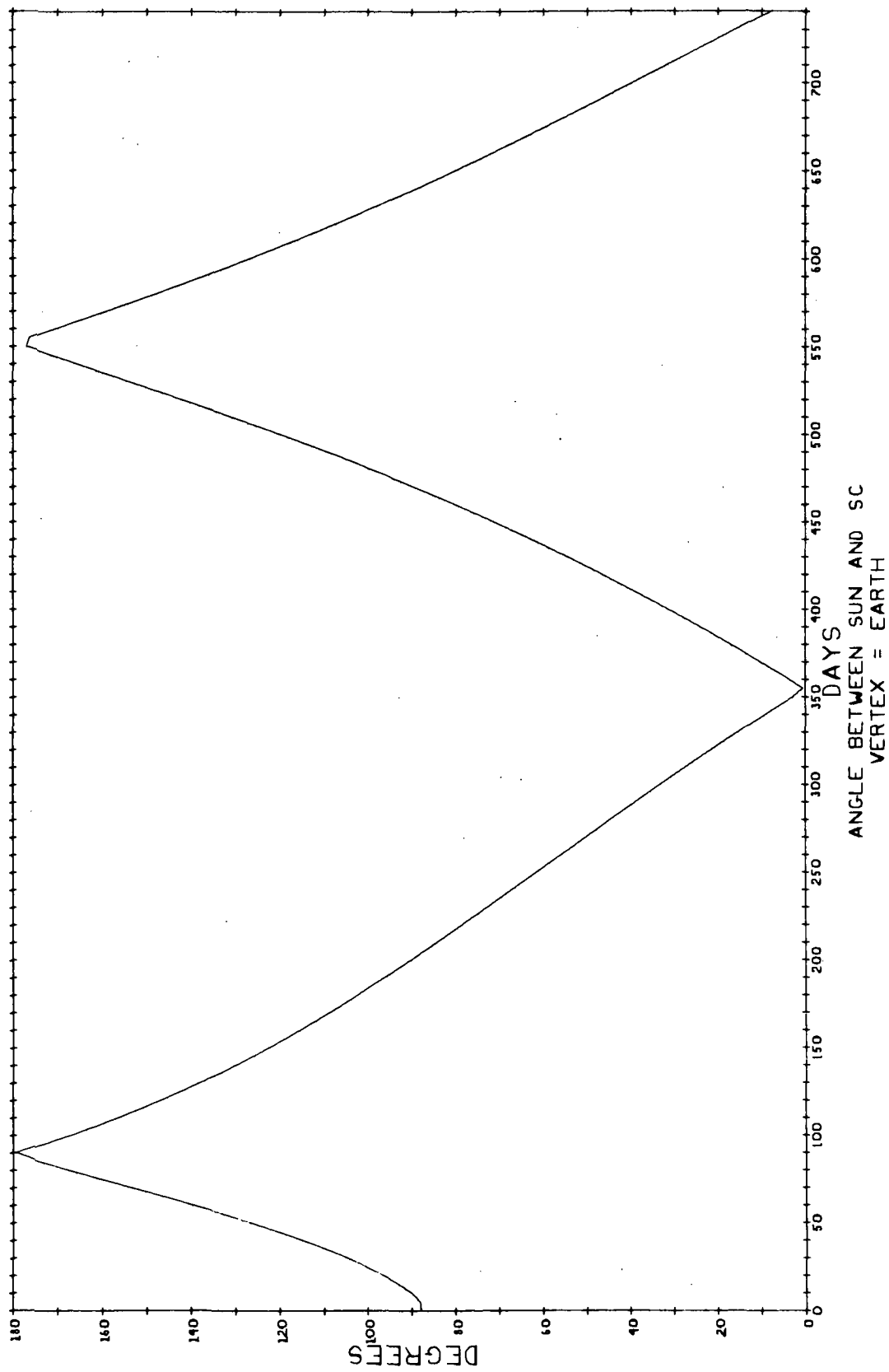


Fig. B.1.1.3 Spacecraft-Earth-Sun Angle for the Interplanetary (Earth-Jupiter) Leg of the Jupiter Mission

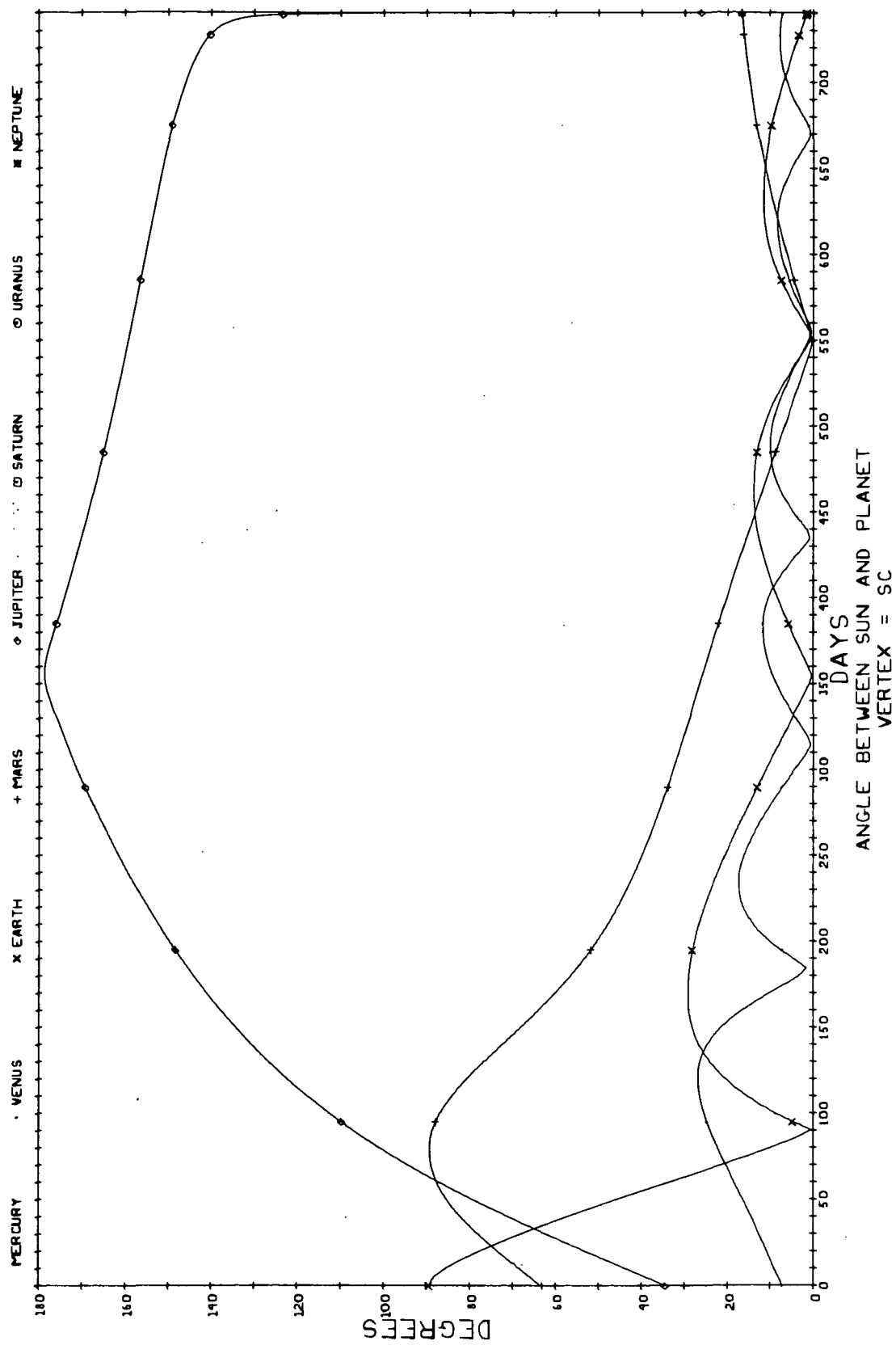


Fig. B. 1.4 Sun-Spacecraft-Planet Angles for the Interplanetary
(Earth-Jupiter) Leg of the Jupiter Mission
VERTEX = SC

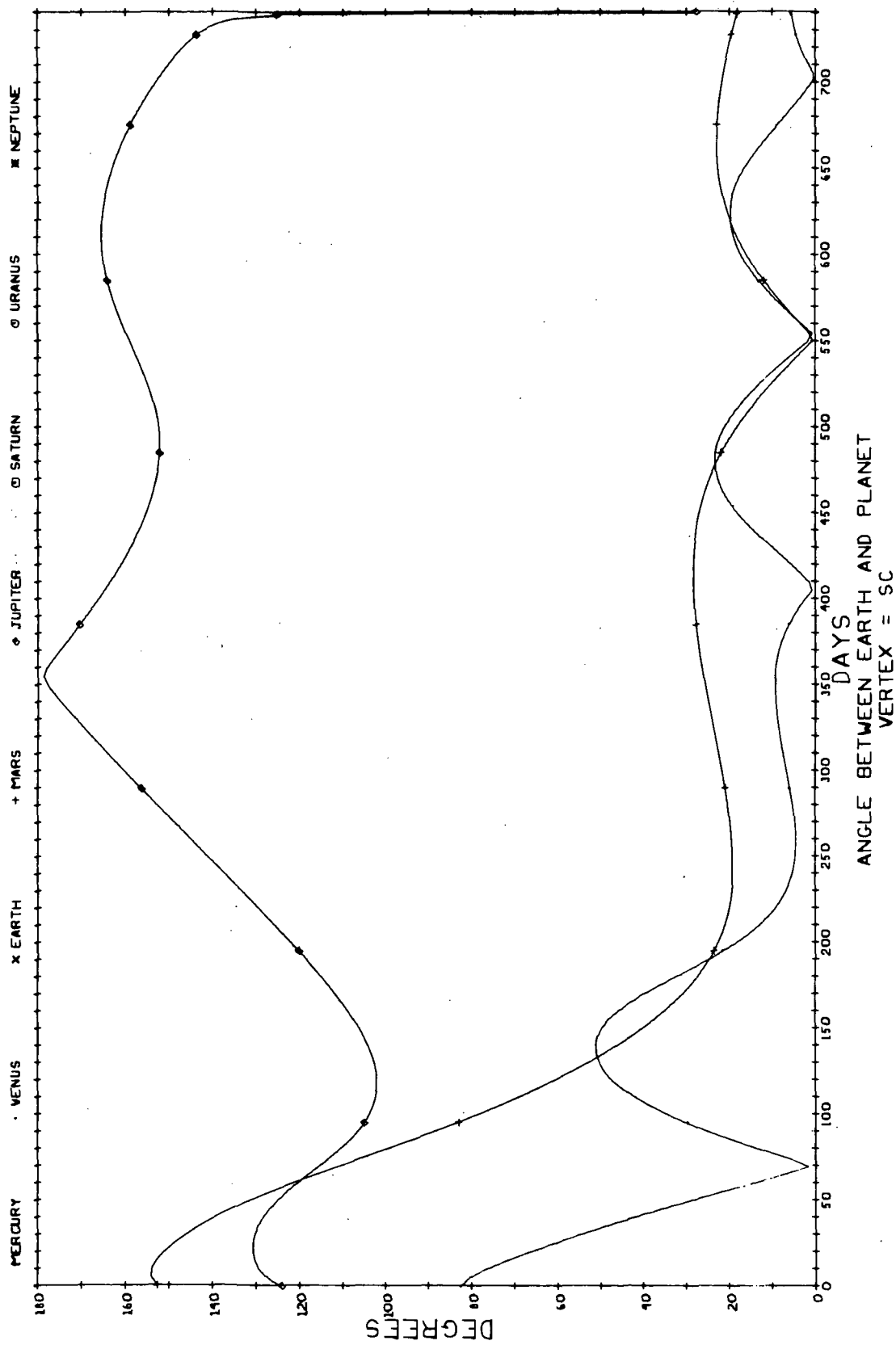


Fig. B.1.1.5 Earth-Spacecraft-Planet Angles for the Interplanetary (Earth-Jupiter) Leg of the Jupiter Mission
VERTEX = SC

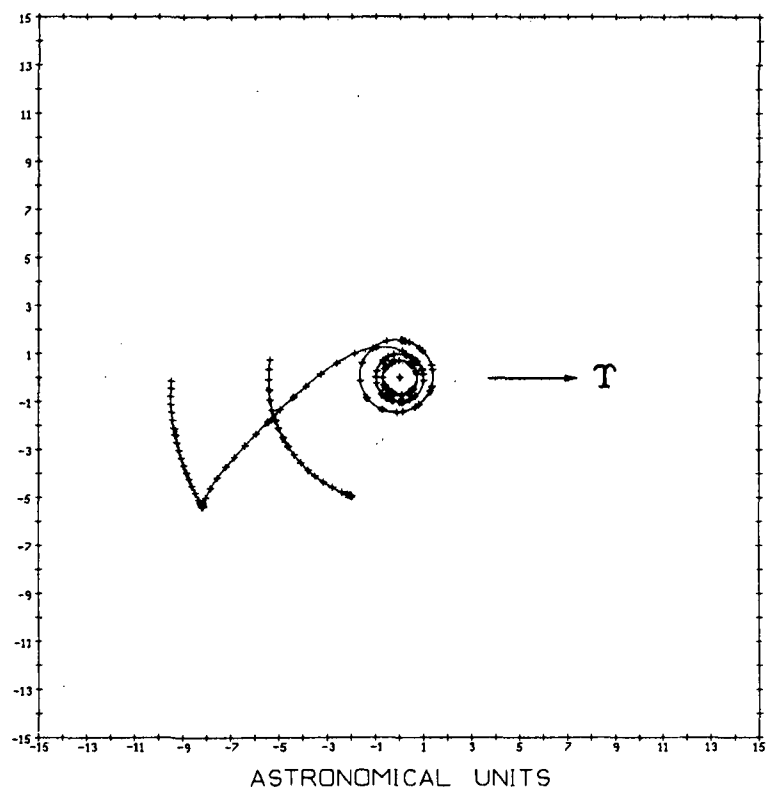


Fig. B.2.1 Trajectory Diagram for Saturn Mission

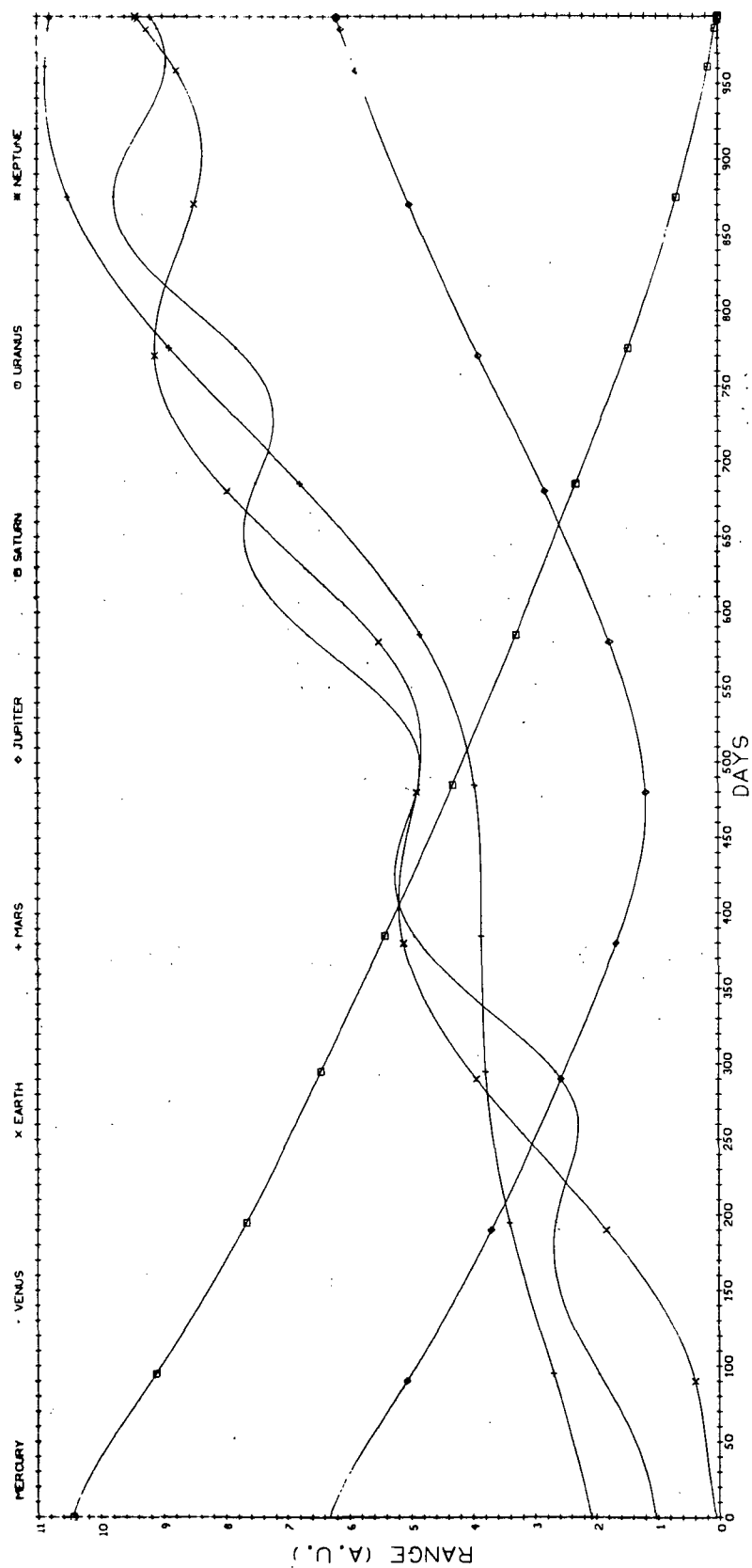


Fig. B. 2.2 Ranges to Solar System Planets for Interplanetary (Earth-Saturn) leg of the Saturn Mission

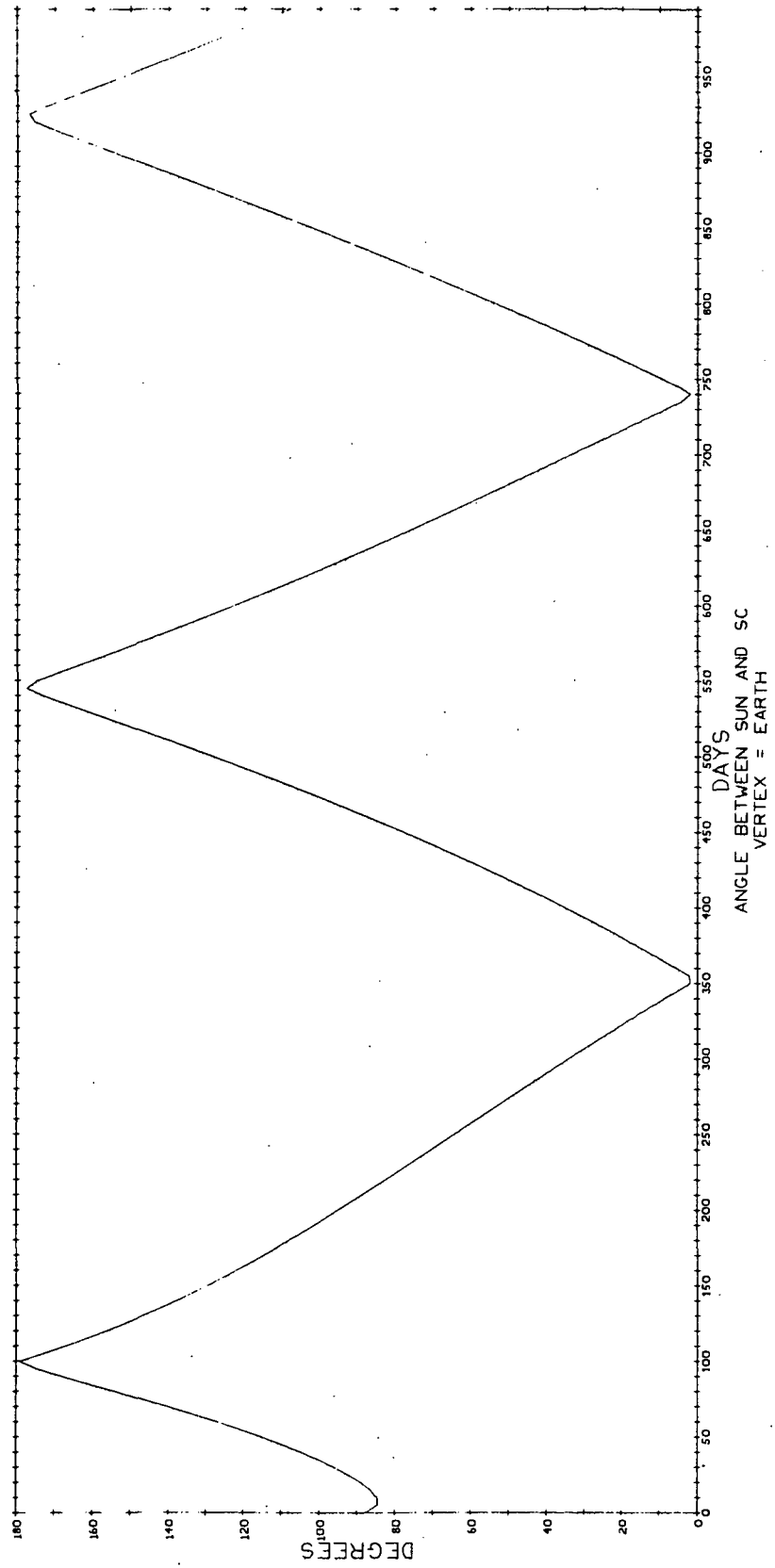


Fig. B. 2.3 Spacecraft-Earth-Sun Angle for the Interplanetary (Earth-Saturn) Leg of the Saturn Mission

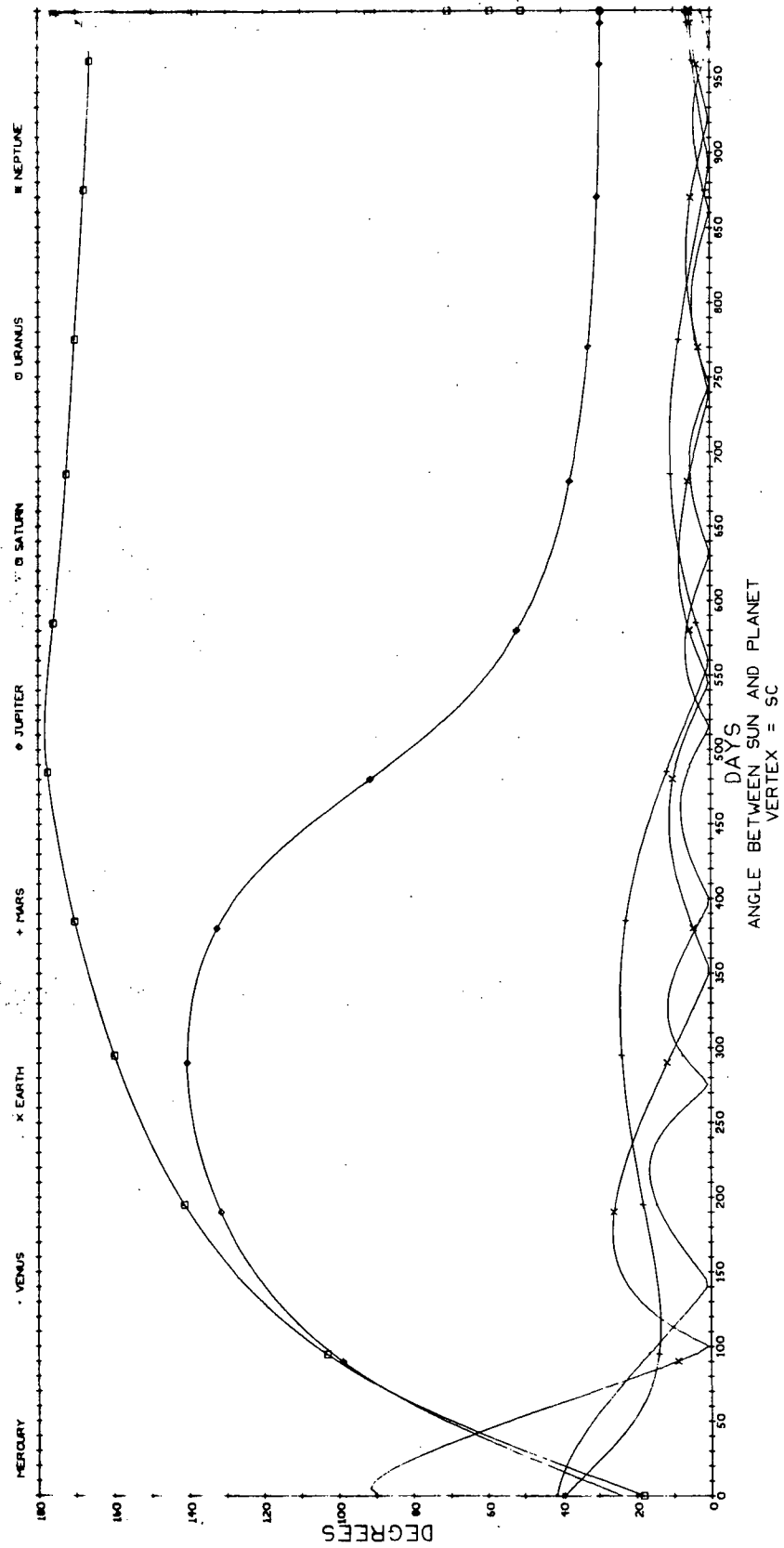


Fig. B.2.4 Sun-Spacecraft-Planet Angles for the Interplanetary (Earth-Saturn) Leg of the Saturn Mission

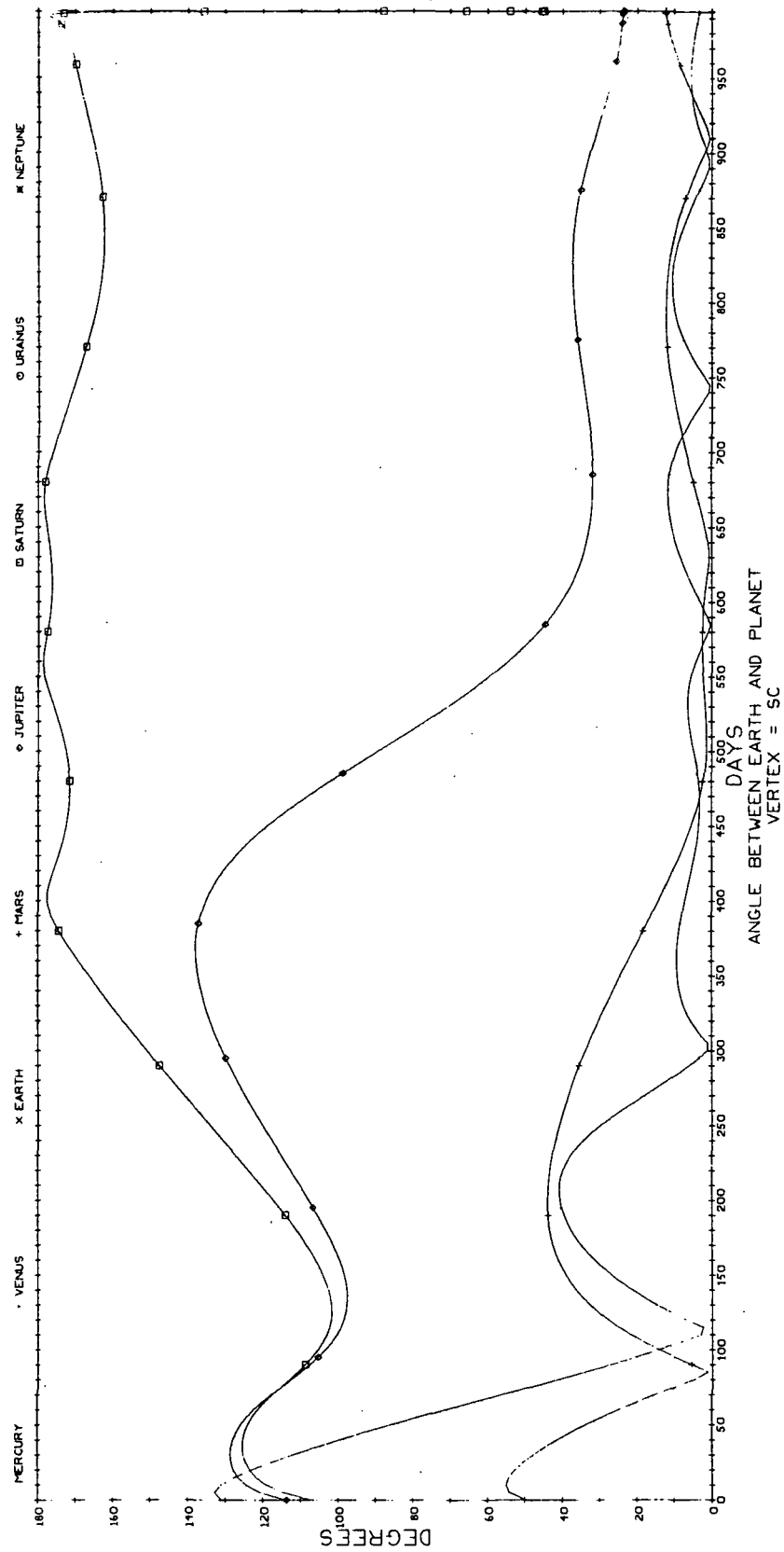


Fig. B.2.5 Earth-Spacecraft-Planet Angles for the Interplanetary (Earth-Saturn) Leg of the Saturn Mission

Page intentionally left blank

APPENDIX C

PLANETARY PASSAGE TRAJECTORY GEOMETRIES

In this appendix are presented those physical parameters which are indispensable for a preliminary analysis of the use of an onboard navigation system during the period in which the spacecraft is well within the sphere of influence of a planet. These characteristics are illustrated here for the two planetary encounters of the two missions used as examples in this study. The value of the data contained in these plots should not be underestimated—the overall scheduling and measurement selection which can be performed with this information eliminates the need for a costly computer search through a much larger set of possible measurement combinations.

The format of the presentation of the planetary passage geometries presented in this appendix is a sequence of seven plots for each mission. These plots were created by a computer program designed for use on flyby missions such as those discussed in Volume II. Since these missions are potentially orbiter missions, no post-perihelion region would exist and only the pre-perihelion part of the plots should be used. This means that the right half of the first plot and the left half of the other six contain the data to be used if the two example missions are considered to be orbiter missions.

The first plot in each series is a plane view of the hyperbolic pass of the planet. It provides an overall view of the passage. The direction of the sun is indicated in each case. By using this plot, one determines which is the sunlit side of the terminator line (shown drawn on the planet). In all cases passage is from right to left around the planet, thus in the Saturn case the approach is made from the direction of the sun. This results in an approach to the light side and a retreat from the dark side of the planet. In the case of Saturn, the inner edge of the rings is drawn on the plane

view. The dotted edge is below the plane of the paper. The plane view is also useful for determining when star occultations might be available. Star occultations are potentially useful measurements only when the relative motion is such that a dark edge of the planet passes into the star field. Note that until the spacecraft is very close to the planet there is little relative motion of this type. If the planet has an atmosphere, as the outer planets have, the intersection of the star with the edge of the planet must occur far enough from the terminator line so that there is no light leakage. If we assume a central angle value of about 20° for this distance, we see that when the approach is made from out of the sun there isn't much opportunity to find good star occultations. The final use to be mentioned here is that by simply noting whether a light edge is available at any given time one can determine whether or not an IR capability is required to make a measurement at that time.

The second plot in each group gives the range to the planet in planet radii and kilometers. Note that in each case very little time is spent close to periplanet. Use of this plot together with the ranges to the planetary satellites given in the sixth plot of each group, enables one to determine whether or not a satellite might be a better navigational target than the planet. This could be the case if the distance to the satellite is much less than the distance to the planet.

The third graph gives the angle subtended by the planet versus time. Again the tremendous speed at which the probe passes periplanet is apparent from this plot. This plot and the previous one have much meaning to the instrument designer as they provide information on the size and distance of the near body. In addition, this plot is useful to determine during what period planet diameter measurements will be useful. The geometry is favorable only during the time the subtended angle is large—which isn't very long.

The fourth plot gives either the Earth-probe-planet angle, or sun-probe-planet angle, or both, for each case. Besides giving information to the systems designer and mission planner, the Earth-probe-planet angle

plot reveals during what period the spacecraft is behind the planet as viewed from Earth. Note that it is never occulted for more than a few hours. The sun-spacecraft-planet angle is extremely useful to onboard system scheduling because it reveals when the lines-of-sight to the planet and sun are too close to permit using the planet for sightings. For the near planet passages this doesn't occur for any significant length of time.

The fifth plot in each group gives the ranges to the principle satellites of each planet. A use of this plot was discussed above in conjunction with the planetary range figure. The code for the satellites is given in Table C.1. For example, moon 3 at Jupiter is Ganymede. It is interesting to note that on the Jupiter mission the approach to Europa is actually closer than to the planet itself. The mission might be planned either to avoid such a close encounter in order to limit the perturbation on the trajectory, or to capitalize upon it for scientific information. In either case, the orbital period of Jupiter's satellites is so small compared to the trip time to Jupiter that fixed-time-of-arrival guidance would be a necessity for mission success.

The sixth graph in each group gives the moon-spacecraft-planet angle and thus reveals the location of the satellite relative to the planet. Although satellite-planet measurements have been eliminated due to the large phenomena error that would result, this plot is still useful because it identifies those times when the satellite is not visible from the spacecraft. The sun-satellite-spacecraft angle is used to determine whether or not the satellite is sunlit at a potential navigation sighting time. This information, which is given in the seventh plot of each group, reveals whether or not an IR capability is required to make a measurement.

The final plot in each group gives the sun-probe-satellite angle. This has precisely the same uses as the sun-probe-planet angle. For example, on the Jupiter mission moon 1 (Io) might still be useful before periplanet but the line-of-sight to the moon is too close to the line-of-sight to the sun for this to be a useable measurement.

Tables C.2 and C.3 give the results of using these plots to determine candidate onboard measurement schedules. The measurements actually used to generate the results given in Chapter IV were selected from those indicated as available in these tables. These tables correspond to Tables B.1 and B.2 and the selection of individual entries in Tables C.2 and C.3 is performed in the same way as outlined in the example in Appendix A of the Volume II. As an example of how to read these tables, note in Table C.2 that in the period from 21 hours before pericenter to pericenter the following measurement types are searched for the optimum measurement every hour using Jupiter, Io, and Europa as near bodies:

1. Planet/moon diameter measurement.
2. Planet/moon center to star measurements.
3. Planet/moon limb to star measurements.

Table C.1

Code For Planetary Satellites

Planet	Satellite	Code Number
Jupiter	Io	1
	Europa	2
	Ganymede	3
	Callisto	4
Saturn	Titan	1

Table C.2

Onboard Measurement Schedule
for the

Near Planet Leg of the Jupiter Mission

Beginning of Interval (hrs)	End of Interval (hrs)	Time Step for Interval (hrs)	Satellites Used	Planet/Moon Diameter Measurement	Planet/Moon Center to Star Measurement	Planet/Moon Limb to Star Measurement
Jupiter Sphere of Influence	-21 hrs	gradually decreasing from 10 days to 2 minutes	none	no	yes	yes
-21 hrs periplanet			IO, Europa	yes	yes	yes

Table C. 3
Onboard Measurement Schedule
for the
Near Planet Leg of the Saturn Mission

Beginning of Interval (hrs)	End of Interval (hrs)	Time Step for Interval (hrs)	Satellites Used	Planet/Moon Diameter Measurement	Planet/Moon Center to Star Measurement	Planet/Moon Limb to Star Measurement
Saturn Sphere of Influence	-36 hrs	1.5 da.	none	no	yes	yes
-36 hrs	periplanet	1 hr	rings	yes	yes	yes

Planetary Passage Geometries

Summary of Figures

1. 1979 Jupiter Mission

- Fig. C1.1 Trajectory Plan View During Jovian Passage on Jupiter Mission.
- Fig. C1.2 Range to Planet During Jovian Passage on Jupiter Mission.
- Fig. C1.3 Angle Subtended by Planetary Limbs During Jovian Passage on Jupiter Mission.
- Fig. C1.4a Earth-SC-Planet Angle During Jovian Passage on Jupiter Mission.
- Fig. C1.4b Sun-SC-Planet Angle During Jovian Passage on Jupiter Mission.
- Fig. C1.5 Range to Principle Moons During Jovian Passage on Jupiter Mission.
- Fig. C1.6 Moon-SC-Planet Angle During Jovian Passage on Jupiter Mission.
- Fig. C1.7 Sun-Moon/SC Angle During Jovian Passage on Jupiter Mission.
- Fig. C1.8 Sun-SC-Moon Angle During Jovian Passage on Jupiter Mission.

2. 1981 Saturn Mission

- Fig. C2.1 Trajectory Plan View During Saturn Passage on Saturn Mission.
- Fig. C2.2 Range to Planet During Saturn Passage on Saturn Mission.
- Fig. C2.3 Angle Subtended by Planetary Limbs During Saturn Passage on Saturn Mission.
- Fig. C2.4a Earth-SC-Planet Angle During Saturn Passage on Saturn Mission.
- Fig. C2.4b Sun-SC-Planet Angle During Saturn Passage on Saturn Mission.

Fig. C2.5 Range to Principle Moons During Saturn Passage on Saturn Mission.

Fig. C2.6 Moon-SC-Planet Angle During Saturn Passage on Saturn Mission.

Fig. C2.7 Sun-Moon-SC Angle During Saturn Passage on Saturn Mission.

Fig. C2.8 Sun-SC-Moon Angle During Saturn Passage on Saturn Mission.

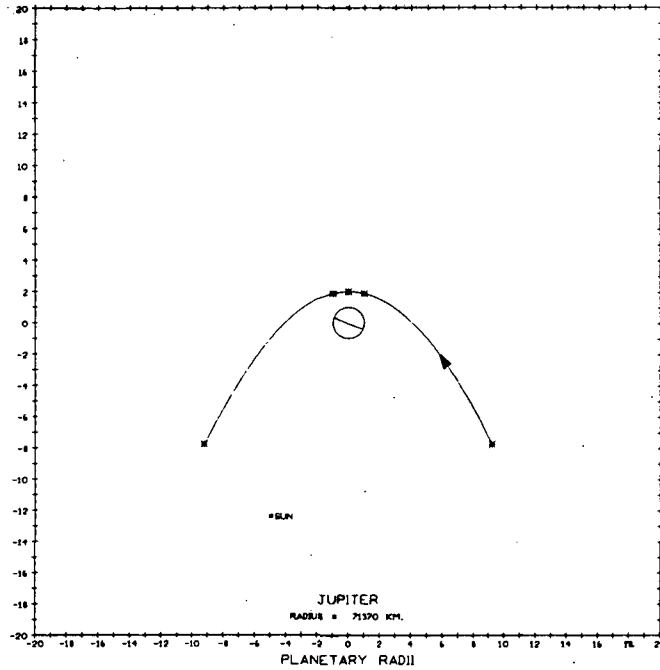


Fig. C. 1. 1 Trajectory Plan View During Jovian Passage on Jupiter Mission

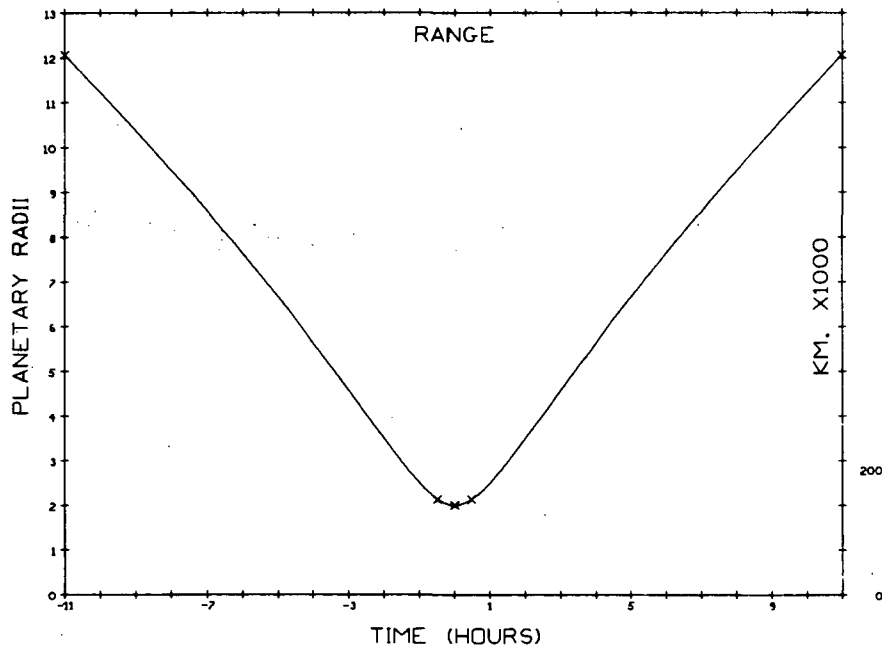


Fig. C. 1. 2 Range to Planet During Jovian Passage on Jupiter Mission

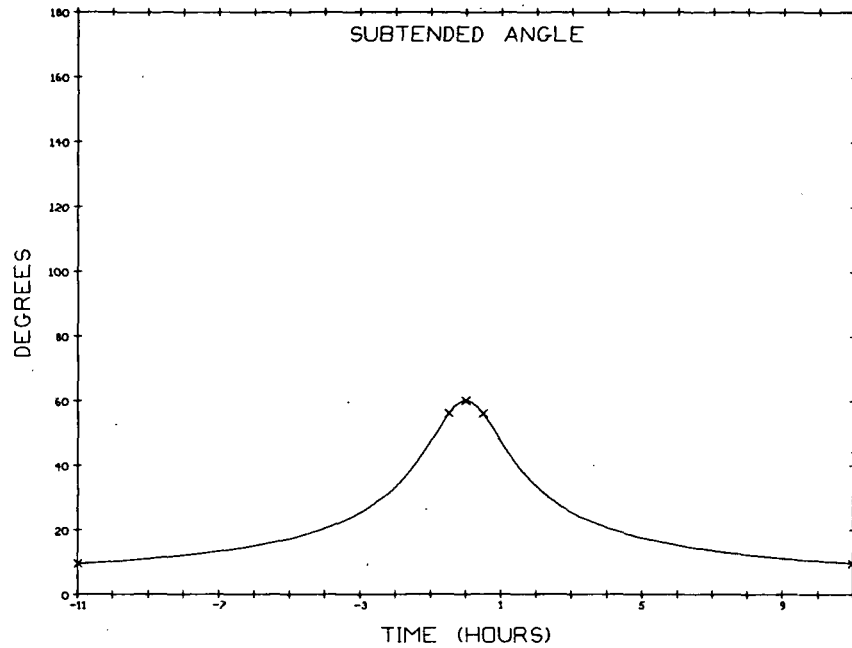


Fig. C.1.3 Angle Subtended by Planetary Limbs During Jovian Passage on Jupiter Mission

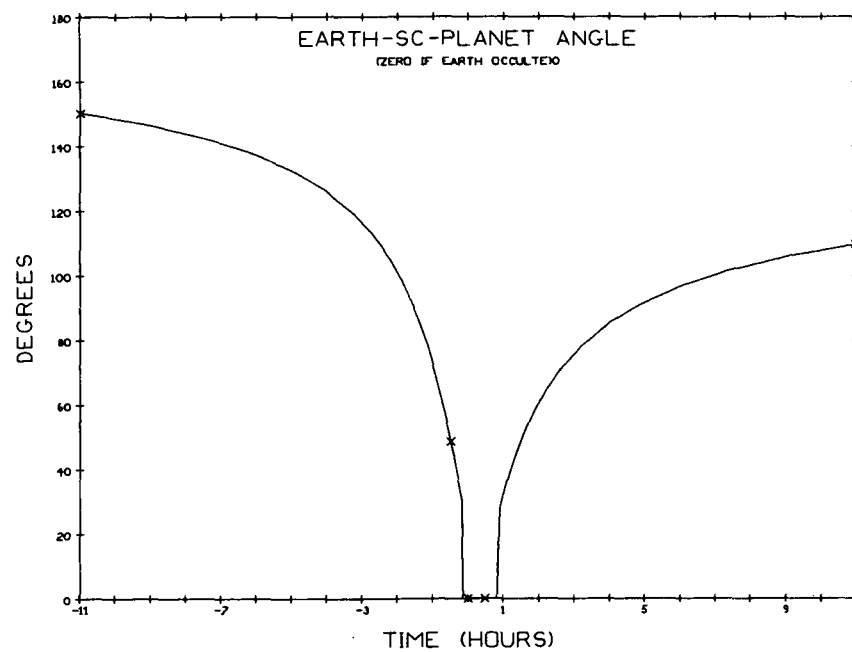


Fig. C.1.4a Earth-SC-Planet Angle During Jovian Passage on Jupiter Mission

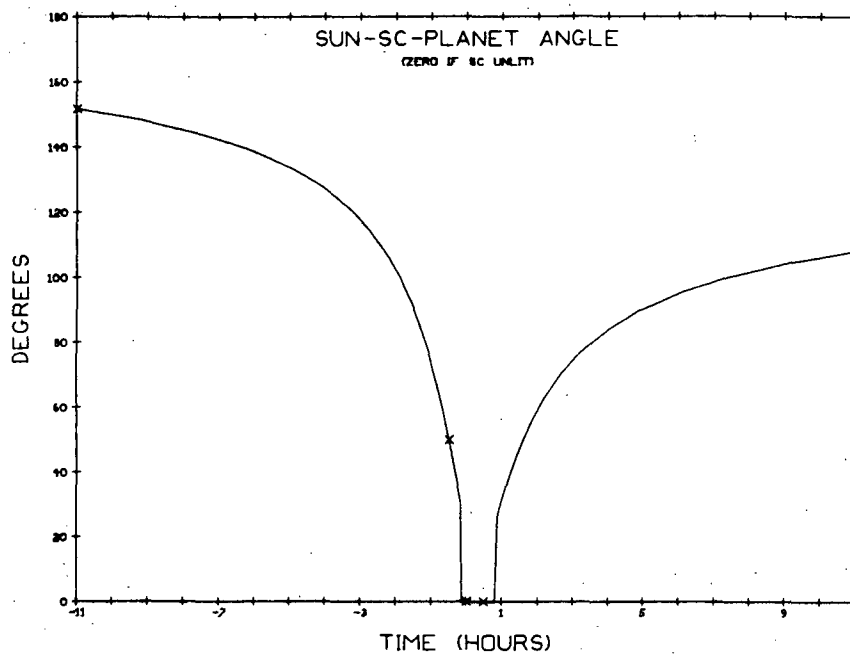


Fig. C . 1. 4b Sun-SC-Planet Angle During Jovian Passage on Jupiter Mission

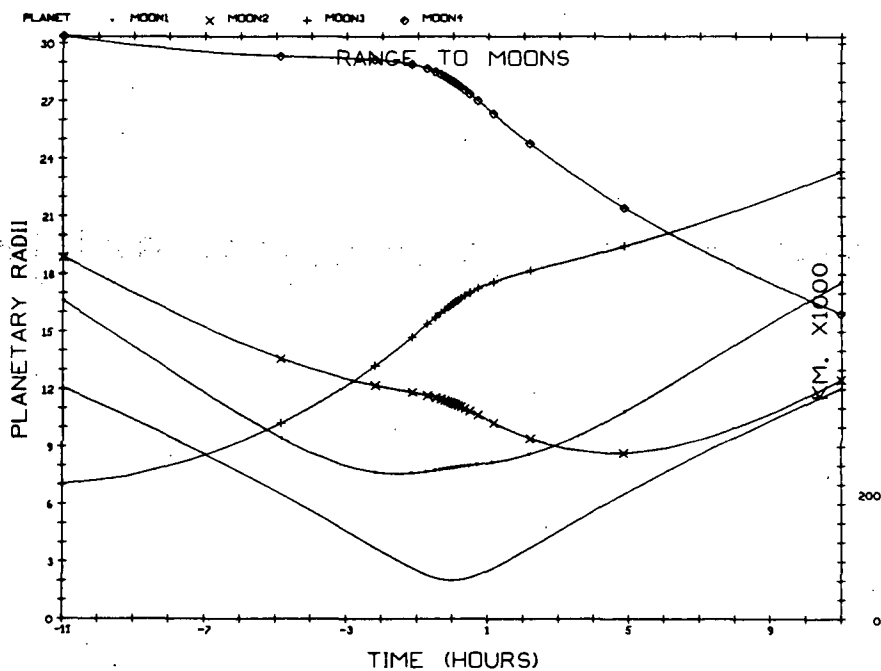


Fig. C . 1. 5 Range to Principle Moons During Jovian Passage on Jupiter Mission

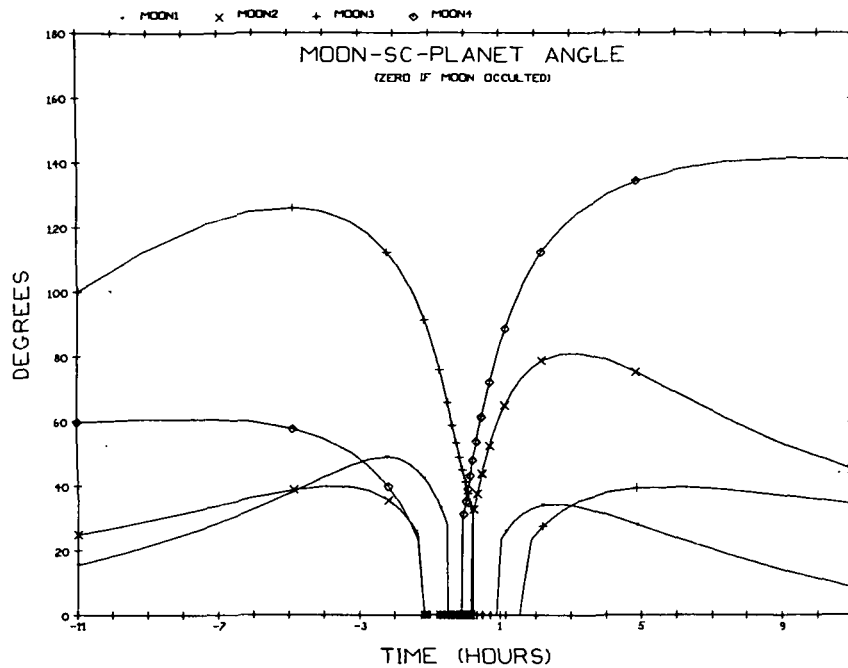


Fig. C.1.6 Moon-SC-Planet Angle During Jovian Passage on Jupiter Mission

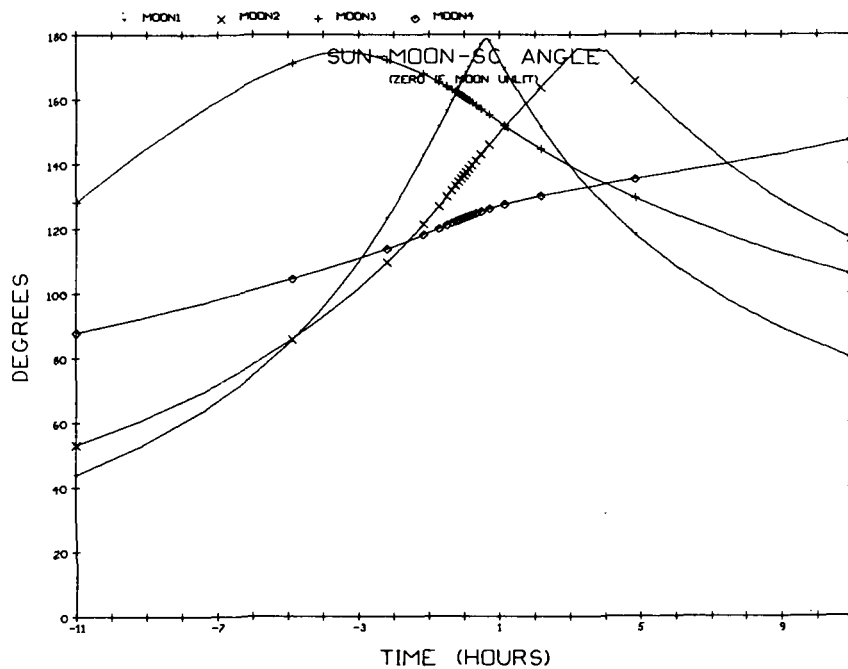


Fig. C.1.7 Sun-Moon-SC Angle During Jovian Passage on Jupiter Mission

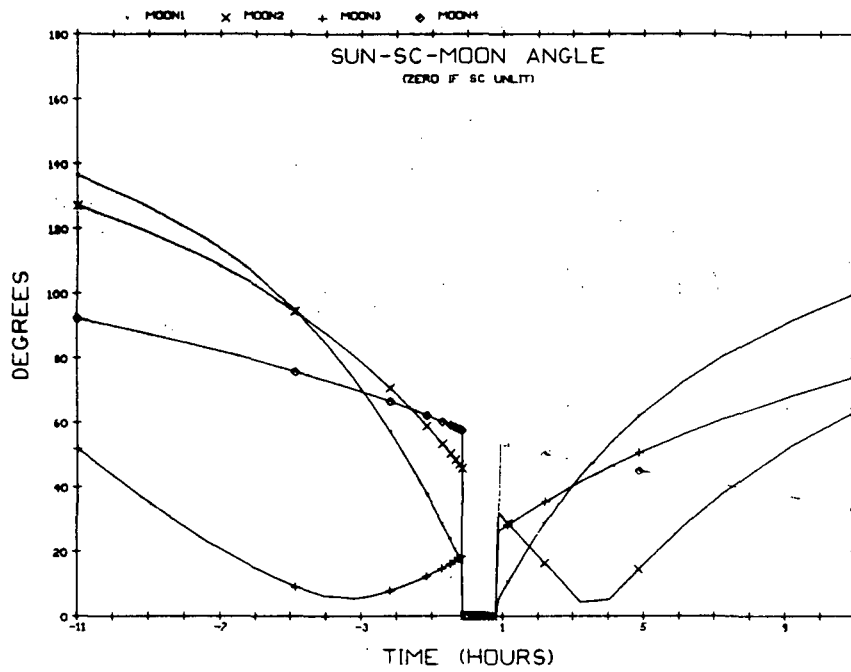


Fig. C.1.8 Sun-SC-Moon Angle During Jovian Passage on Jupiter Mission

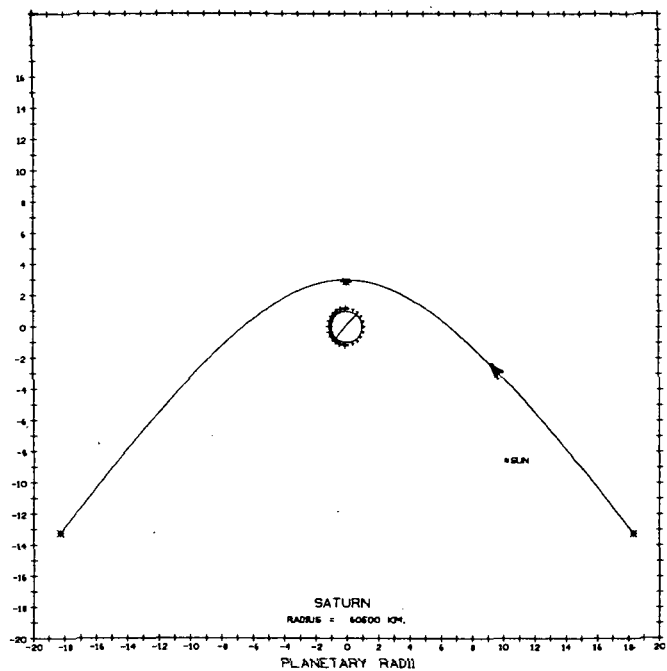


Fig. C.2.1 Trajectory Plan View During Saturn Passage on Saturn Mission; 40-Radii Field

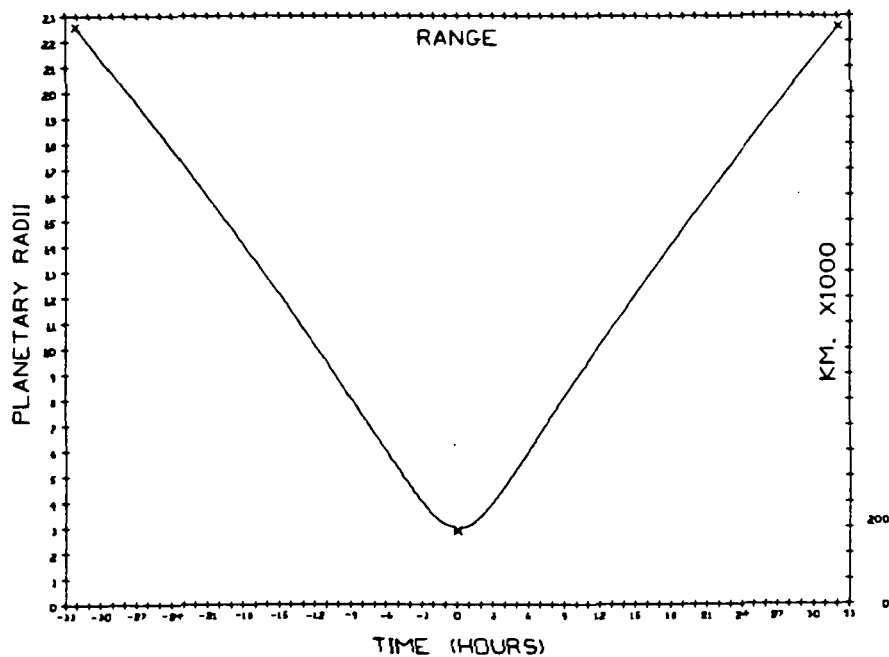


Fig. C.2.2 Range to Planet During Saturn Passage on Saturn Mission

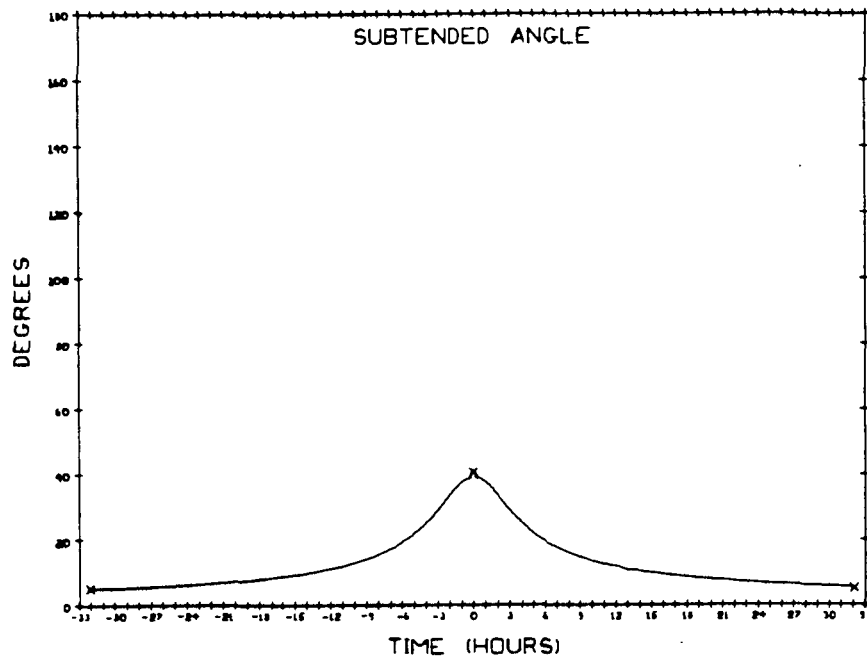


Fig. C. 2. 3 Angle Subtended by Planetary Limbs During Saturn Passage on the Saturn Mission

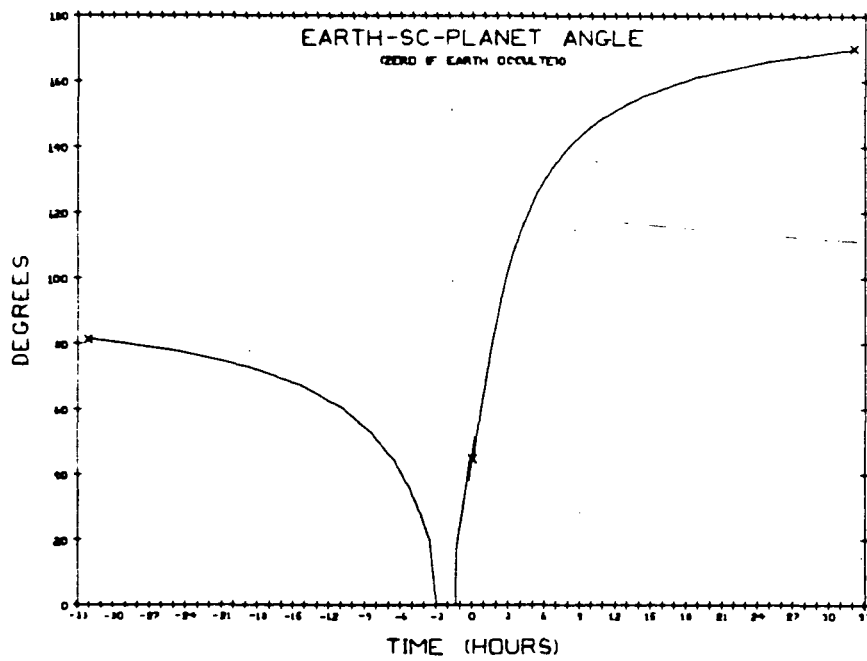


Fig. C. 2. 4a Earth-SC-Planet Angle During Saturn Passage on the Saturn Mission

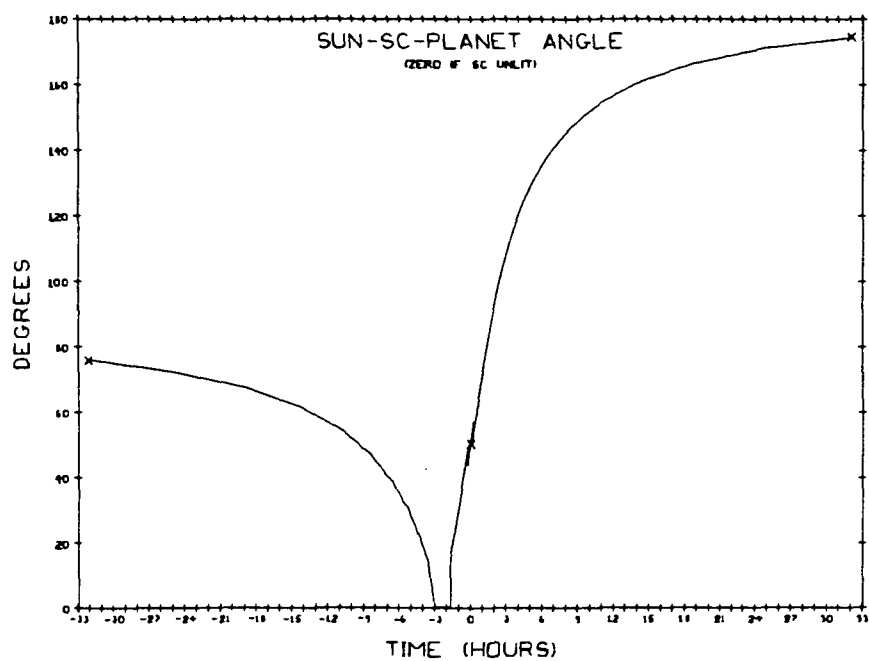


Fig. C.2.4b Sun-SC-Planet Angle During Saturn Passage on the Saturn Mission

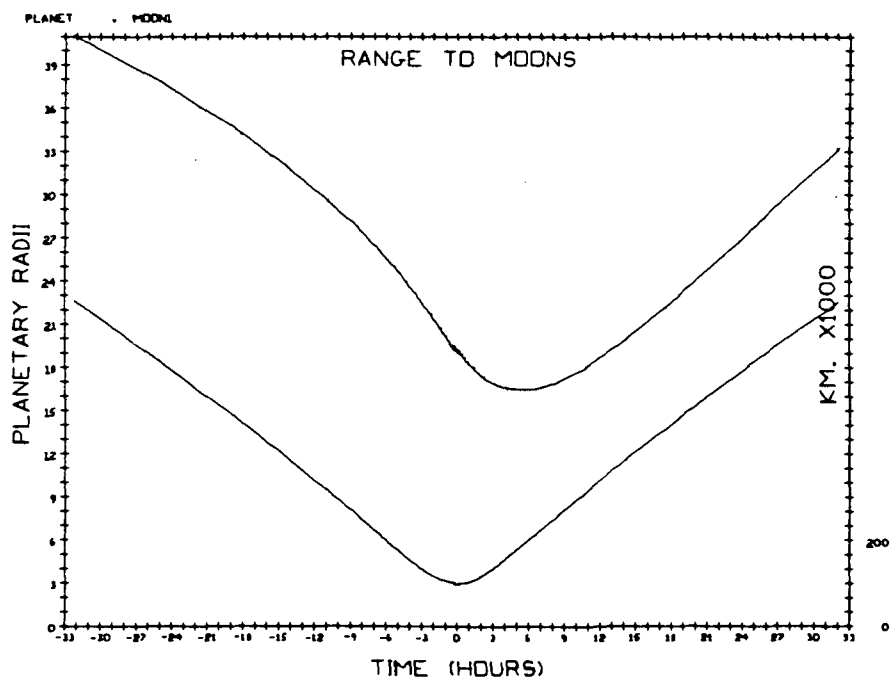


Fig. C.2.5 Range to Principle Moons During Saturn Passage on Saturn Mission

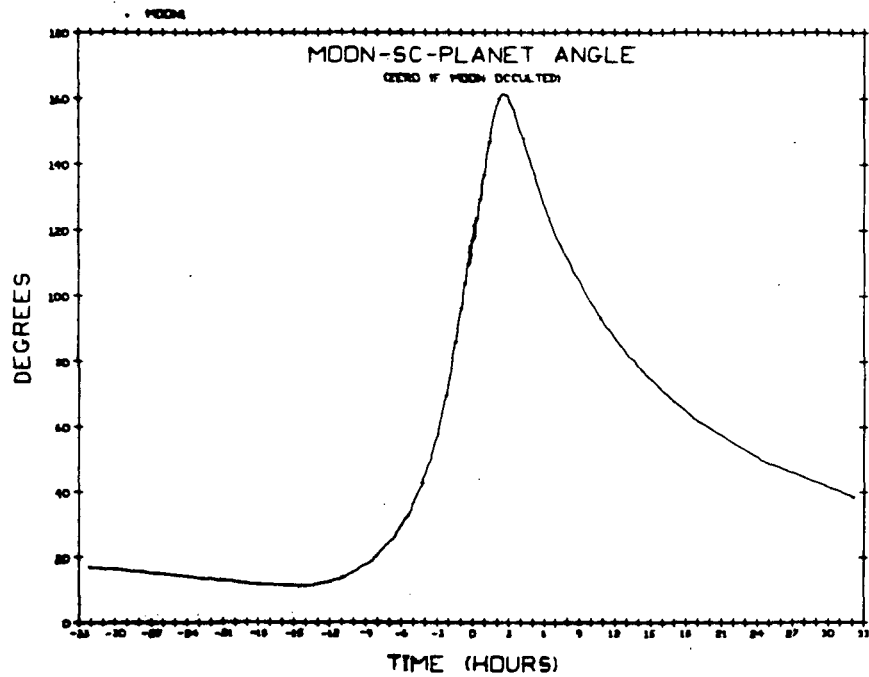


Fig. C. 2. 6 Moon-SC-Planet Angle During Saturn Passage on the Saturn Mission

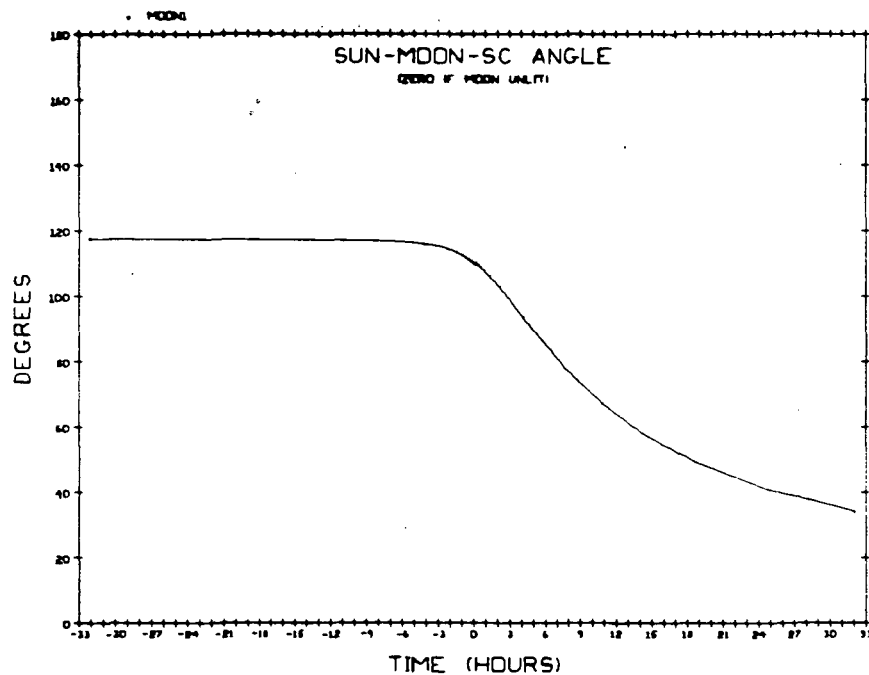


Fig. C. 2. 7 Sun-Moon-SC Angle During Saturn Passage on the Saturn Mission

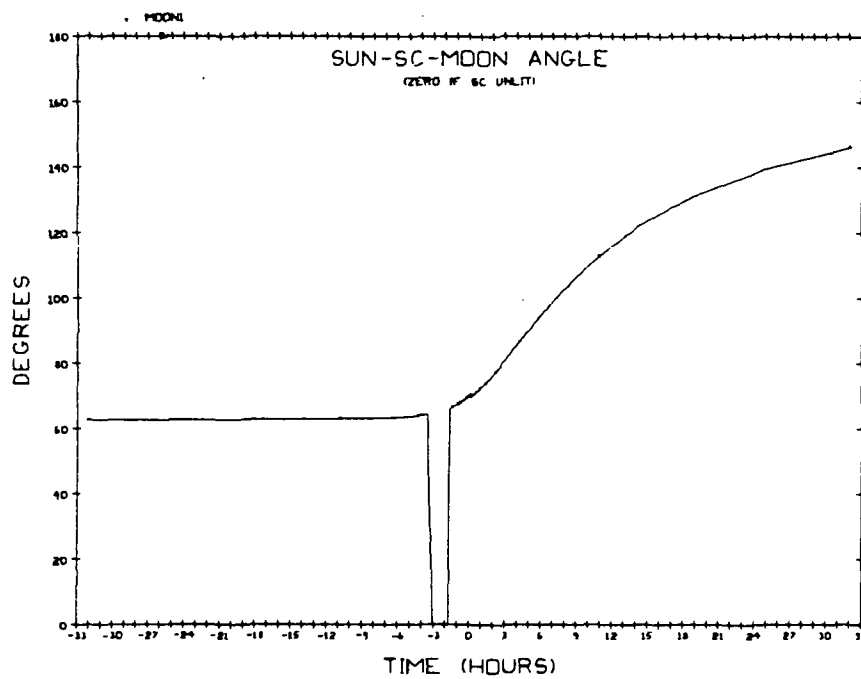


Fig. C.2.8 Sun-SC-Moon Angle During Saturn Passage on the Saturn Mission

Page intentionally left blank

APPENDIX D

STATISTICS

The purpose of this appendix is to derive and present the equations used for the statistical propagation, for accelerometer, DSN, and onboard measurement incorporations and for measurement selection.

D.1 State

For the combined navigation and low thrust guidance system a 12 dimensional state was used, where

$$\delta \underline{x} = \begin{bmatrix} \delta \underline{r} \\ \delta \underline{v} \\ \delta \underline{d} \\ \delta m \\ \underline{u}_{ma} \end{bmatrix}$$

\underline{r} and \underline{v} are the spacecraft position and velocity, respectively, in whichever coordinate system we are operating, and m is the mass of the spacecraft. The differential equations for \underline{r} , \underline{v} and m , which will be needed below for the development of the statistical navigation equations, are:

$$\begin{aligned} \dot{\underline{r}} &= \underline{v} \\ \dot{\underline{v}} &= \frac{-\mu_s \underline{\rho}}{\rho^3} - \frac{\mu_p \underline{a}}{a^3} - \frac{\mu_p \underline{d}}{d^3} + \frac{\beta c \hat{\underline{u}}}{m} \end{aligned}$$

for the interplanetary or sun centered leg, and by

$$\dot{\underline{v}} = \frac{-\mu_s \underline{\rho}}{\rho^3} - \frac{\mu_p \underline{a}}{a^3} + \frac{\mu_s \underline{d}}{d^3} + \frac{\beta c \hat{\underline{u}}}{m}$$

for the near planet or planet centered leg,

$$\dot{m} = -\beta$$

It will be assumed that the thrust vector misalignment, \underline{u}_{ma} , is composed of independent brownian motions. Its driving noise will be represented by $\underline{w}_d(t)$ which has a known covariance. The ephemeris error, $\delta \underline{d}$, is modeled as a constant bias with known initial covariance. It is added to the state vector with a zero time derivative.

D.2 Variational Equations

From the state differential equations given in the previous section, one finds that the variational state satisfies the following differential equation

$$\begin{aligned} \delta \dot{\underline{x}} = & \left. \frac{\partial \dot{\underline{x}}}{\partial \underline{x}} \right|^* \delta \underline{x} + \left. \frac{\partial \dot{\underline{x}}}{\partial \underline{u}_c} \right|^* \delta \underline{u}_c + \left. \frac{\partial \dot{\underline{x}}}{\partial T} \right|^* \delta T \\ & + \left. \frac{\partial \dot{\underline{x}}}{\partial \mu} \right|^* \delta \mu + \left. \frac{\partial \dot{\underline{x}}}{\partial \beta} \right|^* \delta \beta + \left. \frac{\partial \underline{x}}{\partial \underline{w}_d} \right|^* \underline{w}_d \end{aligned} \quad (D.1)$$

where * indicates the expressions are evaluated on the reference or nominal trajectory. Note that $\delta \underline{u}_c$ is the deterministic deviation in control where no variation in switch time is considered; δT is the variation in thrust magnitude and is modeled as an unbiased white noise; $\delta \mu$ is the variation in the gravitational constant of the sun (for the interplanetary leg of the mission) or of the target planet (for the near planet leg) and is modeled as

a bias; $\delta\beta$ is the variation in mass flow rate and is modeled as the sum of a bias and an unbiased white noise. The partials are given by

$$\frac{\partial \dot{\underline{x}}}{\partial \underline{x}} = \begin{bmatrix} 0^{3 \times 3} & I^{3 \times 3} & 0^{3 \times 3} & 0^{3 \times 1} & 0^{3 \times 2} \\ \frac{\partial \dot{\underline{y}}}{\partial \underline{r}} & 0^{3 \times 3} & \frac{\partial \dot{\underline{y}}}{\partial \underline{d}} & \frac{\partial \dot{\underline{y}}}{\partial \underline{m}} & \frac{\partial \dot{\underline{y}}}{\partial \underline{u}_{ma}} \\ 0^{3 \times 3} & 0^{3 \times 3} & 0^{3 \times 3} & 0^{3 \times 1} & 0^{3 \times 2} \\ & & 0^{3 \times 12} & & \end{bmatrix}$$

and

$$\begin{aligned} \frac{\partial \dot{\underline{y}}}{\partial \underline{r}} &= \frac{-\mu_s I}{\rho^3} + \frac{3\mu_s \underline{\rho} \underline{\rho}^T}{\rho^5} - \frac{\mu_p I}{a^3} + \frac{3\mu_p \underline{a} \underline{a}^T}{a^5} \\ \frac{\partial \dot{\underline{y}}}{\partial \underline{d}} &= \frac{\mu_p I}{a^3} - \frac{3\mu_p \underline{a} \underline{a}^T}{a^5} - \frac{\mu_p I}{d^3} + \frac{3\mu_p \underline{d} \underline{d}^T}{d^5} && \text{interplanetary leg} \\ &= \frac{-\mu_s I}{\rho^3} + \frac{3\mu_s \underline{\rho} \underline{\rho}^T}{\rho^5} + \frac{\mu_s I}{d^3} - \frac{3\mu_s \underline{d} \underline{d}^T}{d^5} && \text{near planet leg} \\ \frac{\partial \dot{\underline{y}}}{\partial \underline{m}} &= -\frac{T}{m^2} \hat{\underline{u}} \sigma && \sigma = 1, \text{ thrust on} \\ &&& \sigma = 0, \text{ thrust off} \\ \frac{\partial \dot{\underline{y}}}{\partial \underline{u}_{ma}} &= \frac{T}{m} \frac{\partial \hat{\underline{u}}}{\partial \underline{u}_c} \sigma \end{aligned}$$

$$\frac{\partial \dot{\underline{x}}}{\partial \underline{u}_c} = \frac{\partial \dot{\underline{x}}}{\partial \hat{u}} \frac{\partial \hat{u}}{\partial \underline{u}_c} = \begin{bmatrix} 0^{3 \times 2} \\ \frac{T}{m} \frac{\partial \hat{u}}{\partial \underline{u}_c} \sigma \\ 0^{6 \times 2} \end{bmatrix}$$

where

$$\frac{\partial \hat{u}}{\partial \underline{u}_c} = \frac{1}{||\underline{\lambda}_v||}$$

$$\begin{bmatrix} -\lambda_{v2} & \frac{-\lambda_{v3} \lambda_{v1}}{\sqrt{\lambda_{v1}^2 + \lambda_{v2}^2}} \\ \lambda_{v1} & \frac{-\lambda_{v2} \lambda_{v3}}{\sqrt{\lambda_{v1}^2 + \lambda_{v2}^2}} \\ 0 & \sqrt{\lambda_{v1}^2 + \lambda_{v2}^2} \end{bmatrix}$$

$$\frac{\partial \dot{\underline{x}}}{\partial T} = \frac{\hat{u}}{m} \sigma$$

$$\frac{\partial \dot{\underline{x}}}{\partial \mu} = \begin{bmatrix} 0^{3 \times 1} \\ -\frac{\underline{\rho}}{\rho^3} \\ 0^{6 \times 1} \end{bmatrix}$$

interplanetary leg

$$= \begin{bmatrix} 0 \\ -\frac{\underline{a}}{a^3} \\ 0^{6 \times 1} \end{bmatrix}$$

near planet leg

$$\frac{\partial \dot{\underline{x}}}{\partial \underline{\beta}} = \begin{bmatrix} 0^{9 \times 1} \\ -1\sigma \\ 0^{2 \times 1} \end{bmatrix}$$

$$\frac{\partial \dot{\underline{x}}}{\partial \underline{w}_d} = \begin{bmatrix} 0^{10 \times 2} \\ I^{2 \times 2} \end{bmatrix}$$

Following is a derivation of $\frac{\partial \hat{\underline{u}}}{\partial \underline{u}_c}$ where we recall that $\hat{\underline{u}}$ is a three dimensional unit vector of directional cosines defining the direction of the control and \underline{u}_c is the two dimensional vector of angles (θ, ψ) . Noting that

$$\hat{\underline{u}} = \frac{\underline{\lambda}_v}{\|\underline{\lambda}_v\|}$$

from Fig. A.2

$$\cos \theta = \lambda_{v1} / \sqrt{\lambda_{v1}^2 + \lambda_{v2}^2}$$

$$\sin \theta = \lambda_{v2} / \sqrt{\lambda_{v1}^2 + \lambda_{v2}^2}$$

$$\cos \psi = \frac{\sqrt{\lambda_{v1}^2 + \lambda_{v2}^2}}{\|\underline{\lambda}_v\|}$$

$$\sin \psi = \lambda_{v3} / \|\underline{\lambda}_v\|$$

$$\hat{\underline{u}} = \begin{bmatrix} \cos \theta & \cos \psi \\ \sin \theta & \cos \psi \\ \sin \psi \end{bmatrix}$$

$$\frac{\partial \hat{u}}{\partial u_c} = \begin{bmatrix} -\cos \psi \sin \theta & -\sin \psi \cos \theta \\ \cos \theta \cos \psi & -\sin \theta \sin \psi \\ 0 & \cos \psi \end{bmatrix}$$

or from Eq. E. 1 in terms of λv 's

$$\frac{\partial \hat{u}}{\partial u_c} = \frac{1}{\prod \lambda_v} \begin{bmatrix} -\lambda_{v_2} & \frac{-\lambda_{v_3} \lambda_{v_1}}{\sqrt{\lambda_{v_1}^2 + \lambda_{v_2}^2}} \\ \lambda_{v_1} & \frac{-\lambda_{v_2} \lambda_{v_3}}{\sqrt{\lambda_{v_1}^2 + \lambda_{v_2}^2}} \\ 0 & \sqrt{\lambda_{v_1}^2 + \lambda_{v_2}^2} \end{bmatrix}$$

The derivation of $\frac{\partial \dot{v}}{\partial u_{ma}}$ can also be shown in more detail.

Since

$$u_c = u_c^* + u_{ma}$$

$$\frac{\partial \dot{v}}{\partial u_{ma}} = \frac{\partial \dot{v}}{\partial \hat{u}} \frac{\partial \hat{u}}{\partial u_c} \frac{\partial u_c}{\partial u_{ma}}$$

where

$$\frac{\partial u_c}{\partial u_{ma}} = I^{2 \times 2}$$

and

$$\frac{\partial \dot{v}}{\partial \hat{u}} = \frac{T}{m} I$$

The variational equation, D.1, can be rewritten grouping the state, command, biases, and white noise components by defining

$$\underline{w}(t) = \begin{bmatrix} \delta T \\ \underline{w}_d \\ \beta_r \end{bmatrix} \quad \text{white noise}$$

$$\underline{\gamma} = \begin{bmatrix} \beta_b \\ \delta \mu \end{bmatrix} \quad \text{biases}$$

(where $\delta\beta = \beta_r + \beta_b$)

then

$$\delta \dot{\underline{x}} = A(t) \delta \underline{x} + B_u(t) \delta \underline{u}_c + B_w(t) \underline{w}(t) + D(t) \underline{\gamma} \quad (D.2)$$

where

$$A(t) = \frac{\partial \dot{\underline{x}}}{\partial \underline{x}}$$

$$B_u(t) = \frac{\partial \dot{\underline{x}}}{\partial \underline{u}_c}$$

$$B_w(t) = \begin{bmatrix} 0^{3 \times 1} & | & 0^{10 \times 2} & | & 0^{9 \times 1} \\ \frac{\hat{\underline{u}}}{m} \sigma & | & I^{2 \times 2} & | & -\sigma \\ 0^{6 \times 1} & | & & | & 0^{2 \times 1} \end{bmatrix}$$

$$D(t) = \left[\begin{array}{c|c} 0^{9 \times 1} & 0^{3 \times 1} \\ \hline -\sigma & \frac{-\underline{r}}{r^3} \\ \hline 0^{2 \times 1} & 0^{6 \times 1} \end{array} \right]$$

If we assume that we have a continuous estimate of the state, $\delta \hat{\underline{x}}(t)$, and that the control is a linear functional of this estimate, then

$$\delta \underline{u}_c = \Lambda(t) \delta \hat{\underline{x}}(t).$$

If

$$\underline{e}(t) = \delta \hat{\underline{x}}(t) - \delta \underline{x}(t)$$

then we have the following differential equations for $\delta \underline{x}$, $\delta \hat{\underline{x}}$ and \underline{e}

$$\dot{\delta \underline{x}} = A \delta \underline{x} + B_u \Lambda \delta \hat{\underline{x}} + B_w \underline{w}(t) + D \underline{y}$$

$$\dot{\delta \hat{\underline{x}}} = A \delta \hat{\underline{x}} + B_u \Lambda \delta \hat{\underline{x}}$$

$$\dot{\underline{e}}(t) = A \underline{e} - B_w \underline{w}(t) - D \underline{y}$$

$\delta \underline{x}(t)$, $\delta \hat{\underline{x}}(t)$, and $\underline{e}(t)$ are considered stochastic processes.

D.3 Statistical Propagation

We are interested in getting the differential equations for the covariances associated with the error $\underline{e}(t)$ and with the deviation in state $\delta \underline{x}(t)$. These will be denoted

$$E(t) = \overline{\underline{e}(t) \underline{e}(t)^T}$$

and

$$X(t) = \overline{\delta \underline{x} \delta \underline{x}^T}$$

where the overbar indicates we are taking the expected value. In order to develop the differential equations, three additional correlation matrices are needed:

$$V(t) = \overline{\underline{e}(t) \underline{y}^T} \quad (12 \times 2),$$

$$J(t) = \overline{\delta \underline{x}(t) \underline{y}^T} \quad (12 \times 2),$$

$$C(t) = \overline{\delta \hat{\underline{x}}(t) \underline{e}(t)^T} \quad (12 \times 12).$$

The derivation of the differential equations follows.

$$\begin{aligned} \dot{V} &= \frac{d}{dt} \overline{\underline{e} \underline{y}^T} = \overline{\dot{\underline{e}} \underline{y}^T} \\ &= A \overline{\underline{e} \underline{y}^T} - B_w \overline{\underline{w}(t) \underline{y}^T} - D \overline{\underline{y} \underline{y}^T} \\ \dot{V} &= AV - D \overline{\underline{y} \underline{y}^T}, \quad V(0) = 0 \\ \dot{E} &= \frac{d}{dt} \overline{\underline{e} \underline{e}^T} = \overline{\dot{\underline{e}} \underline{e}^T} + \overline{\underline{e} \dot{\underline{e}}^T} \end{aligned} \tag{D.3}$$

Since the 2 terms composing the above equations are transposes of each other, only one term needs to be calculated.

$$\begin{aligned} \overline{\dot{\underline{e}} \underline{e}^T} &= A \overline{\underline{e} \underline{e}^T} - B_w \overline{\underline{w} \underline{e}^T} - D \overline{\underline{y} \underline{e}^T} \\ &= AE + 1/2 B_w \overline{\underline{w} \underline{w}^T} B_w^T - DV^T \end{aligned}$$

where, note that if $\Phi(t,s)$ is the state transition matrix for the system $\dot{\underline{y}} = A\underline{y}$ then

$$\underline{e}(t) = \Phi(t, t_0) \underline{e}(t_0) - \int_{t_0}^t \Phi(t, s) B_w(s) \underline{w}(s) ds$$

$$- \int_{t_0}^t \Phi(t, s) D(s) \underline{y} ds$$

$$\overline{\underline{w} \underline{e}(t)^T} = - \int_{t_0}^t \overline{\underline{w}(t) \underline{w}(s)^T B_w(s)^T \Phi(t, s)^T} ds$$

$$= -1/2 \overline{\underline{w}(t) \underline{w}(t)^T} B_w(t)^T$$

where the other terms in $\underline{e}(t)$ are eliminated when taking the expected value.

Thus

$$\dot{\underline{E}} = \underline{A} \underline{E} + \underline{E} \underline{A}^T + B_w \overline{\underline{w} \underline{w}^T} B_w^T - D \underline{V}^T - \underline{V} D^T \quad (D.4)$$

where $\underline{E}(0)$ is given.

$$\begin{aligned} \dot{\underline{J}} &= \frac{d}{dt} \overline{\delta \underline{x} \underline{y}^T} = \overline{\delta \dot{\underline{x}} \underline{y}^T} \\ &= \underline{A} \overline{\delta \underline{x} \underline{y}^T} + B_u \overline{\Lambda(\underline{e} + \delta \underline{x}) \underline{y}^T} + B_w \overline{\underline{w} \underline{y}^T} + D \overline{\underline{y} \underline{y}^T} \\ &= \underline{A} \underline{J} + B_u \overline{\Lambda \underline{e} \underline{y}^T} + B_u \overline{\delta \underline{x} \underline{y}^T} + D \overline{\underline{y} \underline{y}^T} \\ \dot{\underline{J}} &= (\underline{A} + B_u \Lambda) \underline{J} + B_u \overline{\Lambda \underline{V}} + D \overline{\underline{y} \underline{y}^T} \end{aligned} \quad (D.5)$$

where $\underline{J}(0) = 0$

$$\dot{\underline{C}} = \frac{d}{dt} \overline{\delta \hat{\underline{x}}(t) \underline{e}(t)^T}$$

$$\begin{aligned}
&= \overline{\dot{\underline{\hat{x}}} \underline{e}(t)^T} + \overline{\dot{\underline{\hat{x}}} \underline{e}^T} \\
&= A \overline{\underline{\hat{x}} \underline{e}^T} + B_u \wedge \overline{\underline{\hat{x}} \underline{e}^T} + \overline{\underline{\hat{x}} \underline{e}^T} A^T - \overline{\underline{\hat{x}} \underline{w}^T} B_w^T - \overline{\underline{\hat{x}} \underline{l}^T} D^T \\
\dot{\underline{C}} &= (A + B_u \wedge) \underline{C} + \underline{C} A^T - (\underline{V} + \underline{J}) D^T
\end{aligned} \tag{D.6}$$

where $\underline{C}(0) = 0$.

$$\begin{aligned}
\dot{\underline{X}} &= \frac{d}{dt} \overline{\underline{\hat{x}}(t) \underline{\hat{x}}(t)^T} = \overline{\dot{\underline{\hat{x}}} \underline{\hat{x}}^T} + \overline{\underline{\hat{x}} \dot{\underline{\hat{x}}}^T} \\
\overline{\dot{\underline{\hat{x}}} \underline{\hat{x}}^T} &= A \overline{\underline{\hat{x}} \underline{\hat{x}}^T} + B_u \wedge \overline{\underline{\hat{x}} \underline{\hat{x}}^T} + B_w \overline{\underline{w}(t) \underline{\hat{x}}^T} + D \overline{\underline{l} \underline{\hat{x}}^T} \\
&= A \overline{\underline{\hat{x}} \underline{\hat{x}}^T} + B_u \wedge \overline{\underline{\hat{x}} \underline{\hat{x}}^T} + B_u \wedge \overline{\underline{e} \underline{\hat{x}}^T} \\
&\quad + B_w \overline{\underline{w} \underline{\hat{x}}^T} - B_w \overline{\underline{w} \underline{e}^T} + D \underline{J}^T \\
&= (A + B_u \wedge) \underline{X} + B_u \wedge (\underline{e} \underline{\hat{x}}^T - \underline{e} \underline{e}^T) + 1/2 B_w \overline{\underline{w} \underline{w}^T} B_w^T + D \underline{J}^T
\end{aligned}$$

thus

$$\begin{aligned}
\underline{X} &= (A + B_u \wedge) \underline{X} + \underline{X} (A + B_u \wedge)^T + B_u \wedge (\underline{C} - \underline{E})^T + (\underline{C} - \underline{E}) \wedge^T B_u^T \\
&\quad + B_w \overline{\underline{w} \underline{w}^T} B_w^T + D \underline{J}^T + \underline{J} D^T
\end{aligned} \tag{D.7}$$

where $\underline{X}(0)$ is given. The differential equation for the matrix $\underline{S}(t) = \overline{\underline{e}(t) \underline{b}^T}$, where \underline{b} is a two dimensional bias vector associated with DSN tracking station location errors is needed.

$$\begin{aligned}
\dot{\underline{S}} &= \frac{d}{dt} \overline{\underline{e} \underline{b}^T} = \overline{\dot{\underline{e}} \underline{b}^T} \\
&= A \overline{\underline{e} \underline{b}^T} - B_w \overline{\underline{w} \underline{b}^T} - D \overline{\underline{l} \underline{b}^T} \\
\dot{\underline{S}} &= \underline{A} \underline{S} \qquad \underline{S}(0) = 0
\end{aligned} \tag{D.8}$$

Equations D.3 through D.8 are the differential equations for the propagation of the six correlation matrices.

The following initial covariance matrices must be given: $\underline{x}(0)$, $\underline{E}(0)$,

$$\underline{w}\underline{w}^T = \begin{bmatrix} \overline{\delta T^2} & 0^{1 \times 2} & 0 \\ 0 & \underline{w}_d \underline{w}_d^T & 0 \\ 0 & 0^{1 \times 2} & \overline{\beta_r^2} \end{bmatrix}$$

$$\underline{\gamma}\underline{\gamma}^T = \begin{bmatrix} \overline{\beta_b^2} & 0 \\ 0 & \overline{\delta \mu^2} \end{bmatrix}$$

where $\overline{\delta \mu^2}$ is the mean squared uncertainty in the μ of the sun for the interplanetary leg and the uncertainty in the μ of the target planet for the near planet leg.

For reference we will include a summary of the dimensions or units of the terms in $\underline{w}\underline{w}^T$ and $\underline{\gamma}\underline{\gamma}^T$. Here M implies units of mass, L units of length and T units of time (thus δT^2 has units of force squared or $(MLT^{-2})^2$).

TABLE D.1

$\overline{\delta T^2}$	$(MLT^{-2})^2$
$\underline{w}_d \underline{w}_d^T$	$(T^{-1})^2$
$\overline{\beta_r^2}$	$(MT^{-1})^2$
$\overline{\beta_b^2}$	$(MT^{-1})^2$
$\overline{\delta \mu^2}$	$(L^3 T^{-2})^2$

D.4 Coordinate Change

The \underline{E} , \underline{X} , etc., matrices are affected by measurements and by the coordinate change. At the sphere of influence of the target planet we changed from sun centered coordinates to planet centered coordinates. The effect on the 12 dimensional $\underline{\delta x}$ is that

$$\delta \underline{x}' = Q \delta \underline{x}$$

at the time of coordinate change.

Where

$$Q = \begin{bmatrix} I & 0 & -I & 0 \\ 0 & I & 0 & 0 \\ 0 & 0 & I & 0 \\ 0 & 0 & 0 & I \end{bmatrix}$$

where each 0 and I is a 3x3 block. Likewise $\underline{e}' = Q \underline{e}$ and $\delta \hat{\underline{x}}' = Q \delta \hat{\underline{x}}$. It follows that

$$E' = QEQ^T$$

$$V' = QV$$

$$J' = QJ$$

$$C' = QCQ^T$$

$$X' = QXQ^T$$

$$S' = QS$$

D.5 Accelerometer Measurements

In the simulations various measurements or combinations of measurements are optional. For example, accelerometers, various kinds of onboard measurements or DSN measurements could be incorporated.

The formulas for onboard and DSN measurement incorporation are essentially the same as those for Phase A with the accomodation of the

higher dimensional state. Thus the matrix $H = \left(\frac{\partial z}{\partial x}\right)^T$ will have zeros in the last 3 columns. The $H = \left(\frac{\partial z}{\partial x}\right)^T$ for the accelerometer measurement will have zeros in all but the last 3 columns. Measurements by three accelerometers perpendicular to each other and by one accelerometer measuring in the direction of the nominal thrust were considered. Since accelerometer measurements can be taken continuously, expressions can be derived which are added directly into the matrix differential equations. This method led however to numerical difficulties, so expressions were derived which incorporate accelerometer measurements discretely.

If E' is the error covariance matrix before a measurement and E after the measurement, then it is well known that

$$E^{-1} = E'^{-1} + H^T R^{-1} H$$

(for example Ref. 2, Eq. 12.2.8).

If we approximate the accelerometers continuous measurements by several discrete measurements at intervals Δt_0 then

$$E_1^{-1} = E_0^{-1} + H_0 R_0^{-1} H_0$$

$$E_2^{-1} = E_1^{-1} + H_1 R_1^{-1} H_1$$

•

•

$$E_k^{-1} = E_{k-1}^{-1} + H_{k-1} R_{k-1}^{-1} H_{k-1}$$

$$E_k^{-1} = E_0^{-1} + \sum_{j=0}^{k-1} H_j R_j^{-1} H_j$$

And if we assume $H_i R_i^{-1} H_i$ is the constant over an interval ΔT then

$$E^{-1} = E'^{-1} + \frac{\Delta T}{\Delta t_0} H^T R^{-1} H$$

This is identical to the expression for onboard measurements if R is replaced

by $\frac{\Delta t_o}{\Delta T}$ R. Thus using the analogous relationships for onboard measurements in Vol. II,

$$W = EH^T (HEH^T + R \frac{\Delta t_o}{\Delta T})^{-1}$$

$$E = (I - WH) E' (I - WH)^T + W \frac{\Delta t_o}{\Delta T} RW^T$$

$$V = (I - WH) V'$$

$$S = (I - WH) S'$$

$$C = C'(I - WH)^T$$

J and X are unchanged.

Three accelerometers give a measure of the thrust acceleration. Thus

$$\underline{z} = \frac{T}{m} \hat{\underline{u}} + \underline{\eta}$$

where \underline{z} is the measurement and $\underline{\eta}$ is the error in the measurement. Taking the variation

$$\delta \underline{z} = \frac{\partial \underline{z}}{\partial \underline{x}} \delta \underline{x} + \frac{\hat{\underline{u}}}{m} \delta T + \underline{\eta}$$

and

$$H = \frac{\partial \underline{z}}{\partial \underline{x}} = \begin{bmatrix} 0^{3 \times 9} & -\frac{T}{m^2} \hat{\underline{u}} & \frac{T}{m} \frac{\partial \hat{\underline{u}}}{\partial \underline{u}_c} \end{bmatrix}$$

where $\frac{\partial \hat{\underline{u}}}{\partial \underline{u}_c}$ is known and all expression are evaluated on the nominal. R is given by

$$\begin{aligned} R &= (\frac{\hat{\underline{u}}}{m} \delta T + \underline{\eta}) (\frac{\hat{\underline{u}}}{m} \delta T + \underline{\eta})^T \\ &= \underline{\eta \eta}^T + \frac{\overline{\delta T^2}}{m} \hat{\underline{u}} \hat{\underline{u}}^T \end{aligned}$$

For the case of one accelerometer, which measures the thrust accelerations in the nominal thrust direction, the measurement is the component of the three dimensional measurement \underline{z} in the $\hat{\underline{u}}$ direction or $\underline{z} \cdot \hat{\underline{u}}$.

$$z = \underline{z} \cdot \hat{\underline{u}} = \frac{T}{m} \hat{\underline{u}}^T \hat{\underline{u}} + \eta'$$

$$\delta z = \frac{\partial z}{\partial \underline{x}} \delta \underline{x} + \frac{\delta T}{m} + \eta'$$

$$\underline{h}^T = \frac{\partial z}{\partial \underline{x}} = (0^{1 \times 9}, -\frac{T}{m^2}, \frac{\partial z}{\partial \underline{u}_{ma}})$$

where

$$\frac{\partial z}{\partial \underline{u}_{ma}} = \frac{T}{m} \hat{\underline{u}}^T \frac{\partial \hat{\underline{u}}}{\partial \underline{u}_c} \frac{\partial \hat{\underline{u}}_c}{\partial \underline{u}_{ma}} = 0$$

$$\underline{h}^T = (0^{1 \times 9}, -\frac{T}{m^2}, 0^{1 \times 2})$$

and R is given by

$$\begin{aligned} R &= \overline{\left(\frac{\delta T}{m} + \eta' \right) \left(\frac{\delta T}{m} + \eta' \right)} \\ &= \overline{\frac{\delta T^2}{m^2}} + \overline{\eta'^2} \end{aligned}$$

D.6 DSN Measurements

The DSN measurement incorporation is done similarly to Phase A except the H-matrix and the weighting matrix, W, must have zeros added

to make them dimensionally consistent with the 12 dimensional state. Then as in Phase A,

$$\delta \hat{\underline{x}} = \delta \hat{\underline{x}}' + W(\delta \underline{z} - H \delta \hat{\underline{x}}')$$

$$\underline{e} = (I - WH) \underline{e}' + W (G\underline{b} + \underline{\eta})$$

$$\delta \underline{x} = \delta \underline{x}'$$

\underline{b} is the station location bias

G is a rotation matrix

$\underline{\eta}$ is noise

$$\beta = \overline{\underline{b}\underline{b}^T}$$

$$N = \overline{\underline{\eta}\underline{\eta}^T}$$

In the derivations following, we will need the expression

$$\delta \underline{z} - H \delta \hat{\underline{x}}' = -H\underline{e} + G\underline{b} + \underline{\eta}$$

which follows from

$$\delta \underline{z} = \frac{\delta \underline{z}}{\delta \underline{x}} \delta \underline{x} + G\underline{b} + \underline{\eta}$$

$$\delta \underline{x} = \delta \hat{\underline{x}} - \underline{e}$$

$$\delta \underline{z} = H \delta \hat{\underline{x}} - H\underline{e} + G\underline{b} + \underline{\eta}$$

In Vol. II, Appendix E, it is shown that the weighting matrix is

$$W = (EH^T - SG^T)(HEH^T + G\beta G^T + N - GS^TH^T - HSG^T)^{-1}$$

using the expressions for $\delta \hat{\underline{x}}$, \underline{e} , $\delta \underline{x}$,

$$\underline{E} = \overline{\underline{e}\underline{e}^T}$$

$$= \overline{((I - WH) \underline{e}' + W(G\underline{b} + \underline{\eta})) ((I - WH) \underline{e}' + W(G\underline{b} + \underline{\eta}))^T}$$

$$\begin{aligned} \underline{E} = & (I - WH) \underline{E}' (I - WH)^T + W G \beta G^T W^T + W N W^T + (I - WH) S' G W^T \\ & + W G S'^T (I - WH)^T \end{aligned} \quad (D.9)$$

$$\underline{V} = \overline{\underline{e}\underline{\lambda}^T}$$

$$= (I - WH) \underline{V}' + W (G \underline{b} + \underline{\eta}) \underline{\lambda}^T$$

$$\underline{V} = (I - WH) \underline{V}' \quad (D.10)$$

$$\underline{J} = \overline{\delta \underline{x} \underline{\lambda}^T} = \underline{J}' \quad (D.11)$$

$$\underline{C} = \overline{\delta \hat{\underline{x}} \underline{e}^T}$$

$$= \overline{(\delta \hat{\underline{x}}' + W (-H \underline{e}' + G \underline{b} + \underline{\eta})) ((I - WH) \underline{e}' + W(G \underline{b} + \underline{\eta}))^T}$$

$$= \overline{\delta \hat{\underline{x}}' \underline{e}'}^T (I - WH)^T - WH \overline{\underline{e} \underline{e}'}^T (I - WH)^T$$

$$+ W G \underline{b} \underline{e}'^T (I - WH)^T + \overline{\delta \hat{\underline{x}}' \underline{b}}^T G^T W^T$$

$$- WH \overline{\underline{e} \underline{b}}^T G^T W^T + W G \beta G^T W^T + W \overline{\underline{\eta} \underline{\eta}}^T W^T$$

$$= \underline{C}' (I - WH)^T - W H \underline{E}' + W H \underline{E}'^T H^T W^T + W G S'^T$$

$$- W G S'^T H^T W^T$$

$$+ S' G^T W^T - W H S' G^T W^T + W G \beta G^T W^T + W N W^T$$

$$\begin{aligned}
&= C' (I - WH)^T + S'G^T W^T - WHE' + WGS'^T \\
&\quad + W(HE'H^T + G\beta G^T + N - GS'^T H^T - HS'G^T)W^T
\end{aligned}$$

then substituting for

$$W^T = (HE'H^T + G\beta G^T + N - GS'^T H^T - HS'G^T)^{-1} (HE' - GS'^T)$$

$$C = C'(I - WH)^T + S'G^T W^T \quad (D.12)$$

$$X = \overline{\delta \underline{x} \delta \underline{x}^T} = X' \quad (D.13)$$

$$\begin{aligned}
S &= \overline{\underline{e} \underline{b}^T} \\
&= ((I - WH) \underline{e}' + WG\underline{b} + W\underline{\eta}) \underline{b}^T \\
S &= (I - WH) S' + WG\beta \quad (D.14)
\end{aligned}$$

Thus equations D.9 thru D.14 show the effect of a DSN measurement on each of the correlation matrices.

D.7 Onboard Measurements

After a measurement

$$\hat{\delta \underline{x}} = \hat{\delta \underline{x}'} + \underline{w}(\delta z - \underline{h}^T \hat{\delta \underline{x}})$$

$$\underline{e} = (I - \underline{w} \underline{h}^T) \underline{e}' + \underline{w} \eta$$

$$\delta \underline{x} = \delta \underline{x}'$$

z is the measurement

$$\underline{h} = \left(\frac{\partial z}{\partial \underline{x}} \right)^T$$

$$\underline{w} = E' \underline{h} (\underline{h}^T E' \underline{h} + r)^{-1}, \text{ weighting vector}$$

η is white measurement noise, and

$$r = \overline{\eta^2}$$

$$-\underline{h}^T \underline{e}' + \eta = \delta z - \underline{h}^T \delta \underline{x}'$$

where again accommodation is made for the large state vector by the addition of zeros in the last 3 places of the \underline{h} vector. Then

$$\begin{aligned} E &= \overline{\underline{e} \underline{e}^T} \\ &= \overline{((I - \underline{w} \underline{h}^T) \underline{e}' + \underline{w} \eta) ((I - \underline{w} \underline{h}^T) \underline{e}' + \underline{w} \eta)^T} \\ E &= (I - \underline{w} \underline{h}^T) E' (I - \underline{w} \underline{h}^T)^T + \underline{w} r \underline{w}^T \end{aligned} \quad (D.15)$$

$$\begin{aligned} V &= \overline{\underline{e} \underline{e}^T} = \overline{[(I - \underline{w} \underline{h}^T) \underline{e}' + \underline{w} \eta] \underline{e}'^T} \\ V &= (I - \underline{w} \underline{h}^T) V' \end{aligned} \quad (D.16)$$

$$J = \overline{\delta \underline{x} \underline{e}^T} = J' \quad (D.17)$$

$$\begin{aligned} C &= \overline{\delta \hat{\underline{x}} \underline{e}^T} \\ &= \overline{(\delta \hat{\underline{x}}' + \underline{w} (-\underline{h}^T \underline{e}' + \eta)) [(I - \underline{w} \underline{h}^T) \underline{e}' + \underline{w} \eta]^T} \\ &= \overline{\delta \hat{\underline{x}} \underline{e}'^T} (I - \underline{w} \underline{h}^T)^T - \underline{w} \underline{h}^T E' (I - \underline{w} \underline{h}^T)^T + \underline{w} r \underline{w}^T \\ &= C' (I - \underline{w} \underline{h}^T)^T - \underline{w} (\underline{h}^T E' \underline{h} + r) \underline{w}^T + \underline{w} \underline{h}^T E' \end{aligned}$$

substituting

$$\underline{w}^T = (\underline{h}^T \underline{E}' \underline{h} + r)^{-1} \underline{h}^T \underline{E}'$$

$$\underline{C} = \underline{C}' (\underline{I} - \underline{w} \underline{h}^T)^T \quad (\text{D.18})$$

$$\underline{X} = \overline{\delta \underline{x} \delta \underline{x}^T} = \underline{X}' \quad (\text{D.19})$$

$$\begin{aligned} \underline{S} &= \underline{e} \underline{b}^T \\ &= ((\underline{I} - \underline{w} \underline{h}^T) \underline{e}' + \underline{w} \eta) \underline{b}^T \\ &= (\underline{I} - \underline{w} \underline{h}^T) \underline{S}' \end{aligned} \quad (\text{D.20})$$

Equations D.15 thru D.20 then show the effect of an onboard measurement on each of the correlation matrices. The \underline{h} vector is dependent on the specific measurement taken and it, with the measurement noise, determines the weighting vector, \underline{w} .

D.8 Measurement Selection

The following measurement selection criteria to be minimized were implemented

- 1) the trace of the covariance matrix of estimation errors,
- 2) the mean squared position error at a preselected target point (usually the destination point).

The first is the sum of the diagonal elements of the \underline{E} matrix which would result from the measurements.

For the second criterion, we need an expression for $\underline{E}(T)$ where T is the preselected target time. The cost is then given by the trace of

$LE(T)L^T$ where L is a 3×12 matrix which picks off the top 3×3 block of E , i.e.

$$L = (I^{3 \times 3}, 0^{3 \times 9})$$

From the differential equation for E and V we can get expressions which extrapolate $E(t)$, $V(t)$ where t is the measurement time, forward to time T , assuming no other measurements are made afterwards. From

$$\dot{E} = AE + EA^T - DV^T - VD^T + B_w \overline{w w^T} B_w^T$$

$$\dot{V} = AV - D \overline{z z^T}$$

thus

$$E(t) = \Phi(T, t) E(t) \Phi(T, t)^T$$

$$+ \int_t^T \Phi(T, s) \{-DV^T + VD^T + B_w \overline{w w^T} B_w^T\} \Phi(T, s) ds$$

$$V(s) = \Phi(s, t) V(t) - \int_t^s \Phi(s, t) D \overline{z z^T} dt$$

where $\Phi(t, t_1)$ is the transition matrix for the system $\dot{z} = Az$.

Since neither the terms $B_w \overline{w w^T} B_w^T$ nor $D \overline{z z^T}$ contributes to the cost, the terms involving them in the formulas for $E(T)$ and $V(S)$ can be dropped. Thus

$$\begin{aligned} E(T) &= \Phi(T, t) E(t) \Phi(T, t)^T - \int_t^T \Phi(T, s) D(s) V^T(t) \Phi^T(s, t) \Phi^T(T, s) ds \\ &\quad - \int_t^T \Phi(T, s) \Phi(s, t) V(t) D(s)^T \Phi^T(T, s) ds \\ &= \Phi(T, t) E(t) \Phi(T, t)^T + \int_T^t \Phi(T, s) D(s) ds V(t) \Phi^T(T, t) \end{aligned}$$

$$+ \Phi(T,t) V(t) \int_T^t D(s)^T \Phi^T(T,s) ds$$

let

$$K(t) = L\Phi(T,t)$$

and

$$M(t) = \int_T^t L\Phi(T,s) D(s) ds$$

then

$$\dot{K} = L\dot{\Phi}(T,t) = -L\Phi(T,t) A$$

or

$$\dot{K} = -K A \quad , \quad K(T) = (I, 0^{3 \times 9})$$

and

$$\dot{M}(t) = K(t) D(t) \quad , \quad M(T) = 0$$

and

$$\begin{aligned} \text{cost} = \text{tr} [& K(t) E(t) K(t)^T + K(t) V(t) M(t)^T \\ & + M(t) V(t)^T K(t)^T] \end{aligned} \quad (D.21)$$

The K and M matrices can be precalculated.

The K matrix is affected at the coordinate change since $K = L\Phi(T,t)$ and $\Phi(T,t)$ has a discontinuity there. At the coordinate change

$$\underline{e}(t_{cc}^+) = B \underline{e}(t_{cc}^-)$$

where

$$B = \begin{bmatrix} I & 0 & -I & 0 \\ 0 & I & 0 & 0 \\ 0 & 0 & I & 0 \\ 0 & 0 & 0 & I \end{bmatrix}$$

also

$$\underline{e}(t) = \Phi(T,t) \underline{e}(t) + \text{driving terms.}$$

thus

$$\begin{aligned}\underline{e}(t) &= \Phi(T, t_{cc}^+) \underline{e}(t_{cc}^+) + \underline{e}_d(t_{cc}) \\ &= \Phi(T, t_{cc}^-) \underline{e}(t_{cc}^-) + \underline{e}_d(t_{cc}) \\ &= \Phi(T, t_{cc}^+) B \underline{e}(t_{cc}^-) + \underline{e}_d\end{aligned}$$

implies that

$$\Phi(T, t_{cc}^-) = \Phi(T, t_{cc}^+) B$$

$\Phi(T, t)$ is the solution to

$$\dot{\Phi}(T, t) = -\Phi(T, t) A(t) \quad , \quad \Phi(T, T) = I$$

If Φ is partitioned into four 3×12 matrices

$$\Phi = \begin{bmatrix} \Phi_1 \\ \Phi_2 \\ \Phi_3 \\ \Phi_4 \end{bmatrix}$$

then

$$\dot{\Phi}_1 = -\Phi_1 A \quad , \quad \Phi_1 = (I, 0^{3 \times 9})$$

$$\dot{\Phi}_3 = -\Phi_3 A \quad , \quad \Phi_3 = (0^{3 \times 6}, I, 0^{3 \times 3})$$

and

$$\Phi_1(T, t_{cc}^-) = \Phi_1(T, t_{cc}^+) - \Phi_3(T, t_{cc}^+)$$

but

$$K = \Phi_1$$

Therefore at the coordinate change

$$K(t_{cc}^-) = K(t_{cc}^+) - \tilde{K}(t_{cc}^+)$$

where $\tilde{K} = \Phi_3$ is the solution of

$$\dot{\tilde{K}} = -A\tilde{K} \quad , \quad \tilde{K}(T) = (0^{3 \times 6}, I, 0^{3 \times 3})$$

The K and the M matrices were precomputed and stored to be used in the main program for measurement selection when this mode of selection was desired.

Repeating Eq. D.21

$$\begin{aligned} \text{cost} = \text{tr}[(K(t) E(t) K(t)^T + K(t) V(t) M(t)^T \\ + M(t) V(t)^T K(t)^T)] \end{aligned}$$

The following procedure is used to select the set of measurements which will be incorporated: The various possible combinations of measurements are used to calculate new E(t) and V(t). The above cost function is then evaluated using the stored K(t) and M(t). The combination of measurements is then selected for incorporation which minimizes the cost.

Page intentionally left blank

APPENDIX E

GUIDANCE

This appendix contains the details of the derivations of various aspects of the guidance problem, including the derivation of the nominal optimal control and descriptions of the candidate perturbation guidance schemes.

Note that there are two separate aspects of the guidance of the spacecraft to be considered. First is the derivation of the optimal control for the nominal trajectory. The control history includes the direction of the thrust and the times at which the thrust is turned on and off. Once the nominal trajectory and the accompanying nominal control history is determined, the perturbed control or guidance must be determined. Here we assume we are near the nominal but not quite on it, what slightly perturbed control should be used to get the spacecraft near the desired terminal conditions? This analysis is done by linearizing about the nominal trajectory and control. There are various kinds of perturbation controls that could be used. In the first section of the appendix the nominal control is derived. In the second section the perturbation control which was used in this study is derived. In the remaining section the use of a "terminal controller" as a perturbation guidance scheme is discussed.

E.1 Nominal Optimal Control

In this section we will apply optimization theory to derive the deterministic nominal optimal control. In deriving the deterministic nominal control a seven-dimensional state will be used made up of spacecraft position, velocity and mass. Using this seven-dimensional state, the target planet's location is obtained from an ephemeris and thus its gravitational effect is just a known function of time and spacecraft position.

The differential equation satisfied by the state of the system under consideration is

$$\dot{\underline{x}} = \begin{bmatrix} \dot{\underline{r}} \\ \dot{\underline{v}} \\ \dot{m} \end{bmatrix} = \begin{bmatrix} \underline{v} \\ \underline{\ddot{r}} \\ -\beta \end{bmatrix}$$

where

$$\underline{\ddot{r}} = -\frac{\mu_s}{\rho^3} \underline{\rho} - \frac{\mu_p}{a^3} \underline{a} + \frac{\beta c}{m} \hat{\underline{u}} + \frac{\mu}{d^3} \underline{d}$$

and where β is the mass flow rate, equal to β_{\max} or 0, c is the exhaust velocity of the rocket ($c = g_o I_{sp}$ where g_o is the standard acceleration of gravity and I_{sp} is the specific impulse of the rocket), m is the spacecraft's mass. In sun centered coordinates \underline{r} and \underline{v} are the spacecraft's position and velocity relative to the sun and $\mu = -\mu_p$, the gravitation constant of the planet. In planet centered coordinates \underline{r} and \underline{v} are the spacecraft's position and velocity relative to the planet and $\mu = \mu_s$, the gravitational constant of the sun. $\underline{\rho}$ is the spacecraft position relative to the sun, \underline{a} is the spacecraft position relative to the planet. (See Fig. A.1.)

For the problem considered here the initial position, velocity, mass, and time are specified as are the final position, velocity, and time. For this system, "optimal control" will refer to the control which causes the spacecraft to go from the initial conditions to the final conditions while minimizing fuel. The control parameters are θ , ψ , and β where the control angles θ , and ψ were defined in Fig A.2. We will use the nomenclature $\underline{u}_c = \begin{bmatrix} \theta \\ \psi \end{bmatrix}$ to refer to the two dimensional control angles and

$$\hat{\underline{u}} = \begin{bmatrix} \cos \theta \cos \psi \\ \sin \theta \cos \psi \\ \sin \psi \end{bmatrix}$$

is the three dimensional unit vector of directional cosines.

Let the cost functions be

$$J = -m(t_f)$$

which is to be minimized. This is equivalent to maximizing final mass or minimizing fuel. Applying the maximum principle, one forms the Hamiltonian

$$H = \underline{\lambda}^T \underline{\dot{x}} = \underline{\lambda}_r^T \underline{v} + \underline{\lambda}_v^T \underline{\ddot{r}} - \underline{\lambda}_m \beta$$

where $\underline{\lambda}$ is the costate which satisfies

$$\dot{\underline{\lambda}}_r = \left\{ \left[\frac{\mu_s}{\rho^3} + \frac{\mu_p}{a^3} \right] \underline{I} - \frac{3\mu_s \underline{\rho} \underline{\rho}^T}{\rho^3} - \frac{3\mu_p}{a^3} \underline{a} \underline{a}^T \right\} \underline{\lambda}_v$$

$$\dot{\underline{\lambda}}_v = -\underline{\lambda}_r$$

$$\dot{\underline{\lambda}}_m = \frac{\beta c}{m} \hat{\underline{u}}^T \underline{\lambda}_v$$

The only part of the Hamiltonian containing the control angles is

$$H^{\theta, \psi} = \frac{\beta c}{m} \underline{\lambda}_v^T \hat{\underline{u}}$$

To maximize this, the control angles should align $\hat{\underline{u}}$ with $\underline{\lambda}_v$, i.e.

$$\hat{\underline{u}} = \frac{\underline{\lambda}_v}{||\underline{\lambda}_v||}$$

This implies

$$\begin{aligned} \sin \theta &= \lambda_{v2} / \sqrt{\lambda_{v1}^2 + \lambda_{v2}^2} \\ \cos \theta &= \lambda_{v1} / \sqrt{\lambda_{v1}^2 + \lambda_{v2}^2} \\ \sin \psi &= \lambda_{v3} / ||\underline{\lambda}_v|| \end{aligned} \tag{E. 1}$$

$$\cos \psi = \sqrt{\lambda_{v_1}^2 + \lambda_{v_2}^2} / ||\underline{\lambda}_v||$$

or

$$\theta = \tan^{-1} (\lambda_{v_1} / \lambda_{v_2})$$

$$\psi = \tan^{-1} (\lambda_{v_3} / \sqrt{\lambda_{v_1}^2 + \lambda_{v_2}^2})$$

where

$$\underline{\lambda}_v = \begin{bmatrix} \lambda_{v_1} \\ \lambda_{v_2} \\ \lambda_{v_3} \end{bmatrix}$$

The portion of H containing β is

$$\begin{aligned} H^\beta &= \frac{\beta c}{m} \underline{\lambda}_v^T \hat{u} - \lambda_m \beta \\ &= \left(\frac{c}{m} ||\underline{\lambda}_v|| - \lambda_m \right) \beta \end{aligned}$$

To maximize this let

$$\begin{aligned} \beta &= \beta_{\max} & \text{if } K > 0 \\ &= 0 & \text{if } K < 0 \end{aligned}$$

where

$$K = \frac{c}{m} ||\underline{\lambda}_v|| - \lambda_m$$

is the switching function. Applying transversality conditions we get

$$\lambda_m(t_f) = 1$$

There is a discontinuity in \underline{x} at the sphere of influence; $\underline{\lambda}$ is continuous across this point (see Ref. 2, Section 3.7).

The above conditions are necessary conditions for an extremal. We have a two point boundary value problem in 14 variables ($\underline{x}; \underline{\lambda}$). With the initial and final time specified, there are seven variables specified at the initial time and seven at the final time. The solution to this problem gives an extremal control and extremal trajectory. The NASA Mission Analysis Division derived the initial conditions for the state and costate for the optimal trajectory. These were then supplied to the MIT Draper Laboratory allowing the reproduction of the optimal control and trajectory.

E.2 A Nonoptimal Perturbation Guidance Scheme

This section describes the nonoptimal perturbation guidance scheme which was used to get the guidance plots in Appendix C. The scheme is derived and the motivation for the plots is given.

The deterministic variation equation has the form

$$\delta \dot{\underline{x}} = A(t) \delta \underline{x} + B(t) \delta \underline{u}_c$$

where

$$A(t) = \left. \frac{\partial \dot{\underline{x}}}{\partial \underline{x}} \right| * \quad \text{and} \quad B(t) = \left. \frac{\partial \dot{\underline{x}}}{\partial \underline{u}_c} \right| *$$

where the * indicates the expressions are evaluated on the nominal trajectory. If the thrust switching times are not allowed to vary, but occur at the times specified by the nominal trajectory, then the only control available in the event we get off the nominal is steering, i.e., changing the angles in the two-dimensional control \underline{u}_c . Thus there is no control during the coast periods and the system is not completely controllable during the thrusting phases. In particular, it is not possible to eliminate positional errors in the direction of the velocity vector. Since we are interested in

minimizing the terminal position error, one criterion we could use is to try and eliminate the components of terminal position error perpendicular to the final velocity vector. We could ask: given a deviation from the nominal state at the current time, $\delta \underline{x}(t)$, what is the constant control, $\delta \underline{u}$, which would cause the positional components perpendicular to the final velocity to be nulled at the final time? Positional error in the direction of the final velocity could be reduced by turning off the control earlier or later than the nominal final time.

Let $\Phi(t, t_0)$ be the transition matrix for the system $\dot{\underline{z}} = A(t) \underline{z}$, then

$$\delta \underline{x}(t_f) = \Phi(t_f, t_0) \delta \underline{x}(t_0) + \int_{t_0}^{t_f} \Phi(t_f, s) B(s) \delta \underline{u}_c ds \quad (E.2)$$

where t_f is the final time and t_0 is the present time. Let C be the 2×12 rotation matrix which takes the positional components of $\delta \underline{x}$ and results in the two positional components perpendicular to the final nominal velocity vector, e.g.,

$$C = \begin{bmatrix} (\underline{r}_f \times \underline{v}_f)^T & | & \\ & | & 0^{2 \times 9} \\ (\underline{v}_f \times (\underline{r}_f \times \underline{v}_f))^T & | & \end{bmatrix}$$

We would like the constant control $\delta \underline{u}$ which causes $C \delta \underline{x}_f = 0$. Since $\delta \underline{u}$ is assumed constant it can be taken outside the the integral in E.2 and thus

$$0 = C \delta \underline{x}_f = C \Phi(t_f, t_0) \delta \underline{x}_0 + \left[\int_{t_0}^{t_f} C \Phi(t_f, s) B(s) ds \right] \delta \underline{u}$$

Solving for $\delta \underline{u}$ gives

$$\delta \underline{u} = - \left[\int_{t_0}^{t_f} C \Phi(t_f, s) B(s) ds \right]^{-1} C \Phi(t_f, t_0) \delta \underline{x}_0$$

$C \Phi(t_f, t)$ is the solution obtained by integrating the differential equation

$$C \dot{\Phi}(t_f, t) = -C \Phi(t_f, t) A(t)$$

backwards from t_f , where at t_f

$$C \Phi(t_f, t_f) = C$$

Define the 2x2 matrix

$$\Gamma(t) = - \int_t^{t_f} C \Phi(t_f, s) B(s) ds$$

$\Gamma(t)$ is the solution found by integrating backwards from t_f the differential equation

$$\dot{\Gamma}(t) = C \Phi(t_f, t) B(t) , \quad \Gamma(t_f) = 0$$

Inverting $\Gamma(t)$ and letting

$$\Lambda(t) = \Gamma(t)^{-1} C \Phi(t_f, t)$$

gives a 2x12 gain matrix which can be precalculated and used as a feedback guidance law, i.e.

$$\delta \underline{u} = \Lambda(t) \delta \underline{x}(t)$$

Again, this is the constant control that would null two components of position which are perpendicular to the nominal velocity at the final time. If at a later time, $\delta \underline{x}(t)$ were to be changed due to revised measurements or disturbances other than the control, then a different constant $\delta \underline{u}$ would result.

This guidance scheme was tested by integrating the system

$$\dot{\delta \underline{x}} = (A + B \Lambda) \delta \underline{x}$$

with an initial $\delta \underline{x}(t_0)$ given and also using a random number generator to alter $\delta \underline{x}(t)$ at the end of each integration step, then rotating the resultant

$\delta \underline{x}_f$ to see if the off-velocity components of position were nulled.

As $t \rightarrow t_f$ the gain matrix gets very large ($\Gamma(t) \rightarrow 0$, $\Gamma(t)^{-1} \rightarrow \infty$); the larger $\delta \underline{x}(t)$, the larger $\delta \underline{u}$. We want to limit the magnitude of $\delta \underline{u}$ to represent operational or physical constraints and in order that the linear analysis remain valid. In the deterministic test runs $\delta \underline{u} = \Lambda(t) \delta \underline{x}$ was evaluated and in the statistical simulation runs the diagonal elements of $\Lambda(t) \delta \underline{x} \delta \underline{x}^T \Lambda(t)^T = \delta \underline{u} \delta \underline{u}^T$ were evaluated to see if the magnitude was greater than a prescribed limit. If so the magnitude of $\delta \underline{u}$ was set to that limit.

Because of numerical difficulties, the guidance scheme was not utilized in the statistical simulation. However, a number of results can be obtained by looking at the characteristics of the guidance equations. By using the gain matrix, given a maximum value for the magnitude of the components of $\delta \underline{u}$, one can determine the approximate maximum deviation of the state at a given time, $\delta \underline{x}(t)$, which results in the positional components perpendicular to the final velocity being nulled. Let

$$\delta \underline{u} = \begin{bmatrix} \delta u_1 \\ \delta u_2 \end{bmatrix}$$

$$\delta \underline{x} = \begin{bmatrix} \delta x_1 \\ \delta x_2 \end{bmatrix}$$

$$\Lambda(t) = \begin{bmatrix} \Lambda_{11} \cdots \Lambda_{1,12} \\ \Lambda_{21} \cdots \Lambda_{2,12} \end{bmatrix}$$

Then

$$\delta u_i = \sum_{j=1}^{12} \Lambda_{i,j} \delta x_j, \quad i = 1, 2$$

If all the $\delta x_j = 0$ except for $j = k$ then

$$\delta u_i = \Lambda_{ik} \delta x_j$$

If $\Lambda_{ik} \neq 0$, we can plot

$$\delta x_k / \delta u_i = \Lambda_{ik}^{-1}$$

as a function of time.

These plots are given in Appendix F for $i = 1, 2$ and for the k of interest. This set of plots will be referred to as the "first set". Given a deviation in the state at a particular time, the required deviation in control is given by the product of the state deviation and the inverse value of the curve at that time.

If $|\delta x(t)|$ is larger than the maximum $|\delta x|$ that can "be nulled" (i.e. the positional components perpendicular to the final velocity can be nulled), it would be of interest to know what values of $\underline{z} = C \delta \underline{x}_f$ would result. Say there is a deviation $\delta x_k(t)$ that would result in a δu_i greater than allowable for $i = 1$ or 2 or both, and that $\delta \tilde{x}_k$ is the extreme value that can be nulled, then

$$0 = C \delta \underline{x}_f = C \Phi_{\underline{x}x_k}(t_f, t) \delta \tilde{x}_k(t) + C k(t) \delta \tilde{u}$$

$$\underline{z} = C \delta \underline{x}_f = C \Phi_{\underline{x}x_k}(t_f, t) \delta x_k(t) + C k(t) \delta \underline{u}$$

where at least one component of $\delta \underline{u}$ is equal to the corresponding component of $\delta \tilde{u}$. Then

$$\underline{z} = C \Phi(t_f, t) [\delta x_k(t) - \delta \tilde{x}_k(t)] + C k(t) [\delta \underline{u} - \delta \tilde{u}]$$

To find the effect on \underline{z} of excess state deviation, that is of $(\delta x_k - \delta \tilde{x}_k)$ the second set of curves are plots of each element of $C \Phi(t_f, t)$. The

effect of the nonzero component of $(\delta \underline{u} - \delta \tilde{\underline{u}})$ is given by the elements of $C \Phi$ corresponding to thrust vector misalignment since both control deviations and thrust vector misalignment propagate identically.

$$z_l / (\delta x_k(t) - \delta \tilde{x}_k(t)) = [C \Phi(t_f, t)]_{lk}$$

for

$$l = 1, 2$$

$$k = 1, 2, \dots, 12$$

This is the second set of plots given in Appendix F. One way of using these plots would be: given the $\max |\delta u_i|$ and a deviation in the k^{th} component of $\delta \underline{x}$, $\delta x_k(t_1)$ at time t_1 , go to the "first set" of plots corresponding to k , read the value of the curve for time t_1 for both control components. Multiply this value by $\max |\delta u_i|$ to get $\delta x_k^m(t_1)$.

If $|\delta x_k(t_1)| < |\delta x_k^m(t_1)|$ then $|\delta x_k(t_1)|$ can "be nulled". If

$$|\delta x_k(t_1)| > |\delta x_k^m(t_1)|,$$

then there would be a terminal position error perpendicular to the final velocity which can be obtained from the second set of plots.

Let

$$\Delta = \delta x_k(t_1) - \delta x_k^m.$$

On the two plots corresponding to k (one for each component of \underline{z}) read the value of the curve at time t_1 . This value multiplied by Δ gives the resultant value of \underline{z} due to this deviation. To it must be added the effect of the excess control deviation in the control component which did not saturate. Its effect on \underline{z} is found from taking the product of the excess and the value for the time t_1 given on the appropriate curve for thrust vector misalignment.

Thus, using the two sets of plots, if we assume a maximum magnitude on the variational control, $\max |\delta u_i|$, we can find the effect of a deviation

in one component of the state at any time during the flight. The first set of plots tells us if we can null the final positional components perpendicular to the final velocity. If not, the second set of plots tells us what these positional components will be. Also using the first set of plots, given the state deviation one can get the resultant deviation in control by forming the product of the state deviation and the inverse of the value on the curve.

The gain matrices and plots were formed over two legs of a trajectory rather than over the whole trajectory. Thus gain matrices were computed from the initial time to the time of the coordinate change at the sphere of influence of the target planet. The "final time" for this leg is thus the time of arrival at the sphere of influence, and these gain matrices are those which would null the positional components perpendicular to the velocity vector at the nominal time of arrival at the sphere of influence. Then gain matrices and corresponding plots were done for the leg of the trajectory from the sphere of influence to the final conditions at the terminal time. Plots for these two legs are given separately for each mission.

E.3 Terminal Controller with Quadratic Cost

Another perturbation guidance scheme studied was a terminal controller with a quadratic penalty function on the terminal error. The switch times were fixed at the nominal values. The system was linearized about the nominal and the idea was to minimize deviations from that nominal, weighting heavily the quadratic function of the terminal position. We have the variational equation

$$\dot{\delta \underline{x}} = F(t) \delta \underline{x} + G(t) \delta \underline{u}_c$$

We want $\delta \underline{x}(t_f) \approx \underline{0}$

So minimize

$$J = 1/2 \left[(\delta \underline{x}^T S_f \delta \underline{x})_{t_f} + \int_{t_0}^{t_f} (\delta \underline{x}^T A \delta \underline{x} + \delta \underline{u}_c^T B \delta \underline{u}_c) dt \right]$$

where S_f , $A(t)$, $B(t)$ are positive definite matrices. This problem has an exact explicit solution which is given in Ref. 2 Section 5.2. A suggestion for picking S_f , A , and B is given there.

One method of solution is using a sweep method where the matrix Ricatti equation

$$\dot{S} = -SF - F^T S + SGB^{-1}G^T S - A$$

with $S(t_f) = S_f$ is integrated backwards from t_f . The control is then given by

$$\delta \underline{u}_c(t) = -C(t) \delta \underline{x}(t)$$

where the feedback gain matrix is

$$C(t) = B(t)^{-1} G^T(t) S(t)$$

In attempting to implement this scheme, numerical problems prevented the solution of the Ricatti equation and before these problems were resolved the nonoptimal scheme of the previous section was developed and utilized.

APPENDIX F

GUIDANCE SENSITIVITY RESULTS

F.1 Introduction

This appendix contains the plots associated with the guidance scheme. Their derivation and use are discussed in Appendix E. In the following pages are a summary of possible uses and examples and some comments about special characteristics of the actual curves.

The plots are given for interplanetary and the near planet legs of the Jupiter and Saturn missions. For each of these divisions there are two kinds of plots. One set is the inverse of each component of the gain matrix, $\Lambda(t)$, versus time to go. Actually only those elements corresponding to position and velocity are plotted for this set. Thus there are twelve plots for each leg of a mission; six correspond to the in-plane control angle θ and six to the out-of-plane control angle ψ . From these plots can be obtained the control angle deviation resulting from a perturbation in position or velocity (note that the control deviation resulting from a thrust vector misalignment would just be the negative of the thrust vector misalignment). Also, given a maximum value for the thrust deviation magnitude, the greatest magnitude of position or velocity deviation which can be nulled can be obtained.

The second group of plots given for each leg of a mission gives the two position components perpendicular to the nominal velocity at the end of each leg which will result per unit excess deviation in a component of the state. These are denoted z_1 and z_2 . By excess deviation is meant the difference between the actual deviation and that which can be nulled out, given a limit on the magnitude of the deviation in control angles. These plots are given for deviations in position, velocity, and thrust vector misalignment. The plots corresponding to thrust vector misalignment can also be used to find the effect of a deviation in control since they propagate identically. They can be used to find the effect of the deviation control

component which does not saturate when the other component of deviation control has reached its limit in magnitude due to a large state deviation. Note that the plots for thrust vector misalignment are given in units of kilometers per radian and not kilometers per degree. Plots corresponding to deviation in ephemeris and mass are not included since their effect is very small.

F.2 Characteristics of the Plots

In this section, some of the unusual results illustrated in these plots are identified and discussed. The next three paragraphs discuss some of the unusual characteristics of the state deviation per control deviation plots. The last three paragraphs are concerned with the final position per state deviation plots.

For the interplanetary phase, during the coast there is no thrust, thus the curves are fairly flat through this phase, usually showing that a larger deviation can be nulled out the closer the time is to the thrust on period. This is because deviations earlier would have more time to build into larger deviations before any control could be used to start diminishing the deviations. This is illustrated in Fig. F3.1.1. During coast, the perturbed control angle has no meaning until thrusting begins again.

When a curve goes through infinity, this implies that the control angle component has no effect in nulling out deviations in the state component at that time. (See Fig. F1.1.1a.) If curves for both control components for a state deviation component go through infinity at the same time, this implies any resulting final position deviation would be in the direction of the final nominal velocity vector which this guidance scheme is not designed to null except by changing the arrival time.

When a curve goes through zero this indicates that at that time deviations in that component of the state are uncontrollable. (See Fig. F2.1.1.) A curve may not be monotone since the uncontrollable final

direction component varies with time due to the curvature of the trajectory. The guidance scheme equations are based on the assumption that the two deviation components of position, perpendicular to the final nominal velocity, can be nulled given a large enough deviation in control. Because of the curvature of the trajectory, singularities exist and so this is not always possible.

Another phenomena which warrants some explanation is displayed in the near planet extrapolation plots for the effects on z_1 and z_2 of the earlier deviations in position. (See e.g., Figs. F2.3.1, F2.3.2, and F2.3.3.) The appearance of these curves is due to the rapid curvature of the trajectory during the last few days of the flight and to peculiarities of geometry. For both missions, the final velocity is nearly lined up with the y-axis. The directions of z_1 and z_2 are perpendicular to the final velocity. In fact z_1 in all cases nearly lines up with the planetocentric z-axis (out of the ecliptic) and z_2 with the x-axis. Early near planet out-of-plane deviations are "stable" in that a unit out-of-plane deviation propagated to the final time has less than unit magnitude. This is reasonable since any deviation out of the original plane of motion will tend to be pulled in toward the center of the planet and thus toward the original plane of motion. Thus the plots show that near pericenter, as time-to-go increases, the effect of out-of-plane position deviation decreases. Further from pericenter, the trajectory is curving much less and the vehicle is moving much more slowly. Thus the curves tend to flatten out.

By examining the transition matrix which gives the effect of early position deviations on all three components of position, one finds that for the Jupiter near planet case deviations in both the x and y directions have the most effect on the final y direction and less on the final x direction. Since the y direction corresponds closely with the final velocity direction, this is the component which is not illustrated in the plots. If there were three additional plots showing the effect of position deviations on the final position component in the direction of the final velocity, the curves would show a magnitude increase as time to go increased. A similar situation would hold for the other mission.

When one of the final position per state deviation plots passes through zero it indicates that deviations in that component of state have no effect on that component of final position. (See Fig. F1.3.1.)

F.3 Example 1

Consider the Saturn near planet case and a time to go of 40 days. First assume that a deviation exists in the y component of velocity which is equal to .02 km/sec. From Fig. F4.1.5 the in-plane control deviation, $\Delta\theta$, is given by the product of the inverse value of the curve at 40 days and $\Delta V_y = .02$,

$$\Delta\theta = \frac{1}{.0105} (.02) \approx 2^\circ$$

From Fig. F4.2.5 the out of plane control deviation, $\Delta\psi$, is given by

$$\Delta\psi = \frac{1}{.3} (.02) \approx .067^\circ$$

Thus if

$$\Delta V_y = .02 \text{ km/sec}$$

then

$$\Delta\theta = 2^\circ$$

$$\Delta\psi = .067^\circ$$

Now say that there is a limit imposed on the magnitude of $\Delta\theta$ and $\Delta\psi$ of 1° .* Since 2° exceeds the 1° limit the $\Delta V_y = .02 \text{ km/sec}$ cannot be nulled.

*This one degree limit is used here for example purposes only. If such a limit is not imposed by operational or vehicle design constraints it would be necessary to satisfy the linearization assumption of the first

Using Fig. F4.1.5 and Fig. F4.2.5 the greatest value of ΔV_y that can be nulled can be found. The product of the value of the curve at 40 days in Fig. F4.1.5 and $\Delta\theta = 1^\circ$ is

$$(.0105) 1^\circ \approx .01 \text{ km/sec}$$

The product of the value of the curve at 40 days in Fig. F4.2.5 and $\Delta\psi = 1^\circ$ is

$$(.3) (1^\circ) = .3 \text{ km/sec}$$

Thus the limit imposed on $\Delta\psi$ would allow a deviation $\Delta V_y = .3$ but the limit on $\Delta\theta$ allows only $\Delta V_y = .01 \text{ km/sec}$. Thus, in order for the deviation in V_y to be nulled, $|\Delta V_y| \leq .01 \text{ km/sec}$. That is $|\Delta\theta| \leq 1^\circ$, $|\Delta\psi| \leq 1^\circ$ implies maximum $|\Delta V_y| \leq .01 \text{ km/sec}$.

At the beginning of this example, we hypothesized a $\Delta V_y = .02$. This is greater than the maximum nullable value if $|\Delta\theta| \leq 1^\circ$, $|\Delta\psi| \leq 1^\circ$. The maximum nullable $\Delta V_y = .01$. The excess is then

$$.02 - .01 = .01 \text{ km/sec.}$$

There is also a difference in the $\Delta\psi$ which would result from a $\Delta V_y = .02$ and a $\Delta V_y = .01$. Both the excess ΔV_y and the excess $\Delta\psi$ will have an effect on the two components of position perpendicular to the nominal final velocity. $\Delta\psi$ for $\Delta V_y = .01$ is found from Fig. F4.2.5.

$$\Delta\psi_1 = \frac{.01}{.3} \approx .033^\circ$$

For $\Delta V_y = .02$

order perturbation technique. The latter limit will be greater than one degree but further study is necessary to determine what it should actually be.

$$\Delta\psi_2 = \frac{.02}{.3} \approx .067^\circ$$

The excess $\Delta\psi$ is then

$$.067 - .033^\circ = .034^\circ$$

First we can get the effect on one component of the final position by looking at Fig. F4.3.5 and Fig. F4.3.8. The product of the value of the curve at 40 days in Fig. F4.3.5 and the excess ΔV_y of .01 gives the effect on z_1 of excess ΔV_y

$$(.01) (130,000) = 1300 \text{ km.}$$

The product of the value of the curve at 40 days in Fig. F4.3.8 and the excess $\Delta\psi$ of .034 gives the effect on z_1 of the excess $\Delta\psi$.

$$.034 (600,000) / 57^\circ / \text{rad} = 400 \text{ km}$$

The total effect on z_1 is

$$z_1 = 1300 + 400 = 1700 \text{ km}$$

Similarly the effect on the other component of position z_2 can be found using Fig. F4.4.5 and Fig. F4.4.8. The effect of excess ΔV_y is

$$(.01) (1,900,000) = 19,000.$$

The effect of excess $\Delta\psi$ is

$$(-300,000) (.034) / 57^\circ / \text{rad} = -200 \text{ km.}$$

The total effect on z_2 is

$$z_2 = 19,000 - 200 = 18,800 \text{ km.}$$

To summarize, given a deviation in $\Delta V_y = .02$ km/sec. This would result in $\Delta \theta = 2^\circ$ and $\Delta \psi = .067^\circ$. If there is a limit on $\Delta \theta$ and $\Delta \psi$ of 1° then the maximum nullable ΔV_y is .01 km/sec. The maximum nullable ΔV_y would result in $\Delta \theta = 1^\circ$ and $\Delta \psi = .033^\circ$. The actual value of $\Delta V_y = .02$ would result in the maximum $\Delta \theta = 1^\circ$ and a $\Delta \psi = .067^\circ$. The excess $\Delta V_y = .02 - .01 = .01$ and the excess $\Delta \psi = .067^\circ - .033^\circ = .034^\circ$ will have an effect on the two components of position perpendicular to the nominal final velocity. The effect of excess ΔV_y on z_1 is added to the effect of excess $\Delta \psi$ on z_1 and similarly for the effect on z_2 .

F.4 Example 2

In this example one possible method of obtaining the effect of deviations in two components of the state will be shown. This method could be generalized to deviations in more than two components. Look again at the Saturn near planet case and a time to go of 40 days. Say there is a $\Delta V_y = .02$ km/sec as in the previous example and in addition a deviation in the z-velocity $\Delta V_z = .001$ km/sec. The $\Delta \theta$ and $\Delta \psi$ which would result from the ΔV_y was calculated in the previous example using Fig. F4.1.5 and Fig. F4.2.5.

$$\Delta \theta = \frac{1}{.01} (.02) = 2^\circ$$

$$\Delta \psi = \frac{1}{.3} (.02) = .067^\circ$$

The $\Delta \theta$ and $\Delta \psi$ due to ΔV_z can be added to the above. From Fig. F4.1.6, take the product of the inverse value of the curve at 40 days and ΔV_z .

$$\Delta \theta = \frac{1}{2} (.001) = .0005^\circ$$

Similarly from Fig. F4.2.6

$$\Delta \psi = \frac{1}{-.014} (.001) = -.07^\circ$$

The total $\Delta\theta$ and $\Delta\psi$ is found by adding the effects due to both deviations.

$$\Delta\theta = 2^\circ + .0005^\circ \approx 2^\circ$$

$$\Delta\psi = .067^\circ - .007^\circ = .060^\circ$$

If there is a limit on $\Delta\theta$ and $\Delta\psi$ of 1° and since the above $\Delta\theta$ exceeds that limit, the total of these deviations cannot be nulled. Actually, since it is clearly the ΔV_y which is causing $\Delta\theta$ to exceed 1° , the maximum nullable ΔV_z would just be .01 km/sec as in the previous example. The maximum nullable ΔV_z would be determined by the limit on $\Delta\psi$ and can be found from Fig. F4.2.6.

$$\max |\Delta V_z| = 0.014 (1^\circ) = .014 \text{ km/sec}$$

Suppose there is a $\Delta V_y = .02 \text{ km/sec}$ and a $\Delta V_z = .001 \text{ km/sec}$ and that $\Delta\theta$ is saturated at $\Delta\theta = 1^\circ$ and that $\Delta\psi = -.06^\circ$. The effect on z_1 and z_2 can be found in a different fashion than given in the previous example. In this case "excess" values will not be considered but rather, using the propagation plots for thrust vector misalignment, the effect on z_1 and z_2 from a ΔV_y , ΔV_z , $\Delta\theta$, $\Delta\psi$ will be found separately, then added to give the total resultant z_1 and z_2 . First looking at z_1 the effect of $\Delta V_y = .02$ is found from Fig. F4.3.5 by taking the product of the value of the curve at 40 days and the ΔV_y .

$$(.02) (130,000) = 2600 \text{ km.}$$

Similarly the effect of ΔV_z is obtained from Fig. F4.3.6.

$$.001 (800,000) = 800 \text{ km}$$

The effect of $\Delta\theta$ is found from Fig. F4.3.8

$$(1^\circ) (-100,000)/57^\circ/\text{rad} = -2000 \text{ km}$$

The effect of $\Delta\psi$ is found from Fig. F.4.3.8

$$.060 (600,000)/57^\circ/\text{rad} = 600 \text{ km}$$

The resultant value of z_1 is then

$$2600 + 800 - 2000 + 600 = 2000 \text{ km.}$$

Note that if $\Delta\theta = 2^\circ$ then its contribution to z_1 would have been -4000 and the resultant z_1 would have been zero as expected. A similar procedure can be used to find the effect on z_2 .

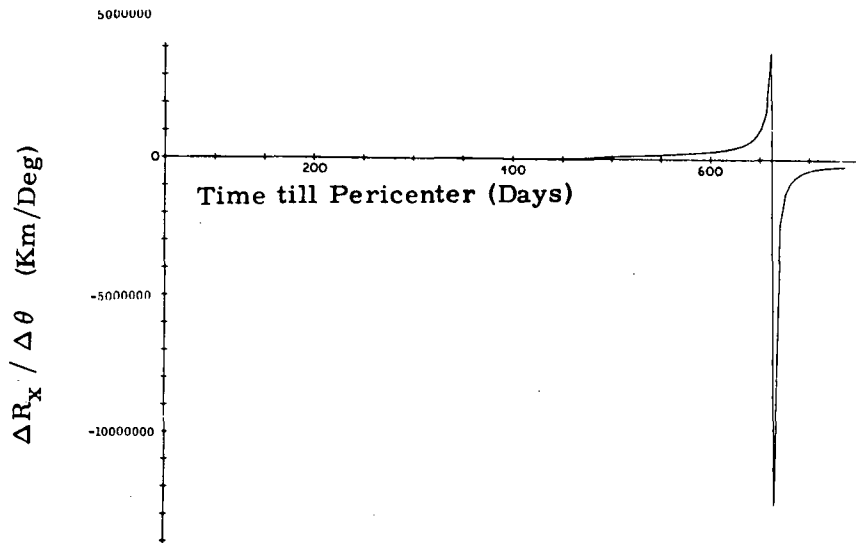


Fig. F. 1. 1. 1 X Component of Position Deviation per Unit Control Angle θ Deviation
Interplanetary Leg-Jupiter Mission

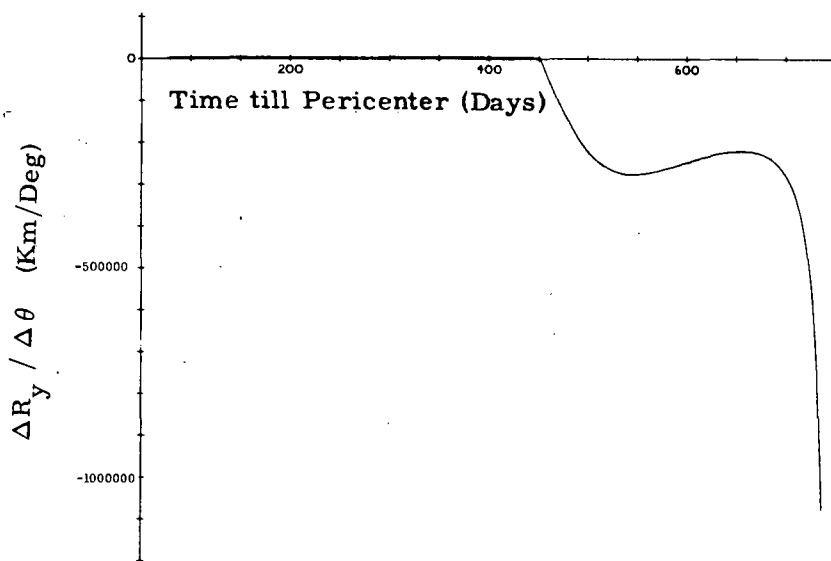


Fig. F. 1. 1. 2 Y Component of Position Deviation per Unit Control Angle θ Deviation
Interplanetary Leg-Jupiter Mission

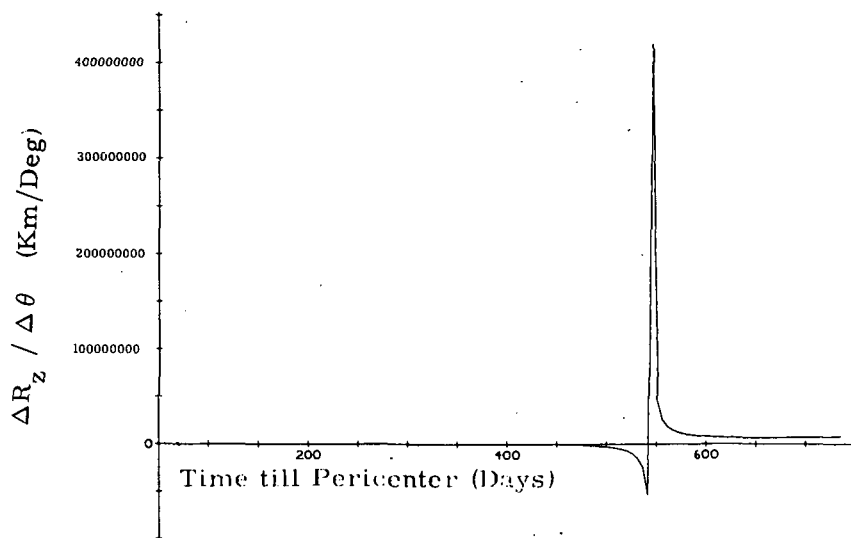


Fig. F. 1. 1. 3 Z Component of Position Deviation per Unit Control Angle θ Deviation
Interplanetary Leg-Jupiter Mission

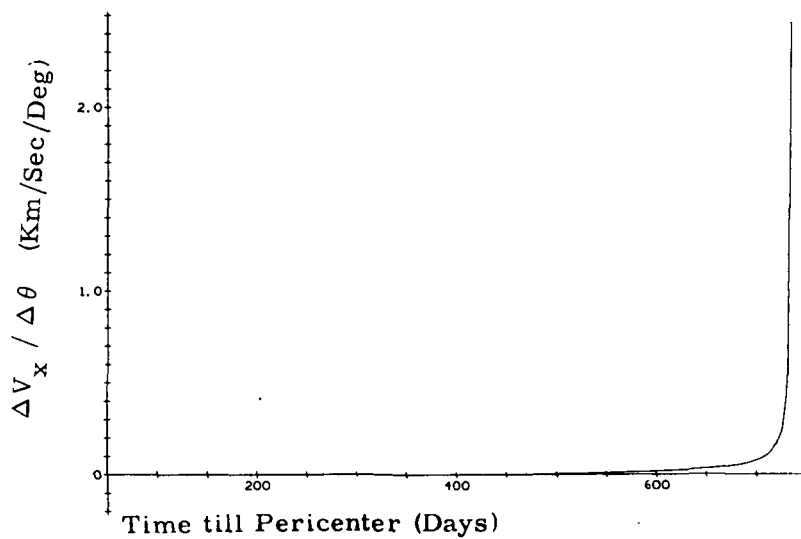


Fig. F. 1. 1. 4 X Component of Velocity Deviation per Unit Control Angle θ Deviation
Interplanetary Leg-Jupiter Mission

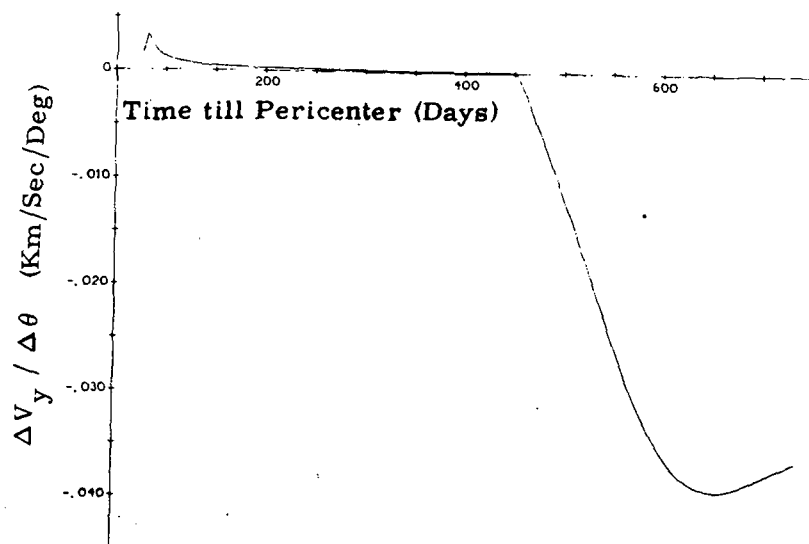


Fig. F. 1. 1. 5 Y Component of Velocity Deviation per Unit Control Angle θ Deviation
Interplanetary Leg-Jupiter Mission

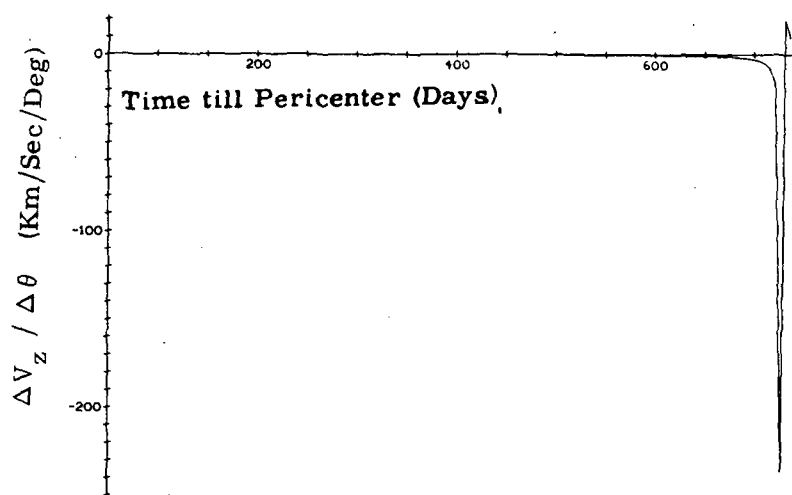


Fig. F. 1. 1. 6 Z Component of Velocity Deviation per Unit Control Angle θ Deviation
Interplanetary Leg-Jupiter Mission

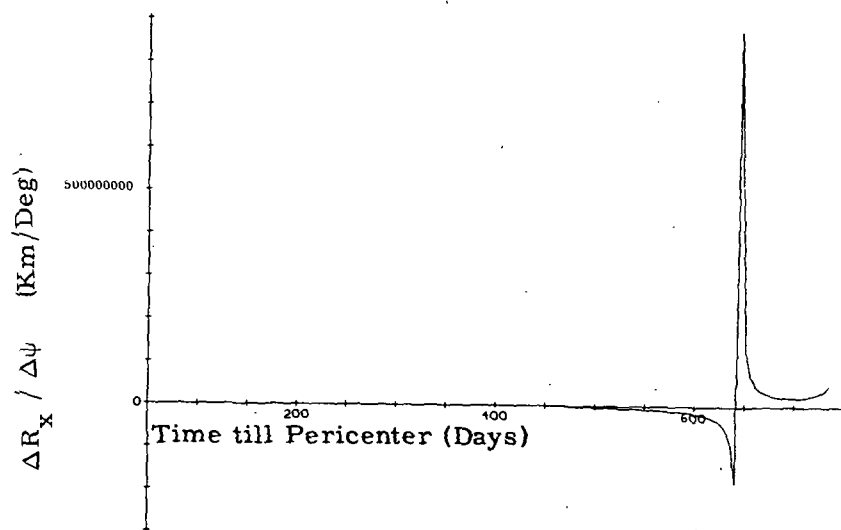


Fig. F. 1. 2. 1 X Component of Position Deviation per Unit Control Angle ψ Deviation
Interplanetary Leg-Jupiter Mission

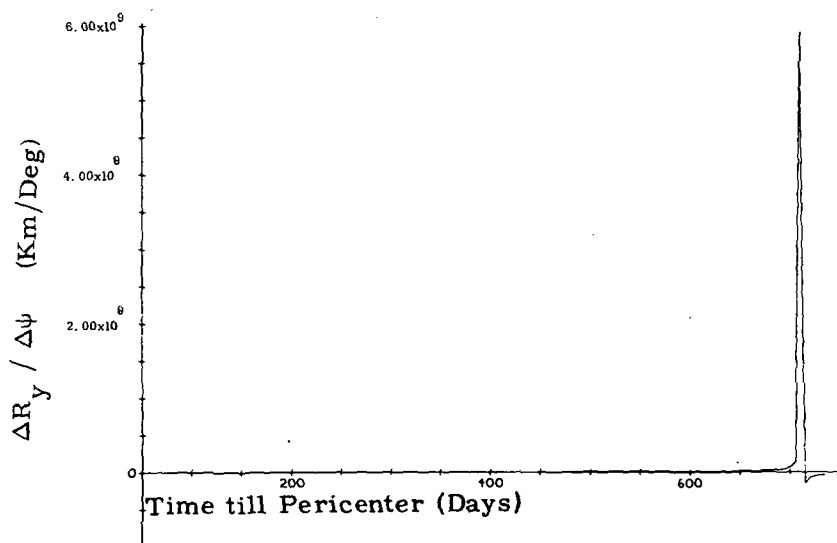


Fig. F. 1. 2. 2 Y Component of Position Deviation per Unit Control Angle ψ Deviation
Interplanetary Leg-Jupiter Mission

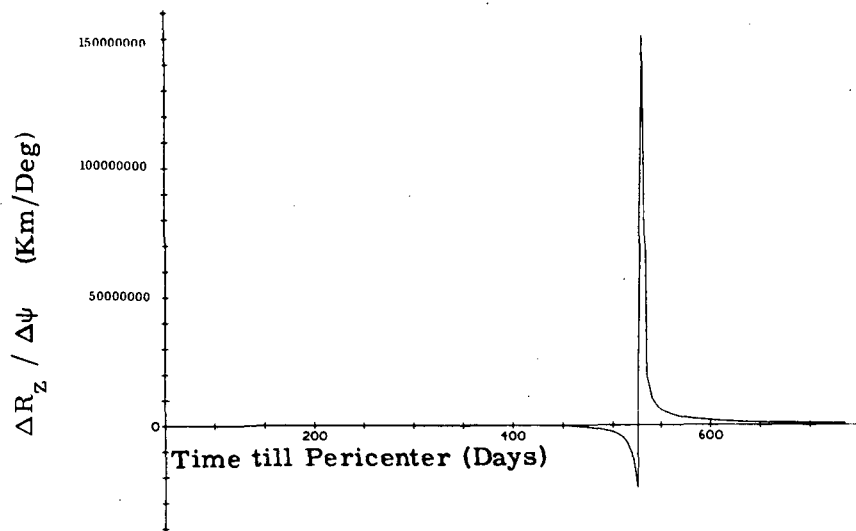


Fig. F. 1. 2. 3 Z Component of Position Deviation per Unit Control Angle ψ Deviation
Interplanetary Leg-Jupiter Mission

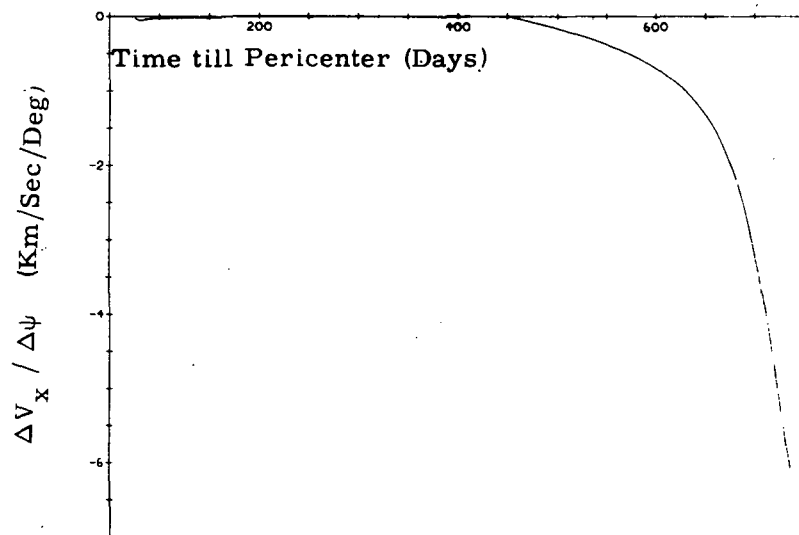


Fig. F. 1. 2. 4 X Component of Velocity Deviation per Unit Control Angle ψ Deviation
Interplanetary Leg-Jupiter Mission

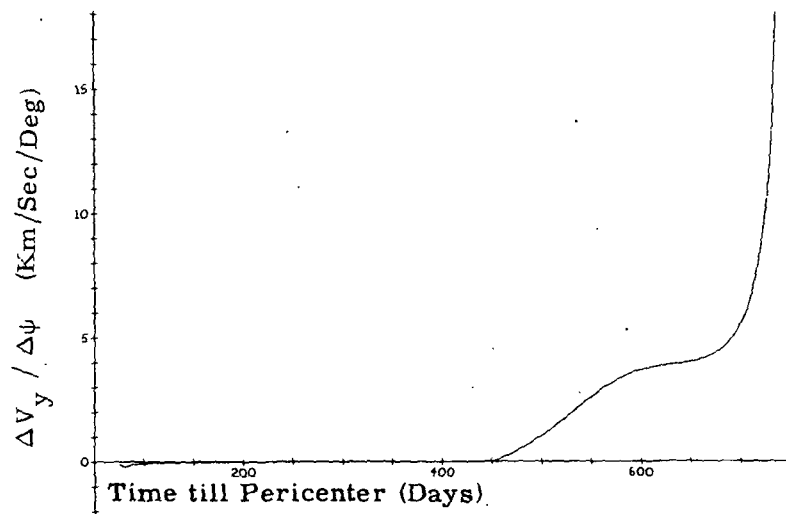


Fig. F. 1. 2. 5 Y Component of Position Deviation per Unit Control Angle ψ Deviation
Interplanetary Leg-Jupiter Mission

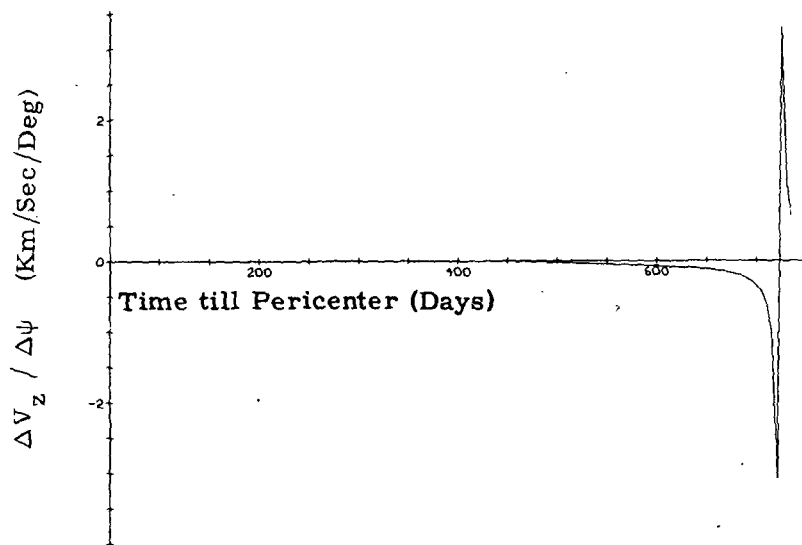


Fig. F. 1. 2. 6 Z Component of Velocity Deviation per Unit Control Angle ψ Deviation
Interplanetary Leg-Jupiter Mission

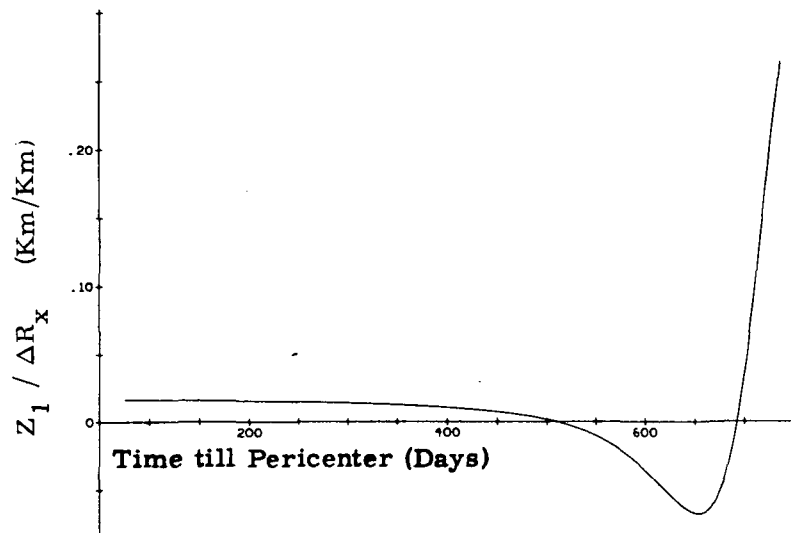


Fig. F. 1. 3. 1 Z_1 Component of Final Position per X Component of Excess Position
Interplanetary Leg-Jupiter Mission

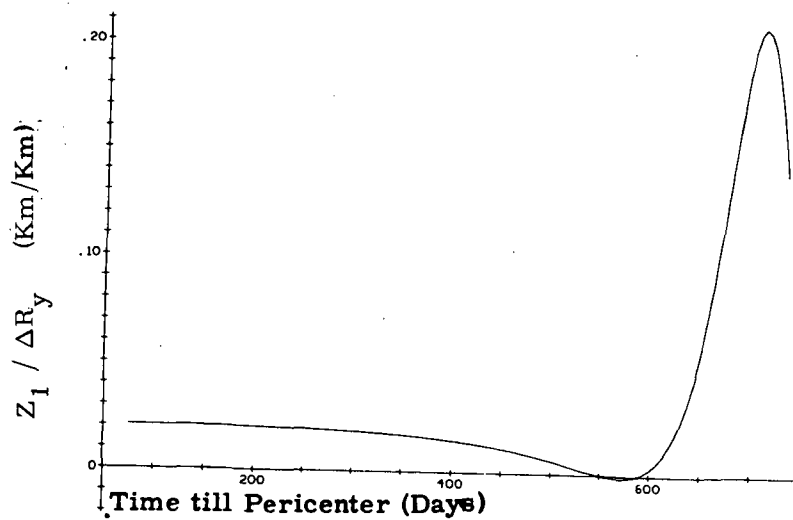


Fig. F. 1. 3. 2 Z_1 Component of Final Position per Y Component of Excess Position
Interplanetary Leg-Jupiter Mission

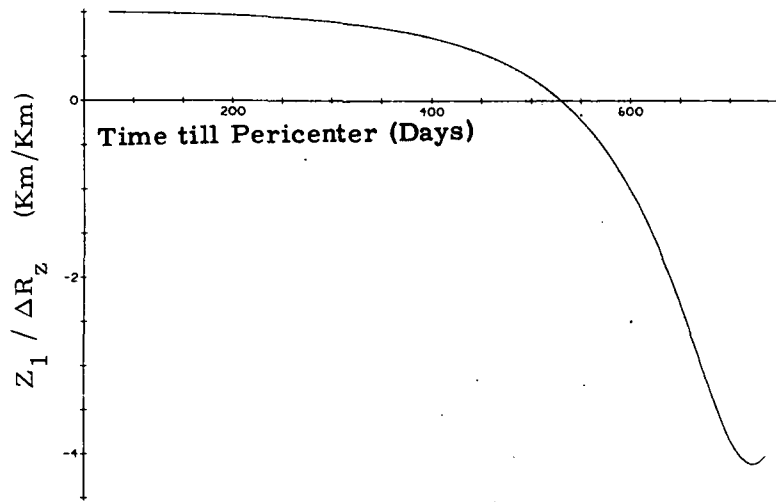


Fig. F. 1. 3. 3 Z_1 Component of Final Position per Z Component of Excess Position
Interplanetary Leg-Jupiter Mission

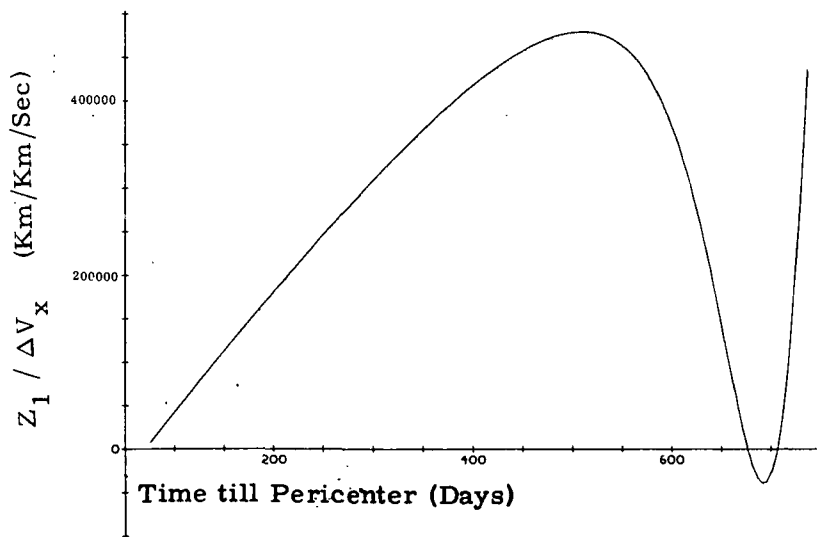


Fig. F. 1. 3. 4 Z_1 Component of Final Position per X Component of Excess Velocity
Interplanetary Leg-Jupiter Mission

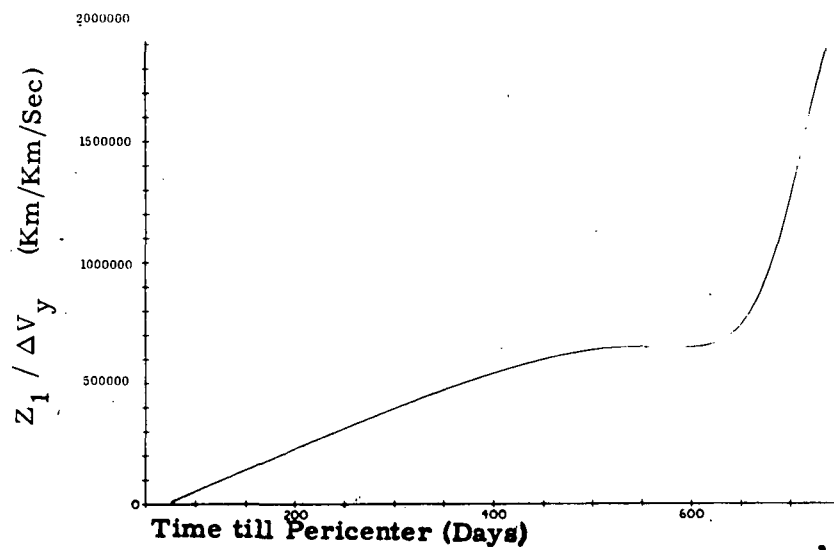


Fig. F. 1. 3. 5 Z_1 Component of Final Position per Y Component of Excess Velocity
Interplanetary Leg-Jupiter Mission

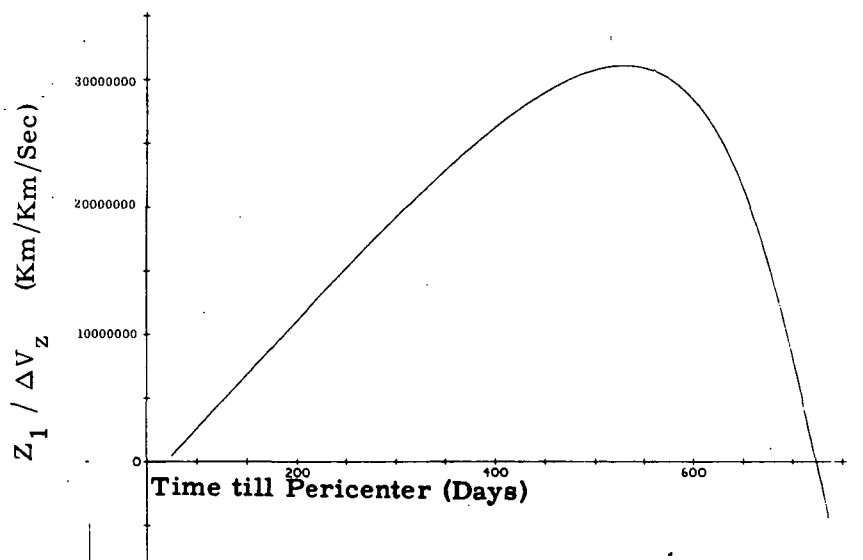


Fig. F. 1. 3. 6 Z_1 Component of Final Position per Z Component of Excess Velocity
Interplanetary Leg-Jupiter Mission

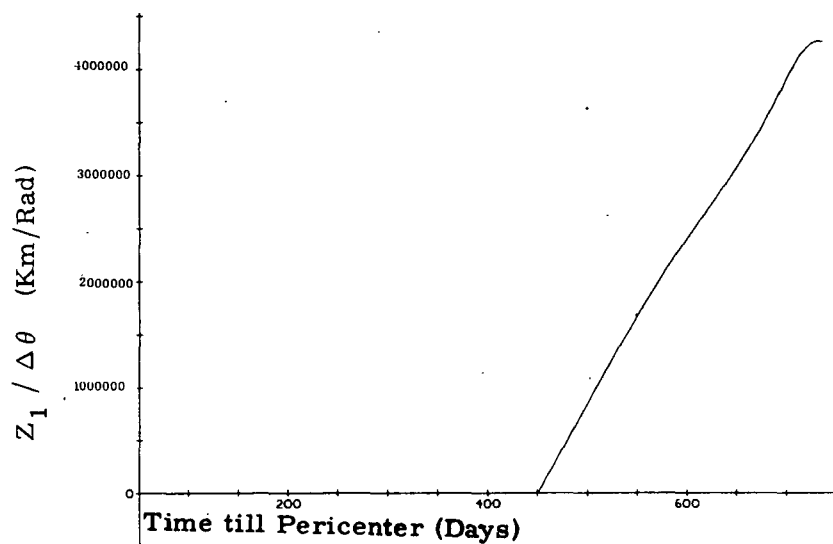


Fig. F. 1 3. 7 Z_1 Component of Final Position per Excess Control Angle θ
Interplanetary Leg-Jupiter Mission

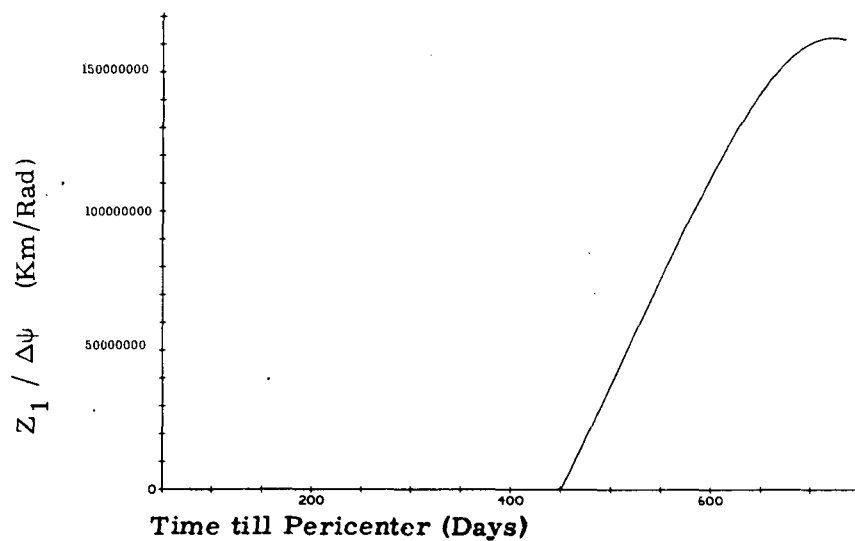


Fig. F. 1. 3. 8 Z_1 Component of Final Position per Excess Control Angle ψ
Interplanetary Leg-Jupiter Mission

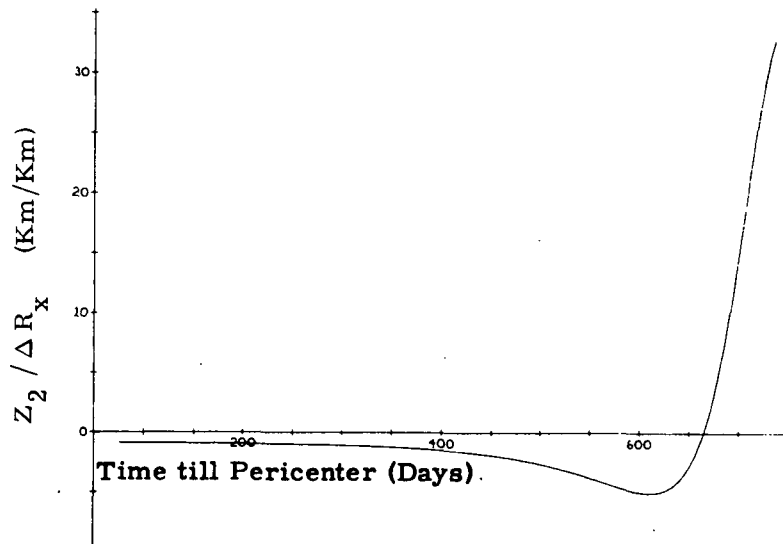


Fig. F. 1. 4. 1 Z_2 Component of Final Position per X Component of Excess Position
Interplanetary Leg-Jupiter Mission

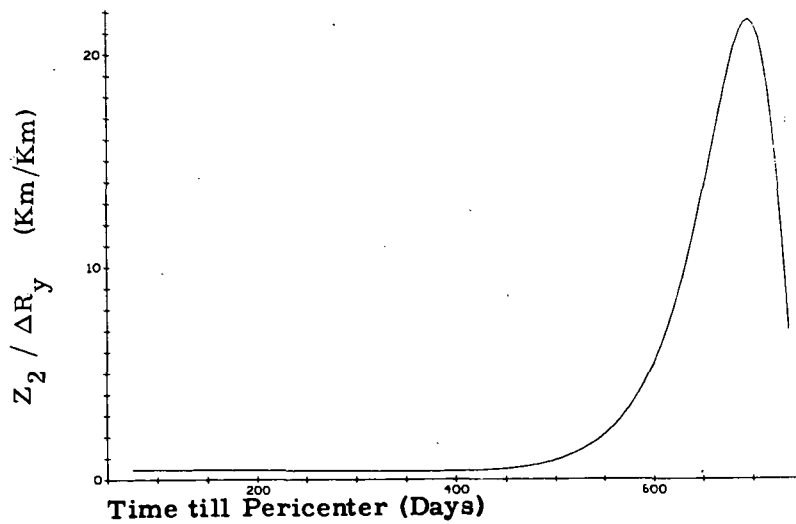


Fig. F. 1. 4. 2 Z_2 Component of Final Position per Y Component of Excess Position
Interplanetary Leg-Jupiter Mission

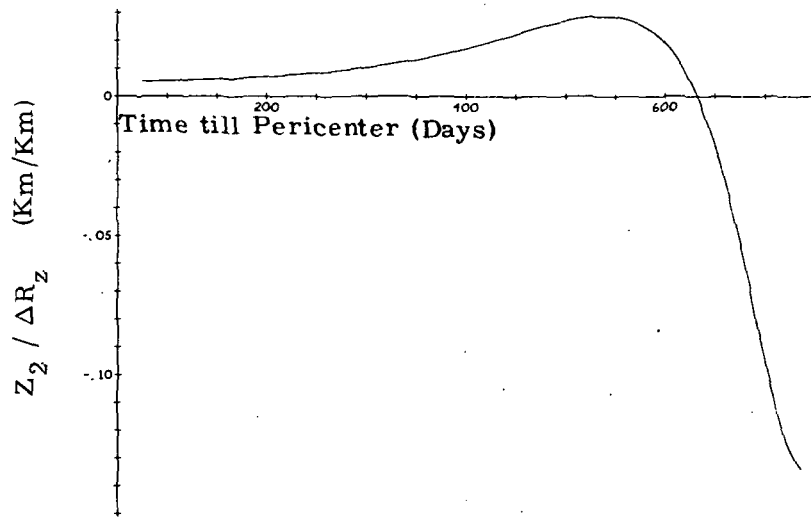


Fig. F. 1. 4. 3 Z_2 Component of Final Position per Z Component of Excess Position
Interplanetary Leg-Jupiter Mission

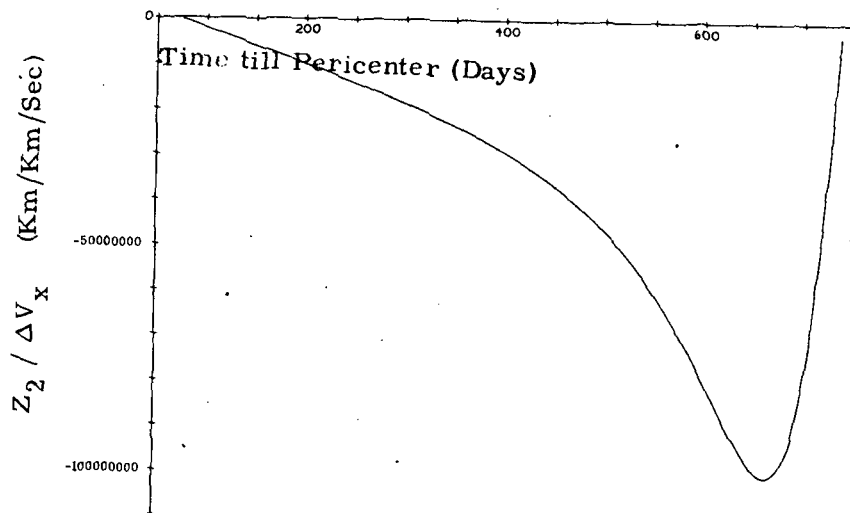


Fig. F. 1. 4. 4 Z_2 Component of Final Position per X Component of Excess Velocity
Interplanetary Leg-Jupiter Mission

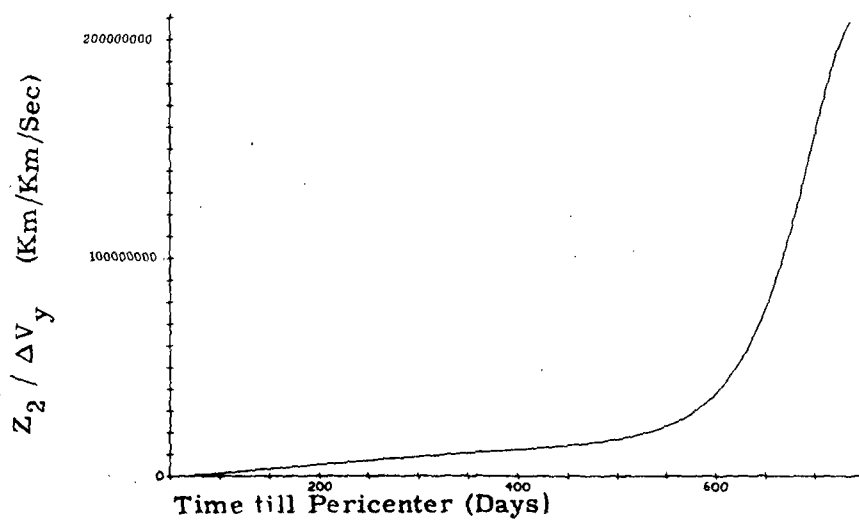


Fig. F. 1. 4. 5 Z_2 Component of Final Position per Y Component of Excess Velocity
Interplanetary Leg-Jupiter Mission

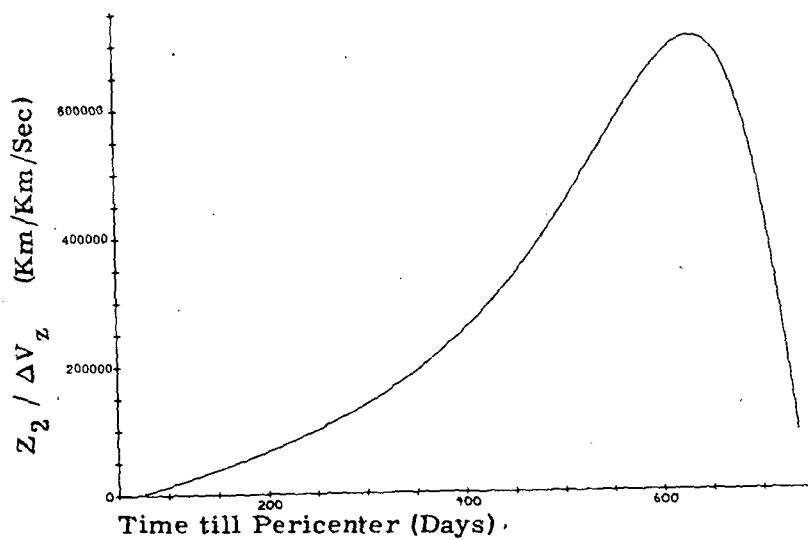


Fig. F. 1. 4. 6 Z_2 Component of Final Position per Z Component of Excess Velocity
Interplanetary Leg-Jupiter Mission

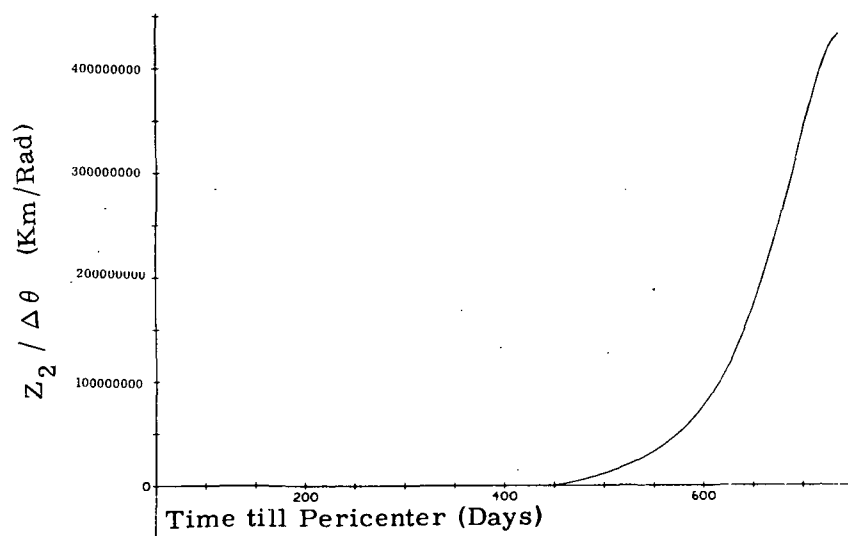


Fig. F. 1. 4. 7 Z_2 Component of Final Position per Excess Control Angle θ
Interplanetary Leg-Jupiter Mission

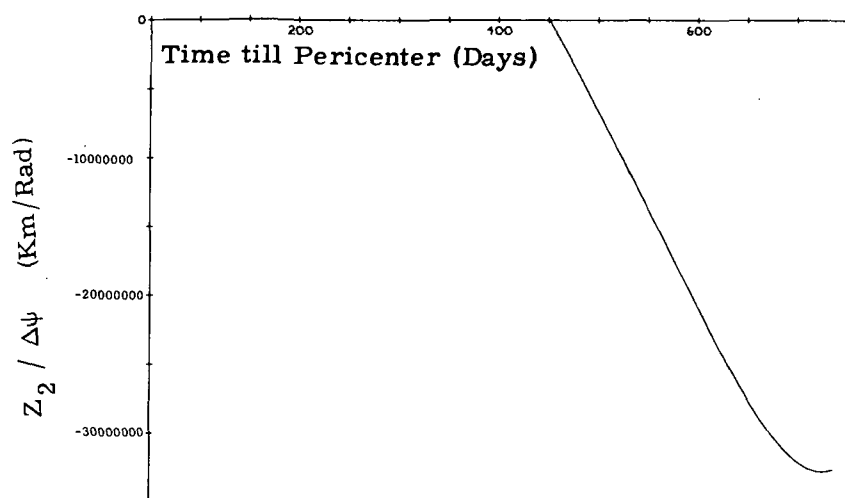


Fig. F. 1 4. 8 Z_2 Component of Final Position per Excess Control Angle ψ
Interplanetary Leg-Jupiter Mission

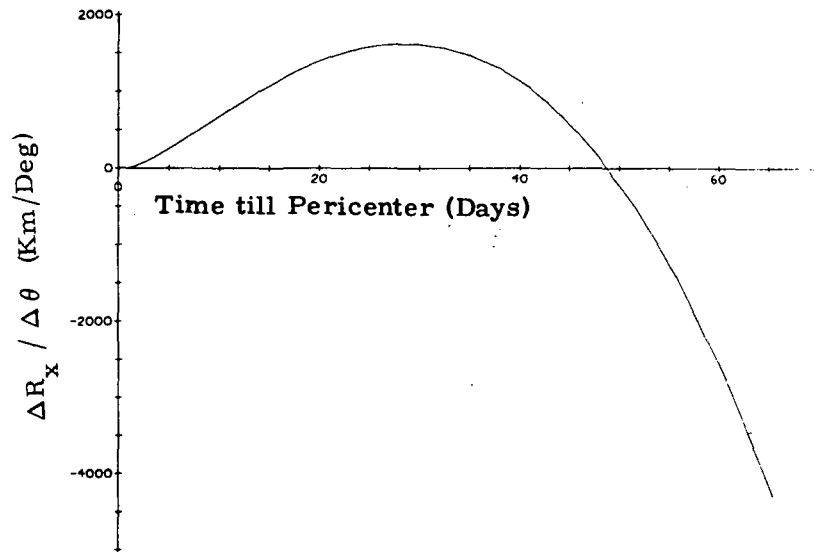


Fig. F.2.1.1 X Component of Position Deviation per Unit Control Angle θ Deviation
Near Planet Leg-Jupiter Mission

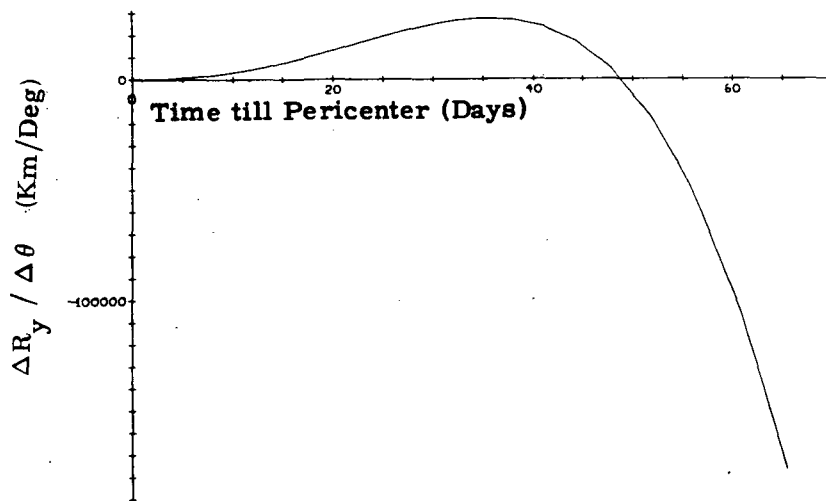


Fig. F.2.1.2 Y Component of Position Deviation per Unit Control Angle θ Deviation
Near Planet Leg-Jupiter Mission

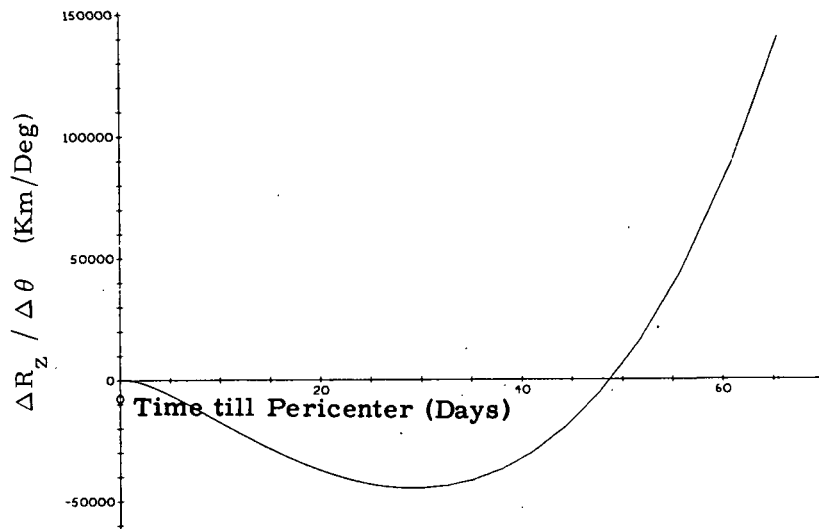


Fig. F. 2. 1. 3 Z Component of Position Deviation per Unit Control Angle θ Deviation
Near Planet Leg-Jupiter Mission

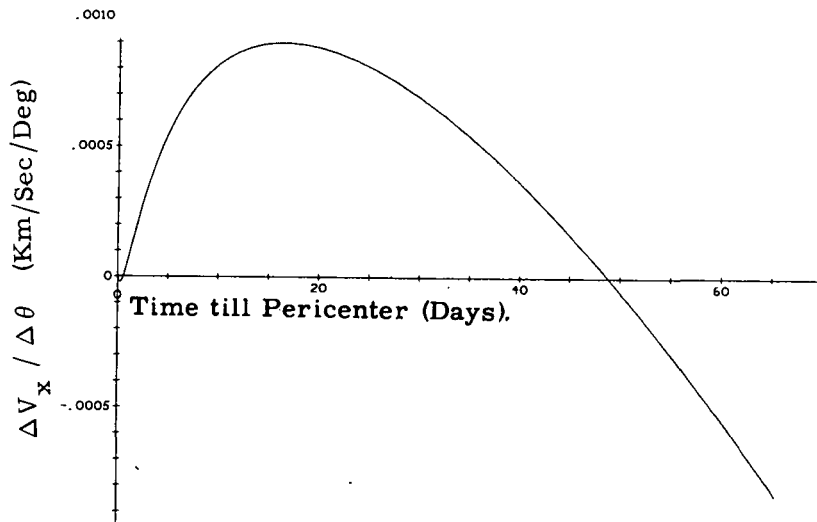


Fig. F. 2. 1. 4 X Component of Velocity Deviation per Unit Control Angle θ Deviation
Near Planet Leg-Jupiter Mission

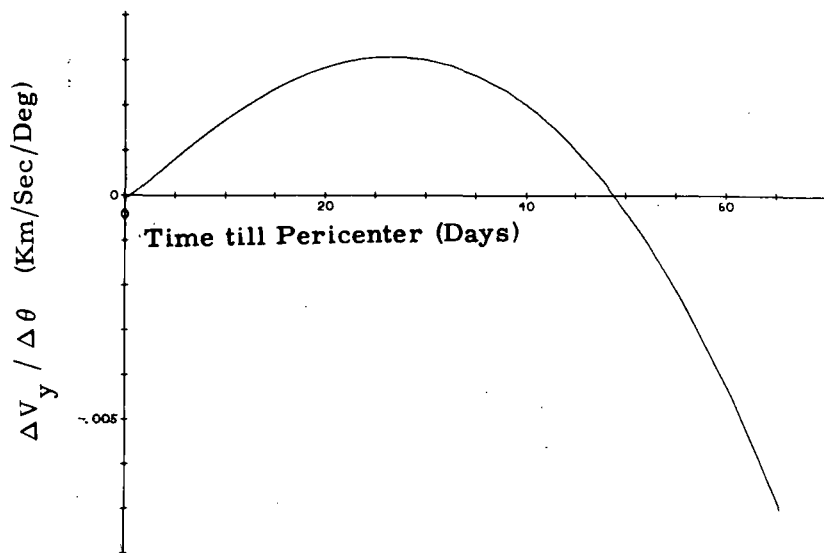


Fig. F.2.1.5 Y Component of Velocity Deviation per Unit Control Angle θ Deviation
Near Planet Leg-Jupiter Mission

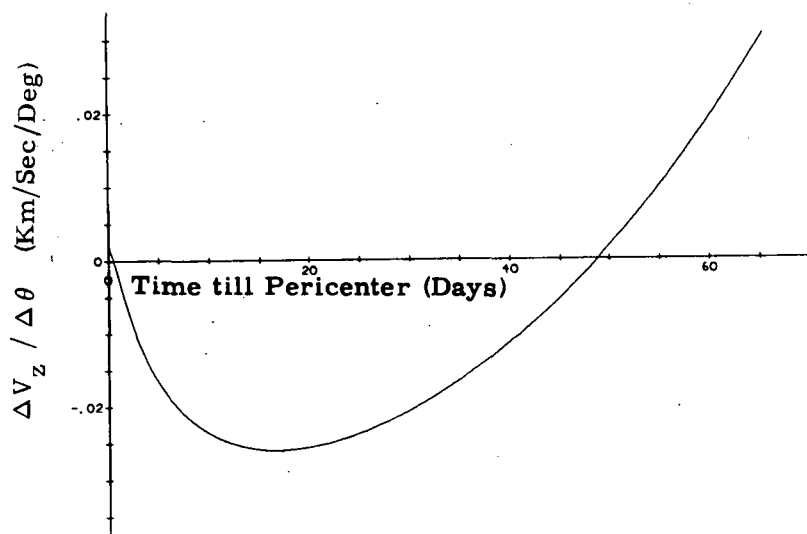


Fig. F.2.1.6 Z Component of Velocity Deviation per Unit Control Angle θ Deviation
Near Planet Leg-Jupiter Mission

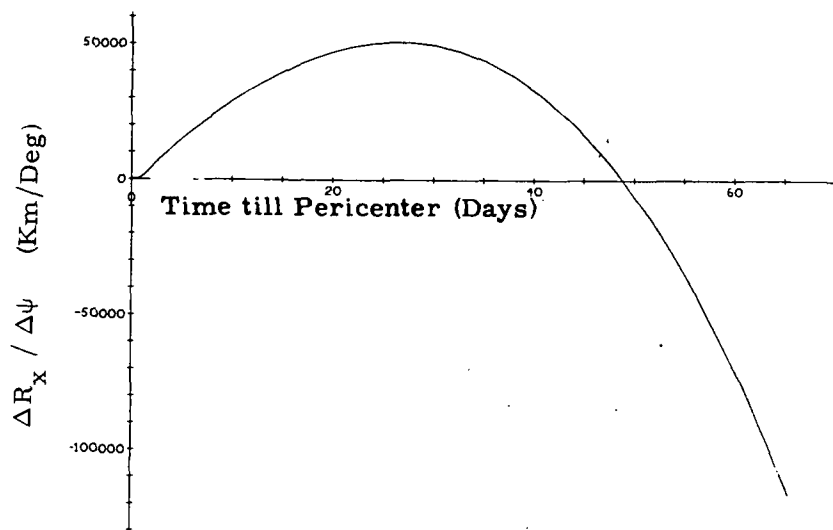


Fig. F.2.2.1 X Component of Position Deviation per Unit Control Angle ψ Deviation
Near Planet Leg-Jupiter Mission

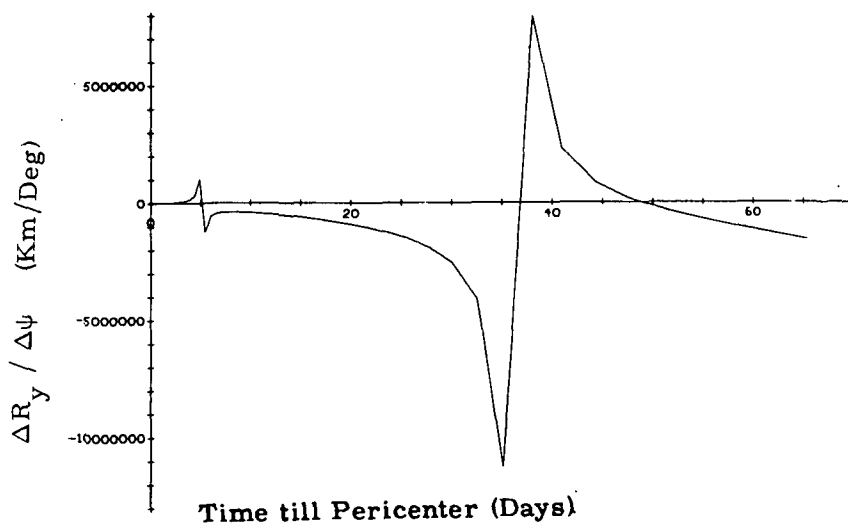


Fig. F.2.2.2 Y Component of Position Deviation per Unit Control Angle ψ Deviation
Near Planet Leg-Jupiter Mission

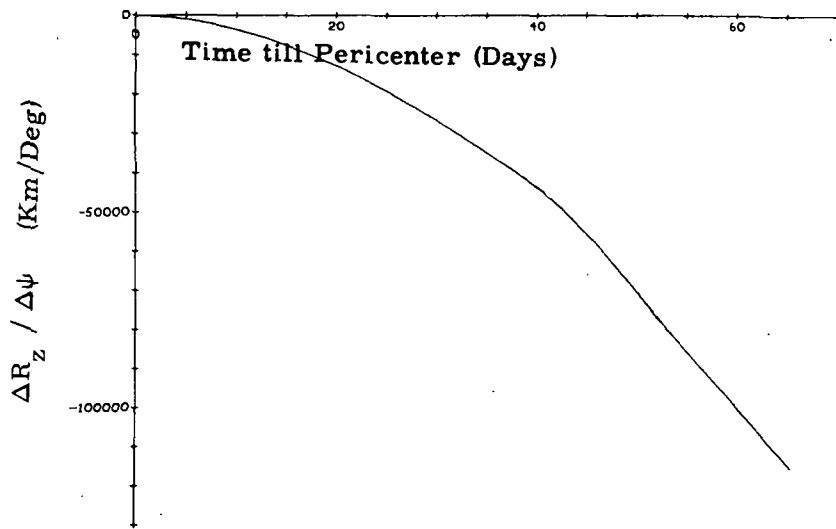


Fig. F. 2. 2. 3 Z Component of Position Deviation per Unit Control Angle ψ Deviation
Near Planet Leg-Jupiter Mission

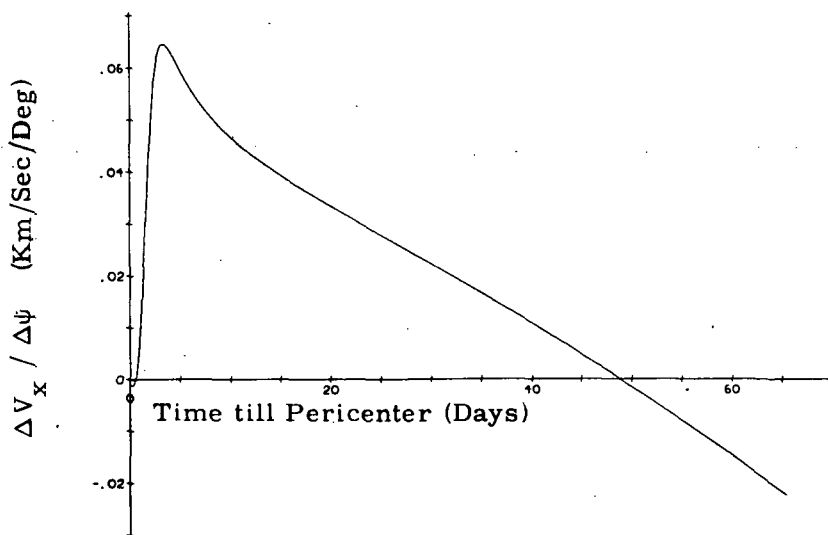


Fig. F. 2. 2. 4 X Component of Velocity Deviation per Unit Control Angle ψ Deviation
Near Planet Leg-Jupiter Mission

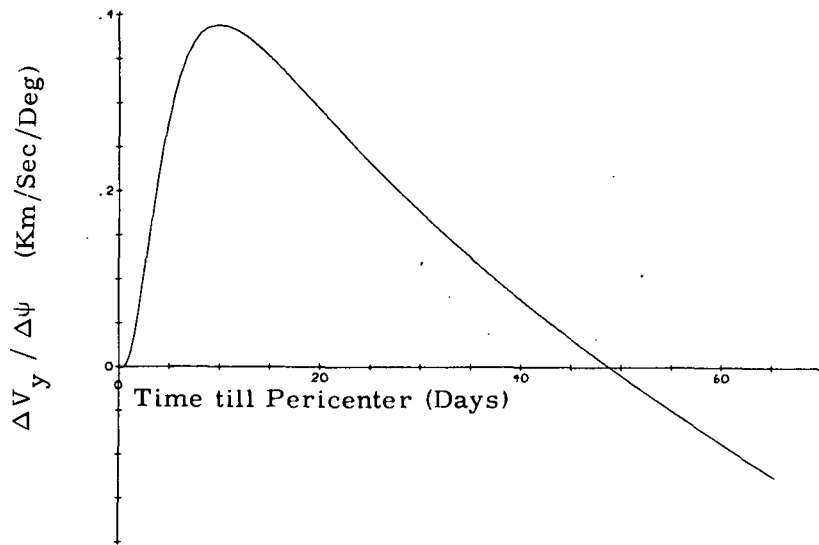


Fig. F. 2. 2. 5 Y Component of Velocity Deviation per Unit Control Angle ψ Deviation
Near Planet Leg-Jupiter Mission

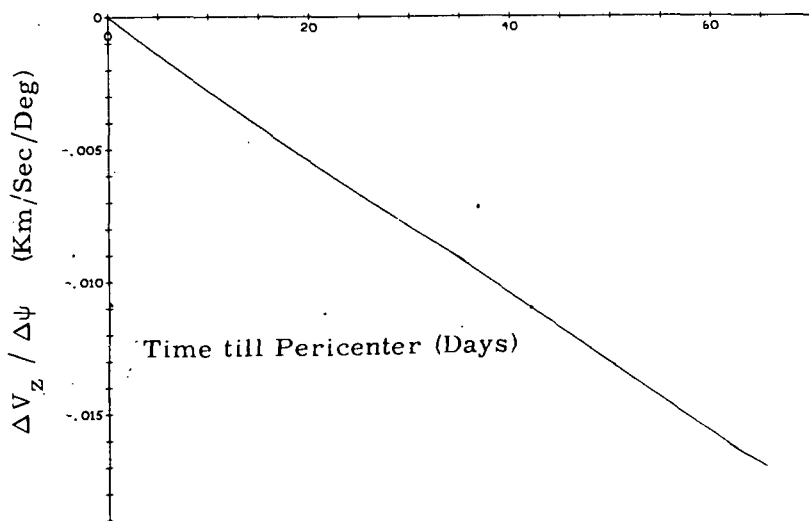


Fig. F. 2. 2. 6 Z Component of Velocity Deviation per Unit Control Angle ψ Deviation
Near Planet Leg-Jupiter Mission

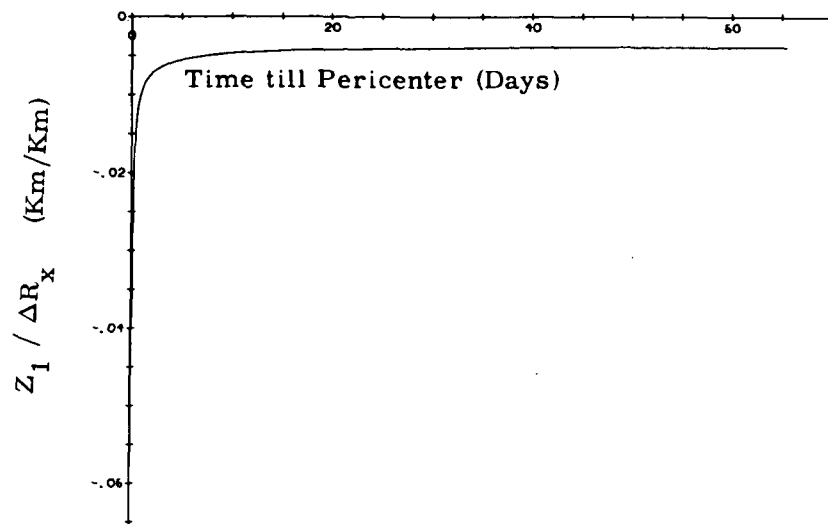


Fig. F. 2. 3. 1 Z_1 Component of Final Position per X Component of Excess Position
Near Planet Leg-Jupiter Mission

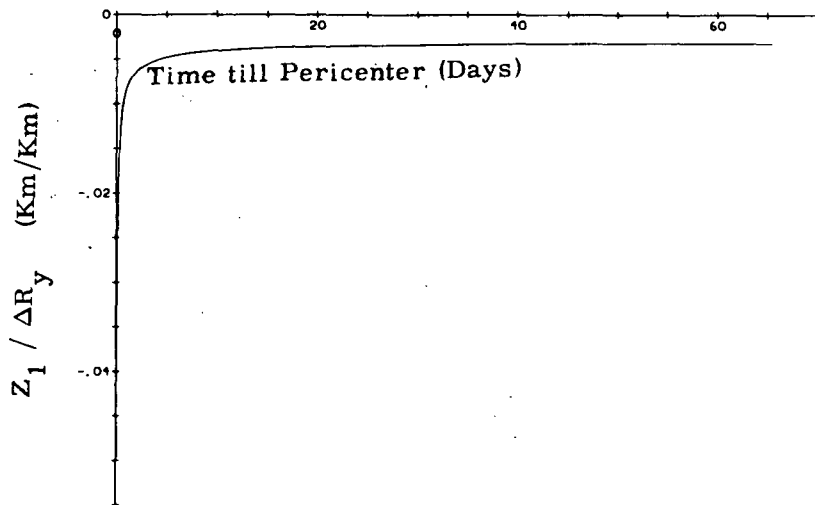


Fig. F. 2. 3. 2 Z_1 Component of Final Position per Y Component of Excess Position
Near Planet Leg-Jupiter Mission

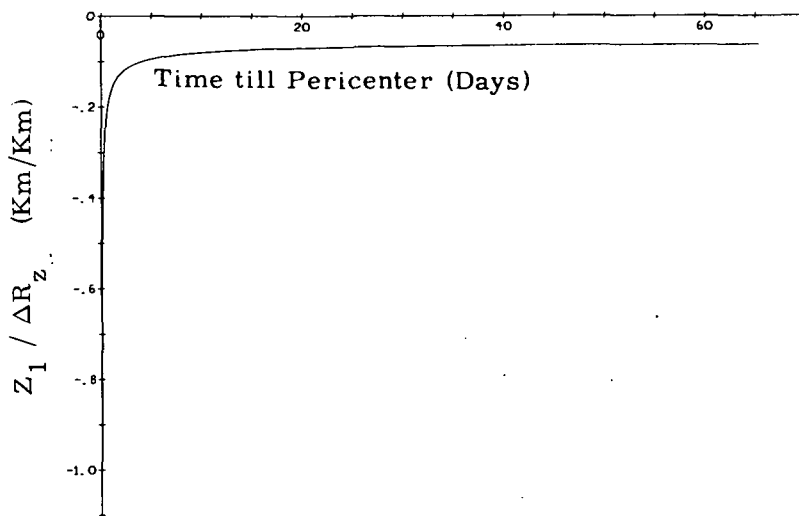


Fig. F. 2. 3. 3 Z_1 Component of Final Position per Z Component of Excess Position
Near Planet Leg-Jupiter Mission

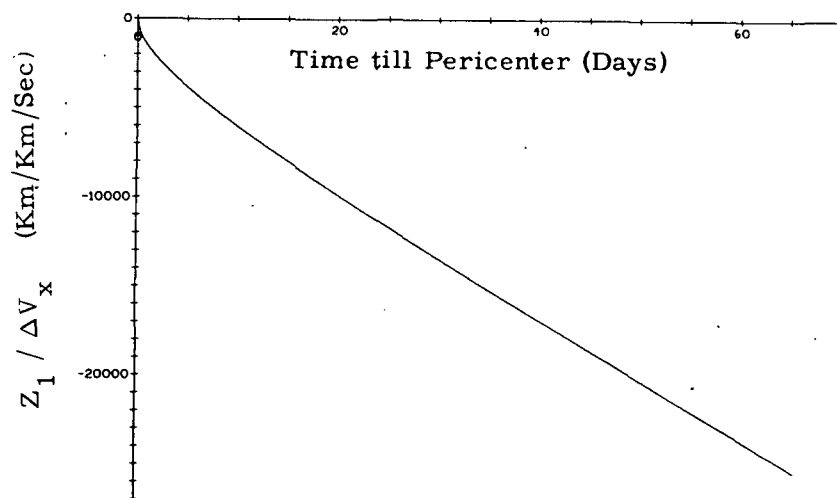


Fig. F. 2. 3. 4 Z_1 Component of Final Position per X Component of Excess Velocity
Near Planet Leg-Jupiter Mission

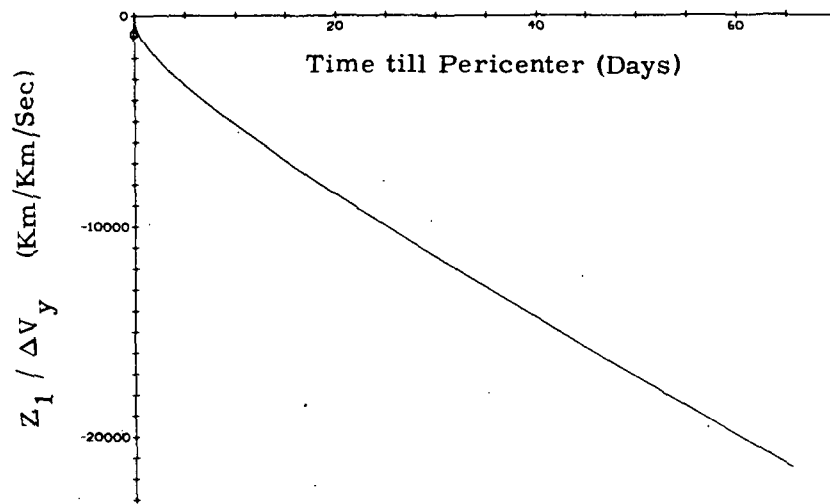


Fig. F. 2. 3. 5 Z_1 Component of Final Position per Y Component of Excess Velocity
Near Planet Leg-Jupiter Mission

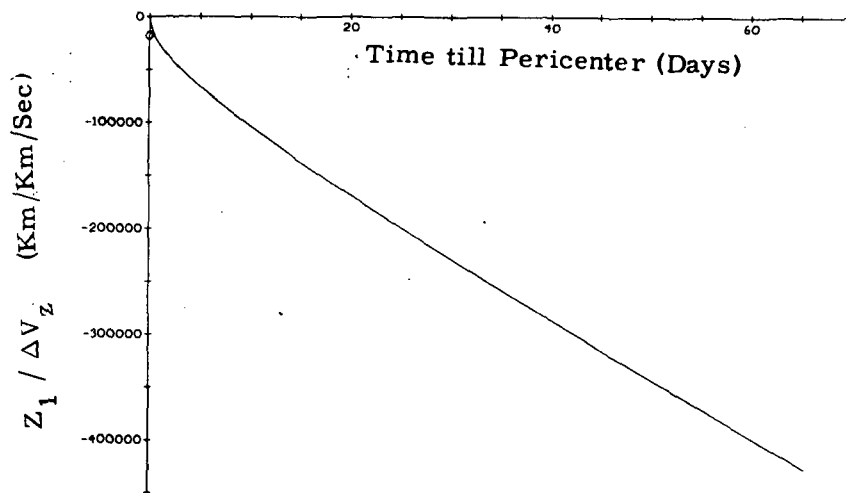


Fig. F. 2. 3. 6 Z_1 Component of Final Position per Z Component of Excess Velocity
Near Planet Leg-Jupiter Mission

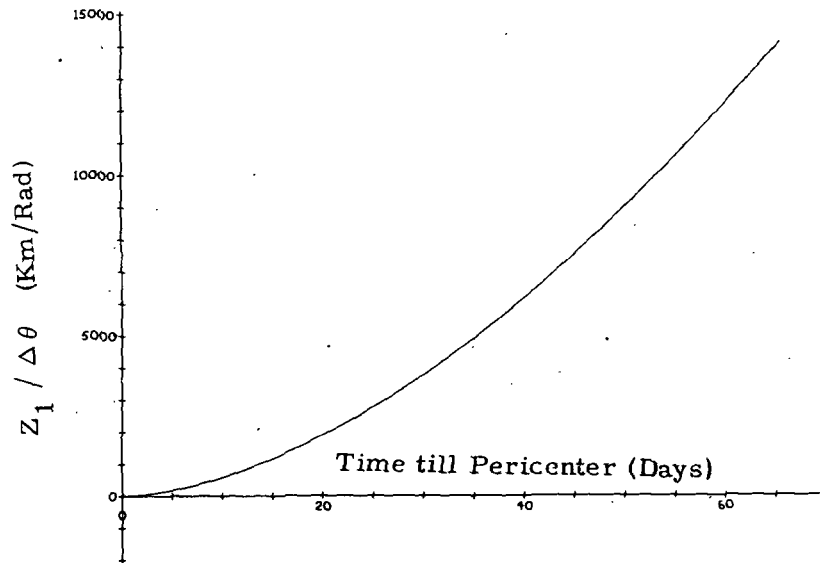


Fig. F. 2. 3. 7 Z_1 Component of Final Position per Excess Control Angle θ
Near Planet Leg-Jupiter Mission

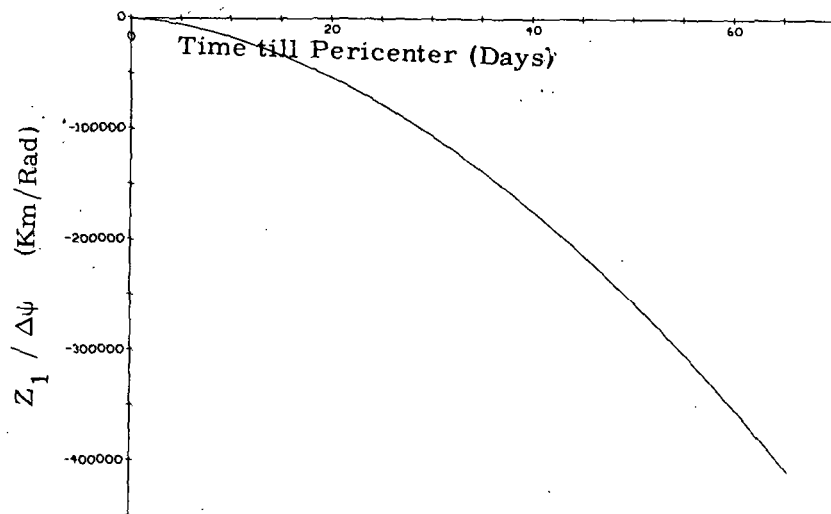


Fig. F. 2. 3. 8 Z_1 Component of Final Position per Excess Control Angle ψ
Near Planet Leg-Jupiter Mission

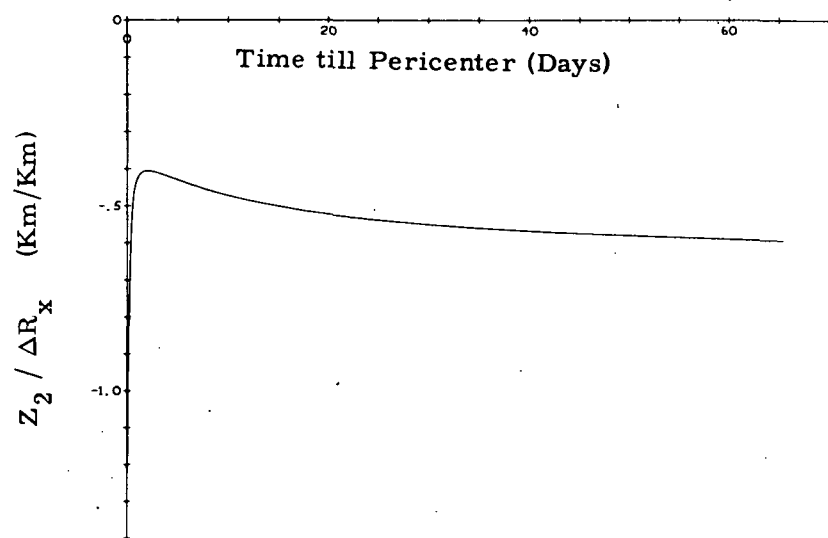


Fig. F. 2. 4. 1 Z_2 Component of Final Position per X Component of Excess Position
Near Planet Leg-Jupiter Mission

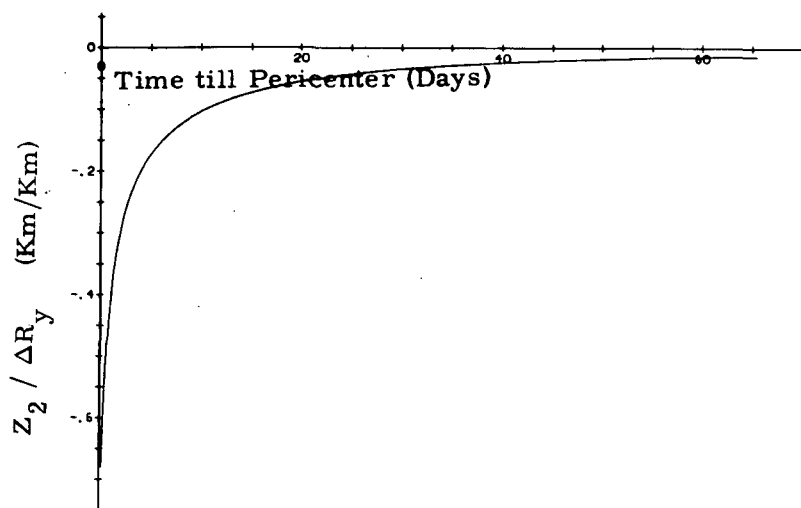


Fig. F. 2. 4. 2 Z_2 Component of Final Position per Y Component of Excess Position
Near Planet Leg-Jupiter Mission

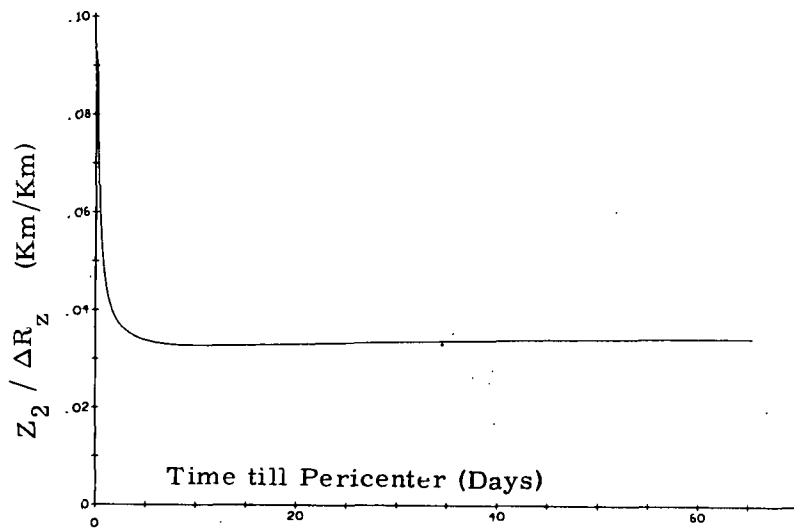


Fig. F. 2. 4. 3 Z_2 Component of Final Position per Z Component of Excess Position
Near Planet Leg-Jupiter Mission

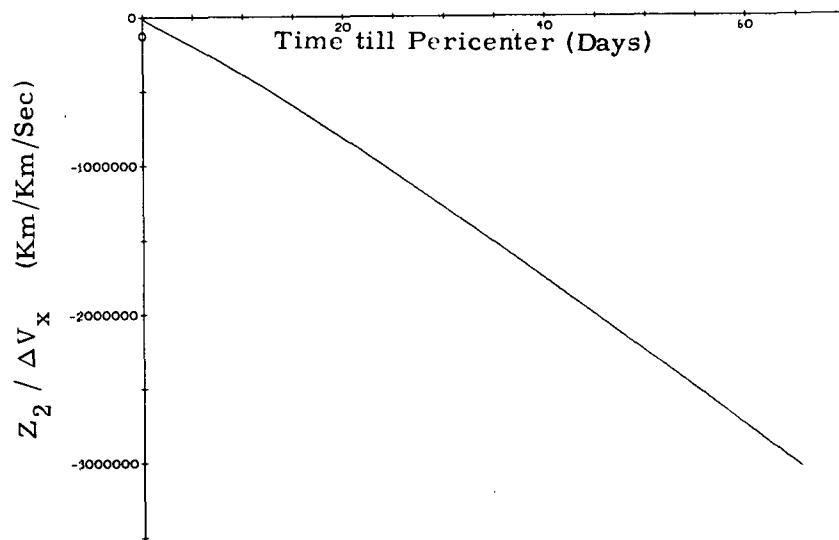


Fig. F. 2. 4. 4 Z_2 Component of Final Position per X Component of Excess Velocity
Near Planet Leg-Jupiter Mission

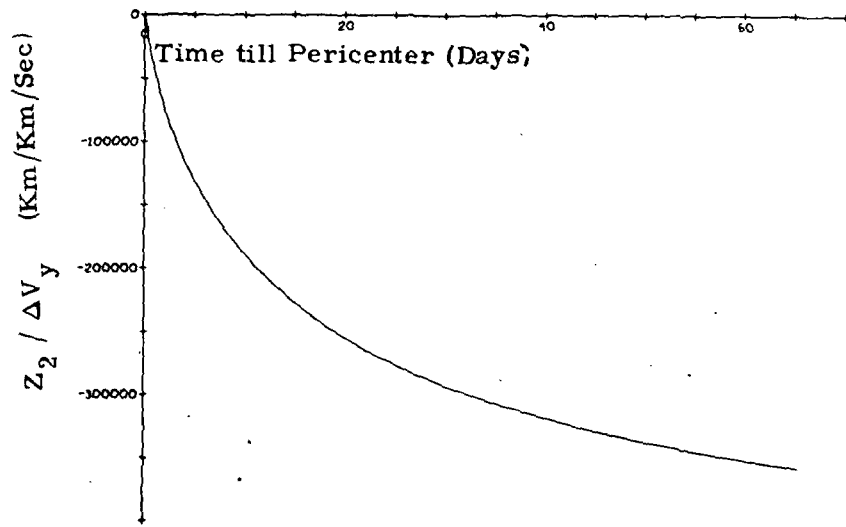


Fig. F. 2. 4. 5 Z_2 Component of Final Position per Y Component of Excess Velocity
Near Planet Leg-Jupiter Mission

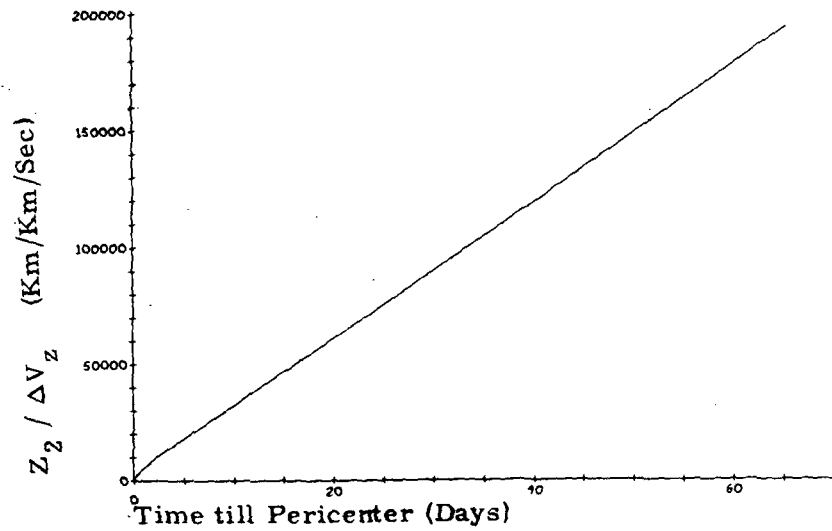


Fig. F. 2. 4. 6 Z_2 Component of Final Position per Z Component of Excess Velocity
Near Planet Leg-Jupiter Mission

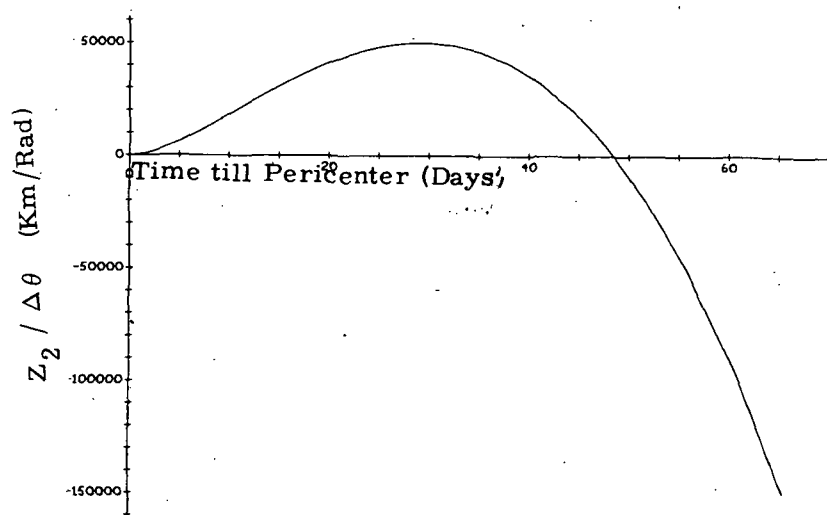


Fig. F. 2. 4. 7 Z_2 Component of Final Position per Excess Control Angle θ
Near Planet Leg-Jupiter Mission

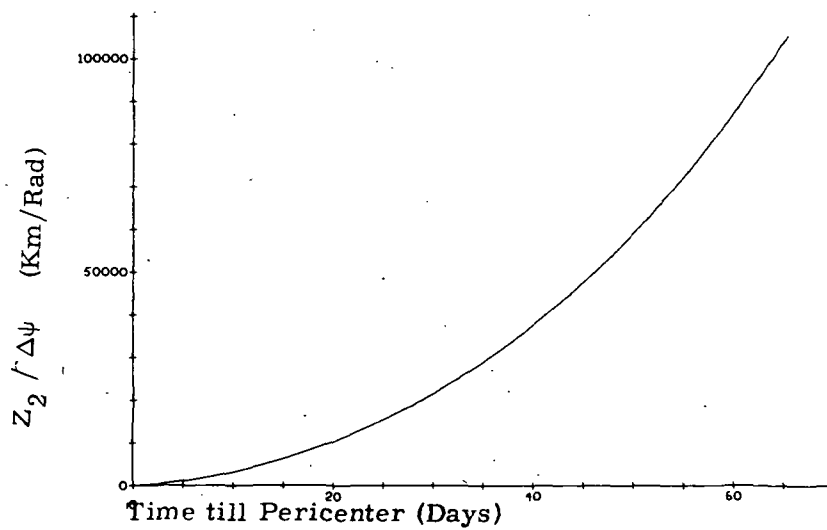


Fig. F. 2. 4. 8 Z_2 Component of Final Position per Excess Control Angle ψ
Near Planet Leg-Jupiter Mission

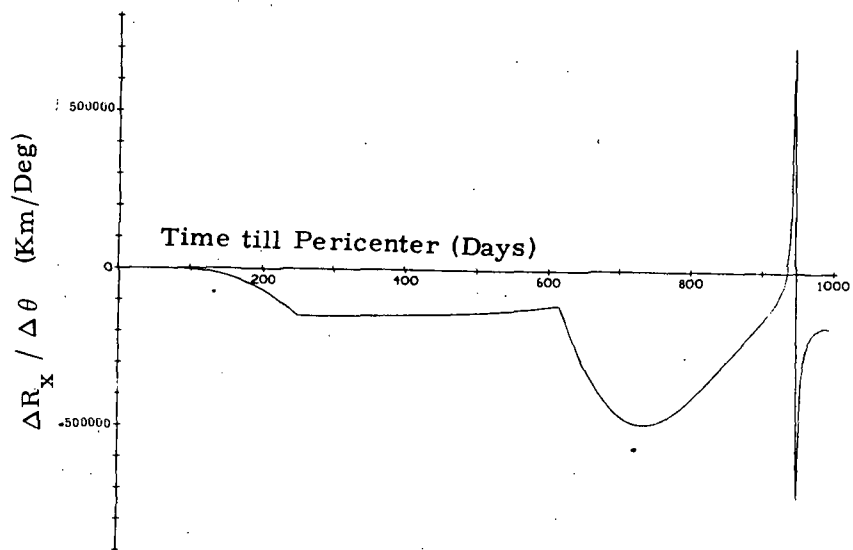


Fig. F. 3. 1. 1 X Component of Position Deviation per Unit Control Angle θ Deviation
Interplanetary Leg-Saturn Mission

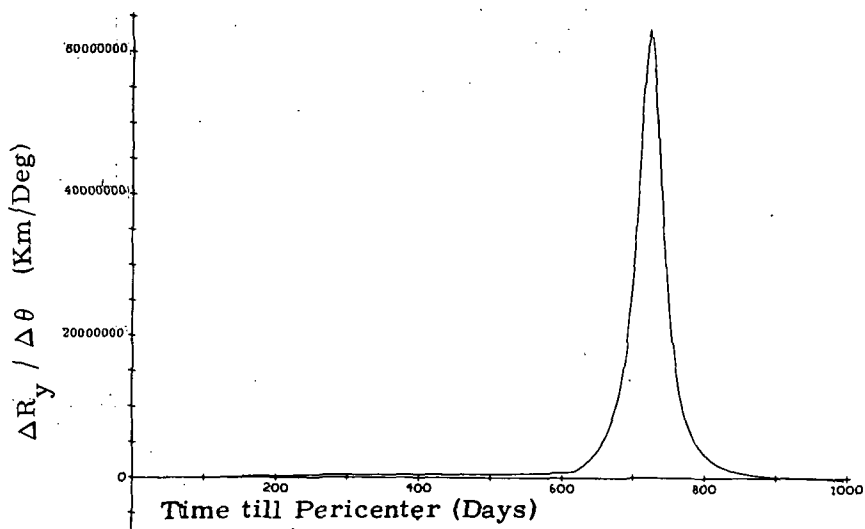


Fig. F. 3. 1. 2 Y Component of Position Deviation per Unit Control Angle θ Deviation
Interplanetary Leg-Saturn Mission

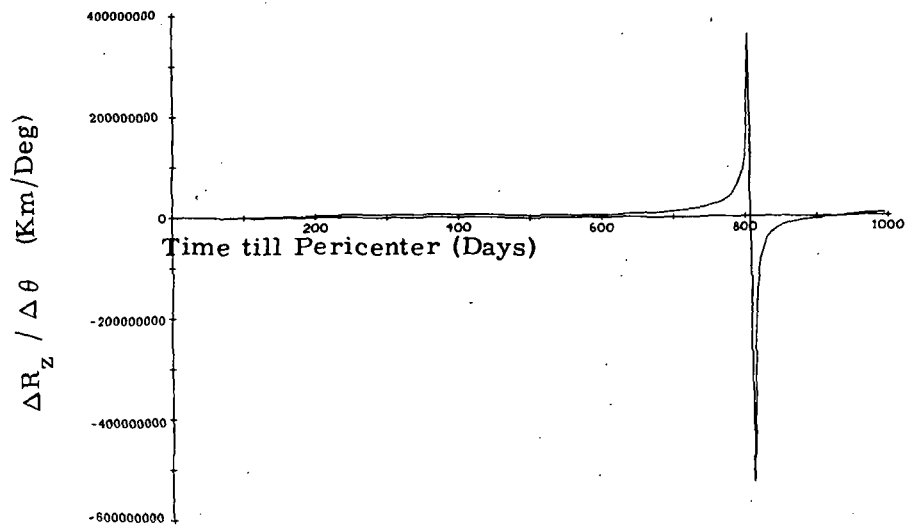


Fig. F. 3. 1. 3 Z Component of Position Deviation per Unit Control Angle θ Deviation
Interplanetary Leg-Saturn Mission

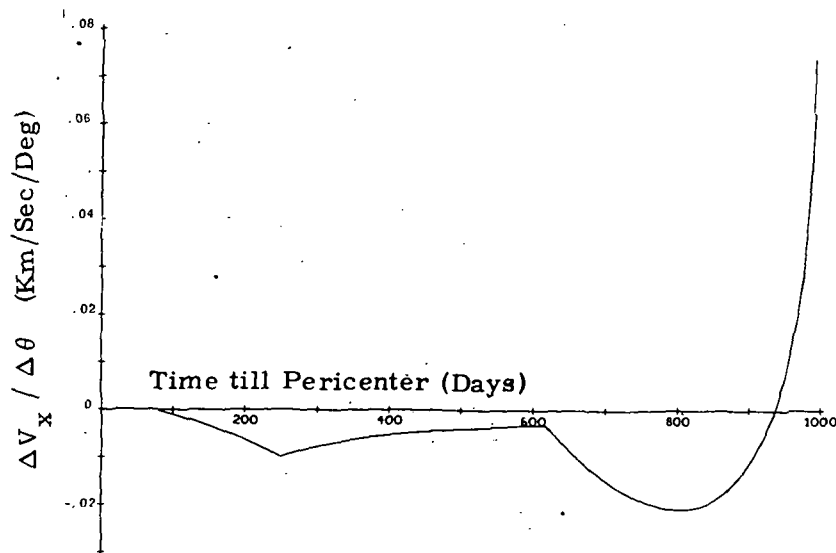


Fig. F. 3. 1. 4 X Component of Velocity Deviation per Unit Control Angle θ Deviation.
Interplanetary Leg-Saturn Mission

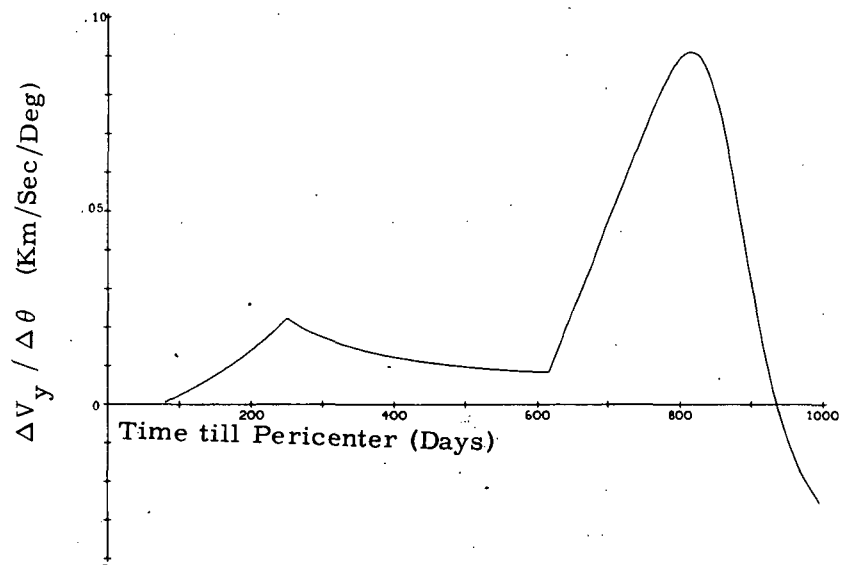


Fig. F. 3. 1. 5 Y Component of Velocity Deviation per Unit Control Angle θ Deviation
Interplanetary Leg-Saturn Mission

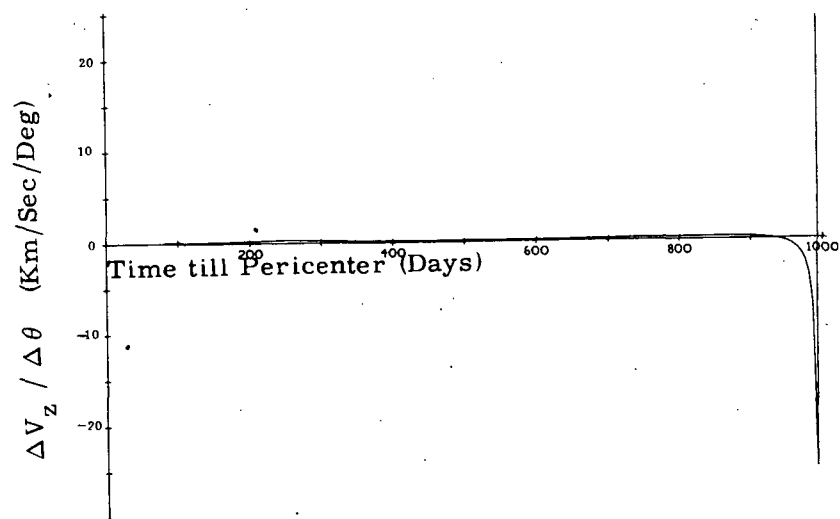


Fig. F. 3. 1. 6 Z Component of Velocity Deviation per Unit Control Angle θ Deviation
Interplanetary Leg-Saturn Mission

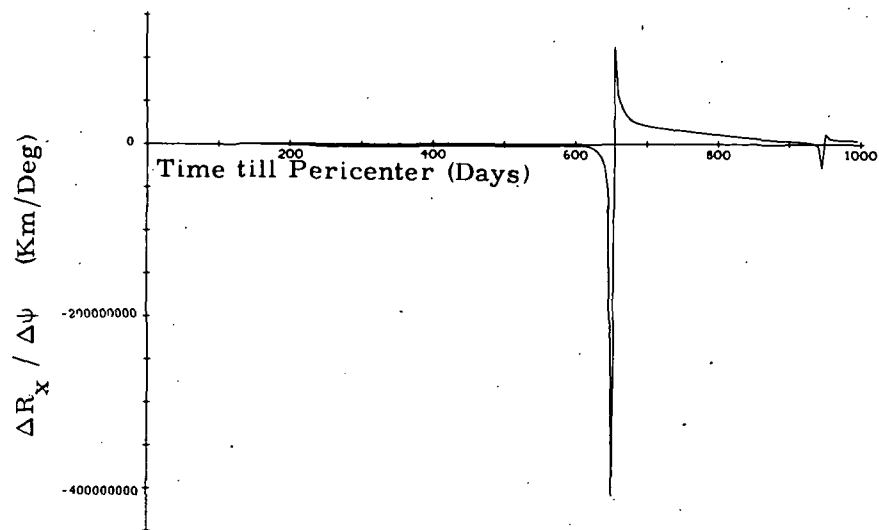


Fig. F. 3. 2. 1 X Component of Position Deviation per Unit Control Angle ψ Deviation
Interplanetary Leg-Saturn Mission

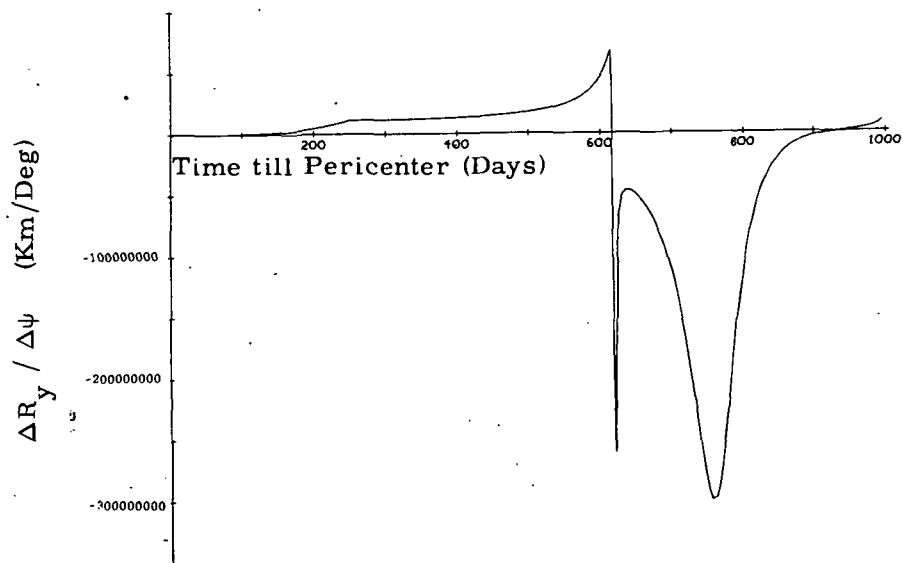


Fig. F. 3. 2. 2 Y Component of Position Deviation per Unit Control Angle ψ Deviation
Interplanetary Leg-Saturn Mission

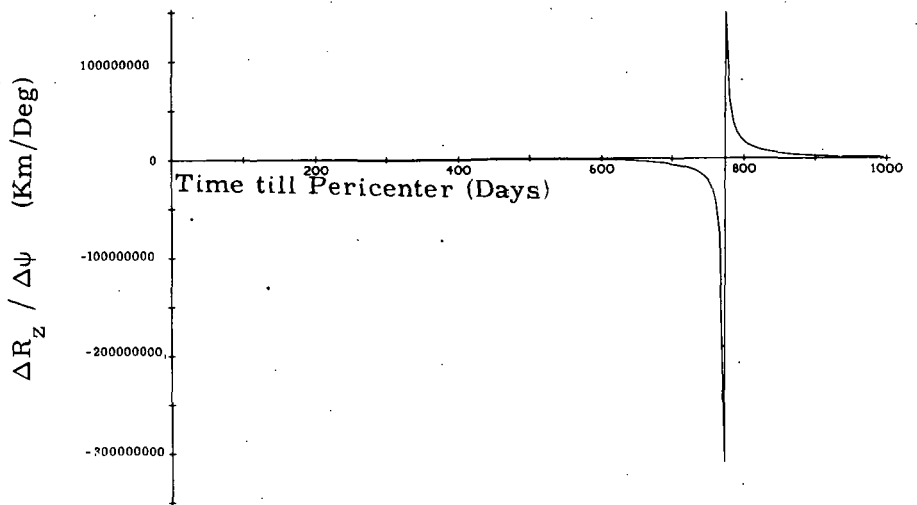


Fig. F. 3. 2. 3 Z Component of Position Deviation per Unit Control Angle ψ Deviation
Interplanetary Leg-Saturn Mission

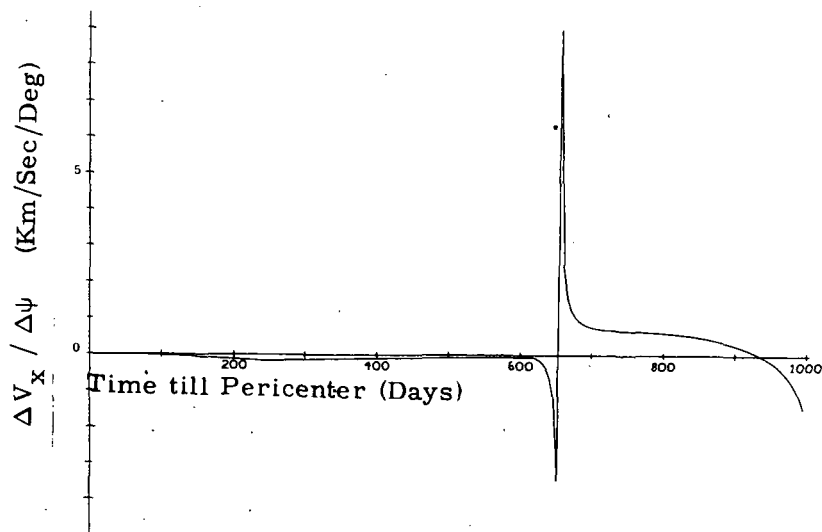


Fig. F. 3. 2. 4 X Component of Velocity Deviation per Unit Control Angle ψ Deviation
Interplanetary Leg-Saturn Mission

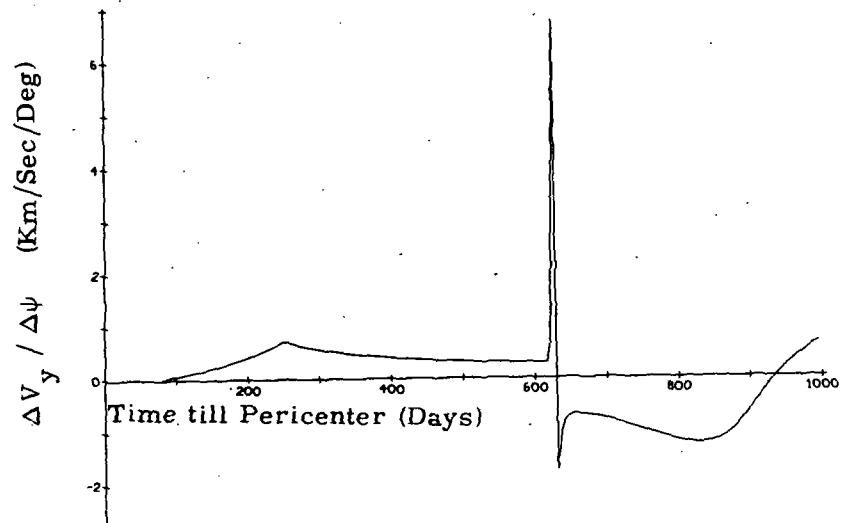


Fig. F. 3. 2. 5 Y Component of Velocity Deviation per Unit Control Angle ψ Deviation
Interplanetary Leg-Saturn Mission

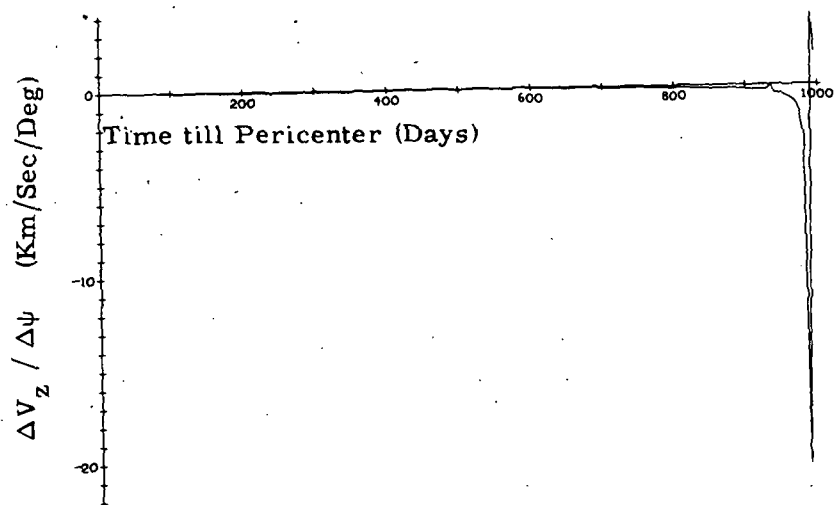


Fig. F. 3. 2. 6 Z Component of Velocity Deviation per Unit Control Angle ψ Deviation
Interplanetary Leg-Saturn Mission

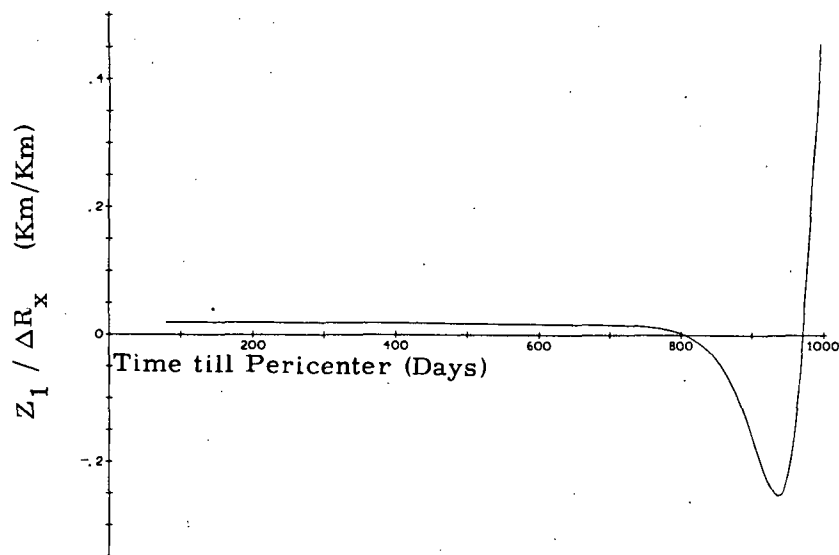


Fig. F.3.3.1 Z_1 Component of Final Position per X Component of Excess Position
Interplanetary Leg-Saturn Mission

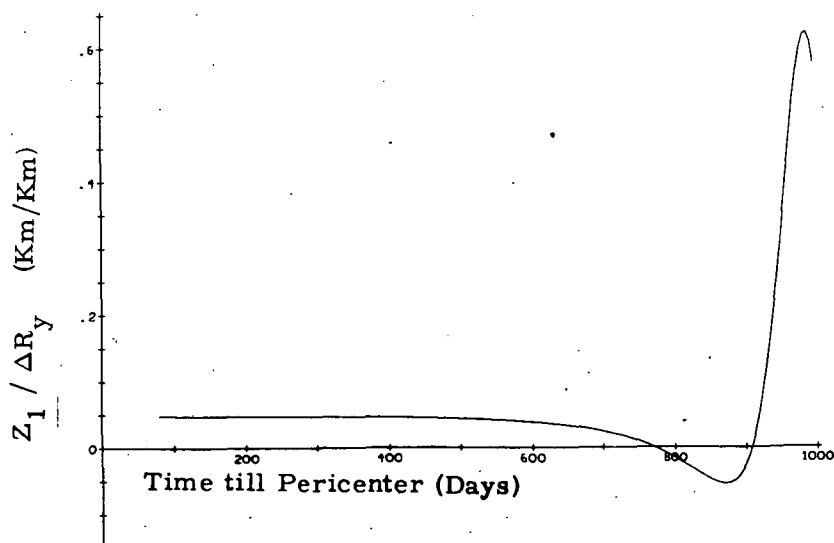


Fig. F.3.3.2 Z_1 Component of Final Position per Y Component of Excess Position
Interplanetary Leg-Saturn Mission

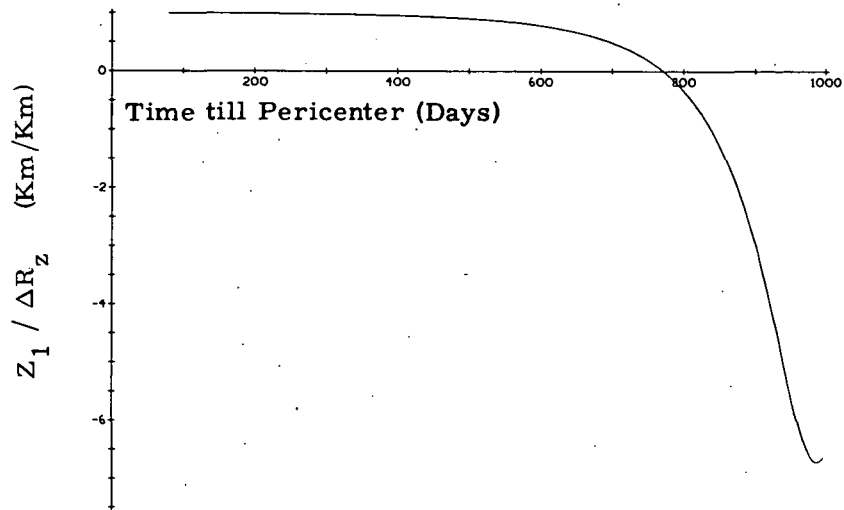


Fig. F. 3. 3. 3 Z_1 Component of Final Position per Z Component of Excess Position
Interplanetary Leg-Saturn Mission

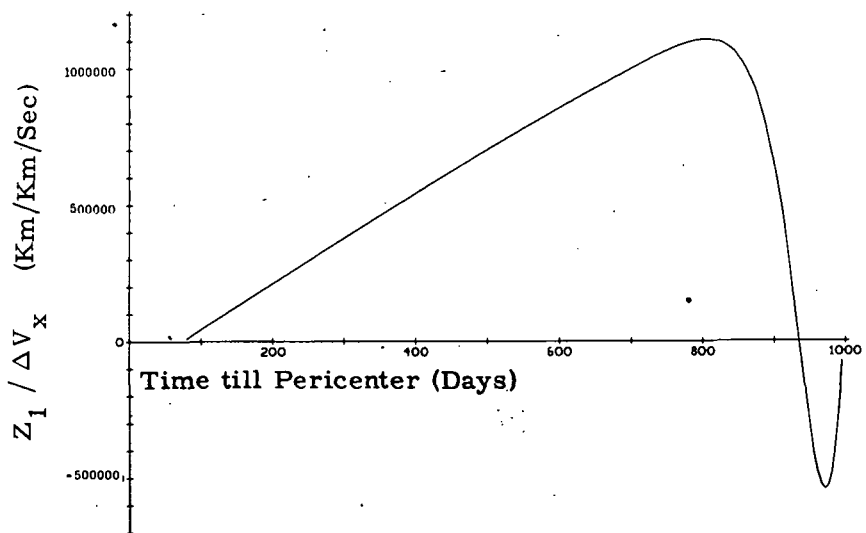


Fig. F. 3. 3. 4 Z_1 Component of Final Position per X Component of Excess Velocity
Interplanetary Leg-Saturn Mission

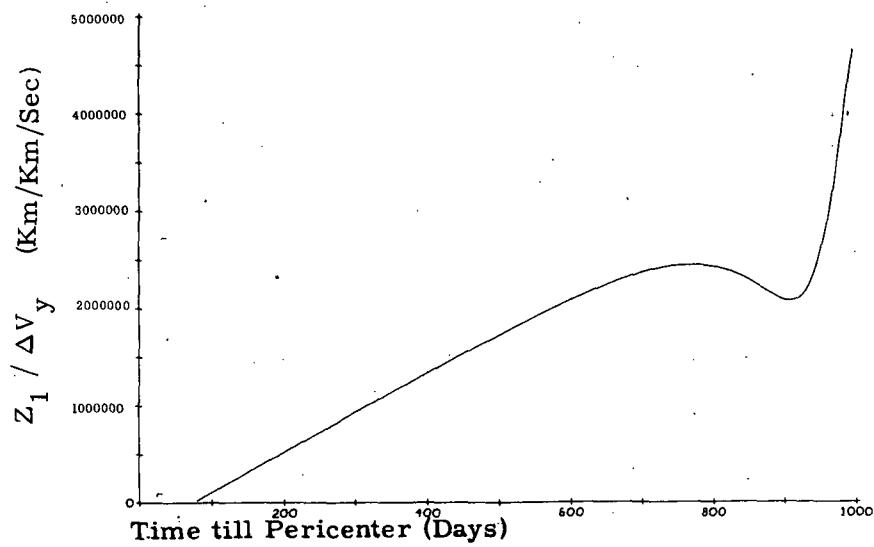


Fig. F. 3. 3. 5 Z_1 Component of Final Position per Y Component of Excess Velocity
Interplanetary Leg-Saturn Mission

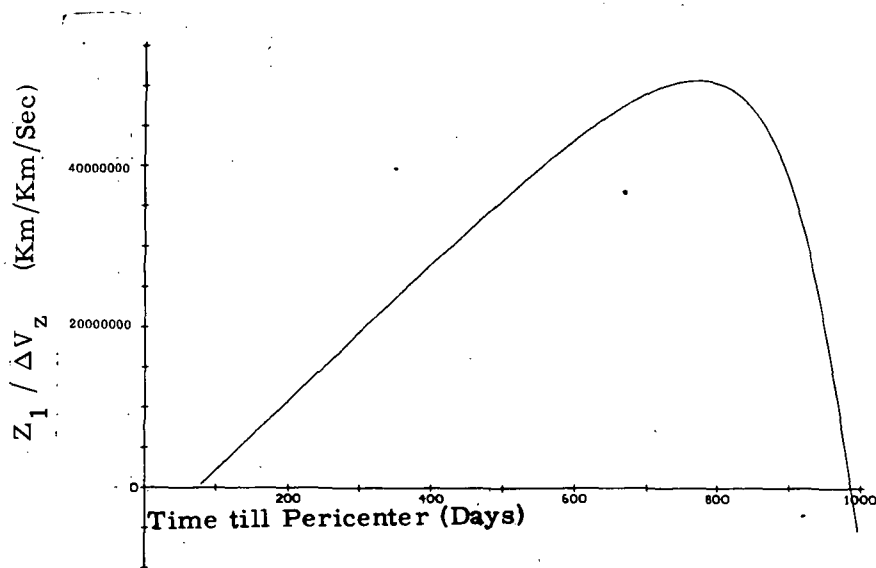


Fig. F. 3. 3. 6 Z_1 Component of Final Position per Z Component of Excess Velocity
Interplanetary Leg-Saturn Mission

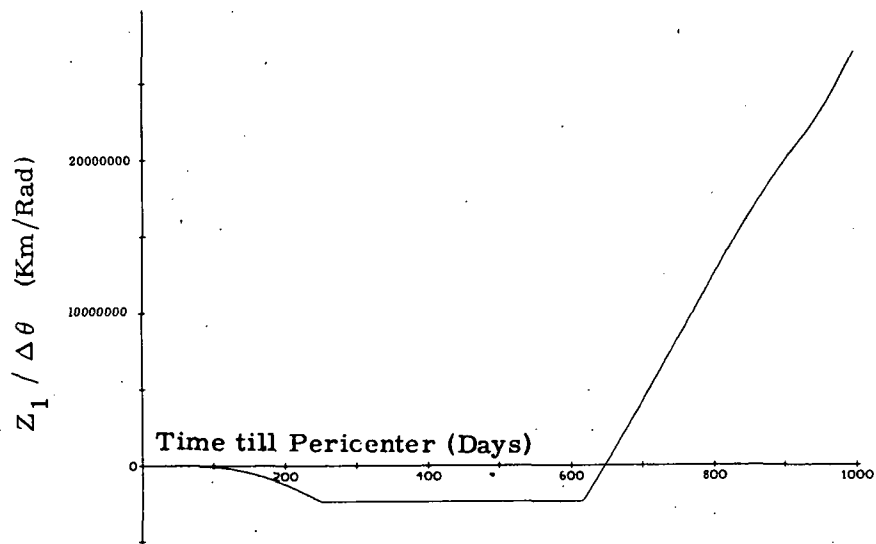


Fig. F. 3. 3. 7 Z_1 Component of Final Position per Excess Control Angle θ
Interplanetary Leg-Saturn Mission

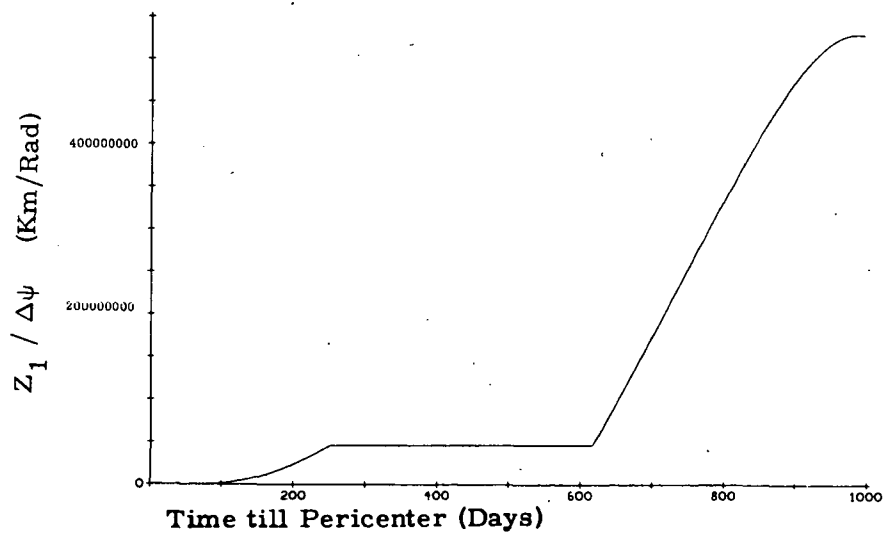


Fig. F. 3. 3. 8 Z_1 Component of Final Position per Excess Control Angle ψ
Interplanetary Leg-Saturn Mission

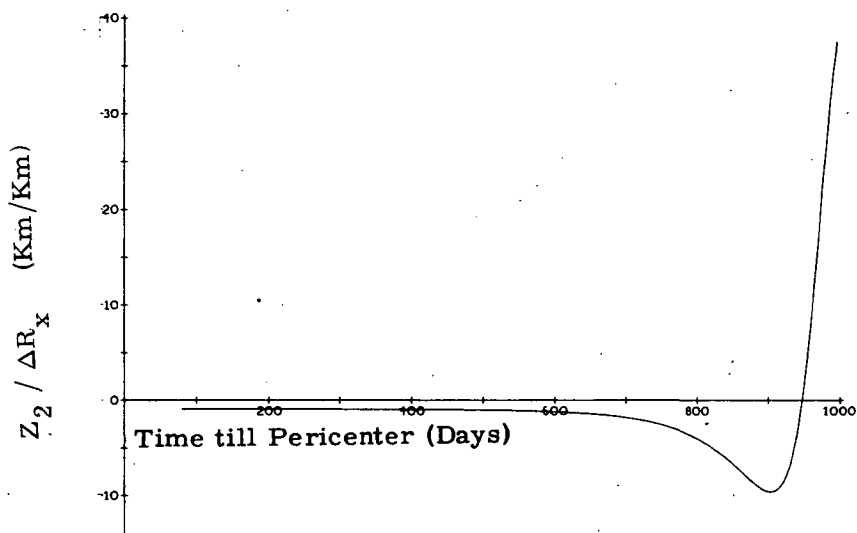


Fig. F. 3. 4. 1 Z_2 Component of Final Velocity per X Component of Excess Position
Interplanetary Leg-Saturn Mission

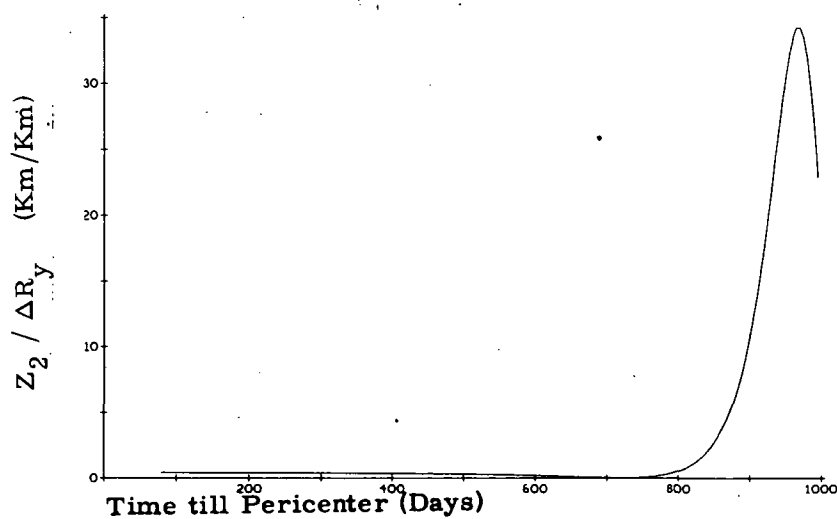


Fig. F. 3. 4. 2 Z_2 Component of Final Position per Y Component of Excess Position
Interplanetary Leg-Saturn Mission

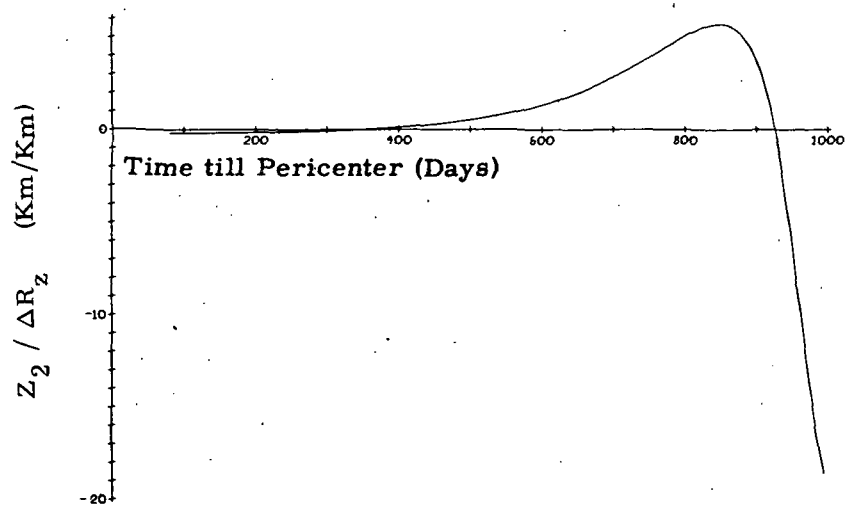


Fig. F. 3. 4. 3 Z_2 Component of Final Position per Z Component of Excess Position
Interplanetary Leg-Saturn Mission

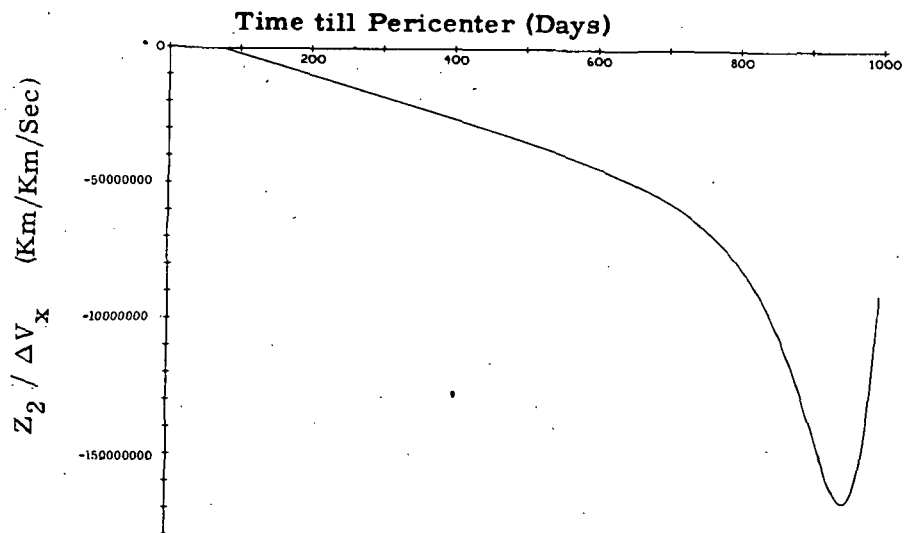


Fig. F. 3. 4. 4 Z_2 Component of Final Position per X Component of Excess Velocity
Interplanetary Leg-Saturn Mission

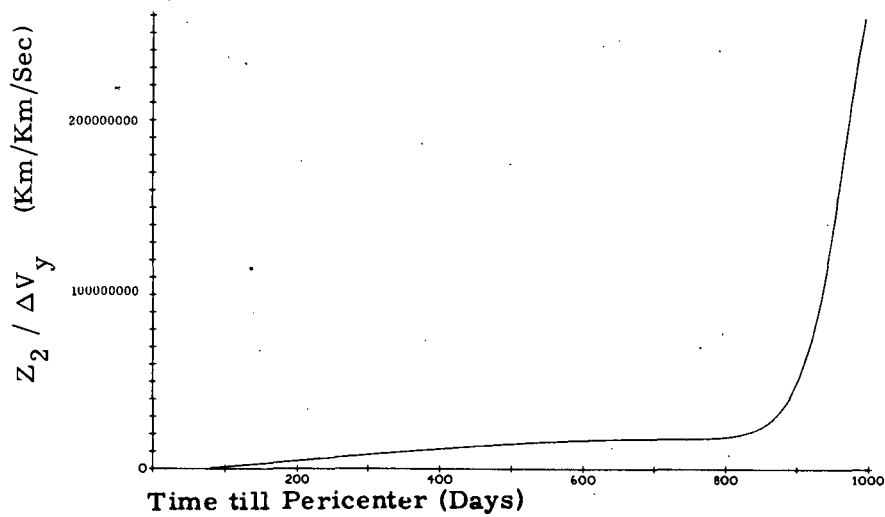


Fig. F. 3. 4. 5 Z_2 Component of Final Position per Y Component of Excess Velocity
Interplanetary Leg-Saturn Mission

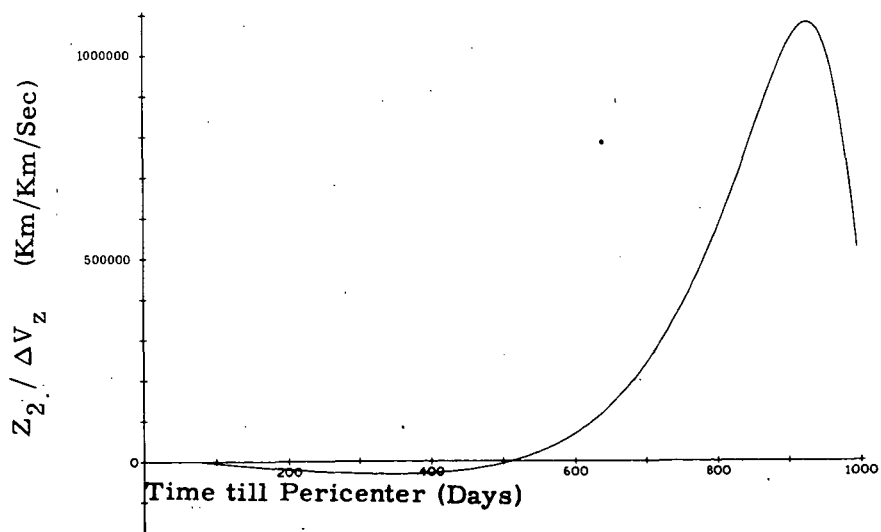


Fig. F. 3. 4. 6 Z_2 Component of Final Position per Z Component of Excess Velocity
Interplanetary Leg-Saturn Mission

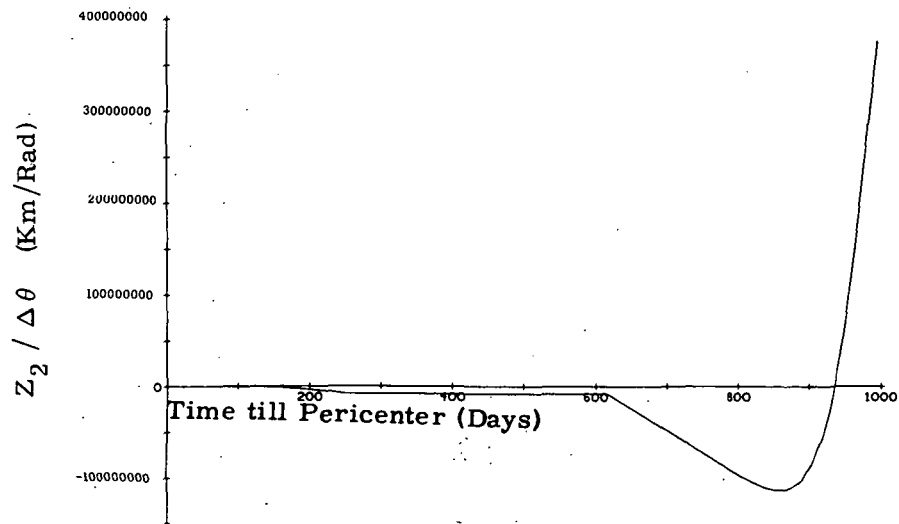


Fig. F.3.4.7 Z_2 Component of Final Position per Excess Control Angle ψ
Interplanetary Leg-Saturn Mission

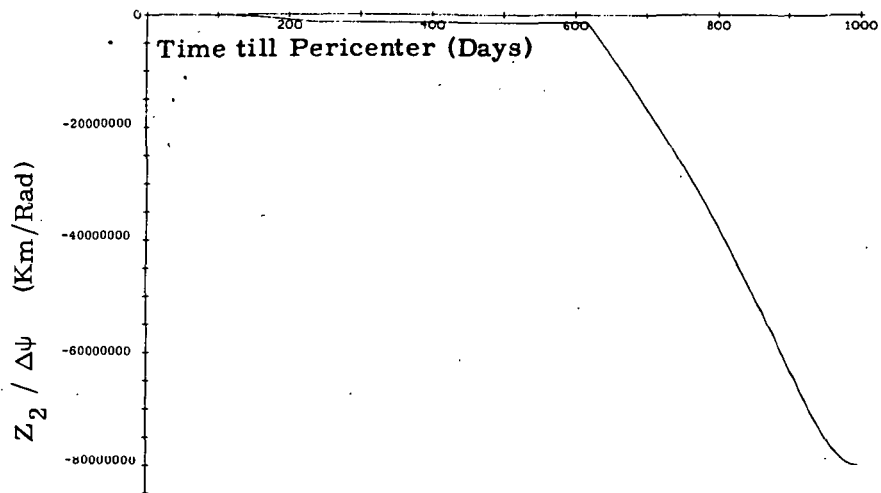


Fig. F.3.4.8 Z_2 Component of Final Position per Excess Control Angle ψ
Interplanetary Leg-Saturn Mission

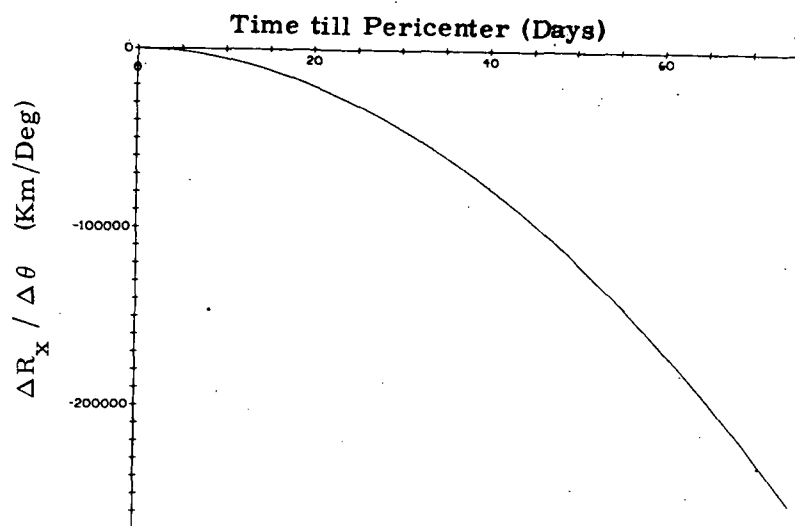


Fig. F. 4. 1. 1 X Component of Position Deviation per Unit Control Angle θ Deviation
Near Planet Leg-Saturn Mission

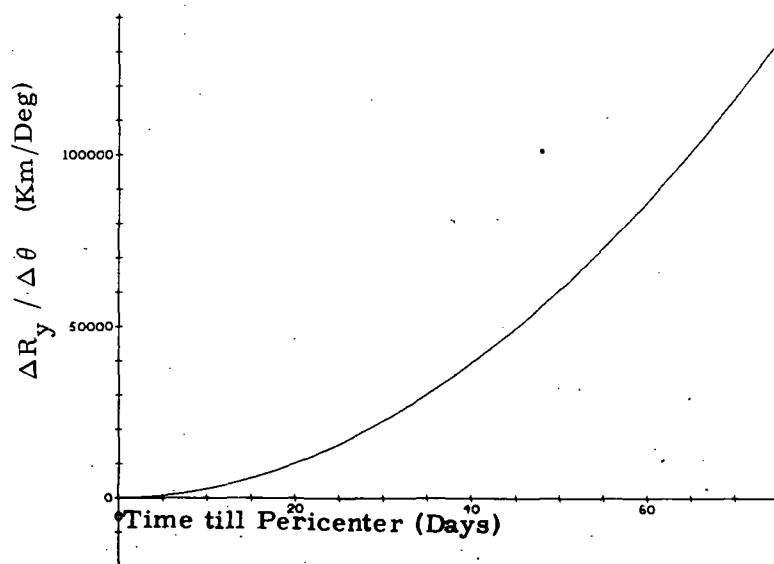


Fig. F. 4. 1. 2 Y Component of Position Deviation per Unit Control Angle θ Deviation
Near Planet Leg-Saturn Mission

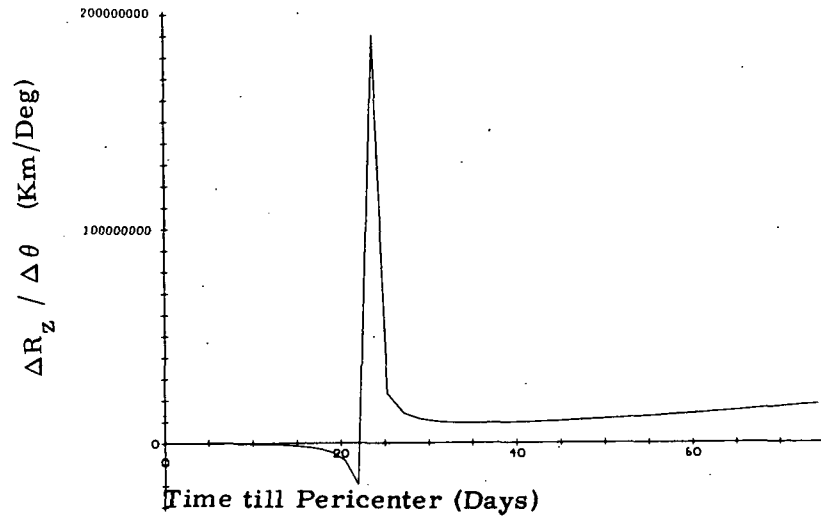


Fig. F. 4. 1. 3 Z Component of Position Deviation per Unit Control Angle θ Deviation
Near Planet Leg-Saturn Mission

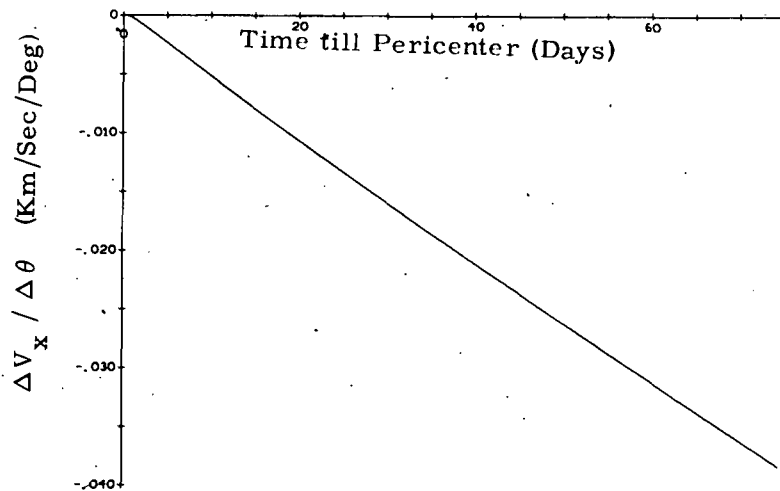


Fig. F. 4. 1. 4 X Component of Velocity Deviation per Unit Control Angle θ Deviation
Near Planet Leg-Saturn Mission

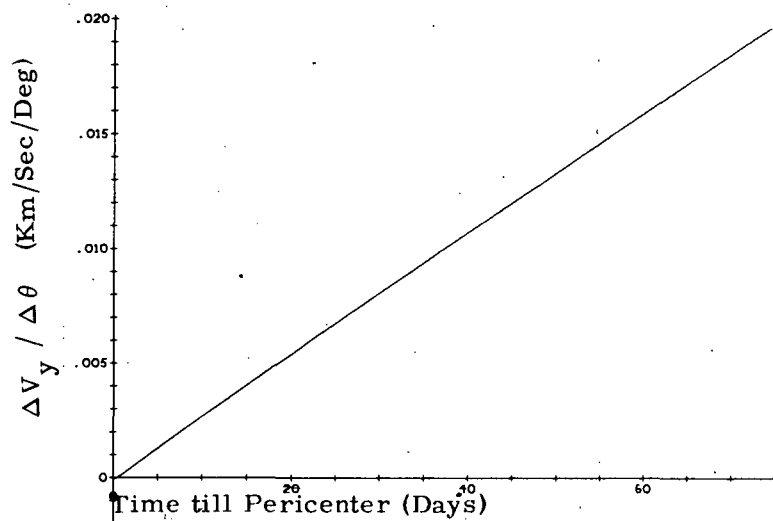


Fig. F. 4. 1. 5 Y Component of Velocity Deviation per Unit Control Angle θ Deviation Near Planet Leg-Saturn Mission

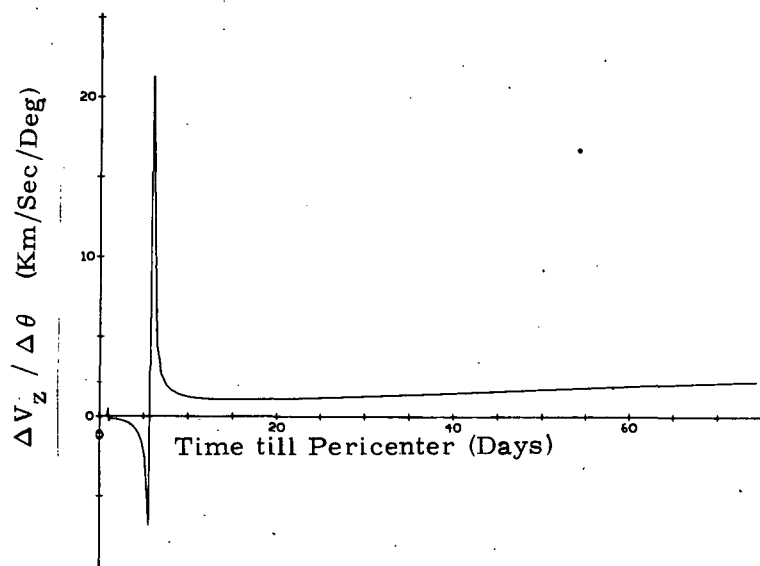


Fig. F. 4. 1. 6 Z Component of Velocity Deviation per Unit Control Angle θ Deviation Near Planet Leg-Saturn Mission

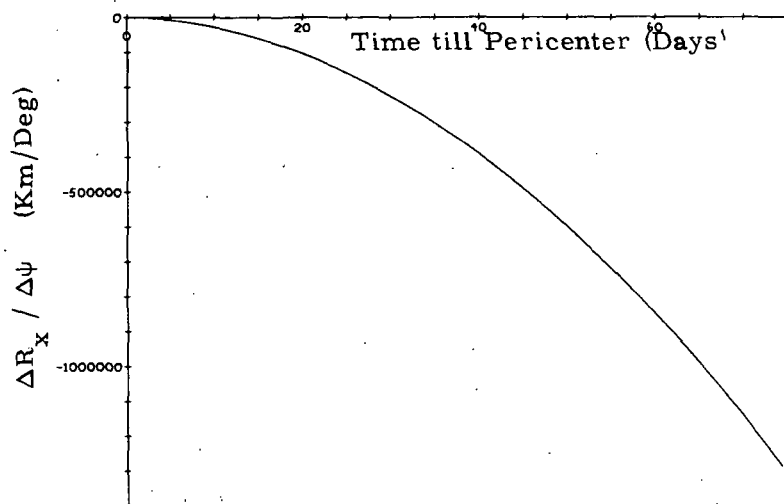


Fig. F. 4. 2. 1 X Component of Position Deviation per Unit Control Angle ψ Deviation Near Planet Leg-Saturn Mission

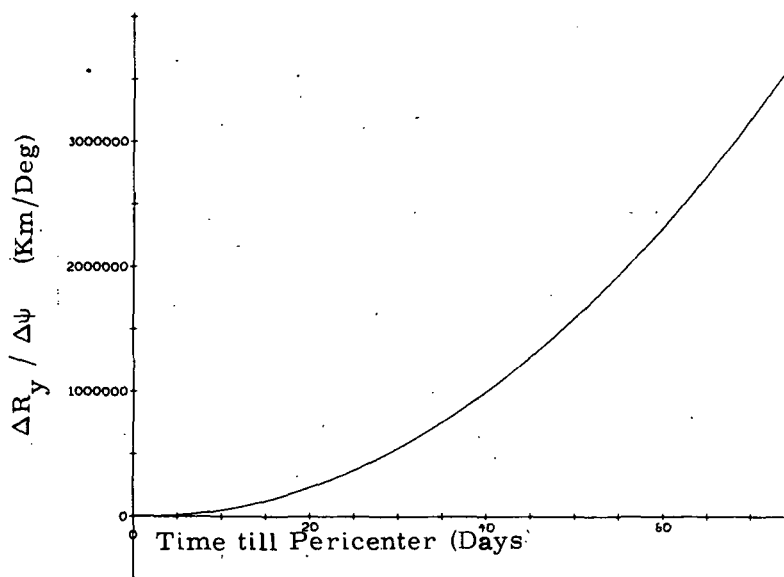


Fig. F. 4. 2. 2 Y Component of Position Deviation per Unit Control Angle ψ Deviation Near Planet Leg-Saturn Mission

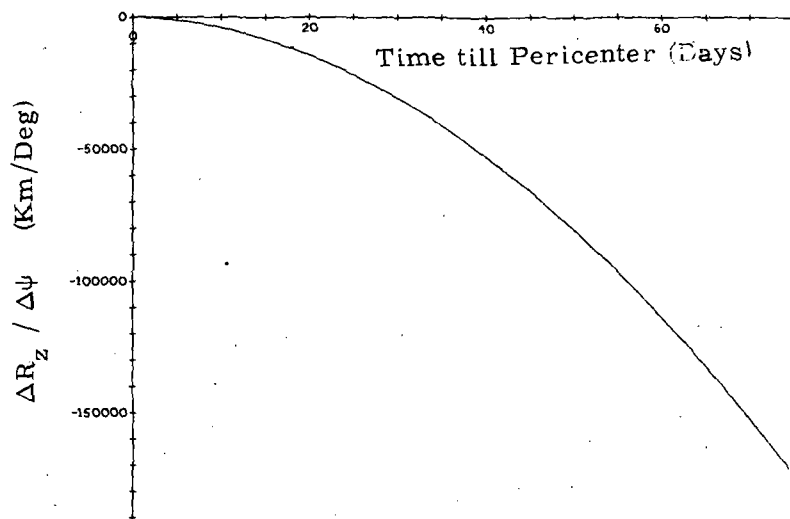


Fig. F. 4. 2. 3 Z Component of Position Deviation per Unit Control Angle ψ Deviation
Near Planet Leg-Saturn Mission

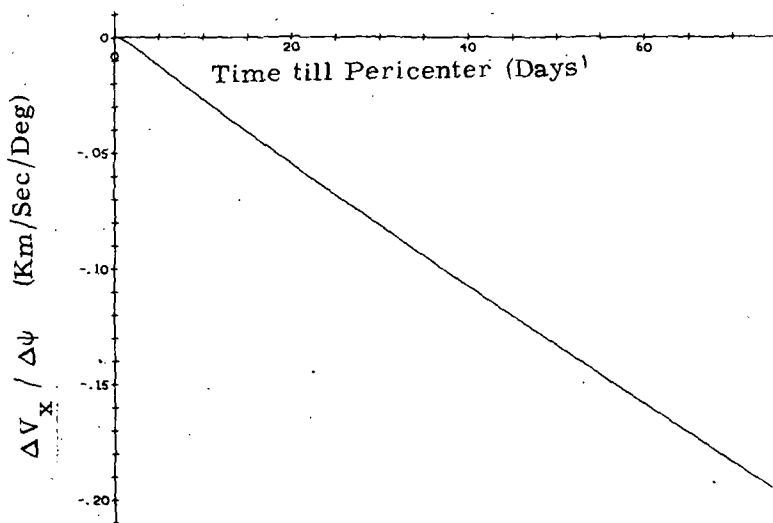


Fig. F. 4. 2. 4 X Component of Velocity Deviation per Unit Control Angle ψ Deviation
Near Planet Leg-Saturn Mission

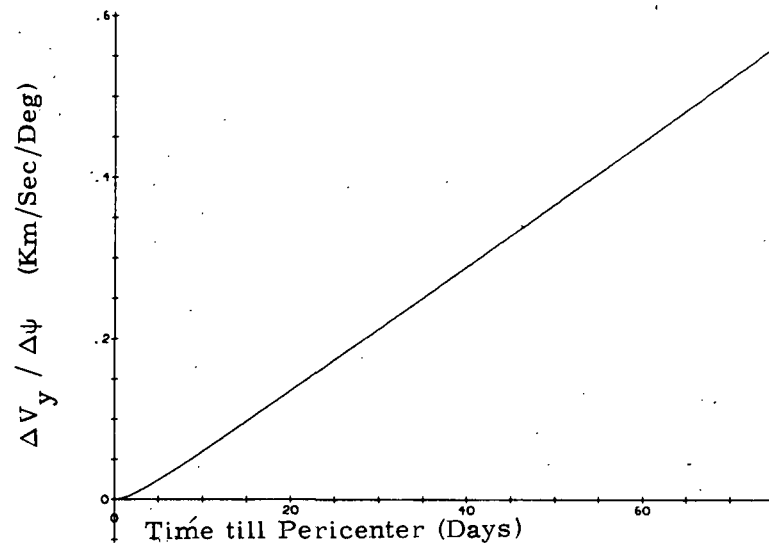


Fig. F. 4. 2. 5 Y Component of Velocity Deviation per Unit Control Angle ψ Deviation Near Planet Leg-Saturn Mission

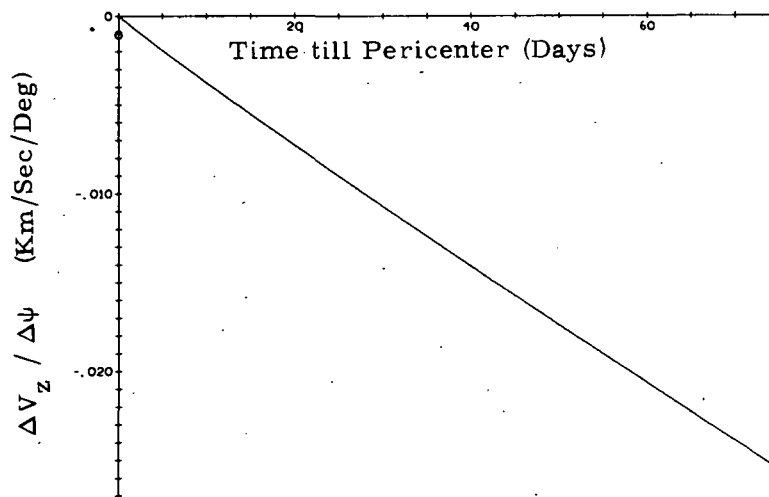


Fig. F. 4. 2. 6 Z Component of Velocity Deviation per Unit Control Angle ψ Deviation Near Planet Leg-Saturn Mission

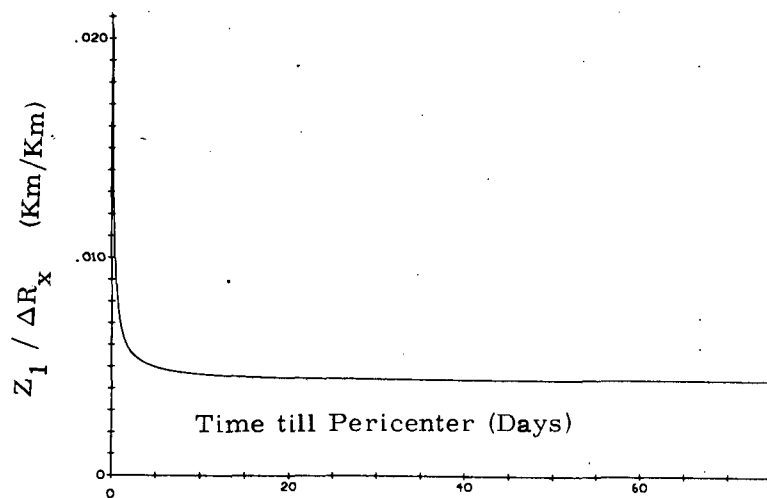


Fig. F. 4. 3. 1 Z_1 Component of Final Position per X Component of Excess Position
Near Planet Leg-Saturn Mission

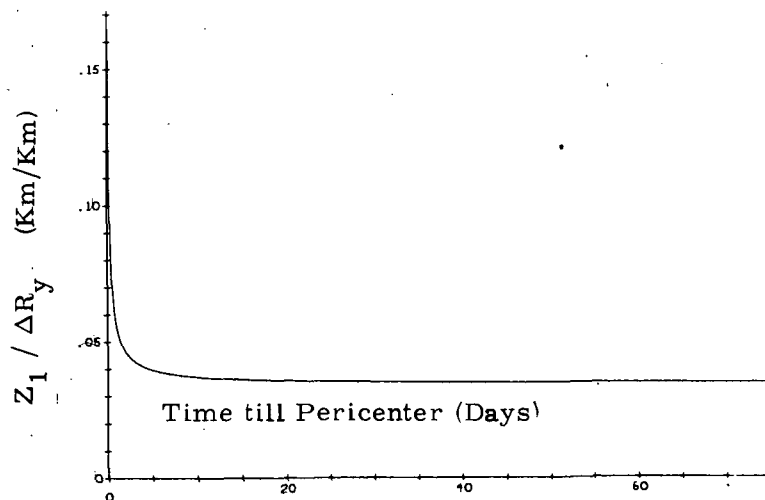


Fig. F. 4. 3. 2 Z_1 Component of Final Position per Y Component of Excess Position
Near Planet Leg-Saturn Mission

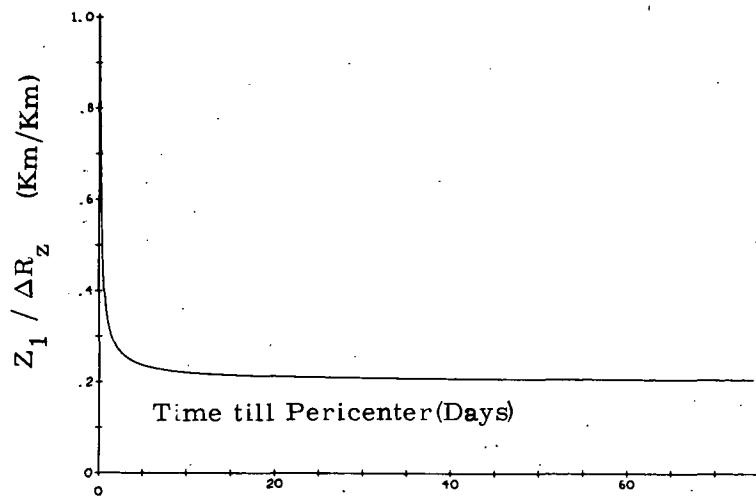


Fig. F.4.3.3 Z_1 Component of Final Position per Z Component of Excess Position Near Planet Leg-Saturn Mission

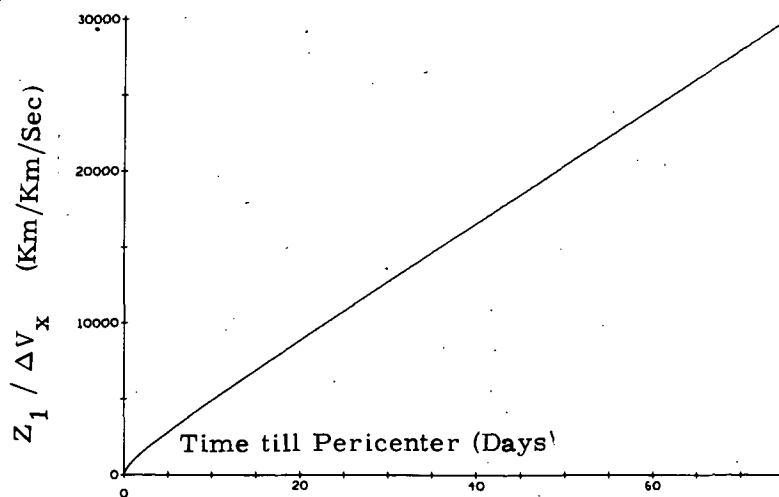


Fig. F.4.3.4 Z_1 Component of Final Position per X Component of Excess Velocity Near Planet Leg-Saturn Mission

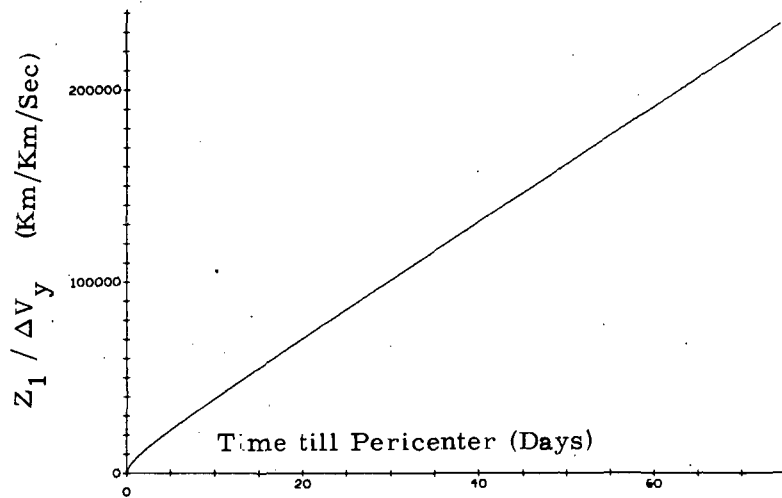


Fig. F. 4. 3. 5 Z_1 Component of Final Position per Y Component of Excess Velocity
Near Planet Leg-Saturn Mission

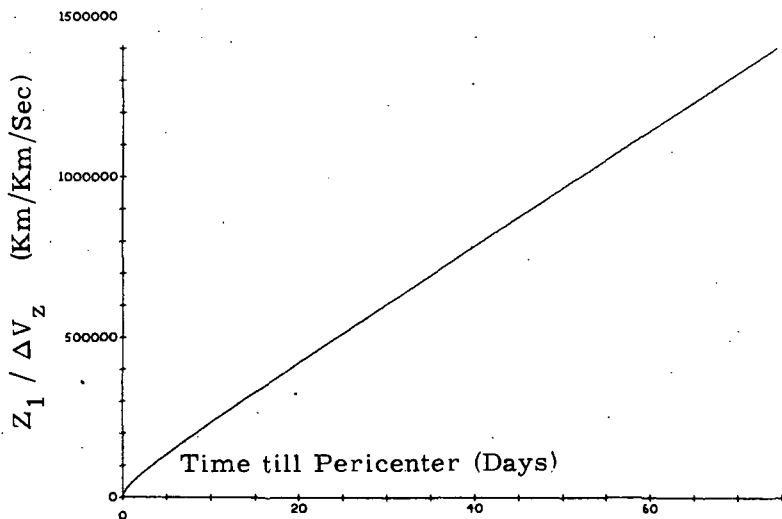


Fig. F. 4. 3. 6 Z_1 Component of Final Position per Z Component of Excess Velocity
Near Planet Leg-Saturn Mission

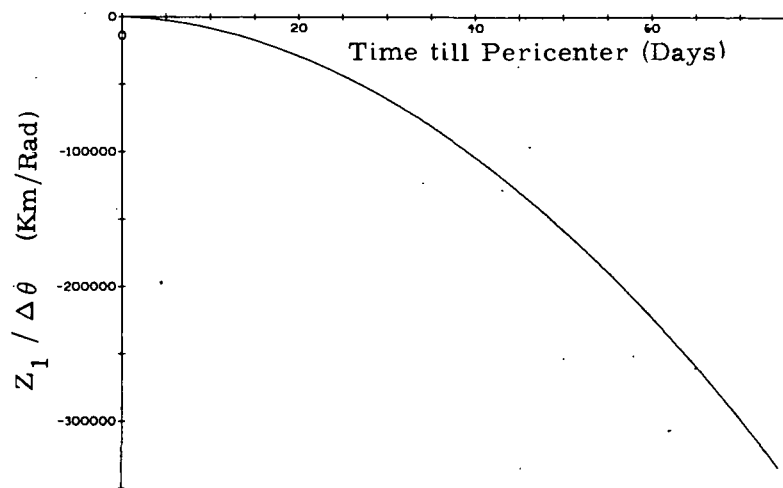


Fig. F. 4. 3. 7 Z_1 Component of Final Position per Excess Control Angle θ
Near Planet Leg-Saturn Mission

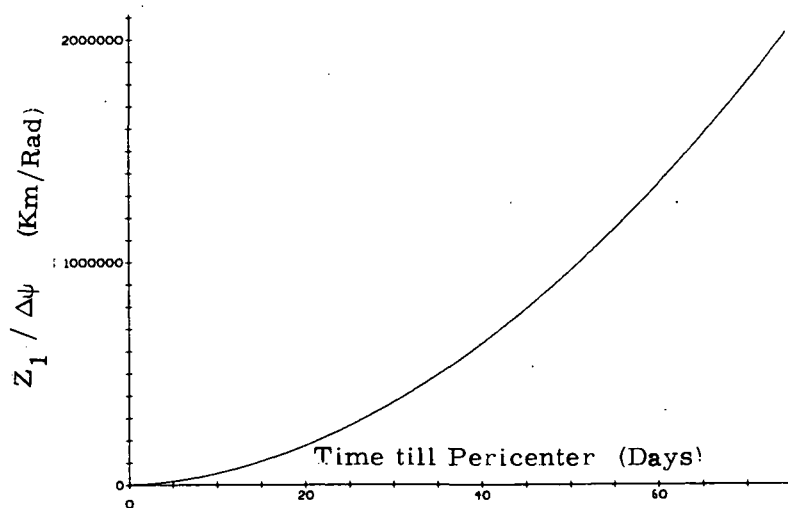


Fig. F. 4. 3. 8 Z_1 Component of Final Position per Excess Control Angle ψ
Near Planet Leg-Saturn Mission

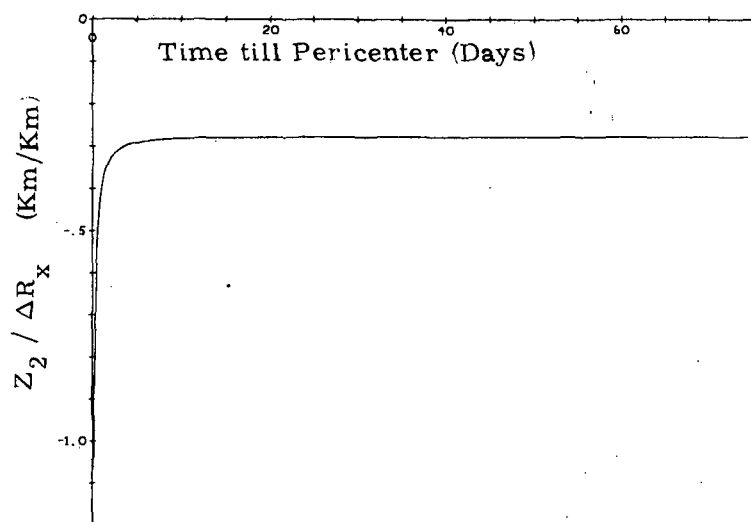


Fig. F. 4. 4. 1 Z_2 Component of Final Position per X Component of Excess Position
Near Planet Leg-Saturn Mission

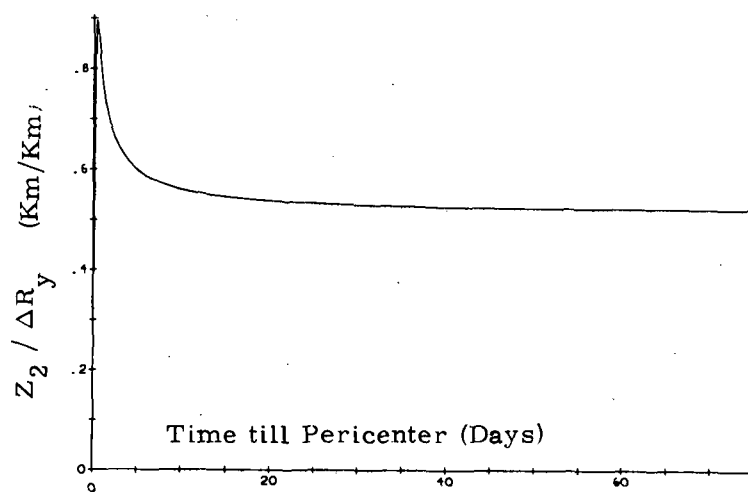


Fig. F. 4. 4. 2 Z_2 Component of Final Position per Y Component of Excess Position
Near Planet Leg-Saturn Mission

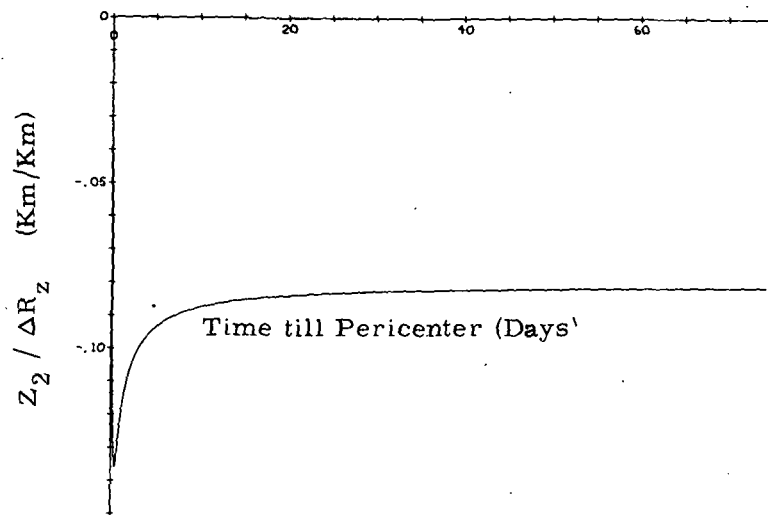


Fig. F. 4. 4. 3 Z_2 Component of Final Position per Z Component of Excess Position
Near Planet Leg-Saturn Mission

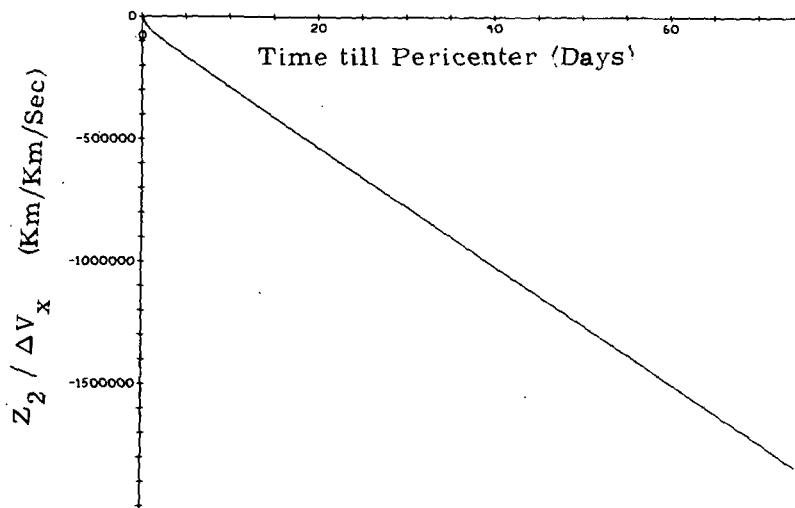


Fig. F. 4. 4. 4 Z_2 Component of Final Position per X Component of Excess Velocity
Near Planet Leg-Saturn Mission

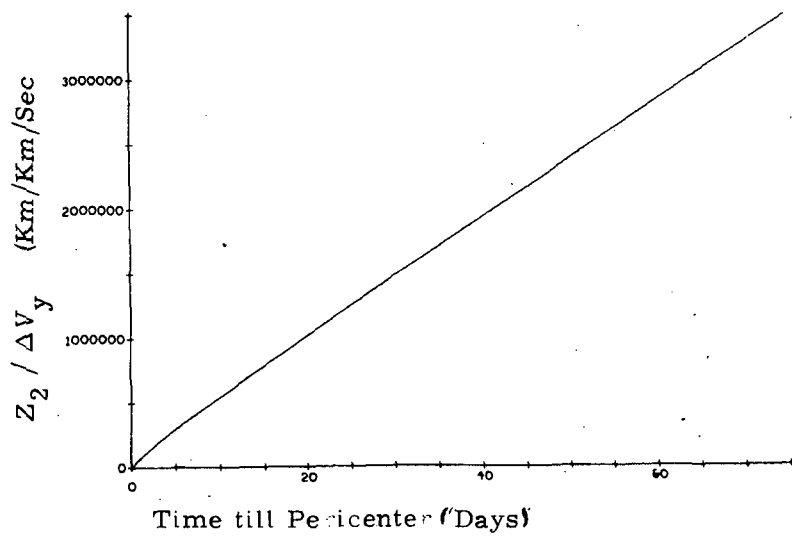


Fig. F. 4. 4. 5 Z_2 Component of Final Position per Y Component of Excess Velocity
Near Planet Leg-Saturn Mission

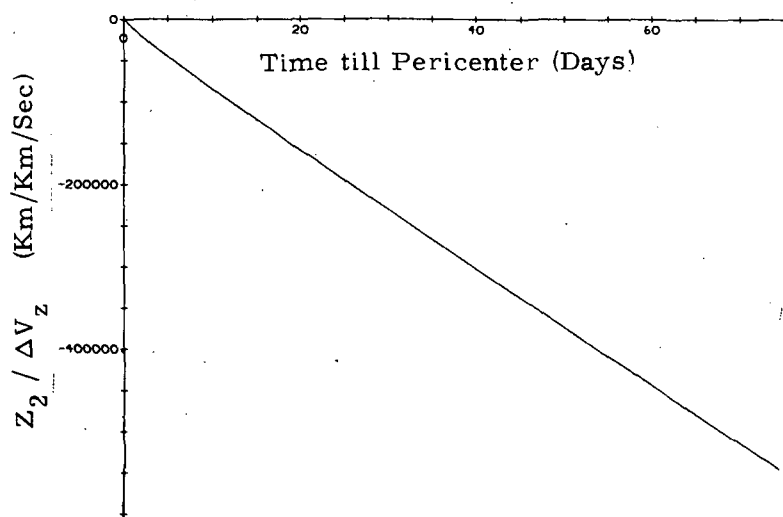


Fig. F. 4. 4. 6 Z_2 Component of Final Position per Z Component of Excess Velocity
Near Planet Leg-Saturn Mission

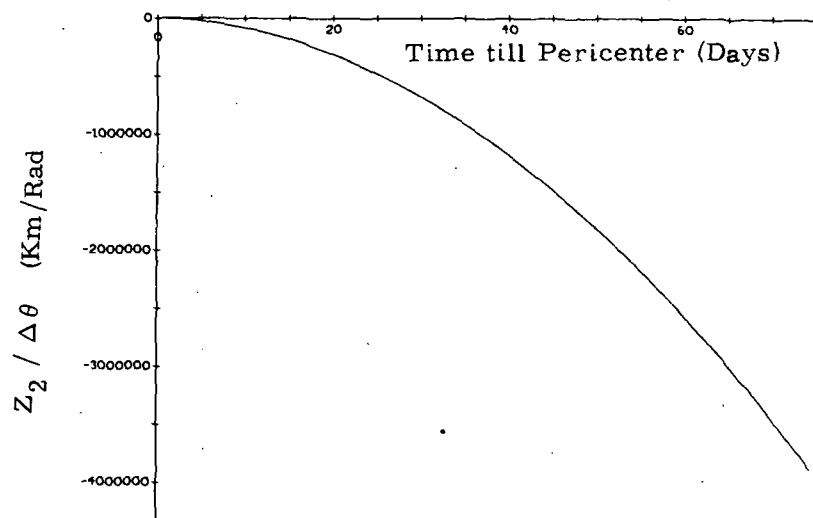


Fig. F. 4. 4. 7 Z_2 Component of Final Position per Excess Control Angle θ
Near Planet Leg-Saturn Mission

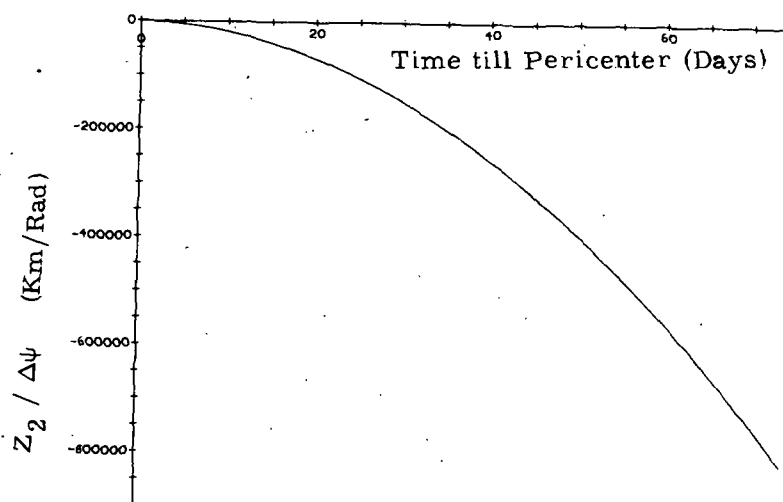


Fig. F. 4. 4. 8 Z_2 Component of Final Position per Excess Control Angle ψ
Near Planet Leg-Saturn Mission

Page intentionally left blank

APPENDIX G

ONBOARD SYSTEMS CONFIGURATIONS

G.1 Navigation Sensor, Weight, Power, and Volume

Most of the mass of a scanning photometer would be composed of beryllium, with the exception of the servomotors, electronics and drive gears. The mirrors would be of beryllium as would the structure for precision angle encoder mounting. Estimated total weight of the navigation sensor is shown in Fig. G.1 as a function of aperture area. The dependence is approximately linear for larger areas, and reduces to angle encoder, servomotor, and electronics weight for small apertures. It is assumed that the angle encoder is a $\pm 5''$ device which is 9 cm in diameter, and is built of beryllium.

The weights estimated here are considerably lower than those presented in Volume II, and this is because the Volume II weights were taken to be the maximum possible in order to demonstrate onboard navigation system generated fuel and weight savings for the worst case. The weights listed here are closer to expected actual weight.

Weight breakdown and power requirements for the single degree of freedom sensor with 100 cm^2 aperture are shown in Table G.1.

Table G.1

Weight Breakdown and Power Requirements for Single Degree of Freedom Scanning Photometer

Telescope Barrel	0.5 kg
Mirrors and Supports	0.5 kg

Supporting Structure	1.0 kg
Angle Encoder Body	0.25 kg
Servo Motor and Gears	0.25 kg
Electronics	0.5 kg
Power Requirement (including servomotor)	9 watts

The addition of two more degrees of freedom would add about 1 kg. If the navigation system includes a computer, 10 kg should be added.

G.2 Low Thrust Accelerometers

Currently under development are a number of accelerometers that will, or could have the capability to sense accelerations at and below the 10^{-8} to 10^{-9} g range. At these levels, considered a minimal requirement for usefulness for these ion thrusted missions, thrust accelerations could be sensed with one percent or better accuracy, and thrust vectoring could be sensed with one arc minute or better accuracy (given a comparably accurate attitude control system). The accelerometers, which will be described individually below, have not been developed specifically for this type of mission, and some could be improved considerably if they were to be recast in light of the expected sensitivity and dynamic range requirements.

As a group, the accelerometers suitable in projection for these missions have a number of common characteristics. Bias and scale factor errors are temperature dependent at a level of about 10^{-6} g/ $^{\circ}$ F and 10^{-6} g/g/ $^{\circ}$ F respectively. This implies that to sense accelerations accurately in the area of say 10^{-10} g's it will be necessary (unless the bias scales with maximum measurable input) to maintain thermal control between the time of bias calibration and acceleration measurement to within 10^{-4} $^{\circ}$ F. What is important is not absolute temperature accuracy, but having enough thermal heat capacity with respect to the flow rates in and out of the heating system to maintain temperature stability for sufficient time. Another characteristic common to the accelerometers is a drifting bias error that

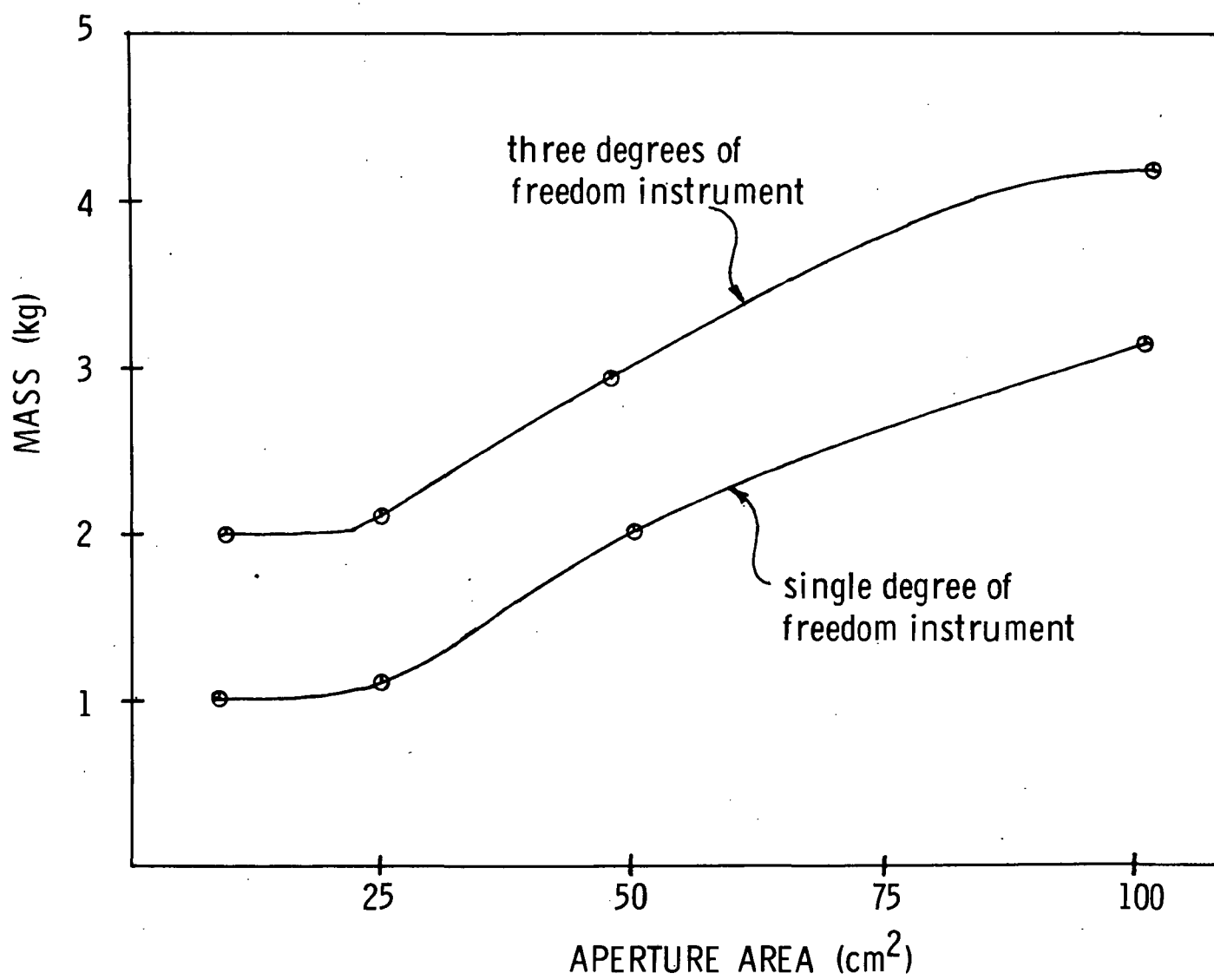


Fig. G.1 Navigation Sensor Weight Instrument

is a time dependent result of various electro-mechanical factors specific to each different mechanization. In the pendulus type accelerometer it results from changes in magnetic permeability of the float, and in the vibrating string it is related to aging of the "string". Regardless of the source of the bias, it is sufficiently large ($10^{-6}g$) that it must be calibrated shortly before making each thrust measurement. The exact meaning of "shortly" depends on bias stability. For example, in one experiment with the vibrating string accelerometer in a 1g environment, a bias drift of $1 \times 10^{-6}g/\text{deg}$ was found.⁷ Assuming linearity of drift for small times, the bias value of $10^{-10}g$ would occur just 9 seconds after calibration for that particular instrument. To function over a large dynamic range, these accelerometers are designed to work over a small displacement from the null position, and, except for the vibrating string, are nulled with a series of force pulses which allow the dynamic range requirements to be met. For the ion thrust missions the dynamic range requirements may be lower, and therefore it is not known presently whether the formerly used pulsing techniques are the optimal solution. Some arrangement may be desired for making bias calibrations during the 1/3 second thrust interruptions caused by high voltage arcing. This would avoid the need for planned thruster shutdown for calibration purposes. However the arcing may cause electronic disturbances in the accelerometer through transients or electromagnetic pulse which are severe enough to preclude calibration during this period.

Size, weight, and power requirements for this accelerometer group are of the same order of magnitude as is shown in Table G.2, and so are the characteristic errors. They differ mainly with regard to mechanization. The pulsed integrating gyroscopic and the vibrating string devices have actively moving mechanical parts. They are therefore mechanically slightly more complex, however each accelerometer type has several parts that present extensive design and precision fabrication problems.

In the area of operational experience, the vibrating string has been tested extensively on surface gravity measurements down to $10^{-9}g$ ⁸ the pulsed

Table G. 2

Accelerometer Weight, Power, Volume

	Weight	Power [*]	Volume
PIPA	0.5 kg	4.7 watts	200 cm ²
V.S.	2.5 kg	10 watts	1200 cm ²
MESA	1 kg	3 watts	800 cm ²

* does not include heater power which depends upon environment. At room temperature with the accelerometer at 140°F, approximately 1/2 watt is required for heating.

integrating pendulum has had extensive, successful, operational use on Apollo flights; and the electrostatic suspension device is currently being space tested on the ion thrusted SERT II vehicle, and has been specifically developed for low thrust applications.

The possible merits of assembling and checking out these spacecraft on a space station have been occasionally questioned. For the low thrust accelerometers this procedure would have the advantages of allowing for a study of bias drift in a zero g environment, and for the avoidance of misalignment errors between accelerometer and optical attitude sensors caused by launch stresses. However, a new technique would have to be devised for aligning attitude sensors and accelerometers in the absence of a well determined g vector.

The Vibrating String Accelerometer⁹ measures the frequency difference between a pair of matched natural frequency vibrating strings that are coupled through a pair of identical suspended inertial masses. This frequency difference is then converted to acceleration via the instrument scale factor. An early version of the vibrating string accelerometer (D4E) has been tested by Ed Spitzer of NASA ERC. He was able to obtain a sensitivity of about 10^{-6} g which was determined mainly by an apparent temperature sensitivity of 5 ppm/°F. It was observed that there was a

tendency for the two strings to synchronize at very small frequency differences which could lead to problems at very small acceleration levels. Bias error was found to increase with temperature while the scale factor decreased. By carefully controlling the temperature environment, Charles Wing of the M.I.T. geology department has been able to measure changes in gravitational force with the D4E vibrating string to within an error of $5 \times 10^{-9} g$. He has been operating the device at $70^{\circ}F$ inside a double walled, thermister controlled oven, which maintains the temperature to within $10^{-40} F$. Temperature control to this precision requires the use of specially selected and aged thermistors. At the $5 \times 10^{-9} g$ level, and with temperature controlled to within 10^{-4} deg, bias errors due to mechanical aging are predominant. In a new D4E one observes about $10^{-6} g/day$ change in the bias level. Wing observed a tendency for the strings to synchronize under zero g conditions along the input axis. One of the D4E's has been operating for two years, and to date string breakage has not occurred. The vibrating string electronics has been designed for automatic bias calibration.¹⁰ It appears to have a linear bias drift for small time intervals so that the bias drift is predictable accordingly. The main problems seem to be a high bias temperature sensitivity, and a lack of space testing.

The Miniature Electrostatic Accelerometer (MESA) has an electrostatically suspended float and electrostatic pulse rebalancing. It has been designed specifically for low g applications,¹¹ and is currently being space tested on an ion engine thrusted vehicle.¹² Dynamic range is designed to be 10^6 , with the upper limit set at $10^{-4} g$ for the current SERT II mission. Maximum measurable input is $1g$, and the upper limit is adjustable down to a desiderative $10^{-6} g$. Measurement accuracy is designed to be 0.1% of the reading value, however the SERT II results are showing 1%. The null bias is designed to scale (including temperature biasing) as 10^{-6} times the maximum input setting. On the SERT II mission with a max. reading setting of $10^{-4} g$ one would expect a $10^{-10} g$ null bias, however the results show more like $10^{-9} g$, and this may be an indication that bias is not easily scaled away at the ultra low g levels.

On the current SERT II mission, the MESA was turned on several days before the thrusters. It failed to work at first, then gave 4 days of good output measuring gravity gradient forces at about $0.75 \times 10^{-6} g.p$ after

the thrusters were turned on the MESA continued to function for 1 day, then began to give spurious output which has continued as of 4/13/70. Cause of the malfunction is currently unknown, but ion engine arcing is suspected to have generated damaging transients.

The Pulsed Integrating Gyroscopic Accelerometer, (PIGA) determines acceleration by counting the number of torque pulses required to null the torque resulting from rotating a gyro wheel axis about a line in the gyro wheel plane. The rotation is induced by acceleration forces which rotate an unbalanced mass to which the gyro is fixed. Capability for this device by mid 1970 is expected to be 5×10^{-7} g of bias stability, and 2×10^{-7} g of scale factor stability, and resolution. The instrument will be designed for 100,000 hour life. Operating temperature will be in the $125^{\circ} - 140^{\circ}$ Fahrenheit range, with about 1×10^{-6} g error caused by a 1°F temperature change. The long term design goal for scale factor for this device is $10^{-8} - 10^{-9}$ g by 1972.

The Pulsed Integrating Pendulous Accelerometer, (PIPA) determines acceleration by counting the number of pulses needed to torque the pendulum back to its null position. This is done via electromagnetic induction. Present capability for this device is about 10^{-6} g scale factor and sensitivity. One of the main problems with this device is the change of permeability effect which results from large float excursions. This could be combatted by redesigning the accelerometer so that it is restricted to a small dynamic range, hence to small excursions. The larger g forces present during launch would be measured by a separate instrument. It has been estimated that with a restricted dynamic range the PIPA could be designed to sense $10^{-8} - 10^{-9}$ g without a major redesign effort. No program to develop the PIP accelerometer for these small accelerations has been funded at the MIT Draper Laboratory. Thermal sensitivity for the PIPA is currently 10^{-6} g/ $^{\circ}\text{F}$. Operating temperature is around 140°F .

The weight, power and volume values shown in Table G.2 are of specific designs and are not optimized for these missions. All are capable of being reduced by redesign and should therefore be taken only as an indication of the order of these quantities.

G.3 Thrust Vector Misalignment

There are a number of misalignment possibilities occurring in the various combinations of thrust vector, accelerometer, spacecraft, attitude sensors, and celestial references. Two types of thrust vector misalignments are important to the system design and guidance capability, namely misalignment of the vector with respect to the vehicle inertial centroid, and misalignment of the thrust vector with respect to inertial space. Misalignment with respect to the vehicular inertial centroid results in a torque which probably cannot be tolerated for burn times lasting years. It has been estimated that the uncertainty in thrust vectoring for an ion engine freshly assembled and mounted is of the order of a couple of degrees.¹³ For a misalignment of this magnitude it is interesting to see what attitude control system jet requirements would be to maintain attitude for a Jupiter mission. The torque is of course dependent on engine-inertial centroid distance, and if this distance could be reduced to zero the problem could be transformed into a different misalignment problem. If one assumes a 1 meter separation between thruster and inertial centroid on a 700 kg spacecraft, with 2° misalignment and .081 newton thrust (18 millipounds), then the torque is 0.0027 newton meters. Over the thrust time of a Jupiter mission (about 3×10^7 seconds) the total rotational impulse is 8×10^4 newton meter seconds. This would be 100 times the estimated requirement for a high thrust mission using the TOPS spacecraft configuration.¹⁴ Clearly it will be necessary to reduce this level of gas expenditure by either moving the thruster close to the inertial centroid, or by adding thrust vector control as has been done on the experimental ion engine SERT II mission. Thrust vector control in the sense that the vector passes through the vehicle inertial centroid could be obtained via control moment gyros, while the inertial space pointing was accomplished with reaction wheels or rotation thrusters. However, a more attractive system would result if electrostatic or thermal expansion thrust vectoring were used, coupled directly to the attitude sensor output. This would eliminate the use of gyros and gas jets during the thrust on cruise mode (however these mechanisms would probably still be required during the thrust off period). Pitch, roll, and yaw rates within the attitude sensor deadband would be affected by charging appropriate plates or heating various mounting pads. Expected rotational accelerations are of the order of $0.00018 \text{ deg/sec}^2$ for a spacecraft that:

- a) has a mass of 1000 kg;
- b) is a sphere of uniform density and 2 meter radius;
- c) has thrusters which yield an acceleration of 10^{-5} g;
- d) has thrusters placed 2 meters from inertial centroid.
- e) has thrust vector pointing 1° away from centroid.

with this rotational acceleration level it would take about two minutes to rotate the spacecraft through an angle of about 1° , while a 90° , torqued up and down rotation would take about 14 minutes which is very close to the time required for this rotation using the TOPS proposed reaction wheels.

The second form of thruster misalignment is with respect to celestial coordinates. This error has several sources including star and sun sensor electrical bias and mechanical misalignment with respect to spacecraft mechanical coordinates, thermal bending of the structure, uncertainty in the location of the inertial centroid with respect to the thruster beam center, and structural deformation due to launch stresses. Launch stresses and thermal bending are the major problems here, and could lead to arcminute sized misalignments. A one arcminute misalignment between thrust vector and celestial coordinates over a 400 meter/sec ΔV input lasting 10^7 seconds (first Jupiter burn) produces a 0.5×10^3 km position error. Experience on the Orbiting Astronomical Observatory program¹⁵ showed that misalignments of 2 to 5 arcminutes occurred due to launch stress, and 0.5 to 1.5 arcminute misalignments were the result of thermal strain.

One possible scheme to account for these errors would consist of mounting three orthogonal accelerometers accurately with respect to the star and sun sensors, and carefully aligning these in a lab. Then thrust misalignment with respect to the celestial sensors would be indicated by off axis accelerometer output using the orthogonal axis output ratio to eliminate thrust magnitude uncertainties, and corrections could be made by biasing the attitude sensor output. This would require alignment of the accelerometers with respect to the radiation sensors with arcsecond precision, and it would require extremely sensitive accelerometers. If the nominal thrust is 10^{-5} g's, then a 10^{-8} g accelerometer would sense an "off axis" thrust angle as small as 3.5 arcminutes, but it would take a 10^{-10} g accelerometer to sense arcsecond like thrust misalignments. The DSN alone can drive celestial thrust misalignments down to the few arcminute level. Figure G.2 shows the various alignment capabilities in relation to accelerometer sensitivity based upon a 10^{-5} g thrust acceleration.

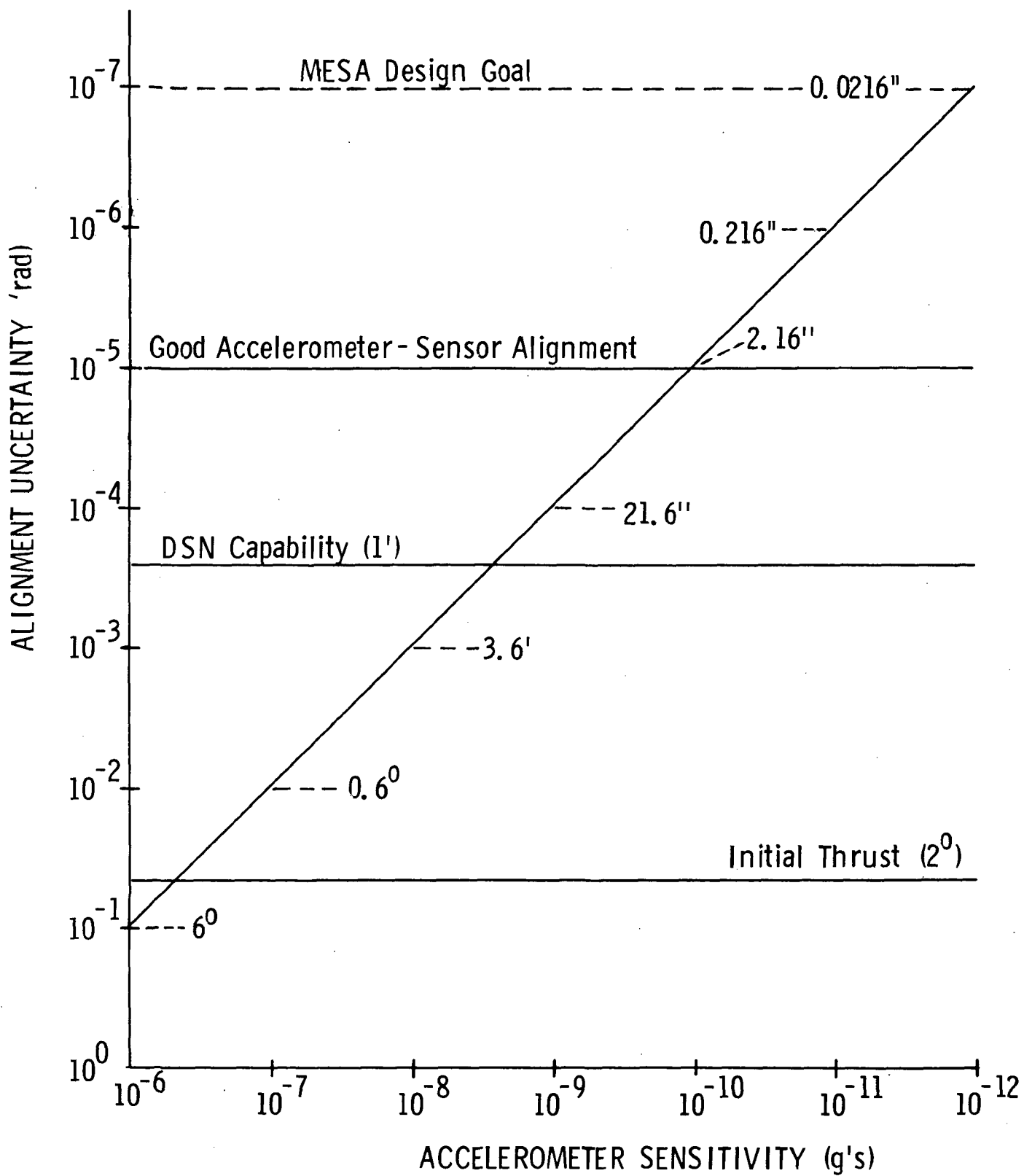


Fig. G.2 Thrust Alignment Hierarchy

Another possible accelerometer scheme uses a single low g accelerometer mounted on two degree of freedom gimbals with precision angle readout. If the single accelerometer were strapped down its output would be of little use because of the uncertainty in the thrust vector magnitude which would be indistinguishable from a misalignment uncertainty (unless, of course, by chance the accelerometer sensitive axis happened to be perfectly lined up with the thrust vector). If the accelerometer were gimbaled, it could be moved to maximize its output thus insuring alignment with respect to the thrust vector. Accelerometer alignment with respect to the altitude sensors could then be achieved with precision angle encoders.

Page intentionally left blank

REFERENCES

1. Explanatory Supplement to the Ephemeris, Her Majesty's Stationary Office, London, 1961.
2. Bryson, Jr., A.E., Ho, Y-C, Applied Optimal Control, Blaisdell Publishing Co., Waltham, 1969.
3. Hand, J., "Recent Advances in Star Tracker Technology," MIT Draper Lab Internal Memo, August 22, 1969.
4. Koso, D.A., Kollodge, J.C., "Solar Attitude Reference Sensors, Honeywell Internal Memo," October 15, 1969.
5. Fraser, D.C., and Malchow, H.L., "Onboard Navigation Instrument Requirements for Outer-Planet Flyby Missions, I.O.N. National Space Meeting, Moffet Field, California," February, 1970.
6. Manning, L.A., Letters to J.H. Flanders of MIT/IL, NASA/OART Mission Analysis Division, August 5, 1968 and October 8, 1968.
7. Mihm, J.J., "D4E-Vibrating String Accelerometer Research for Strapdown Navigation," NASA ERC Report GSC-67-02, October, 1967.
8. Wing, C. "MIT Vibrating String Surface-Ship Gravimeter", Journal of Geophysical Research, Vol. 74, No. 25, November 15, 1969.
9. Book, Robert O., "The Vibrating String Accelerometer," American Bosch Arma Corporation, March 1, 1968.
10. Sporn, S.R., "An Orbiting Velocity Meter," Arma Division American Bosch Arma Corporation, July, 1968.

11. Meldrum, M.A., Harrison, E.J., and Milburn, Z., "Development of a Miniature Electrostatic Accelerometer (MESA) for Low g Applications, NASA CR-54137," April, 1965.
12. Kerslake, W.R., Byers, D.C., Staggs, J.F., "SERT II Experimental Thruster System," AIAA paper No. 67-700, September, 1967.
13. Sohl, Gordon, and Fosnight, Verryl F., "Thrust Vectoring of Ion Engines", Journal of Spacecraft, Vol. 6, No. 2, February, 1969.
14. Dorroh, W.E., Jr., "Baseline Attitude Control Subsystem for the Thermoelectric Outer Planet Spacecraft", JPL Space Programs Summary 37-58, Vol. III.
15. DesJardins, R., "In Orbit Startracker Misalignment Estimation on the OAO," Goddard Space Flight Center Memo No. X-542-69-418, September, 1969.

R-678
Distribution

O. Anderson
R. Battin
P. Bowditch
S. Croopnick
J. Deckert
T. Edelbaum
P. Felleman
D. Fraser (50)
C. Gray
D. Gustafson
D. Hoag
P. Kachmar
A. Klumpp
B. Kriegsman
L. Larson
G. Levine
H. Malchow (5)
E. Muller
G. Ogletree
T. Parr
P. Philliou
P. Pollock
W. Robertson
L. Sackett(2)
N. Sears
W. Tempelman
MIT/CSDL Library (10)
Apollo Library (2)

R-678

Distribution - External

NASA Headquarters - Washington, D. C. 20546

OART

R/Mr. Oran W. Nicks
RP/Mr. Adelbert O. Tischler
RE/Mr. Frank J. Sullivan
REE/Mr. Charles E. Pontious
REG/Mr. Jules I. Kanter
REI/Mr. Gene A. Vacca
RES/Mr. Charles H. Gould
RET/Mr. Henry L. Anderton
RN/Mr. William H. Woodward
RNT/Mr. James Lazar
RMD/Mr. Richard J. Wisniewski
RR/Dr. Hermann H. Kurzweg
RV/Mr. Milton B. Ames, Jr.
REG/Mr. Theodore S. Michaels

OSSA

S/Dr. John E. Naugle
SS/Dr. Henry J. Smith
SL/Mr. Robert S. Kraemer
SL/Mr. Norri Sirri

OMSF

M/Mr. Dale D. Myers

Ames Research Center - NASA, Moffett Field, California 94035

Mr. C. A. Syvertson, Mail Stop 200-2
Dr. Leonard Roberts, Mail Stop 200-3
Mr. John S. White, Mail Stop 210-3
Mr. Charles F. Hall, Mail Stop 244-8
Mr. Howard F. Matthews, Mail Stop 244-7

Goddard Space Flight Center - NASA, Greenbelt, Maryland 20771

Mr. Donald P. Hearth, Code 100
Dr. Rydolf A. Stampfl, Code 401
Mr. Robert T. Groves, Code 551
Mr. Kenneth I. Duck, Code 734

Jet Propulsion Laboratory - 4800 Oak Grove Dr., Pasadena, Calif. 91103

Dr. Donald Rea, Mail Stop 180-404
Mr. Peter N. Hauran, Mail Stop 180-302
Dr. R. Rhoads Stephenson, Mail Stop 156-203
Mr. James Long, Mail Stop 180-302
Mr. Tom W. Hamilton, Mail Stop 180-402
Mr. John R. Scull, Mail Stop 198-226
Dr. James F. Jordan, Mail Stop 156-229
Dr. Roger D. Bourke, Mail Stop 126-235
Mr. Robert G. Nagler, Mail Stop 180-703

Langley Research Center - NASA, Langley Station, Hampton, Va. 23365

Mr. William H. Phillips, Mail Stop 152
Mr. George B. Graves, Jr., Mail Stop 476
Mr. Richard C. Dingeldein, Mail Stop 156

Lewis Research Center - NASA, 21000 Brookpark Road, Cleveland, Ohio 44135

Dr. Seymour C. Himmel, Mail Stop 173-303
Mr. Richard J. Wever, Mail Stop 501-302

Marshall Space Flight Center - NASA, Marshall Space Flight Center, Ala. 35812

PD/DIR/Mr. William R. Lucas
S&E-Aero-G/Mr. Clyde D. Baker
S&E-Aero-M/Mr. J. P. Lindberg

Outside Agencies

North American Rockwell
Space Division
12214 Lakewood Boulevard
Downey, California 90241

Mr. Robert Epple, D192-400
Mr. J. R. Eyman, BB77
Mr. E. J. Dazzo, BB57

Mr. George Townsend
North American Rockwell
Suite 143
3322 South Memorial Parkway, S. W.
Huntsville, Alabama 35801

TRW Systems Group
One Space Park
Redondo Beach, California 90278

Mr. H. F. Meissinger, R5/2291
Mr. Robert A. Park, R5/2291

Mr. Brian T. Howard
Director, Space Sciences and
Advanced Manned Missions Division
Bellcomm, Inc.
955 L'Enfant Plaza No. S.W.
Washington, D. C. 20024

Mr. Alan L. Friedlander
IIT Research Institute
10 West 35 Street
Chicago, Illinois 60616

Mr. B. Gentry Lee
Viking Projects Mission Analysis
SSB 8947
Martin Marietta Corp.
P.O. Box 179
Denver, Colorado 80201

Mr. B. Galman
Re-Entry and Environmental Systems Div.
General Electric Co.
3198 Chestnut Street
Philadelphia, Pennsylvania 19101

Mr. D. D. Fields
AVCO Systems Division
201 Lowell Street
Wilmington, Massachusetts 01887